APPLICATION OF CHIRAL CELLULAR MATERIALS FOR THE DESIGN OF INNOVATIVE COMPONENTS

A Thesis
Presented to
The Academic Faculty

by

Alessandro Spadoni

In Partial Fulfillment
of the Requirements for the Degree
Doctor of Philosophy in the
School of Aerospace Engineering

Georgia Institute of Technology
December 2008

APPLICATION OF CHIRAL CELLULAR MATERIALS FOR THE DESIGN OF INNOVATIVE COMPONENTS

Approved by:

Dr. Massimo Ruzzene, Advisor
School of Aerospace Engineering
Georgia Institute of Technology

Dr. S. Hanagud
School of Aerospace Engineering
Georgia Institute of Technology

Dr. D. H. Hodges
School of Aerospace Engineering
Georgia Institute of Technology

Dr. M. J. Leamy
School of Mechanical Engineering
Georgia Institute of Technology

Dr. D. L. McDowell
School of Mechanical Engineering
Georgia Institute of Technology

Date Approved: August 21, 2008

To my beautiful wife Tiffany,

my mother Maria.

ACKNOWLEDGEMENTS

I am most grateful to two people in particular for guiding me and supporting me through the strenuous endeavor of graduate school, the greatest achievement of my professional life. The first is my advisor Dr. Massimo Ruzzene with whom I began working as an unproven undergraduate student. I would like to thank him for the endless conversations, unconditional availability and his trust. I am also deeply appreciative for the vast scientific exposure I received, well beyond the achievements presented in this thesis. I am certain this will benefit me considerably. I am also very thankful to him for the extracurricular activities in which I participated, such as a wonderful summer visit at the Politecnico di Milano and many engineering conferences. I realize now this is no ordinary guidance.

The second person to whom I owe my most recent achievements is my wife Tiffany. She has believed in me unconditionally and taught me that extraordinary accomplishments are within reach and only dependent upon one's desires. These are great gifts that so deeply changed my life outcome. I also would like to express my infinite gratitude to her for setting aside her own ambitions for the past eight years, to support both my undergraduate and graduate degrees. I wish my diplomas could bear her name also.

I must thank Dr. Hanagud for the many personal and professional conversations, in addition to his enthusiasm and vast knowledge provided in his engineering courses that I attended.

I also would like to thank my Thesis Committee Members for dedicating me their time and providing me with insightful comments, instrumental for the completion of this Thesis.

I finally sincerely appreciate the critical help I received from my French teacher Cristina Riccobon.

TABLE OF CONTENTS

LIST OF TABLES

LIST OF FIGURES

SUMMARY

Low-density cellular solids have demonstrated superior mechanical properties as well as multifunctional characteristics, which may provide a basis for the development of novel structured materials. In particular, cellular solids offer great design flexibility, owing to their topology, which can provide desired functionalities via targeted geometric design and proper selection of the constituent material. While stochastic configurations such as metallic foams have proven to be effective for both thermal insulation and mechanical-energy absorption, the topology of deterministic architectures is not constrained by physical processes. This allows for a variety of configurations to be tailored to simultaneously fulfill disparate tasks. An additional aspect of deterministic cellular structures is the possibility of assembling materials or structures by the spatial repetition of a unit cell. The resulting periodicity of such systems simplifies the characterization of physical properties, which can be established by analyzing the unit cell only, and will provide new opportunities in the fields of structural dynamics, where periodicity-induced impedance leads to the control of both constructive and destructive interference on propagating waves.

The objective of this work is to investigate the application of the chiral cellular topology for the design of novel macrostructural, mesostructural and microstructural configurations. A truss-core airfoil, and a truss-core beam are employed as a basis to demonstrate both large-displacement capabilities within the elastic regime of the constituent material, as well as operational deflection shapes with localized dynamic deformations. Large deformation capabilities and unique operational deflection shapes are to be attributed to the unusual deformation mechanism of the chiral lattice.

Mesostructural and microstructural configurations, on the other hand, are characterized by an unique mechanical behavior, complex geometry, as well as geometric design flexibility to control both static and dynamic phenomena. The propagation of elastic waves, moreover, is characterized by significant band-gap density as well as strong energy focusing dependent on frequency and wavenumber. These features suggest the chiral topology as a basis for the development of acoustic meta-materials.

CHAPTER I

INTRODUCTION

Low-density cellular solids have demonstrated superior mechanical properties as well as multifunctional characteristics, which can be exploited for the development of novel structured materials. In particular, cellular solids offer great design flexibility, owing to their composition, which can provide desired functionalities via targeted geometric design and proper selection of the constituent material. While stochastic topologies such as metallic foams have proven to be effective for both thermal insulation and mechanical energy absorption, the topology of deterministic architectures is not constrained by physical processes, such as chemical reactions, thus allowing for a variety of configurations to be tailored to simultaneously fulfill disparate tasks. Deterministic cellular structures, indeed, can be designed to achieve a larger set of desirable characteristics than currently possible with their stochastic counterparts. An important aspect of deterministic cellular configurations is the possibility of assembling materials, or structures, by the spatial repetition of a unit cell. The resulting periodicity of such systems simplifies the characterization of physical properties, which can be established by analyzing the unit cell only, and will provide new opportunities in the fields of structural dynamics, where periodicity-induced impedance zones leads to constructive and destructive interference of propagating waves.

1.1 Objectives

This work explores the application of the chiral cellular topology, first presented by [76] and depicted in fig. 1, for the design of novel structural concepts. The considered geometry features a number of interesting and unique properties which include a

negative, in-plane Poisson's ratio, a geometry determined by a relatively large number of parameters which can be independently adjusted to tailor the behavior of the assembly, and a unique deformation mechanism that allows large deformations within the linear regime of the constituent material [76].

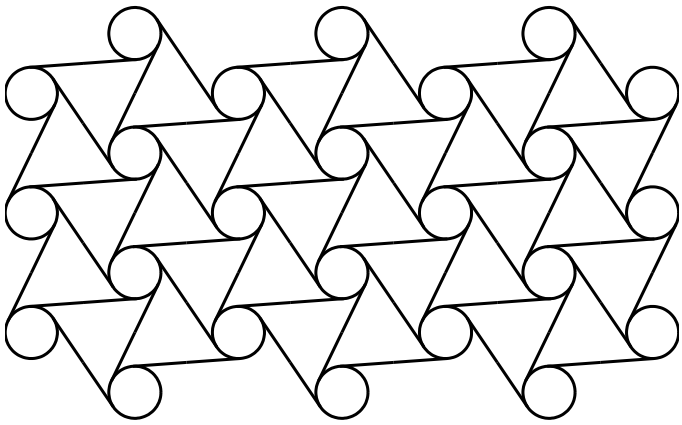

Figure 1: Chiral geometry

Specifically, this work investigates the application of the chiral topology as part sandwich panels with novel core configuration (fig. 2.a), truss-core structures with static and dynamic morphing capabilities (fig. 2.b), as well as phononic lattices as acoustic meta-materials (fig. 2.c).

The considered applications span various scales and deformation regimes, and are here classified as macro-scale, meso-scale and micro-scale. This classification relies on the dimensions of the unit cell with respect to those of the structural component. Specifically, the truss-core airfoil is considered as a macro-scale application of the topology at hand, since the unit cells have dimensions comparable to that of the airfoil. Sandwich structures are considered as meso-scale applications, due to the fact that the cells are small compared to the overall honeycomb panel, and that the mechanical behavior of the assembly can be described through homogenized properties defining an equivalent-continuum material of analogous behavior. Finally, the phononic configuration is denoted as micro-scale application of the chiral lattice for

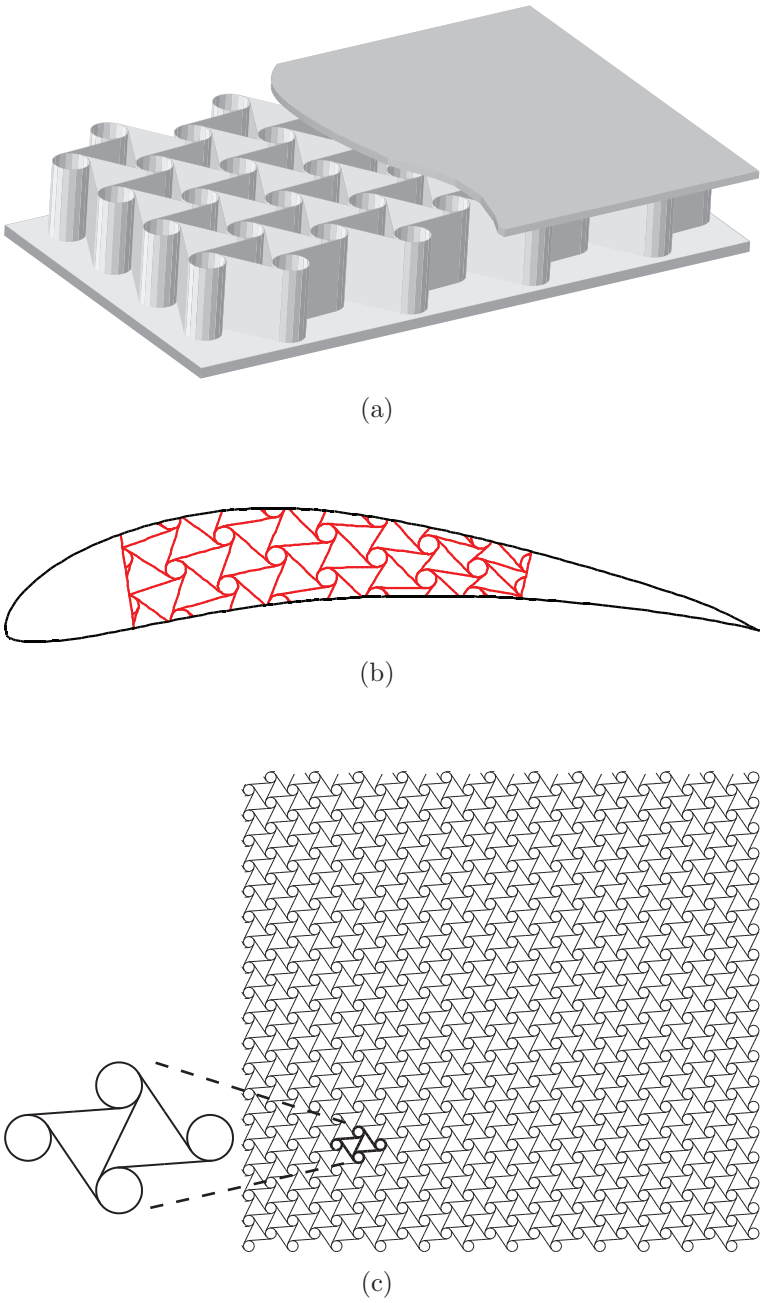

Figure 2: Sandwich panel with chiral-honeycomb core (a), truss-core airfoil (b) and phononic chiral lattice (c)

two reasons. First, the unit cell size is typically small compared to the overall phononic device, and second, the anomalous wave propagation characteristics which make this class of structures interesting from a scientific and a practical standpoint mostly rely on deformations internal to the unit cell, which cannot be easily captured by current

homogenization techniques and equivalent-continuum modeling procedures.

The remainder of this chapter is devoted to brief introductions to the state-of-the-art in the areas where the application of chiral topology is proposed, namely cellular materials for sandwich construction, morphing structures, and acoustic metamaterials.

1.2 Cellular solids

Cellular solids are both naturally-occurring and man-made materials or structures, depending on the characteristic length scale, and may feature both ordered (or deterministic) and disordered (or stochastic) topologies, two examples of which are shown in fig. 3. Both stochastic and deterministic instances are characterized by assemblies of cells with solid boundaries, which may be beam-like and plate-like components yielding open and closed-cell configurations respectively [40]. Metallic foams, for

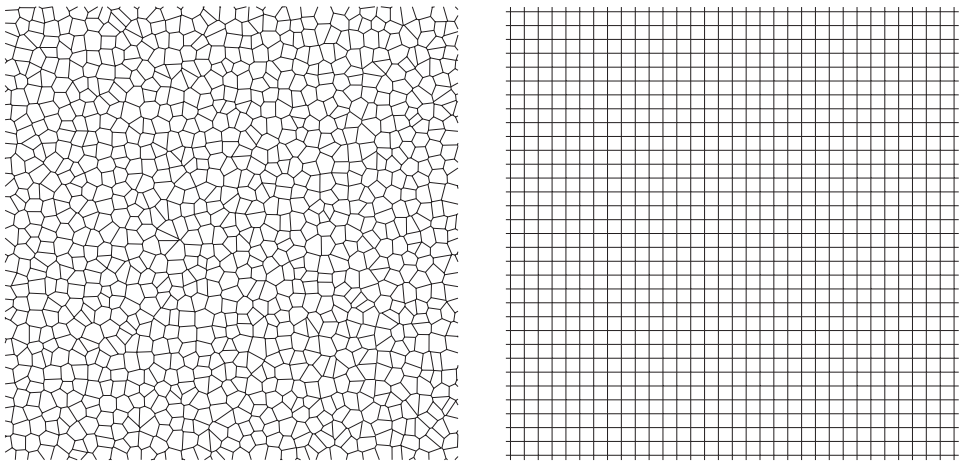

(a) Voronoi honeycomb (b) square lattice

Figure 3: Stochastic (a) and deterministic (b) cellular solids

example, may feature both open and closed-cell arrangements as depicted in fig. 4. Cellular solids, moreover, feature a two-phase composition comprising a solid part encapsulating the second phase, usually a liquid or a gas. The solid portion contributes most of the effective density, while the liquid or gaseous phase contributes most of

the occupied volume. Cellular solids, thus, boast a low relative density, usually lower than 30% than that of the constituent material of the solid phase. Two-phase materials with higher relative density are known as porous solids [40]. Naturally-occurring cellular materials usually feature heterogenous (or amorphous) topology, while for their man-made counterpart stochastic as well as deterministic arrangement of the solid phase is possible. Stochastic topologies are prevalent in cellular foams, like the instances illustrated in fig. 4, while deterministic configurations are most common in honeycombs (2-D cellular assemblies), characterized by the spatial repetition of a unit cell. The novel chiral topology depicted in fig. 1, hence, represents a deterministic

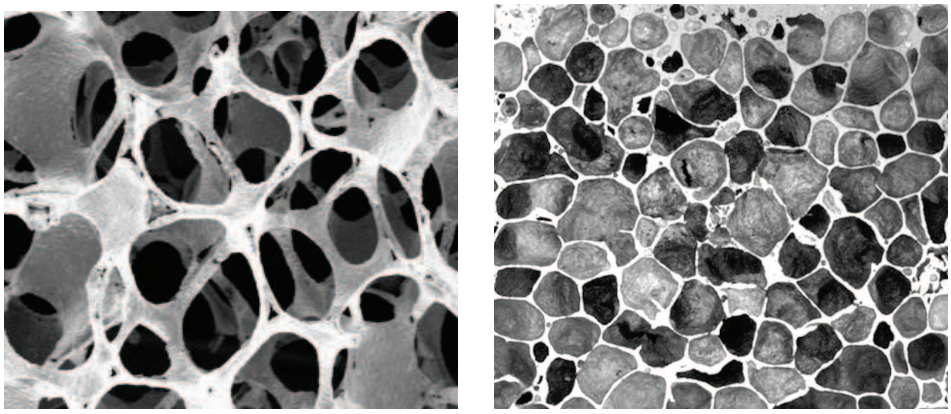

(a) (b)

Figure 4: Open (a) and closed-cell (b) metallic foams

cellular structure.

1.2.1 Applications of cellular solids

The wide-spread use of cellular solids in the aerospace, automotive, and naval industries, among others, is to be attributed primarily to unique physical properties: low relative density, low electrical conductivity, low Young's modulus and strength [40]. Low density facilitates the design components with high specific (mass-normalized) stiffness, and provides effective thermal insulation [40, 49]. The latter is to be attributed to the low conductivity of the second phase, most often a gas. Low density

also ideal for naval applications where buoyancy and specific stiffness are required [40]. Low strength is very advantageous in applications where mechanical-energy absorp-

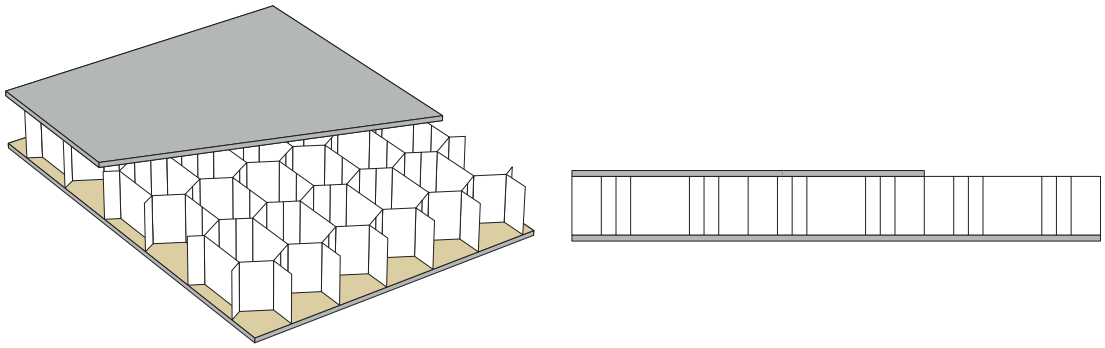

(a) prospective view (b) side view

Figure 5: Hexagonal-honeycomb-core sandwich panel

tion is paramount. This may be the case of crushworthy materials, or of packaging materials for sensitive components, where foams are most applicable [40, 102]. The most recognizable application, however, is that of sandwich panels, one example of which is illustrated in fig. 5. This particular use of cellular structures exploits the high specific stiffness of the honeycomb core, as well as optimal distribution of inertia to produce components with extremely high bending stiffness [40, 102]. Such panels were first adopted by the aeronautical industry [47, 48, 102] but have since become less expensive, and common in the naval, automotive and wind-turbine industries, to name a few [102]. The introduction of affordable core materials and bonding techniques is responsible for widespread utilization of sandwich panels [102], which may feature both foam or honeycomb cores.

Potential improvements in performance of sandwich panels introduced by utilizing the chiral honeycomb, and their implications given the widespread use of such components, motivate the fully characterization of both in-plane and out-of-plane mechanical properties of chiral structures. Particularly, a negative, in-plane Poisson's ratio may facilitate the manufacturing of curved panels [102]. The strong dependency of mechanical properties on a reduced set of geometric parameters suggests design

flexility that may allow tailoring of the mechanical properties for a given application.

1.2.2 Manufacturing techniques

The topology and constituent material of cellular solids determine their performance for any given application. Cost and the challenges presented by the manufacturing of cellular materials, however, lead to restricted available configurations, especially for deterministic arrangements such as honeycombs. Most commercially offered honeycombs, in fact, are made either by corrugation or by expansion [102]. In the first case metal sheets are pressed into a predetermined form, and subsequently glued together, as shown in fig. 6. Blocks of required thickness can then be cut from the stack. The corrugation process is widely adopted when manufacturing metallic cores [40, 102]. The expansion process, on the other hand, is mostly employed to manufacture non-

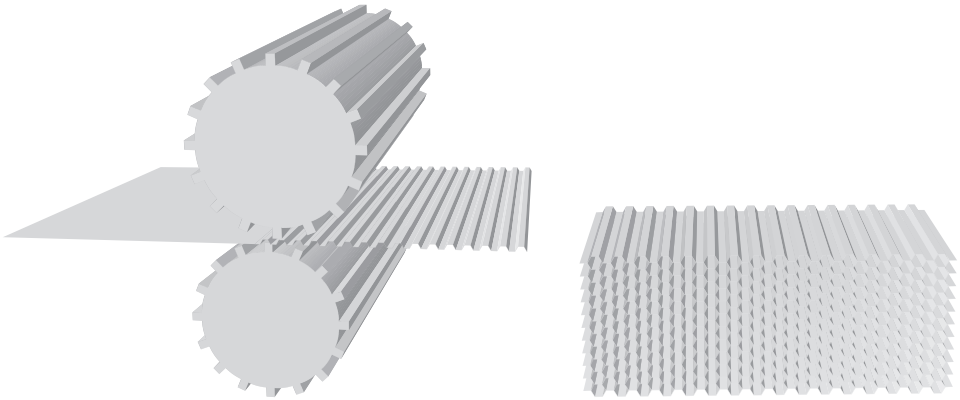

(a) pressing/corrugation (b) completed stack

Figure 6: Corrugation process

metallic cores, such as paper-resin, by first gluing multiple sheets in a predetermined pattern. Upon curing of the adhesive, the stack is pulled in its transverse direction, or expanded, to obtain the desired core configuration [102], as illustrated in fig. 7. As a result, industrial manufacturing techniques have produced core arrangements featuring hexagonal geometry or a variation thereof [102]. Cellular foams, conversely,

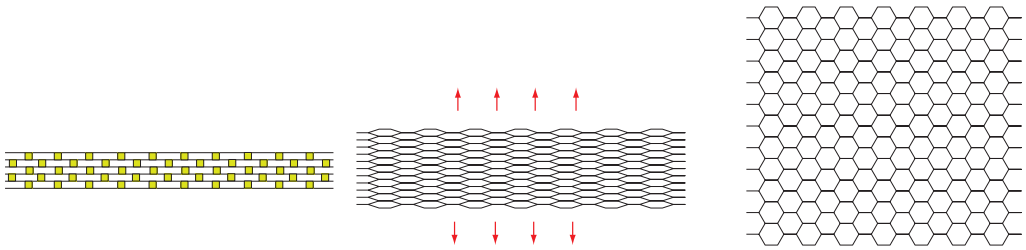

(a) expansion process (b) completed core

Figure 7: Expansion process

benefit from a larger pool of manufacturing techniques as well as constituent materials. Polymeric cellular foams, for example, are obtained by introducing gas bubbles into the liquid monomer or hot polymer. Cooling stabilizes the gaseous phase and hardens the polymer yielding both open or closed-cell foams, depending on the particular process used [40]. Metallic foams are usually created by melting hydride compounds which release hydrogen gas. Subsequent cooling produces the desired metallic foam [40], two examples of which are depicted in fig. 4. Many materials, in addition to polymers and metals, may be used to obtain foams, and a significant number of manufacturing processes [40] complements the examples cited in this work.

1.2.3 Novel cellular solids and their applications

The excellent mechanical properties of honeycomb sandwich panels, such as high stiffness perpendicular to the faces and highest specific shear stiffness and strength of all available core configurations (including foams), have enticed ambitious multifunctional designs to re-evaluate and expand the capabilities of honeycomb-core components. This has led to both novel configurations and their application. A number of innovative core geometries such as open-cell deterministic metallic structures have been analyzed to maximize specific stiffness and heat dissipation in [34, 35], in addition to setting forth performance benchmarks for the next generation of periodic structures. The advantages of periodic structural components offering a combination

of desirable physical properties have suggested their use for multifunctional, multidisciplinary applications, beyond sandwich panel arrangements. A combination of low relative density, superior thermal insulation, and mechanical-energy absorption capabilities, for example, are investigated in [35] for envisioned multifunctional designs, which consider manufacturing constraints also. Among the recently proposed core geometries, periodic configurations such as triangular and mixed-cell lattices, depicted in fig. 8, promise superior in-plane mechanical properties [97]. Interest in cellular structures for multifunctional applications is also confirmed by proposed multi-field performance indices set forth in [34].

Most periodic core topologies suggested above, however, require manufacturing processes that are still not commercially available. The capabilities offered by corrugation and expansion processes (figs 6 and 7), in fact, do not lend themselves for producing even relatively simple core geometries such as the triangular and mixed-cell honeycombs suggested in [96] (fig. 8). Consequently, new manufacturing methods, albeit still in their research stage, have been proposed. In particular, low-melting point

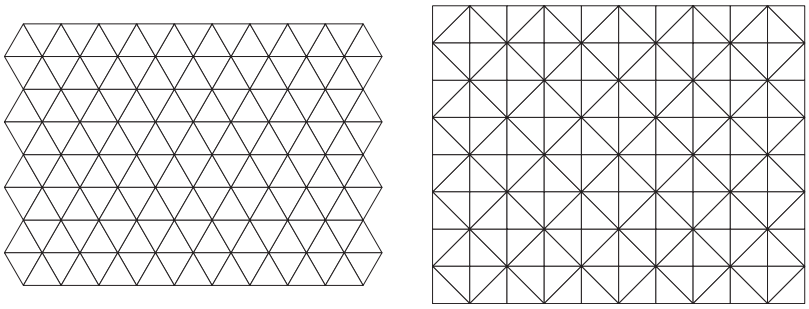

(a) (b)

Figure 8: Triangular (a) and mixed-cell (b) core geometries

materials lend themselves to mould-casting, such as resins and silicones. Extrusion processes whereby lasers are used to solidify polymer or resins compounds are also surfacing [40]. The most encouraging manufacturing technique, proposed in [96], entails the forcing of a ceramic-oxide paste through a die, followed by reduction in a

hydrogen atmosphere and subsequent sintering. This process permits the fabrication of metallic honeycombs of any configuration [96], including those depicted in fig. 8.

Plane sandwich panels such as the one depicted in fig. 5 are easily manufactured, but curved panels are quite difficult to assemble due to Poisson effects when the core is forced to curve [102]. This hurdle may be overcome by employing core geometries featuring zero or negative, in-plane Poisson's ratios [102]. Negative Poisson's ratio is characteristic of re-entrant configurations, proposed by [14], such as the one illustrated in fig. 9, while zero in-plane Poisson's ratio is achieved by employing the square honeycomb [40] as the core component (fig. 3.b).

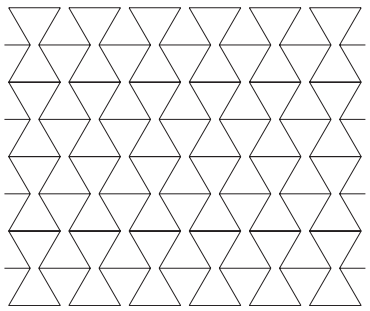

Figure 9: Re-entrant geometry

The advantages of $\nu \approx 0$ lie in the ability to bend a sheet of core into a cylinder only through the application of a unidirectional bending moment. In the case of negative, in-plane Poisson's ratio, on the other hand, the reaction to a unidirectional moment is a synclastic curvature (positive curvature in both plane directions) [36, 102], permitting dome-like core configurations. Finally, a positive, in-plane Poisson's ratio, as in the case of the hexagonal honeycomb depicted in fig. 7, would produce anticlastic (opposite curvature in plane directions or saddle-like) curvature, making core shaping difficult, owing to significant stress during the forming procedure. As a result of curvature considerations, both re-entrant (fig. 9) and chiral (fig. 1) topologies may be attractive alternatives to traditional geometries.

Additional configurations exploiting periodic cellular solids are offered by prismatic structures, which comprise face sheets as well as a core which is rotated by 90° with respect to that of a sandwich panel to form a truss-like structure. Prismatic configurations of the kind depicted in fig 10 have been proposed as effective heat sinks [21], since they offer high surface-area-to-volume ratio and can be manufactured with high-conductivity walls. Additionally, they offer all the advantages

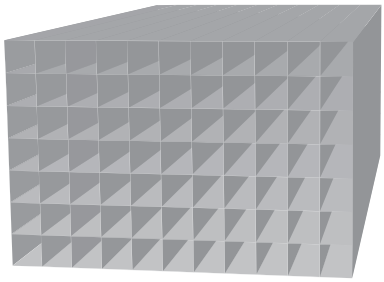

Figure 10: Prismatic structure

provided by the mechanical properties of low-density cellular solids, such as high specific stiffness and strength [33]. Their use as multifunctional components, able to dissipate thermal energy as well as to carry loads, is effective in reducing complexity and improving performance for electronic cooling devices [21] .

All applications described so far in secs 1.2.1 and 1.2.3 propose the use of cellular solids as static components. Recently, however, 2-D prismatic or truss-core structures have been investigated as possible sound-reduction panels. Sound reduction and vibration-transmission-loss performance of a square, truss-core panel, such as the one depicted in fig. 11.a, has been characterized by [31]. A comparison of the same performance indices for more complex core geometries is presented in [80]. Both studies have deemed truss-core panels as viable assemblies for effective sound absorption and vibration reduction, indicating intra-cell resonance as the principal vibration and sound-attenuation mechanism.

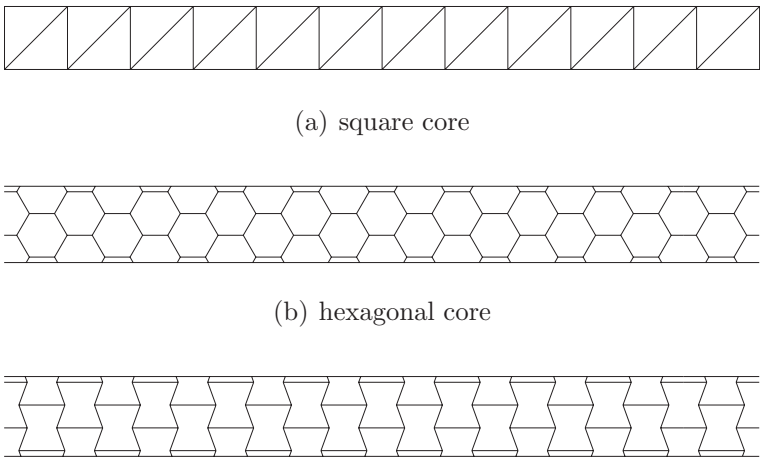

(a) square core

(b) hexagonal core

(c) re-entrant core

Figure 11: Truss-core assemblies

The most exciting opportunities offered by periodic solids, yet, may lie in the ability to control elastic-wave propagation/attenuation. The periodicity of deterministic cellular solids, in fact, is associated with both constructive and destructive interference phenomena which, depending on the wave-length and frequency of the propagating waves, generate frequency bands where elastic waves are free to propagate (pass bands), and frequency bands where elastic wave amplitude is attenuated (stop bands or band gaps). Investigations by [75] have characterized the pass-band/stop-band behavior of 2-D periodic lattices, the triangular, square and hexagonal topologies in particular. The triangular lattice, shown in fig. 8.a, is found to produce a significant stop band at low frequencies (within the first three waves-modes), while the square and hexagonal layouts do present stop bands albeit for higher wave modes. The work presented in [82], moreover, has indicated that elastic waves propagate in preferential directions for certain frequencies and wavelengths, even though the underlying 2-D lattice may be statically isotropic. The same dynamic behavior is found in sandwich panels with honeycomb core [81], such as the one illustrated in fig. 5.

In light of the recent interest and discoveries regarding the propagation of elastic

waves in periodic lattices, the complex geometry and unusual mechanical behavior of the chiral lattice are expected to yield a rich dynamic behavior, possibly offering significant stop/pass band capabilities. The design flexibility featured by the chiral geometry, and the strong topological dependence of mechanical behavior, furthermore, may be exploited for the design of novel acoustic meta-materials.

1.3 Morphing structures

The design of deformable systems may be driven by kinematic or mechanical considerations, according to the manner in which the system's deformations take place. Deformations may be desired to alleviate structural stresses, they may be passive in nature and arise from low structural stiffness, or they may be actively induced, as in the case of structural mechanisms. Often, the ability of a structural system to deform is coupled with stringent requirements mandating high specific stiffness, which are common in applications for which weight considerations are paramount. Multifunctional solutions, however, require a combination of stiffness and compliance in a given component, both to withstand loads as well as to adapt or reconfigure to changing operating conditions. This currently appears to be a paradox as stiffness and compliance are reciprocal of each other. The challenge at hand is to obtain low-complexity structural systems, intrinsically capable of adapting to disparate operating environments as well as possessing stiffness and strength attributes.

A widely accepted definition for a morphing structure is a system or assembly capable of withstanding or producing large deformations, in addition to bearing loads. To this day, operating conditions requiring highly reconfigurable systems have been addressed with the use of structural mechanisms. Aircraft, for example, feature wings with a variety of slats and flaps which are controlled by distributed servo motors, or in the simplest cases by cables and pulleys. The result is a system with few essential

degrees of freedom which may not guarantee efficiency over the entire operational envelope. Improvements to achieve higher efficiency and adaptability are sought by the latest efforts in the design of flying vehicles, which envision continuous structural deformations [67, 99], perhaps employing biologically inspired solutions/materials [39]. At present, a number of solutions are proposed as morphing structures: tensegrity structures, elastically-tailored structures, active structures controlled by distributed sensor-actuator systems, multi-stable composites, as well as inflatable components.

Tensegrity structures are comprised of a set of discontinuous compressed struts, usually a truss-like structure, held together with a continuous web of tensioned cables [70]. They are currently appealing candidates for applications that emulate biological-propulsion methods, such as the flapping tail fin of fish. The major challenge in their design is determining the optimal distribution and the length of struts. This is called form finding [92]. In the case of elastically-tailored structures, mechanical coupling between distinct deformation modes is exploited; favorable coupling between bending and torsion [46, 52], for example, is utilized in morphing wind-turbine blades [6].

Integration of motion and force transmission through elastic deformation is achieved with joint-less monolithic devices called compliant mechanisms [93, 94]. According to [94], compliant mechanisms use flexure and deformation to transmit motion and forces, rather than rigid bodies with conventional mechanical joints, providing several benefits such as elimination of mechanical joints, joint-wear, and joint-clearance. This design paradigm is inspired by nature, where strength and compliance are observed in its designs, as opposed to the goal of strength and stiffness employed in traditional engineering. A hybrid solution comprising of a Kagomé active back plane supporting a face sheet is proposed as a morphing system [25, 26]. Target deformations are achieved by a distribution of actuators that replace some of the truss members. As in the case of tensegrity structures, the distribution of actuators represents the main

challenge [26].

Multi-stable composites take advantage of local minima and maxima of their buckling and post-buckling stability to achieve target deformations [52]. In particular, snap-through phenomena are exploited to transition from the base to the target shape while remaining in the linear range of Hooke's Law [20, 84]. The advantage of this method lies in the limited actuation energy needed to initiate snap-through. The main drawback is control of transition speed from the base to the target configuration (this may require externally induced damping), and more importantly only a limited number of configurations can be achieved.

Inflatable structures are composed of very light membrane-like materials working in tension resulting from internal pressure. Inflatable structures are very resilient to damage from sudden deflection, due to very low inertia, and return to their original design shape after a sudden loading event. Furthermore, they can withstand very large deformations suggesting a hyperelastic stress-strain relationship. At present, inflatable structures are proposed for reconfigurable components such as wings [15, 87], although their load-carrying capabilities appear limited.

Morphing structures are hence an essential component in the quest for truly effective, adaptable structures. The development of new materials can alleviate drawbacks, as well as broaden the capabilities of each of the solutions presented above. To this end, researchers are working on a wealth of promising materials, such as electroactive polymers [5], advanced composites [52], and cellular structures [40] among others. The chiral arrangement, in particular, may enhance current jointless monolithic designs through its unusual deformation mechanism, and its ability to undergo large deformations while in the linear regime of the constituent material makes.

1.4 Phononic Metamaterials

An effort to expand advantages offered by periodic layouts is represented by engineering materials that gain their properties from their structure rather than directly from their material composition [98]. While this characteristic may be attributed to any man-made structured material, such as metallic foams for example, the label metamaterial was initially used to denote materials that exhibit negative electromagnetic refraction [55]. In applications engaging quantum or elasto-dynamic phenomena, metamaterials derive their peculiar wave interaction and propagation properties from embedded resonant structures. Recently, the excitement surrounding meta-materials producing exotic propagation of electromagnetic waves, however, has extended to the field of acoustics, and the propagation of elastic waves. Negative refraction of impinging sound waves, in fact, has been deemed possible if resonance structures are employed in the equivalent material [63]. Particularly, negative refraction of elastic waves may be attained by a double negativity in both density and bulk modulus [63]. This would provide the ability to focus or de-focus transmitted and diffracted waves.

Currently, structural systems engineered to manipulate elastic wave phenomena, known as phononic crystals, gain their authority from mass and/or stiffness periodic modulation in a composite material to obtain scattering and impedance mismatch zones. The width and center frequency of a given stop band are respectively associated with differences in impedance and characteristic length scale in the multi-phase material [73]. Phononic crystals generally comprise a solid phase and a liquid or gaseous phase. The material choice is usually driven by the desired impedance mismatch, while material arrangement and the period of repeating irreducible units determine direction, velocity and angular frequency of propagating waves. Thin-walled cellular solids have recently attracted significant attention because they provide an additional degree of freedom in the design of phononic crystals [75, 81, 82]. The mere mechanical behavior of internal components yields a complex impedance pattern, perhaps

not achievable with traditional phononic devices. The resonance of internal members provides complex interference patterns controllable by selecting the length scale of internal components as well as the global mechanical behavior of the cellular solid. Resonating internal members, moreover, provide authority over wave propagation characteristics even for wavelengths smaller than the characteristic length of the unit cell. This for example is not easily achievable with traditional phononic crystals [73]. The findings in [75, 81, 82], moreover, suggest that periodic cellular solids are also capable of focusing energy in preferential directions due to caustics [101].

The complex geometry of the chiral lattice may provide selective resonance components within the lattice, as well as a rich dynamic behavior, attributes that may prove useful toward achieving phononic meta-materials.

1.5 Organization of the work

An introduction to the characteristics that define chiral media and auxetic structures and the repercussions of such attributes, in addition to hexagonal symmetry, on mechanical behavior is offered in chapter 2. An analysis of the chiral lattice devoted to determining the equivalent, in-plane elastic constants is discussed in chapter 3. The analysis is based on previous findings only addressing stiffness properties documented in [76]. The effective Poisson's ratio and shear modulus are established through an analytical unit-cell model as well as through macro-lattice, finite-element simulations. The mechanical behavior of chiral topologies is also compared to that of the square, triangular and hexagonal lattices. The equivalent, out-of-plane, elastic properties are determined in chapter 4 via a 2-D unit cell analysis and are refined to include effects of out-of-plane thickness with the aid a numerical model. Opportunities offered by the unusual deformation mechanism and large-deformation capabilities of the chiral structure are addressed in chapter 5. Specifically, a chiral truss-core airfoil is analyzed

to determine both passive and active-morphing performance. Experimental measurements of both aluminum and composite-material samples are employed to confirm large camber-wise deflections with the elastic regime of the constituent material. In chapter 6, the dynamic morphing associated with unique operational deflection shapes of a truss-core beam is investigated numerically and experimentally. Chapter 7 is devoted to investigating the phononic performance of the chiral lattice, which is found to be denoted by stop bands of significant extent within the first 10 wave modes. The ability to guide elastic waves along preferential directions resulting from caustics is also demonstrated. A summary of the findings of the research proposed in this thesis, as well as opportunities for future work are provided in chapter 8.

CHAPTER II

GEOMETRY AND DESCRIPTION OF HEXAGONAL CHIRAL LATTICES

2.1 Introduction

The objective of this thesis is to uncover the equivalent mechanical properties, elasto-dynamic behavior, and possible applications of the structural arrangement depicted in fig. 12 known as hexagonal chiral lattice. The attribute hexagonal stems from the lattice's six-fold geometric symmetry in the plane, while chirality indicates a topology non-invariant to reflections. This lattice is a deterministic cellular solid which features a negative in-plane Poisson's ratio, a characteristic of auxetic materials. It is thus helpful at this point to specify what properties make a lattice chiral and/or auxetic. This chapter is hence devoted to introducing the characteristics that define chiral media and auxetic structures and the repercussions of such attributes, in addition to hexagonal symmetry, on mechanical behavior. A brief historical background with respect to man-made, chiral-materials development as well as naturally occurring examples are offered to provide a context for the research presented in this thesis.

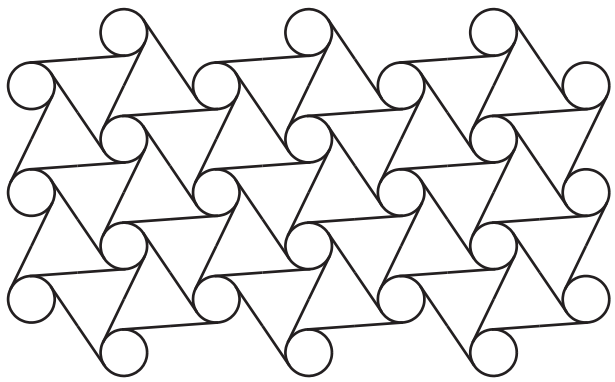

Figure 12: Hexagonal chiral lattice

2.2 Chirality

The first definition of *chirality* (from the Greek *cheir* = hand) or handedness has eloquently been offered by Lord Kelvin in [54], as:

> *I call any geometrical figure, or group of points, chiral, and say it has chirality, if its image in a plane mirror, ideally realized, cannot be brought to coincide with itself.*

Chirality, as it applies to the particular configuration studied in the following chapters, is pictorially represented in fig. 13. The lattice and its mirror image in the xy-plane, or $(x, y, z) \mapsto (x, y, -z)$, are clearly not equal. The lack of reflection symmetry in the

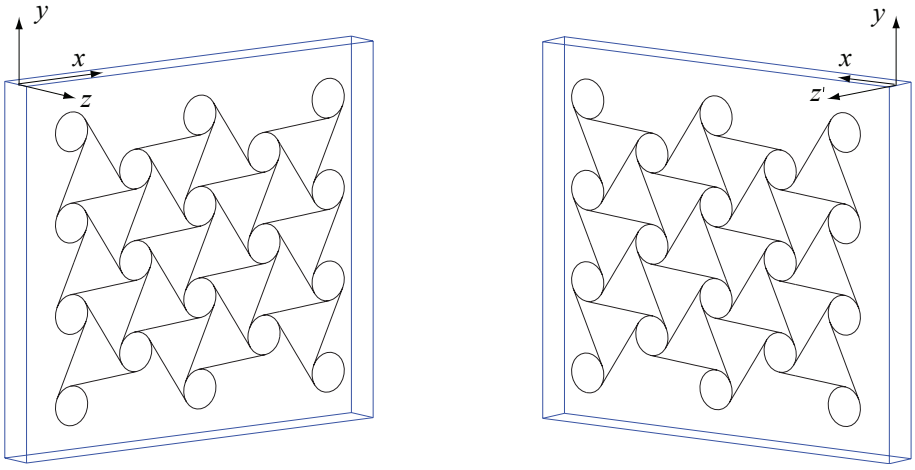

Figure 13: Implication of chirality

xy-plane however does not affect the mechanical properties, so long as Hooke's law is expressed by symmetric stress and strain tensors [76]. This is certainly the case of *Classical Elasticity Theory* as elucidated in [64]. Employing Einstein's notation, Hooke's Law in stress-strain form may be expressed as:

$$\sigma_{ij} = C_{ijkl}\epsilon_{kl}, \tag{1}$$

where C is the elastic modulus tensor. The transformation law for the modulus tensor under coordinate changes is [76]:

$$C'_{ijkl} = a_{im}a_{jn}a_{ko}a_{lp}C_{mnop}, \tag{2}$$

where a's are transformation matrices. For an inversion, the transformation matrix is the negative of a Kronecker delta, yielding $a_{im} = -\delta_{im}$. This produces:

$$C'_{ijkl} = (-1)^4 C_{ijkl} = C_{ijkl}. \tag{3}$$

So the classical elastic modulus tensor is unchanged by chirality [76]. This does not indicate that Classical Elasticity Theory is not applicable, but rather that it does not capture the causes of the particular mechanical behavior associated with chiral media. Generalized continuum theories, on the other hand, contemplate anti-symmetric strain and stress tensors and are capable of capturing mechanical behavior unique to chiral materials [61].

2.3 Auxetic materials

The attribute *auxetic* (from the Greek *auxetos*) is associated with materials that transversally expand when stretched and transversally contract when compressed [37], thus featuring a negative Poisson's ratio. A negative Poisson's ratio per se is not an exotic proposition. Instances of negative-Poisson's-ratio media have been observed and accepted in highly anisotropic materials, such as the cubic "single crystal" pyrite proposed by [64]. Another example is that of the re-entrant honeycomb of fig. 14, an auxetic cellular solid [40]. More interestingly, it is theoretically admissible for an isotropic material to feature auxetic behavior based on energy considerations from the Theory of Elasticity, which indicates that for an isotropic solid $-1 < \nu < 1/2$ [38]. Practical examples of isotropic, auxetic materials had not been common occurrences up to the seminal paper by Lakes [58], which demonstrates that a negative Poisson's ratio is practically achievable even in elastically isotropic materials such as metallic

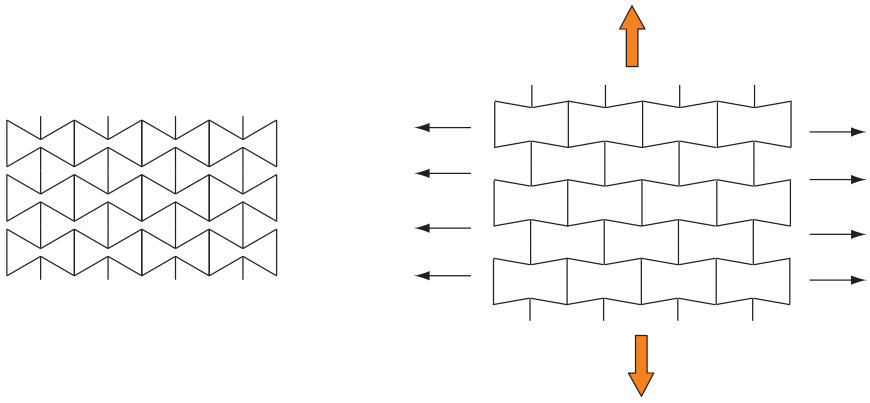

Figure 14: Re-entrant lattice featuring negative Poisson's ratio ν

foams. Among isotropic media, however, auxetic behavior represents a rarity which is to be attributed to two aspects of a material's microstructure: the presence of rotational units and non-affine deformation kinematics [59]. Non-affine kinematics denotes the behavior of a system whose pairs of internal nodal points move apart during stretching while others do not. This is the case of re-entrant, 2-D honeycombs, shown in fig. 14, as well as re-entrant metallic foams [40, 58]. The deformed configuration of a stretched re-entrant lattice (fig. 14.b) clearly demonstrates that points that make up vertical walls feature negligible relative displacements, while points pertaining to the oblique walls move away from each other as the assembly is expanded. The metallic foams featured in [58] are 3-D examples of re-entrant lattices, and thus their auxetic properties are to be attributed to non-affine kinematics also. Rotational units appear in structures or materials which produce internal macro or micro-rotations when loaded even by direct stresses only [59]. Chiral materials often give rise to such phenomena, as many occurrences of chirality are typical of assemblies with non-central forces. This indicates that, as in the case of the lattice depicted in fig. 12, forces not meeting at a common locus produce moments which in turn trigger micro or macro-rotations. Beyond the theoretical notions set forth

by eqs. (2) and (3), demonstrating that Classical Elasticity Theory is unable to capture the effects of chirality, the lack of rotational degrees of freedom in the same theory provides a practical reason for its shortcomings. Refined elasticity theories, such as Micropolar Continuum Theory [32] among others, in fact contemplate the presence of such degrees freedom in all instances. Their employment in engineering structural analysis yet has not achieved broad acceptance owing to the difficulty to experimentally measure micropolar phenomena [72]. In this thesis, however, the aim is to obtain engineering constants to appreciate the mechanical behavior of the chiral lattice and not to obtain equivalent-continuum models which would certainly have to include micropolar effects. Additionally, both elasto-static and elasto-dynamic response is analyzed considering deformations of internal beam-like components, for which Classical Elasticity Theory is certainly appropriate.

2.4 Historical Background of chiral media

The most commonly recognized instances of chirality have historically been in the field of chemistry [65] and particle physics [71]. Recently, however, significant advancements in material science have established both the occurrence and the practicality of chiral solids. The first suggestion of their existence appeared in [64] as twinned crystals, which coincidentally also featured auxetic behavior. Borrowing from the field of chemistry and encouraged by the early demonstrations of negative Poisson's ratio in [58], a wealth of man-made, chiral, cellular solids have been proposed, realized and experimentally studied. In a significant number of cases, chirality in man-made structured solids appears to be linked to negative Poisson's ratio, owing to the presence of rotational units as a consequence non-central forces, that is pairs of internal forces that do not meet at a common locus.

The first conceptual model of a chiral structure has been offered by [100] in the

form of a molecular model exhibiting negative Poisson's ratio due to internal rotational degrees of freedom. The features necessary to have both isotropic and auxetic behaviors, established in [100], suggested chirality as an enabling characteristic. Following [100], the first practical model of a chiral cellular assembly was engineered by [59] (fig. 12). Such topology is the subject of the current work, and as such it will be introduced in all its details in the next sections. Expanding on the possible configurations of chiral assemblies, later authors such as [44] and [86] among others, have proposed chiral assemblies with lower-order geometric symmetry such as those depicted in fig. 15. The lattice shown in fig. 15.a has been proposed by [86] and it

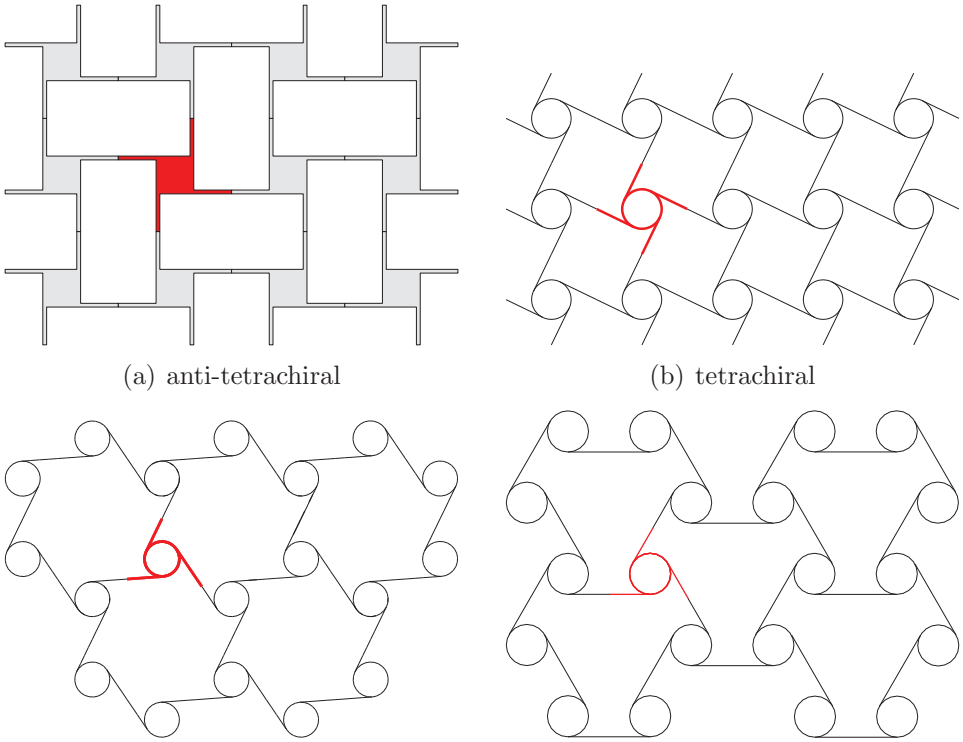

(a) anti-tetrachiral (b) tetrachiral

(c) trichiral (d) anti-trichiral

Figure 15: Known examples of chiral cellular solid configurations

is known as anti-tetrachiral, as it possesses equal "left handed" and "right handed" basic units and is not entirely chiral but it is racemic (annihilated chirality). That

is the each unit cell posses both “left handed” and “right handed” components symmetrically distributed, resulting in a anti-chiral or reflection-symmetric topology. Its counterpart, the tetra-chiral lattice, proposed by [44], is shown in fig. 15.b. The last two configurations of figs. 15.c and d., feature triangular symmetry and they also have been proposed by [44].

While in the field of chemistry solutions comprising chiral molecules are common [65], naturally-occurring, chiral, solid materials are not equally so [60]. Surprisingly, certain species of pine trees produce chiral wood. One such example is the Ponderosa Pine, images of which are shown in fig. 16, taken during a personal excursion in the Colorado Rockies for mere curiosity. Chirality in such trees derives from a non-centrosymmetric cross-section of the trunk. The spirally-structured trunk

(a) (b)

Figure 16: Ponderosa pine with spirally-structured trunk

of Ponderosa Pines is in fact the subject of current research devoted to further the understanding of the mechanical properties of wood [62].

2.5 Geometry of a Hexagonal Chiral Lattice

The structural layout of a hexagonal chiral lattice, shown in fig. 17, consists of circular elements of radius r, acting as nodes, connected by ribs or ligaments, of length L tangent to the nodes themselves. The distance between node centers is denoted as R, while the angle between the imaginary line connecting the node centers and the ribs is defined as β. The angle between adjacent ligaments is denoted as 2θ. Finally, the wall thickness of nodes and ribs is denoted as t_c and t_b respectively. As described in

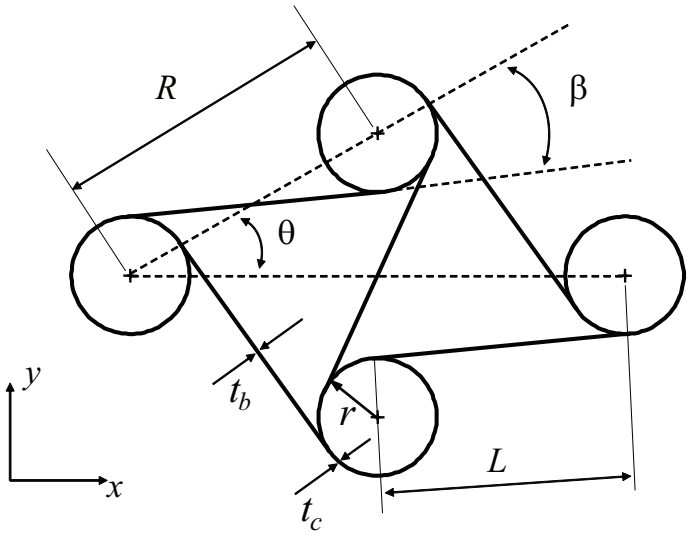

Figure 17: Geometry of a hexagonal, chiral lattice

[76], the following geometric relationships hold:

$$\sin\beta = \frac{2r}{R}, \quad \tan\beta = \frac{2r}{L}, \quad \sin\theta = \frac{R/2}{R}, \quad \cos\beta = \frac{L}{R}. \tag{4}$$

The ratio L/R yields significantly different configurations, as depicted in fig. 18, and thus is here denoted as the *topology parameter*. The unit cell of the honeycomb depicted in fig. 18 is highlighted in dashed lines, and it constitutes the smallest structural domain that encompasses the complete set of geometric entities necessary to analyze the lattice's mechanical behavior. Notably, the possible configurations obtained for variations of the topology parameter span those composed of packed circles

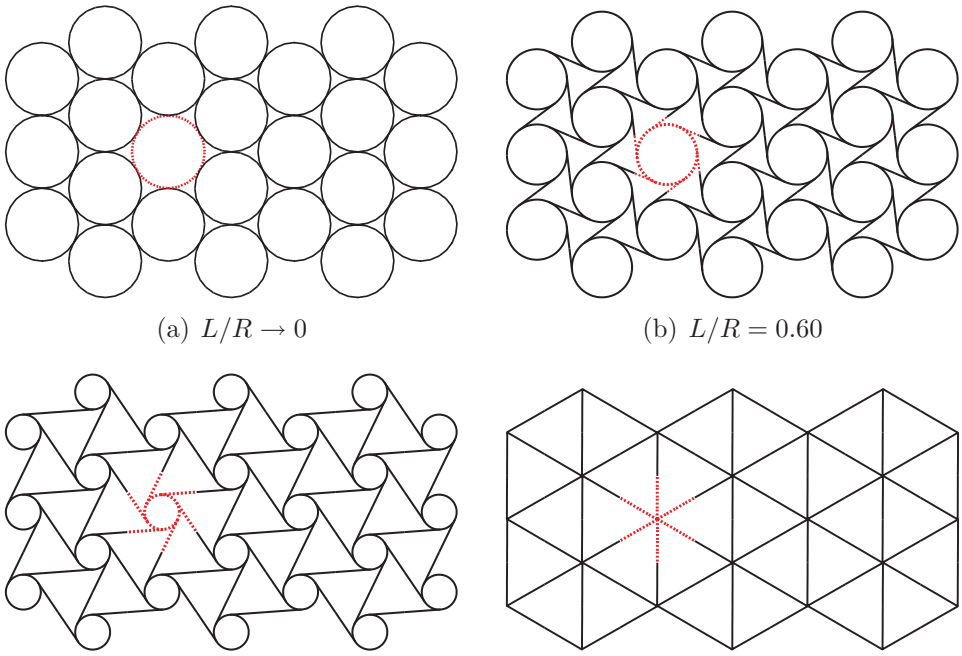

(a) $L/R \to 0$ (b) $L/R = 0.60$

(c) $L/R = 0.90$ (d) $L/R \to 1$

Figure 18: Chiral configurations corresponding to increasing topology parameter L/R

$(L/R \to 0)$ to triangular assemblies $(L/R \to 1$ or $L/r \to \infty)$.

An additional geometric property of the hexagonal chiral lattice, as its name indicates, is its in-plane hexagonal symmetry. As demonstrated by the third of eq. (4), the angle θ is always 30°, indicating that the hexagonal chiral topology is invariant to in-plane rotations by the angle 2θ as shown in fig. 19, regardless of the topology parameter. The influence of hexagonal symmetry on the mechanical behavior results in a mechanical condition of in-plane isotropy [1]. The Young's modulus of a hexagonal material, as a result, is independent of direction in the plane normal to the hexagonal symmetry axis [64]. Such characteristics are very important because they determine the minimum number of coefficients needed to relate stresses and strains. Translations, rotations, reflections or a combination thereof which do not alter the geometry at hand correspond to orthogonal linear coordinate substitutions, such that

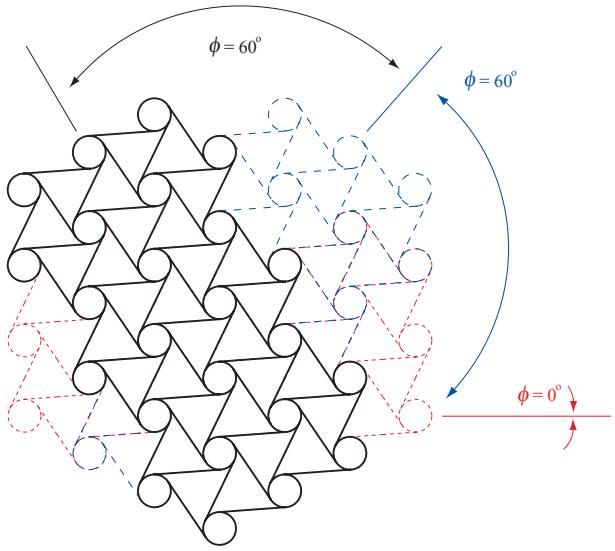

Figure 19: Hexagonal symmetry of the chiral lattice

the strain-energy function is unaltered [64]. Borrowing from notions of crystal symmetry and solid-state physics, it is demonstrated in [64] that, by enforcing uniqueness and invariance of the strain-energy function, any symmetry operation reduces the number of constants required to uniquely express stresses in terms of strains or vice versa. In its most general form, Hooke's Law, relating stresses and strains, can be expressed as:

$$\epsilon_{kl} = S_{klij}\sigma_{ij} \tag{5}$$

where ϵ_{kl} is the strain tensor, σ_{ij} is the stress tensor, while S_{klij} are components of the compliance tensor. Within Classical Elasticity Theory, 3-D anisotropic solids require 21 independent elastic constants to uniquely determine the compliance tensor $\boldsymbol{S}$ [40]. In the current research, the out-of-plane properties of a honeycomb with chiral lattice topology are sought to evaluate the feasibility of this concept as an alternative core for sandwich panels. Since the chiral lattice is expected to feature in-plane isotropy and since one cannot infer the out-of-plane properties at this stage, chiral-core honeycombs are generally expected to be transversally-isotropic components. That is, isotropic in-plane but with different moduli out-of-plane. This implies that the stress-strain

relation is of the kind [64]:

$$\boldsymbol{\epsilon} = \begin{bmatrix} \frac{1}{E_x} & -\frac{\nu_{xy}}{E_x} & -\frac{\nu_{xz}}{E_z} & 0 & 0 & 0 \\ -\frac{\nu_{xy}}{E_x} & \frac{1}{E_x} & -\frac{\nu_{xz}}{E_z} & 0 & 0 & 0 \\ -\frac{\nu_{xz}}{E_z} & -\frac{\nu_{xz}}{E_z} & \frac{1}{E_z} & 0 & 0 & 0 \\ 0 & 0 & 0 & \frac{1}{G_{yz}} & 0 & 0 \\ 0 & 0 & 0 & 0 & \frac{1}{G_{yz}} & 0 \\ 0 & 0 & 0 & 0 & 0 & \frac{2(1-\nu_{xy})}{E_x} \end{bmatrix} \boldsymbol{\sigma} \tag{6}$$

where E denotes the Young's modulus, G the shear modulus and ν the Poisson's ratio. The subscript $(\ )_{i,j}$, with $i, j = x, y$, denotes constants relating shear strains to shear stresses, while the subscript $(\ )_k$, with $k = x, y, z$ denotes constants relating direct strains to direct stresses. In order to characterize the elasto-static behavior of chiral-core sandwich panels within the limitations of Classical Elasticity Theory, 5 elastic constants are then needed.

2.6 Unit Cell Configuration And Lattice Vectors

The structural lattice under investigation is obtained from the assembly of unit cells of the kind shown in fig. 20. As in any periodic assembly, a generic point in a lattice can be described in terms of its location within a reference unit cell and a set of lattice vectors which define the periodicity of the system. Introducing a reference frame in the plane of the lattice $\mathcal{F}_\mathcal{I}$ defined by an orthogonal unit-vector basis $\mathcal{I} = (\boldsymbol{i}_1, \boldsymbol{i}_2)$, the location of a point P in cell n_1, n_2 can be expressed as:

$$\boldsymbol{\rho}_P(n_1, n_2) = \boldsymbol{r}_P + n_1\boldsymbol{e}_1 + n_2\boldsymbol{e}_2, \tag{7}$$

where n_1, n_2 are integers, $\boldsymbol{r}_P$ defines the position of the point corresponding to P in the reference cell $(0, 0)$, and $\boldsymbol{e}_1$ and $\boldsymbol{e}_2$ are lattice vectors. The same vectors shown in fig. 20.a are one of 3 possible sets, given the hexagonal symmetry of the topology. The equations of motion, however, are not affected by one set of lattice vectors versus

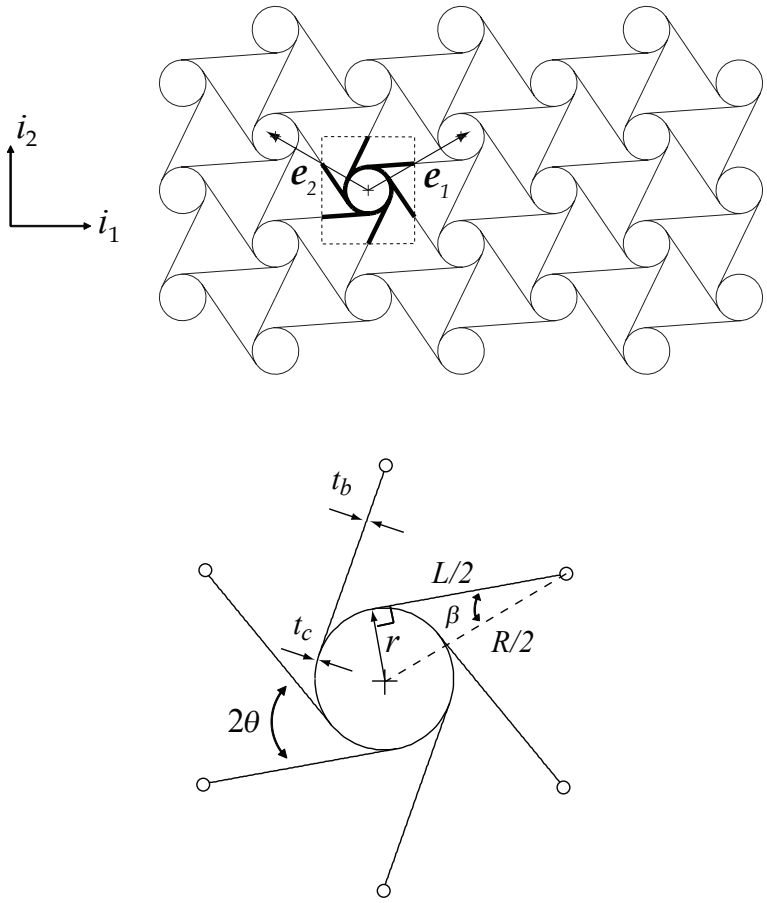

Figure 20: Chiral Structure, lattice vectors, and unit cell parameters

another. This results from the fact that the chiral topology is invariant to 2θ rotations. For the remainder of this thesis, the following convention of mathematical quantities is used: vectors are denoted as bold, lower case letters, capital bold letters identify matrices, and the notation $()^{\mathcal{A}}$ indicates components with respect to the vector basis $\mathcal{A}$. Accordingly, the lattice vectors for the chiral lattice can be expressed as

$$\begin{aligned} \boldsymbol{e}_1^{\mathcal{I}} &= \{R\cos\theta, R\sin\theta\}^T, \\ \boldsymbol{e}_2^{\mathcal{I}} &= \{-R\cos\theta, R\sin\theta\}^T. \end{aligned} \tag{8}$$

2.7 Relative density

As presented in the following chapters, the mechanical behavior of the hexagonal chiral lattice is strongly dependent upon the wall thickness of the lattice's components. This implies that the relative density plays an important role in determining the static and dynamic responses of chiral assemblies. The relative density is thus defined here since its influence is discussed in all subsequent analyses.

A possible irreducible unit cell is the one shown in fig. 20. In general, the relative density $\bar{\rho}$ of a two-phase composite is defined as the volume occupied by one phase, in this case the walls of a unit cell, normalized by the sum of the volumes of both phases. The second phase is here considered simply as a void whose influence on static and dynamic responses is neglected. Assuming that the lattice's walls are thin, the relative density of the hexagonal chiral lattice is:

$$\bar{\rho} = \frac{\rho^*}{\rho_s} = \frac{2\pi r t_c + 6Lt_b/2}{R^2\cos\theta}, \tag{9}$$

where ρ^* is the equivalent density of the lattice, while ρ_s is the density of the constituent material. In most instances, the wall thickness of the node t_c is taken to be the same as that of the ligaments t_b, or $t_c = t_b = t$. Furthermore, since from eq. (4) θ is always 30°, the relative density may be recast as:

$$\bar{\rho} = \frac{\rho^*}{\rho_s} = \frac{2\ \sqrt{3}\ \ (2\pi r + 3L)\ \ t}{3\ R^2}. \tag{10}$$

2.8 Summary

Negative-Poisson's-ratio materials feature unique mechanical behavior, transversally expanding when stretched and transversally contracting when compressed. Such materials are termed auxetic, and their exotic behavior stems from three aspects: non-affine kinematics, rotational units and anisotropy. While it is widely accepted that anisotropic materials may feature a negative Poisson's ratio, isotropic auxetic materials have proven more elusive, and up until recently their existence was questioned. Advances in material science, however, have in the past two decades produced a number of man-made, auxetic cellular solids featuring isotropic mechanical behavior. Metallic foams and re-entrant lattices owe their auxetic behavior to non-affine deformations. Rotational degrees of freedom, on the other hand, are typical of chiral topologies and are the result of non-central forces. Non-centro-symmetric materials in fact, lack reflection symmetry (chirality) and the associated non-central forces produce moments which in turn cause micro or macro rotations within the material. The hexagonal chiral lattice is just such an example. Of the man-made chiral cellular solids, it is the one with the highest-order geometric symmetry (hexagonal symmetry as its name indicates). Furthermore, the hexagonal chiral lattice boasts all the features of other similar cellular solids (fig. 18). Specifically, chirality, internal forces not meeting at a common locus and a bending-dominated deformation mechanism. For these reasons, it will be the only investigated configuration and it will be referred to simply as the chiral lattice.

CHAPTER III

IN-PLANE MECHANICAL PROPERTIES OF THE CHIRAL LATTICE

3.1 Introduction

This chapter is devoted to the analysis of the elasto-static behavior of the chiral lattice. In particular, three aspects instilled curiosity and motivated the research presented in this thesis:

- ◇ strong influence of the topology parameter L/R on the mechanical behavior;
- ◇ negative Poisson's ratio;
- ◇ large global deformations within the elastic regime of the constituent material or solid phase as documented in [9, 76].

The ability to dramatically affect the elastic properties of a lattice, simply by changing a reduced set of geometric parameters, implies ease of mechanical tailoring to a given application. While traditionally different stiffness or compliance requirements have been addressed by employing purposely engineered structural arrangements, the possibility of exploring a large realm of elastic behavior by varying a single parameter may provide new possibilities. This should facilitate analyses of multifunctional components, where stiffness requirements may be accompanied by other criteria. The design of truss-core airfoils discussed in chapter 5, for example, takes advantage of just such capabilities. Previous studies reported in [76], moreover, suggest that the chiral lattice features a Poisson's ratio $\nu = -1$ indicating auxetic behavior, in addition to exhibiting isotropic mechanical characteristics. The Theory of Elasticity

however restricts the Poisson's ratio of isotropic solids to $-1 < \nu < 1/2$ [38]. Any attempts to model an isotropic material with $\nu = -1$ by equivalent continuum models are thwarted by a resulting indeterminate constitutive matrix. The analyses presented in the following sections, hence, are devoted to establishing the magnitude of the Poisson's ratio and of the Young's modulus more accurately with respect to the estimates presented in [76]. The ability of the chiral lattice to withstand large deformations within the elastic regime has been established experimentally by [76], and by experimental models of a composite-material, chiral macro-cell presented in chapter 5.

This chapter is organized as follows: following this introduction, an overview of existing methods to mechanically classify cellular solids is first presented in sec. 3.2. In sec. 3.3 previous investigations on the chiral lattice by [76] are discussed to motivate improvements presented herein. A unit-cell analysis based on relaxing assumptions made by [76] is then illustrated in sec. 3.4. The analyses of sec. 3.4 are supported by FE models of a macro-lattice configuration presented in sec. 3.4.1. Finally a comparison of the mechanical behavior of chiral lattice with other common lattices is offered in sec. 3.6.

3.2 Overview of methods to determine the mechanics of cellular solids

Cellular solids feature low relative density and are commonly constituted by arrangements of beam-like slender components. For this reason, the elastic properties of cellular solids are ordinarily determined by employing beam theory to relate loads and corresponding deformations at the unit cell level, an example of which is shown in fig. 21. The simplest technique considers the symmetry of a specific unit cell and relates externally applied stresses to concentrated loads acting on the unit-cell members. The kinematics of the unit cell are then related to externally-applied stresses, yielding effective constants uniquely defining Hooke's Law for the equivalent material.

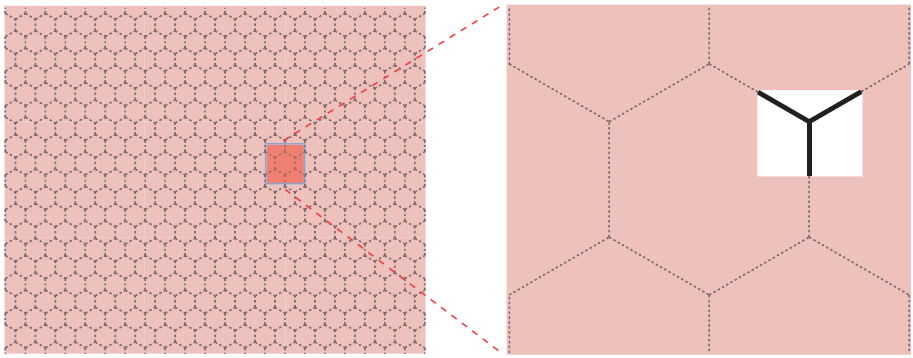

Figure 21: Microstructural detail (unit-cell members) in periodic solids

In the case of the hexagonal lattice depicted in fig. 22, non-affine deformations facilitate the determination of the mechanical behavior as only one topologically-distinct component of the unit cell elastically deflects. As presented in fig. 22, the analysis is carried out by isolating a unit cell from the beam network. One cut of the lattice, the left side of the dashed box in fig. 22.b for example, yields enough equations to resolve all internal forces. Particularly, letting resultant forces be P and W and summing forces in directions parallel and perpendicular to the externally applied stress σ_x yields:

$$P = \sigma_x(H + L\sin\theta)b, \tag{11}$$

and

$$W = \sigma_{xy}(H + L\sin\theta)b = 0, \tag{12}$$

where b is the out-of-plane thickness of the lattice. Isolating one of the oblique members of the unit cell from the rest yields an additional equation relating rectilinear forces to the internal moment M. Enforcing that the sum of the moments at one of the extremities of the isolated oblique ligament (fig. 22.d) be zero, one obtains:

$$M = \frac{PL\sin\theta}{2}. \tag{13}$$

Given that the resultant forces P, W and moment M are now known, one can relate the kinematics of the hexagonal lattice to the externally applied stress employing

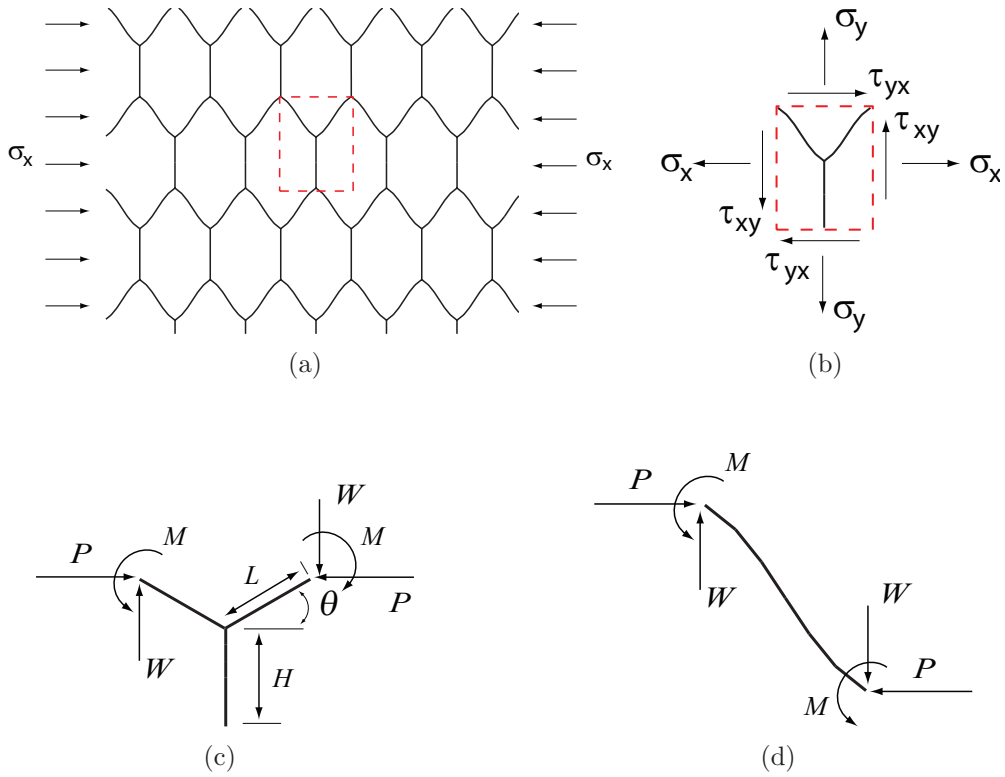

Figure 22: In-plane deformation behavior of the hexagonal lattice

beam theory, providing a relation between resultant forces and moment and deflection δ. In particular [64]:

$$\delta = \frac{PL^3 \sin\theta}{12E_s I}, \tag{14}$$

where E_s is the Young's modulus of the constituent material and I is the area moment of inertia. The resulting strain of the ligament in the x-direction is $\epsilon_x = \delta \sin\theta/(L\cos\theta)$. Since from eqs. (14) and (11) both δ and P are linear functions of σ_x, the equivalent Young's modulus is found simply as $E_x = \sigma_x/\epsilon_x$. The same procedure is applied to determine E_y and G_{xy}. Such analytical procedure leads to es-

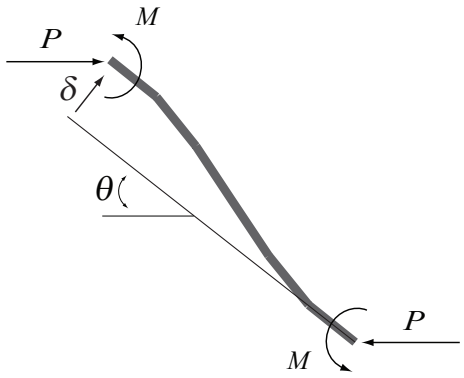

Figure 23: Bending caused by loading in the x-direction

timates of equivalent mechanical properties which are as accurate as the beam model employed to describe the deformation behavior [40]. The same technique has been applied to the square, hexagonal, triangular and Kagomé lattices among others [97]. More sophisticated beam theories may be employed to include shear effects in addition to axial, bending deformations.

A second method relates displacements at the extremities of the unit cell to those of a central joint, or node, relating them through a spatial Taylor-series expansion. In [41], this procedure is referred to as *Homogenization* and it is employed to describe the elasto-dynamic behavior of an equivalent continuum via two partial differential equations. The coefficients of such equations are compared to known equilibrium-equation forms such as Classical Elasticity Theory to obtain the equivalent Lamé

constants. In a similar fashion, the method elucidated in [57], for elasto-static phenomena, relates Taylor-series-linearized displacements at the extremities of the unit cell to those of the central joint. The approximate kinematic variables are then employed to obtain an expression of the unit-cell strain energy in terms of geometric parameters of the lattice. The constitutive matrix relating stress components to strain components is obtained by taking derivatives of the approximated strain-energy function.

In a third procedure, the governing equations of motion, in stress formulation, are expressed in weak form and are solved numerically via the finite-element method. Internal forces acting on each of the beam-like members of the cellular solid are transformed into equivalent continuum stresses by averaging the same internal forces over a representative volume, usually at a scale (fig. 21.b) comprising several unit cells [24, 30]. This particular technique allows the evaluation of global elasto-static phenomena bypassing the determination of elastic constants altogether. This analysis method is particularly suited for stochastic configurations, for which it is not possible to determine elastic constants based on a unit-cell analysis, as the unit cell itself is only statistically described in terms of a characteristic volume or length scale. However, it is certainly applicable to deterministic configurations also, as demonstrated in [24, 30].

Although chiral-lattice topologies have been known for about two decades (the first example was presented by [100] in 1989), few analytical models relating equivalent elastic constants to geometric parameters have been proposed, one of which is offered by [76]. Most publications in fact are concerned with negative-Poisson's ratio characteristics [44]. The unique topology of the chiral lattice investigated in this thesis, moreover, does not present a central joint, thus rendering Taylor-expansion-based techniques not easily applicable. Furthermore, one the objectives of this work is to classify the mechanical behavior of the chiral lattice in terms of its equivalent elastic constants, hence the stress-based formulation of [24, 30] is not applicable either. In

order to circumvent the difficulties posed by chiral topologies, an improved unit-cell analysis based on previous findings by [76] is employed with the objective of removing some of the limiting assumptions and approximations previously considered.

3.3 Previous Studies of in-plane behavior

The dominant deformation mechanism in 2-D structural lattices may be of extensional or bending nature, according to the manner in which the lattice's components are interconnected. A rigorous procedure based on Maxwell's Theorem to determine which deformation mechanism defines a given 2-D lattice is presented by [22]. This is a noteworthy feature since equivalent stiffness for extensional lattices scales as $\bar{\rho}$, where $\bar{\rho}$ is the relative density, as opposed to $\bar{\rho}^3$ for bending dominated lattices. A summary of elastic-constants dependency on $\bar{\rho}$ is offered by [97], which confirms notions previously proposed by [40] suggesting that the most common lattice, the hexagonal lattice, is dominated by cell-wall bending. The same has been observed experimentally for the chiral lattice [76]. A representative deformed configuration obtained through a finite-element (FE) model of the static response of the chiral lattice to uniaxial stress is presented in fig. 24, confirming the findings by [76] indicating that the deformations of the chiral lattice are bending dominated. Accordingly, the deformed ligaments feature a sigmoidal shape. A negative in-plane Poisson's ratio is

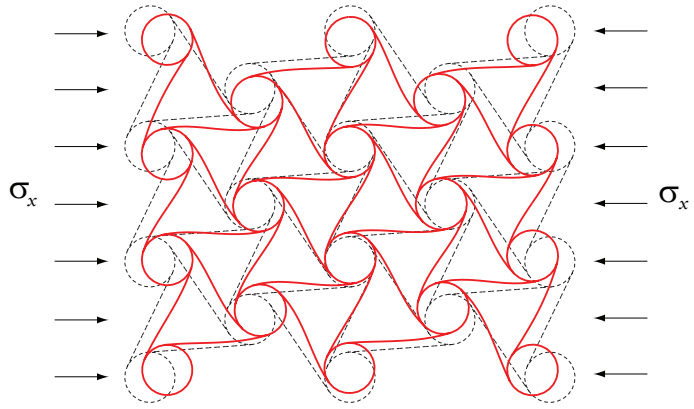

Figure 24: In-plane deformation behavior of a chiral lattice

also evident, given the contraction of the assembly perpendicularly to the imposed stress. Knowledge of the equivalent mechanical properties defining the chiral lattice is currently very limited; the only efforts to uncover the mechanical behavior of this novel lattice to this date have been set forth by [76], where only the relation between Young's modulus and geometric parameters is investigated. A significant obstacle is given by the high degree of static indeterminacy, which renders previously proposed methods [40, 97] not easily applicable. In the case of common arrangements such as the triangular, square, and hexagonal lattices, the assessment of in-plane mechanical properties is based on enforcing equilibrium of externally applied stresses with resulting internal forces, without assuming any particular kinematic behavior [40]. Cutting the lattice and enforcing internal equilibrium, in fact, yields enough equations to uniquely relate each internal force to the externally applied stress as shown in sec. 3.2. Equivalent mechanical properties are then estimated by enforcing equilibrium of a unit cell, as well as compatibility of deformations stemming from the lattice's symmetry. In the case of the chiral lattice, however, significant static indeterminacy hinders the estimation of internal forces resulting from externally applied stresses.

The work presented in [76] makes five assumptions:

a. nodes (or circles) are considered rigid;

b. internal forces oriented in a direction perpendicular to the externally applied stress vanish;

c. internal forces are dictated by the observed kinematic behavior;

d. axial and shear deformations of the ligaments are neglected;

e. all deflections are small.

As it will unfold in the following sections, most of the above assumptions lead to

poor approximations. Nevertheless it is instructive to analyze the procedure suggested by [76], which notably, is based on resolving the internal forces given the observed kinematic behavior, in contrast with methods presented by [40, 97] among others, where resultant internal forces are associated with externally-applied stresses by notions of equilibrium. The analysis of [76] predicts that all ligaments deform equally, owing to hexagonal symmetry, when the lattice is loaded by a uniaxial stress as shown in fig. 25.a. The unusual deformation mechanism that characterizes chiral

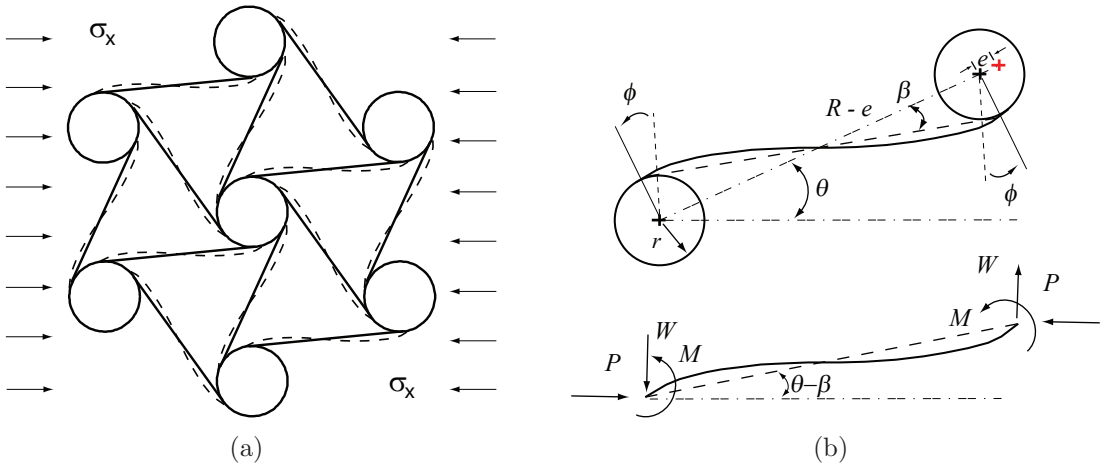

Figure 25: Ligament deformation resulting from applied stress σ_x (a) and associated internal forces (b)

lattices is explained by [76] as,

> *a torque results in bending of the ligaments into a sigmoid shape, and rotation of the nodes ... Both the ligament bending and the equal rotation of all nodes is visible experimentally in the deformation of the model. The ligaments remain rigidly tangent to the node, therefore the deformation is constrained to correspond to a change of area without change of shape ... The orthogonal deformations of the honeycomb result from the displacement of the node centers. ...The angular deflection ϕ [of the ligament] measured at its endpoints coincides with the nodes' rotation through the same angle, ϕ. This is due to the constraint that the slope [of the ligament*

at its end points], remains tangent to the node. So, in order to maintain ϕ and θ, the ligaments must "wind" onto the nodes. This results in a displacement of adjacent nodes along the direction of R. The effective displacement of each node, is as if it were rolling along R.

It is postulated that the internal forces necessary to produce the deformed configuration of fig. 25.a act on ligaments and nodes as shown in fig. 25.b, where P, M and W represent reactant forces in the transverse direction, reactant moment, and reactant force in the longitudinal direction respectively. In the deformed state, the chiral assembly is characterized by a distance between node centers equal to $R - e$ where e is the displacement along R associated with external compressive stress. The following analysis will present the determination of in-plane Young's modulus and Poisson's ratios.

Assuming the nodes to be perfectly rigid in addition to neglecting shear and axial deformations of the ligaments is legitimate provided that the ligaments be slender [76], which in turn requires low relative density (sec. 2.7). Owing to static equilibrium considerations, the resultant force W vanishes as there are no applied stresses in the y-direction, so the reactant moment M depicted in fig. 25.b is:

$$M^{(x)} = \frac{PL\sin(\theta - \beta)}{2}, \tag{15}$$

where the superscript $(\,)^{(\cdot)}$ indicates the direction of externally applied stress with which moments and forces are associated. The same deformation mechanism is observed for an applied stress σ_y depicted in fig. 26. For this loading configuration, it is postulated that the resultant force P vanishes as there is no applied stress in the x-direction, so that the relation between M and W becomes:

$$M^{(y)} = -\frac{WL\cos(\theta - \beta)}{2}. \tag{16}$$

The characteristic cell considered by [76] is shown in fig. 27. The strain energy stored

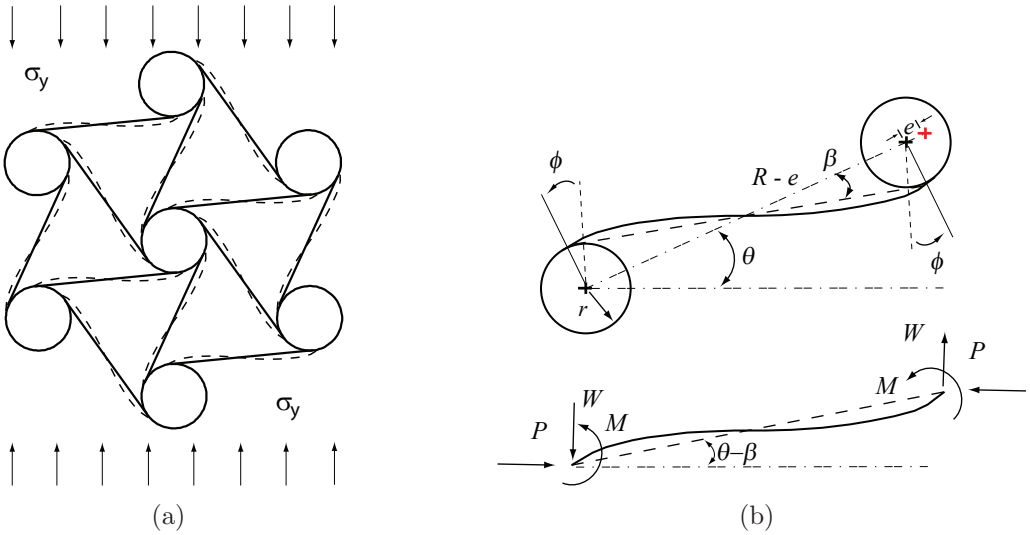

Figure 26: Ligament deformation resulting form applied stress σ_y (a) and associated internal forces (b)

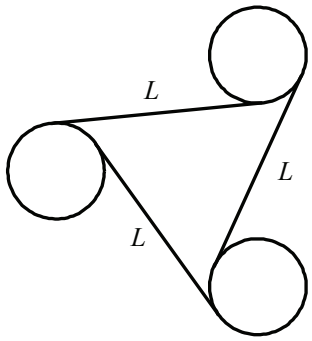

Figure 27: Characteristic cell considered by [76]

in a ligament or rib after a quasi-static deformation is:

$$U_{rib} = 2 \int_0^{\phi} M(\phi')\, d\phi'. \tag{17}$$

Due to cyclic symmetry of the chiral lattice with period 2θ (or 60°), the strain energy expressed by eq. (17) is characteristic of all ribs. Furthermore, each of the three ligaments depicted in fig. 27 is shared by two characteristic cells hence the strain energy stored in the assembly of fig. 27 is:

$$U_{cell} = \frac{3}{2}\, U_{rib}. \tag{18}$$

The strain energy stored in a continuum portion equivalent to the volume occupied by a unit cell can be expressed as:

$$U_{cm} = \int_0^{\epsilon_i} V\sigma_i(\epsilon_i)d\epsilon_i' = V\frac{1}{2}E_i, \epsilon_i^2 \tag{19}$$

where E_i is the Young's modulus of the equivalent continuum, $i = x, y$, V is the unit-cell volume, and ϵ_i is the strain resulting from an applied stress σ_i. The volume V of the characteristic cell, neglecting the contribution of the nodes is:

$$V = bR^2\cos\theta = \frac{\sqrt{3}}{2}\, bR^2. \tag{20}$$

If bending deformations only are considered, the relationship between end reactant moments M and end rotations ϕ can be expressed as:

$$\phi = \frac{ML}{6E_sI}, \tag{21}$$

where E_s is the Young's modulus of the constituent material, and I is the area-moment of inertia defined as $I = bt_b^3/12 = bt^3/12$. The resulting shortening of the ligaments can be expressed as:

$$e = r\sin(\phi) \approx r\phi. \tag{22}$$

The strain associated with ligament end-rotations is then:

$$\epsilon_x = \frac{r\phi\cos\theta}{R\cos\theta},\ \epsilon_y = \frac{r\phi\sin\theta}{R\sin\theta} \quad \Rightarrow \epsilon_x = \epsilon_y = \frac{r\phi}{R}. \tag{23}$$

Applying the definitions for $\nu_{xy} = -\epsilon_y/\epsilon_x$ and $\nu_{yx} = -\epsilon_x/\epsilon_y$, yields:

$$\nu_{xy} = \nu_{yx} = \frac{r\phi/R}{r\phi/R} = -1. \tag{24}$$

Replacing eqs. (15), (17), (20), (21), and (23) into (18), and equating eqs. (18) an eq. (19), one obtains the following expression for in-plane Young's moduli:

$$\frac{E_x}{E_s} = \frac{E_y}{E_s} = \sqrt{3}\ \frac{t^3}{L^3}\ \frac{L^2}{r^2}, \tag{25}$$

which presents the familiar dependency on $(t/L)^3$ as for hexagonal honeycombs [40]. Eq. (25) thus confirms the findings by [22], which indicate that the equivalent stiffness for bending dominated lattices scales as $\bar{\rho}^3$. Finally, having an in-plane Poisson's ratio identically equal to -1 leads to an indeterminacy of the in-plane shear modulus, given the definition of the latter as:

$$G_{xy} = \frac{E_x}{2(1+\nu_{xy})}. \tag{26}$$

At this stage, this indeterminacy prevents a complete description of the mechanical behavior of the chiral lattice in terms of equivalent elastic constants.

3.4 Improved unit cell analysis

In the literature addressing auxetic materials, high specific shear modulus is often mentioned as one of the desirable features associated with negative-Poisson's-ratio behavior [44, 76, 37, 58, 86]. The findings of [76] as discussed in the previous section however, do not allow the determination of such an elastic constant, because the Poisson's ratio is estimated to be exactly -1. Given the geometric hexagonal symmetry of the chiral lattice, it is legitimate to assume isotropic elasto-static characteristics. However as indicated by [38], the Poisson's ratio of isotropic materials is bounded by $-1 < \nu < 1/2$ in 3-D, or $-1 < \nu < 1$ in 2-D, and the associated constitutive matrix would become singular for $\nu = -1$.

In order to alleviate the shortcomings of the procedure above, the analysis proposed by [76] is revisited by relaxing the assumptions listed in the previous section. To investigate the repercussions of each of the above constraints placed upon the mechanics of the lattice, a two-step approach is proposed. In the first phase of the analysis (referred to as case 1), the following conditions are considered:

1.a nodes or circles are considered rigid;

1.b the kinematic behavior is imposed based on the experimental observations

of [76];

1.c internal forces oriented in a direction perpendicular to the externally applied stress are retained;

1.d axial and shear deformations of the ligaments are included in the analysis;

1.e ligament wall thickness t_b is the same as that of the nodes or $t_b = t_c = t$;

1.f all deflections are small.

One of the objectives of case 1 is to isolate the effect of elastic deformations of the ligaments from those of the nodes, hence the latter are considered rigid. The mechanics of the ligaments, moreover, is not limited to bending deformations resulting from rotations only, but is augmented with axial and shear deformations also. The unusual kinematics of the chiral lattice featuring rotational units (the nodes) furthermore, prompts concerns with respect to neglecting any internal forces. Accordingly, resultant forces perpendicular to externally-applied stresses will be retained. In the second phase of the analysis (referred to as case 2), the following conditions are considered:

2.a the deformations of nodes or circles are included in the analysis;

2.b no restrictions are placed upon resultant forces;

3.c a macro-lattice FE model is employed;

2.d axial and shear deformations of the ligaments are included in the analysis;

2.e all deflections are small;

2.f ligament wall thickness t_b is the same as that of the nodes or $t_b = t_c = t$;

The objective of case 2 is to fully determine the mechanical properties of chiral lattices. Deformations of the nodes are hence included in the analysis. The high degree

of indeterminacy and the complexity of the chiral topology, however, do not lend themselves to obtaining tractable analytical expressions. The equivalent elastic constants are then estimated via a macro-lattice, linear, FE model that considers axial, bending and shearing deflections of the lattice's components.

In the following sections the effective Young's modulus of eq. (25) will be referred to as E_P, where the subscript $(\ )_P$ indicates estimates from previous studies; the findings of case 1 will be denoted by $(\ )_C$, where C indicates constrained nodes and results of case 2 will be denoted by $(\ )_U$ where U denotes unconstrained nodes. A full description of macro-lattice numerical models employed to support the analyses of cases 1 and 2 is provided in the following section, followed by the analytical expressions of Young's modulus E^C for case 1 and approximated formulae for E^U of case 2.

3.4.1 Macro-Lattice FE Models

A FE model of the chiral lattice is employed in order to investigate the internal forces resulting from externally applied stresses, the extent of node deformations and the relation between equivalent elastic constants and geometric parameters. The commercially available FE software ANSYS® is employed. Specifically, Timoshenko beam elements featuring axial, bending and shear deflections are used (BEAM3) [2]. Each ligament is discretized by 24 elements, while each node or circle is discretized by 44 straight-beam elements. The base configuration is characterized by the parameters reported in Table. 1.

Given the structural composition of the chiral lattice, no single location is able to withstand a level of stress required to load the entire lattice. Perimeter circles on the sides perpendicular to the desired direction of deformation are kinematically constrained to be rigid, as depicted in fig. 28. A displacement producing the desired level of strain is applied at the center of each constrained perimeter circle. In order to avoid singularities in the stiffness matrix, a circle on each loaded side is constrained

Table 1: Base configuration parameters of FE macro lattice

Geometric parameters	
L	1 m
L/R	$0.6 - 0.999$
t_b	0.01 m
t_c	0.01 m
b	0.01 m
Material properties: Aluminum	
E_s	71 GPa
ν_s	1/3

to displace collinearly with the loading direction. The analysis of shear stiffness, on the other hand, does not require any constraints perpendicularly to the imposed displacements of the perimeter nodes (fig. 28.c) as such boundary conditions ensure an invertible stiffness matrix. The effective applied stress is evaluated by summing the point forces at the center of each perimeter circle constrained kinematically and dividing by the loaded area, depicted as a yellow line in fig. 28. To estimate the shear stiffness the effective engineering strain is computed as follows:

$$\gamma_{yx} = \frac{v_{i+1} - v_i}{x_{i+1} - x_i} + \frac{u_{j+1} - u_j}{y_{j+1} - y_j}, \tag{27}$$

where (x, y) denote the location of the center of each node and (u, v) denote respectively displacements in the x and y directions. The subscripts i and j indicate node centers at the top and left sides of the lattice respectively. The equivalent elastic constants are then computed as: $E_x = \sigma_x/\epsilon_x$ (fig. 28.a), $E_y = \sigma_y/\epsilon_y$ (fig. 28.b), and $G_{yx} = \tau_{yx}/\gamma_{yx}$ (fig. 28.c). Poisson's ratios ν_{xy} and ν_{yx} are evaluated based on the displacements of the extremities of a unit cell located approximately in the center of the lattice. The applicability of assumptions made with regard to internal forces, is investigated by monitoring the nodal-force values sampled at the extremities of a unit cell (yellow points in fig. 28), located approximately at the center of the lattice. For each of the three considered cases a strain level of 500 $\mu\epsilon$ is employed.

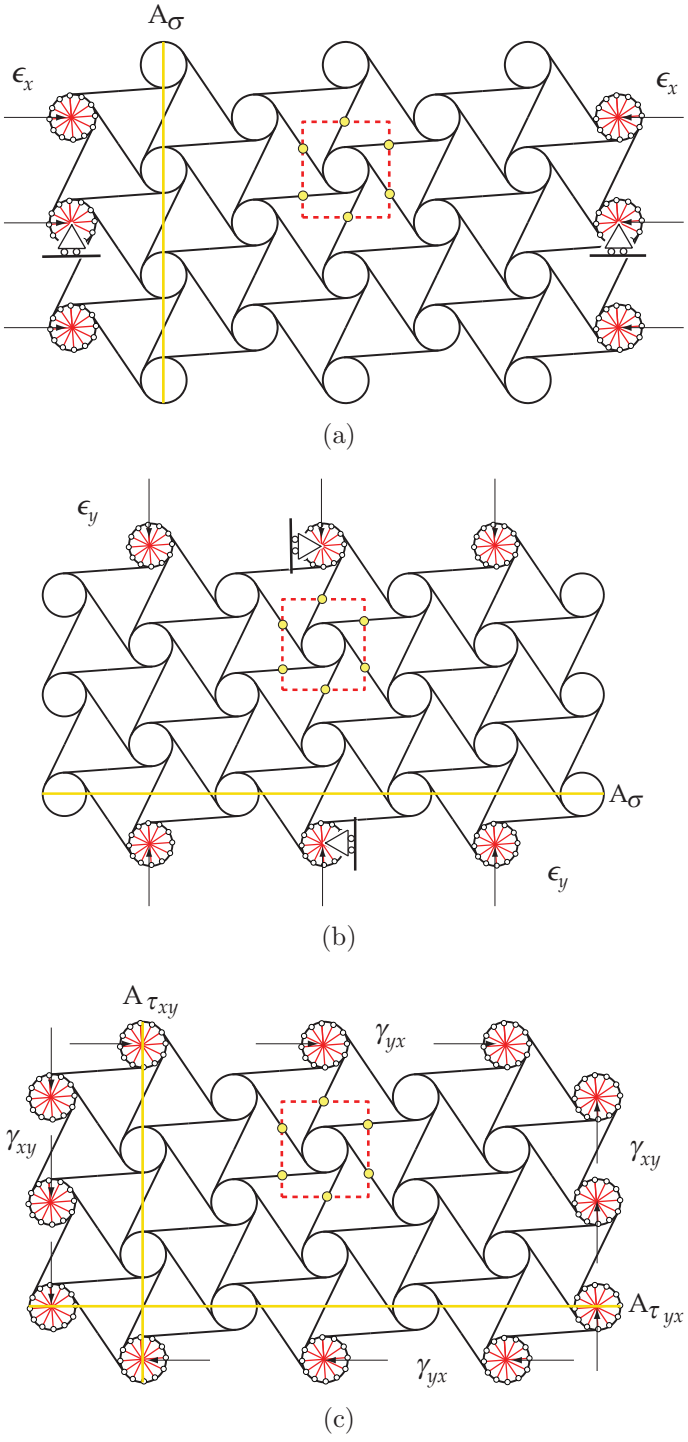

Figure 28: Representative FE macro-lattice configurations employed to study loading in the x-direction (a), y-direction (b) and xy-direction (c)

A convergence study is carried out to establish the minimum number of cells necessary to reasonably estimate stress, strain, and associated elastic constants for each case considered, as well as to reduce the influence of boundary effects. Estimates

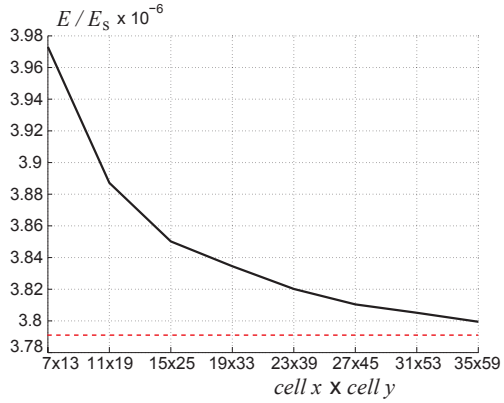

(a) $L/R = 0.64$

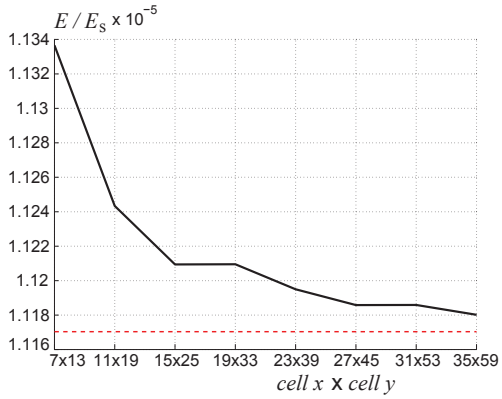

(b) $L/R = 0.86$

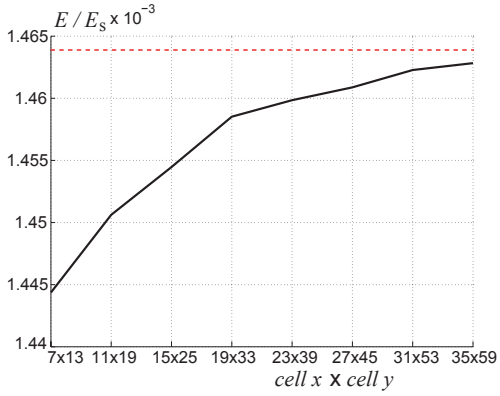

(c) $L/R = 0.999$

Figure 29: Variation of Young's modulus E_x with respect to lattice-cell number $---$, and extrapolated value $---$ for three values of L/R

of E_x shown in figs. 29 do not appear to approach an asymptotic value, suggesting that additional increments in cell numbers in the x and y-directions are required. Due to computing limitations, however, larger models are not feasible. A Richardson extrapolation [78] is used to obtain a limit value of Young's modulus to assess wether the current model size is appropriate. The limit value of E_x, denoted as $\bar{E}_x$, may be expressed as:

$$\bar{E}_x = \lim_{c \to \infty} E_x(c), \tag{28}$$

where $E_x(c)$ is the FE approximation of $\bar{E}_x$ as a function of cell number c, and $c = cell\ x \times cell\ y$. The lattice cells considered here are those depicted in fig. 30. For $c \neq \infty$, eq. (28) may be expressed as:

$$\bar{E}_x - E_x(d) = a_n d^{k_n} + O\left(d^{k_{n+1}}\right),\ a_n \neq 0, \tag{29}$$

where n is an integer, a_n are unknown constants, k_n are known coefficients and $d = 1/c$. According to Richardson extrapolation [78], the term $a_n d^{k_n}$ in eq. (29) can be eliminated to obtain the following formula:

$$\bar{E}_x = \frac{r^{k_n} E_x(d/r) - E_x(d)}{r^{k_n} - 1} + O\left(d^{k_{n+1}}\right), \tag{30}$$

where $k_{n+1} > k_n$ and r is the refinement ratio or $r = d_{n+1}/d_n$. The value k_n represents the order of convergence, which is not known a priori. This may be found with the following expression [79] which considers three values of discretization:

$$k_n = ln\left(\frac{E_{x,3} - E_{x,2}}{E_{x,2} - E_{x,1}}\right)\frac{1}{ln(r)}. \tag{31}$$

For the Young's modulus estimates shown in fig. 29, $k_n \approx 2$. Neglecting the error of order $O\left(d^{k_{n+1}}\right)$ in eq. (30), the Young's modulus for an infinite lattice may be expressed as:

$$\bar{E}_x \cong \frac{r^{k_n} E_x(d/r) - E_x(d)}{r^{k_n} - 1}. \tag{32}$$

For the three sample values of topology parameter depicted in fig. 29, the difference between $E_x(d)$ computed with 35×59 cells and the extrapolated value $\bar{E}_x$ is within 0.3%, which is smaller than the error introduced by approximating equivalent elastic constants with analytical expressions based on curve fitting presented in sec. 3.4.3. Given the small error introduced by limiting the FE lattice model to 35×59 cells of the kind depicted in fig. 30, the error introduced by approximate expressions of sec. 3.4.3 and computational limitations, the maximum number of cells considered in fig. 29 is deemed legitimate as a basis for the estimation of the desired elastic constants.

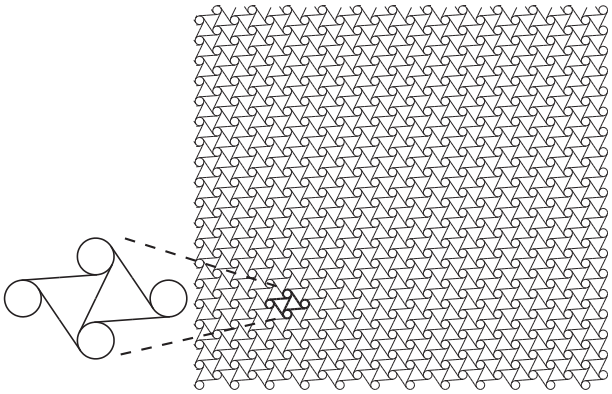

Figure 30: Chiral lattice employed for convergence studies

3.4.2 Case 1: rigid nodes

The notion suggesting that internal forces perpendicular to the externally applied stress vanish is applicable to centrally-symmetric lattices with collinear or central internal forces. This is certainly the case for the hexagonal lattice as discussed in sec. 3.2. For the chiral lattice, however, this should not be assumed a priori. Isolating one unit cell, depicted in fig. 31, one would expect the component of internal stress in the direction perpendicular to the externally applied stress to be 0. However, upon loading of the chiral lattice by uniaxial stress σ_x (see fig. 31), and extraction of one unit cell form the complete structural arrangement shows that 6 reaction forces, F_{x1}, F_{y1}, F_{x2}, F_{y2}, F_{x3} and F_{y3} are present. As depicted in fig. 31.c, such reaction forces satisfy the hexagonal symmetry of the structure mandated by the lattice vectors $\boldsymbol{e}_1$ and $\boldsymbol{e}_2$, discussed in sec. 2.6. The assumption proposed by [76] whereby the vertical force W in fig. 25 vanishes for an applied stress σ_x thus is too restrictive. If internal forces perpendicular to the externally applied stress do not vanish, the internal moment M depicted in fig. 25 then becomes:

$$M = \frac{PL\sin(\theta-\beta)}{2} - \frac{WL\cos(\theta-\beta)}{2}. \tag{33}$$

If eq. (33) is used in the procedure elucidated in sec. 3.3 above, equating eqs. (18) and (19) leads to a non-linear equation which does not permit relating the equivalent

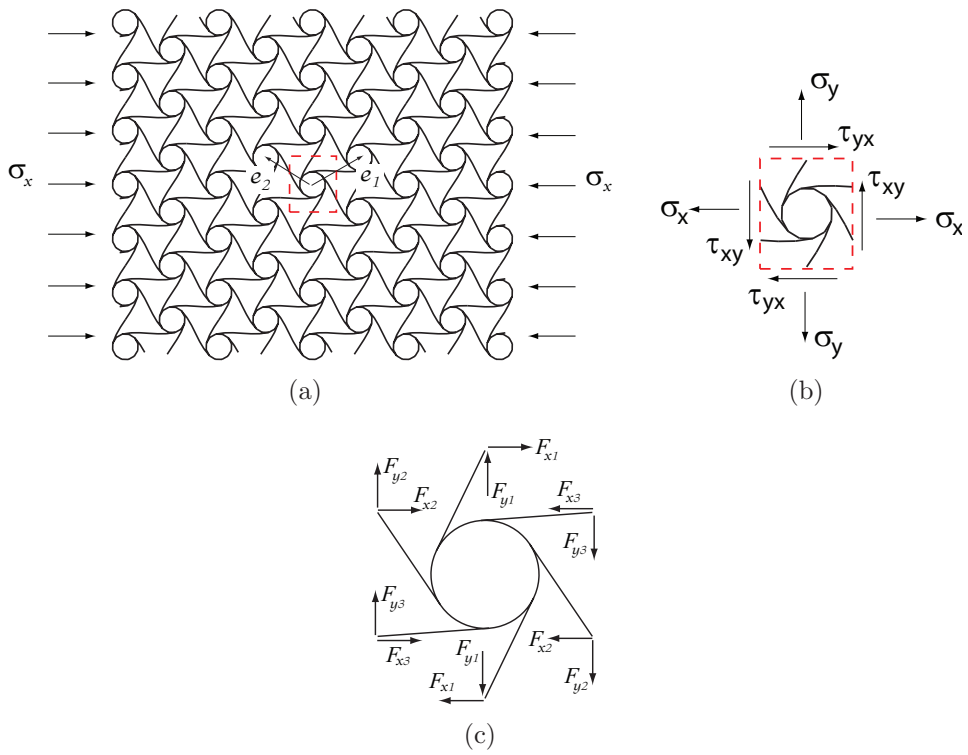

Figure 31: In-plane deformation behavior of the chiral lattice with rigid nodes

Young's modulus to geometric parameters only. A different approach is then devised.

The mechanical behavior of a chiral lattice with rigid nodes is analyzed by employing constraint equations relating the kinematics of the center of each circle to those of material points on the circles themselves according to the following expressions:

$$\begin{aligned} \boldsymbol{x}_{OA} &= \boldsymbol{x}_{OB} + \boldsymbol{x}_{BA} \\ &= \boldsymbol{x}_{OB} + r(\cos\psi\ \hat{\boldsymbol{i}} + \sin\psi\ \hat{\boldsymbol{j}}) \qquad (34) \\ \boldsymbol{x}_{OA'} &= \boldsymbol{x}_{OB} + (u_B\ \hat{\boldsymbol{i}} + v_B\ \hat{\boldsymbol{j}}) + \boldsymbol{x}_{BA'} \\ &= \boldsymbol{x}_{OB} + (u_B\ \hat{\boldsymbol{i}} + v_B\ \hat{\boldsymbol{j}}) + r\left[\cos(\psi+\phi)\ \hat{\boldsymbol{i}} + \sin(\psi+\phi)\ \hat{\boldsymbol{j}}\right] \qquad (35) \\ (u_A\ \hat{\boldsymbol{i}} + v_A\ \hat{\boldsymbol{j}}) &= \boldsymbol{x}_{OA'} - \boldsymbol{x}_{OA} \\ &= (u_B\hat{\boldsymbol{i}} + v_B\hat{\boldsymbol{j}}) + r\left[\cos(\psi+\phi) - \cos\psi\right]\hat{\boldsymbol{i}} + r\left[\sin(\psi+\phi) - \sin\psi\right]\hat{\boldsymbol{j}} \\ &= (u_B\ \hat{\boldsymbol{i}} + v_B\ \hat{\boldsymbol{j}}) - r\phi\sin\phi\ \hat{\boldsymbol{i}} + r\phi\cos\phi\ \hat{\boldsymbol{j}}.. \qquad (36) \end{aligned}$$

Referring to fig. 32, u_A, v_A are the displacement components of point A along $\hat{\boldsymbol{i}}$ and

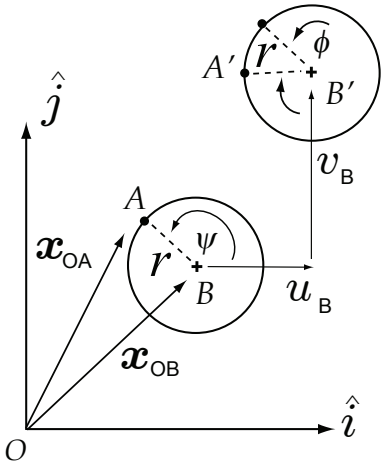

Figure 32: kinematics of rigid nodes

$\hat{\boldsymbol{j}}$ respectively, while u_B, v_B are those of of point B, ϕ is the rotation of the circle and $\boldsymbol{x}_{\diamond,\diamond}$ denotes a position vector. The resulting kinematic constraint of eq. (36) is linearized in compliance with the assumption of small displacements and rotations. The same constraint may be expressed in matrix form as:

$$\left\{ \begin{array}{c} u_A \\ v_A \\ \phi_A \end{array} \right\} = \left[\begin{array}{ccc} 1 & 0 & -r\sin\theta \\ 0 & 1 & r\cos\theta \\ 0 & 0 & 1 \end{array} \right] \left\{ \begin{array}{c} u_B \\ v_B \\ \phi_B \end{array} \right\} = \boldsymbol{T}(\theta) \left\{ \begin{array}{c} u_B \\ v_B \\ \phi_B \end{array} \right\}. \tag{37}$$

In light of the in-plane, hexagonal symmetry of the chiral lattice and the fact that the nodes are considered rigid, the analysis of a single ligament is expected to produce the elasto-static behavior of the entire lattice. The simplified geometric model shown in fig. 33.a is then reduced to that depicted in fig. 33.b by way of eq. (37) thereby enforcing rigid kinematic constraints on the circles. In fig. 33.b the superscript $(\,)'$ indicates displacement components normal or tangential to the lattice vector $\boldsymbol{e}_1$. If the circles are to translate along the imaginary line connecting their centers (or along $\boldsymbol{e}_1$), as presented in fig. 24, one would like to determine what forces and moments produce such deformations. In a FE framework, such forces and moments can be obtained by

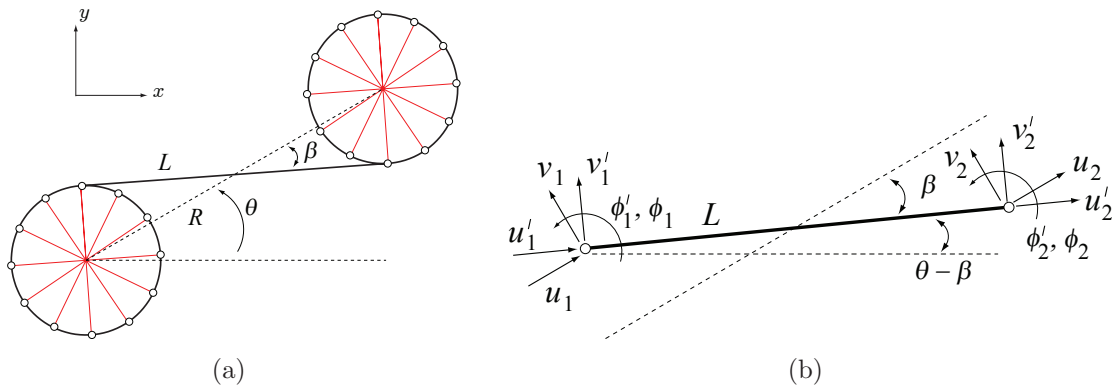

Figure 33: Case 1: single-ligament model (a), and associated generalized displacements (b)

exploiting the ordering of nodal displacements and forces in their respective vectors:

$$\begin{bmatrix} \boldsymbol{K}_{kk} & \boldsymbol{K}_{ku} \\ \boldsymbol{K}_{uk} & \boldsymbol{K}_{uu} \end{bmatrix} \begin{Bmatrix} \boldsymbol{u}_k \\ \boldsymbol{u}_u \end{Bmatrix} = \begin{Bmatrix} \boldsymbol{f}_u \\ \boldsymbol{f}_k \end{Bmatrix}, \tag{38}$$

where the subscripts k and u denote known and unknown values respectively. Two kinematic states are imposed: a strain along the x-direction ϵ_x and subsequently a strain along the y-direction ϵ_y. Invoking eq. (23), direct strains may be related to the unidirectional displacement e along R (see fig. 25). For the case at hand, it is convenient to project the generalized displacements onto the imaginary line connecting the node centers, collinear with $\boldsymbol{e}_1$. This is accomplished as follows:

$$\begin{Bmatrix} u_1 \\ v_1 \\ \phi_1 \\ u_2 \\ v_2 \\ \phi_2 \end{Bmatrix} = \begin{bmatrix} \cos\beta & -\sin\beta & 0 & 0 & 0 & 0 \\ \sin\beta & \cos\beta & 0 & 0 & 0 & 0 \\ 0 & 0 & 1 & 0 & 0 & 0 \\ 0 & 0 & 0 & \cos\beta & -\sin\beta & 0 \\ 0 & 0 & 0 & \sin\beta & \cos\beta & 0 \\ 0 & 0 & 0 & 0 & 0 & 1 \end{bmatrix} \begin{Bmatrix} u_1' \\ v_1' \\ \phi_1' \\ u_2' \\ v_2' \\ \phi_2' \end{Bmatrix} = \boldsymbol{R}(\beta) \begin{Bmatrix} u_1' \\ v_1' \\ \phi_1' \\ u_2' \\ v_2' \\ \phi_2' \end{Bmatrix}. \tag{39}$$

The procedure elucidated so far is general and it is not limited to a particular elastic model. Provided that accounting for shear deformations does not add any more

complexity to the solution procedure, and for the sake of completeness, estimates for E_x and E_y are firstly computed considering axial and bending deformations via Euler-Bernoulli Beam Theory; a refined model that includes axial, bending and shear deformations is then proposed based on Timoshenko Beam Theory [19]. Neglecting shear deformations, one may relate generalized forces to generalized displacements as [19]:

$$\boldsymbol{K}'\boldsymbol{u} = \frac{E_s I_{zz}}{L^3} \begin{bmatrix} 12L^2/t_b^2 & 0 & 0 & -12L^2/t_b^2 & 0 & 0 \\ 0 & 12 & 6L & 0 & -12 & 6L \\ 0 & 6L & 4L^2 & 0 & -6L & 2L^2 \\ -12L^2/t_b^2 & 0 & 0 & 12L^2/t_b^2 & 0 & 0 \\ 0 & -12 & -6L & 0 & 12 & -6L \\ 0 & 6L & 2L^2 & 0 & -6L & 4L^2 \end{bmatrix} \boldsymbol{u} = \boldsymbol{f}, \tag{40}$$

where the superscript $(\,)'$ denotes the local coordinate system of the ligament, while I_{zz} is the area-moment of inertia, or $I_{zz} = bt_b^3/12 = bt^3/12$. If shear deformations are included in the elasticity model, the relation between generalized forces and generalized displacements becomes [19]:

$$\boldsymbol{K}'\boldsymbol{u} = \frac{E_s I_{zz}\mu}{L^3} \begin{bmatrix} 12L^2/\mu/t_b^2 & 0 & 0 & -12L^2/\mu/t_b^2 & 0 & 0 \\ 0 & 12 & 6L & 0 & -12 & 6L \\ 0 & 6L & 4L^2\lambda & 0 & -6L & 2L^2\gamma \\ -12L^2/\mu/t_b^2 & 0 & 0 & 12L^2/\mu/t_b^2 & 0 & 0 \\ 0 & -12 & -6L & 0 & 12 & -6L \\ 0 & 6L & 2L^2\gamma & 0 & -6L & 4L^2\lambda \end{bmatrix} \boldsymbol{u} = \boldsymbol{f}, \tag{41}$$

where $\mu = 1 + 12\omega$, $\gamma = 1 - 6\omega$, $\lambda = 1 + 3\omega$, and $\omega = E_s I_{zz}/(kG_s AL^2)$. In the last expression, k is the shear correction constant, here chosen as $5/6$ given the rectangular cross-sectional area of the ligaments, and G_s is the shear modulus of the constitutive material. In both eqs. (40) and (41), it is assumed that the chiral lattice is made of a

homogeneous, isotropic material, and that the wall thickness t is constant throughout the span of the ligament. Irrespective of the choice of elasticity model, the generalized displacements are projected onto R as:

$$\boldsymbol{K} = \boldsymbol{R}^T(\beta)\ \boldsymbol{K}'\ \boldsymbol{R}(\beta), \tag{42}$$

where $(\ )^T$ denotes the transpose. Imposing that the circles be perfectly rigid is accomplished by enforcing eq. (37) as follows:

$$\widetilde{\boldsymbol{K}} = \boldsymbol{T}(\theta)^T\ \boldsymbol{K}\ \boldsymbol{T}(\theta). \tag{43}$$

Eq. (43) respects the ordering indicated by eq. (38). Employing eq. (38) and noting that enforcing $\boldsymbol{u}_k$ requires $\boldsymbol{f}_u = \boldsymbol{0}$, the unknown nodal displacements $\boldsymbol{u}_u$ are obtained from the second of eq. (38) as:

$$\boldsymbol{u}_u = \widetilde{\boldsymbol{K}}_{uu}^{-1} \left(-\widetilde{\boldsymbol{K}}_{uk}\ \boldsymbol{u}_k \right), \tag{44}$$

where $(\ )^{-1}$ denotes the matrix inverse. The strain energy U^d_{rib} stored in a ligament, analogous to its equivalent-continuous counterpart of eq. (17), can be expressed as:

$$U^d_{rib} = \frac{1}{2}\boldsymbol{u}^T\ \widetilde{\boldsymbol{K}}\ \boldsymbol{u}. \tag{45}$$

The strain energy stored in a unit cell U^d_{cell} follows form eq. (18). Equating the latter to the equivalent strain energy stored in a continuum volume (eq. (19)) equal to that of a unit cell, one obtains estimates for Young's moduli E_x and E_y. In order to derive an expression for the stiffness along the x direction, the following displacements at the extremities of the ligament are imposed as for figs. 25 and 33.b:

$$\boldsymbol{u}_k = \left\{ \begin{array}{c} u_1 \\ v_1 \\ u_2 \\ v_2 \end{array} \right\} = \left\{ \begin{array}{c} 0 \\ 0 \\ \epsilon_x R \\ 0 \end{array} \right\}. \tag{46}$$

The same analysis in the y direction is carried out imposing:

$$\boldsymbol{u}_k = \left\{ \begin{array}{c} u_1 \\ v_1 \\ u_2 \\ v_2 \end{array} \right\} = \left\{ \begin{array}{c} 0 \\ 0 \\ 0 \\ \epsilon_y R \end{array} \right\}. \tag{47}$$

The resulting estimates for Young's moduli in the x and y directions for both Euler-Bernoulli and Timoshenko beam theories are reported in Table 2, where ν_s is the Poisson's ratio of the wall material. As for the procedure presented in sec. 3.3, imposing

Table 2: Estimates of E_x, E_y neglecting node deformations

Including axial and bending deformations
$\frac{E_x}{E_s} = \sin^2\beta \, \frac{\left[4r^2\left(1+1/\cos^2\beta\right)+L^2\right]}{2(t^2+4r^2)} \sqrt{3} \left(\frac{L}{r}\right)^2 \left(\frac{t}{L}\right)^3$
$\frac{E_y}{E_s} = \sin^2\beta \, \frac{\left[4r^2\left(1+1/\cos^2\beta\right)+L^2\right]}{2(t^2+4r^2)} \sqrt{3} \left(\frac{L}{r}\right)^2 \left(\frac{t}{L}\right)^3$
Including axial, bending and shear deformations
$\frac{E_x}{E_s} = \sin^2\beta \, \frac{\left[4r^2\left(1+1/\cos^2\beta\right)+L^2\right]}{2[k(t^2+4r^2)+(1+\nu_s)\tan^2\beta t^2]} \sqrt{3} \left(\frac{L}{r}\right)^2 \left(\frac{t}{L}\right)^3$
$\frac{E_y}{E_s} = \sin^2\beta \, \frac{\left[4r^2\left(1+1/\cos^2\beta\right)+L^2\right]}{2[k(t^2+4r^2)+(1+\nu_s)\tan^2\beta t^2]} \sqrt{3} \left(\frac{L}{r}\right)^2 \left(\frac{t}{L}\right)^3$

that the nodes wind onto the ligaments translating along R constrains the Poisson's ratio to be $\nu_{yx} = -1$. The in-plane shear modulus thus remains undetermined at this stage. The expressions for E_x and E_y derived above present a striking similarity to eq. (25), albeit they exhibit a more complicated dependency on the topology parameter L/R. Expressions for in-plane Young's moduli presented above indicate an isotropic, elasto-static behavior, confirming the findings of [76]. Finally, the factor $(t/L)^3$ indicates that the in-plane deformation mechanism is bending-dominated as suggested in [97] among others.

A comparison between the current estimates for Young's moduli of Table 2 and the one suggested by [76] and reported in eq. (25) is shown in fig. 34, where furthermore, the equivalent stiffness of the triangular lattice (obtained from [97]) is also illustrated. Since the expressions for E_x and E_y in Table 2 are identical, E_C indicates the stiffness

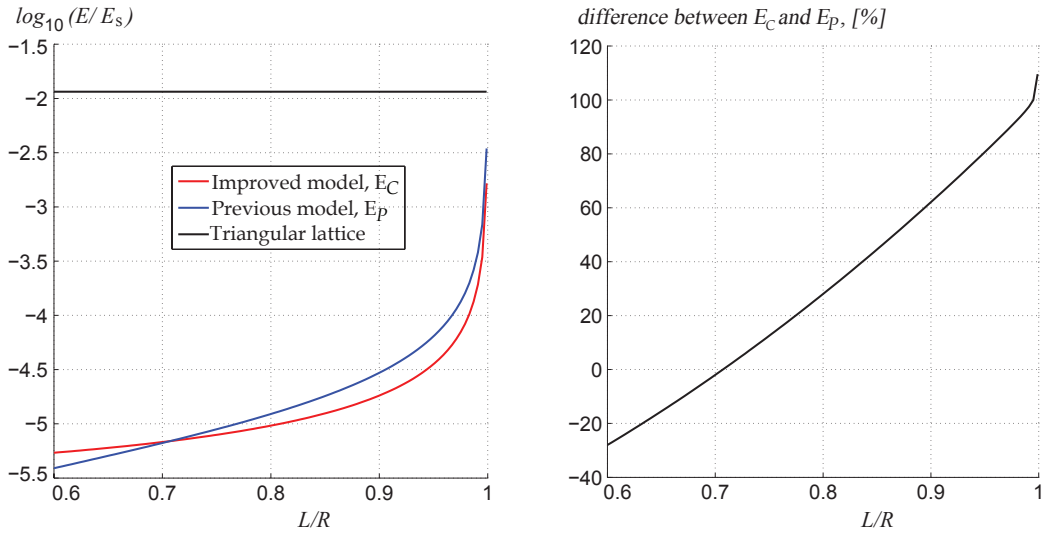

Figure 34: Comparison of improved estimates for the Young's modulus E_C with the one suggested by [76] E_P (a), and percent difference between the two (b)

of the chiral lattice in all directions. Additionally, the difference between E_C obtained neglecting and including shear deformations is within 4%. This may not always be true. For non-slender ligaments for example shear deflections would not be negligible. The envisioned chiral topology, however, is to be utilized for low-relative density applications, and hence the assumption of slender internal components is legitimate. All comparisons with Young's modulus obtained by [76] and with subsequent models, i.e. allowing the nodes to deform, will be carried out with respect to the simpler model not considering shear within the ligaments. As presented in sec. 2.5, the chiral lattice approaches the topology of the triangular lattice as $L/R \rightarrow 1$. Estimates for the Young's modulus of the former thus must approach that of the latter as the topology parameter approaches 1. This is confirmed in fig. 34.a. The expression for

the stiffness of the chiral lattice suggested by [76] (E_P in sec. 3.3) however produces values markedly different than those obtained from the formulae of Table 2. The percent difference between the two is considerable as reported in fig. 34.b. Neglecting internal forces perpendicular to the externally applied stress hence yields significantly different values of Young's modulus than those obtained by including such forces. In order to obtain a more accurate relationship between Young's modulus and geometric parameters, it is worth investigating the implications of including node deformations in the elasto-static analysis. Moreover, the shear modulus remains indeterminate within the assumptions of case 1.

3.4.3 Case 2: deformable nodes

It is again helpful to employ a macro-lattice FE model to guide the analysis by studying how the internal forces and deformations are related to externally applied stresses. For an applied stress σ_x (fig. 35.a) the deformed components are shown in fig. 35.b. Firstly, the nodes of the chiral lattice deform as much as the ligaments for values of the topology parameter $L/R < 0.95$. The assumptions of sec. 3.3 and 3.4.2, whereby node deformations are neglected, hence produce an assembly that is too stiff. Additionally, the computed resultant forces at the extremities of the unit cell (fig. 35.c) are all non-zero, albeit they satisfy the hexagonal symmetry of the lattice along the vectors $\boldsymbol{e}_1$, $\boldsymbol{e}_2$ and their combinations. These forces are obtained at the nodal locations indicated by yellow points in fig. 28.a. The resultant force components are then labeled F_{x_i} and F_{y_i} $(i = 1, 2, 3)$ according to symmetry conditions. No resultant moments are present. The orientation and magnitude of each resultant force, moreover, varies with L/R. Changes in magnitude (fig. 35.e) are to be attributed to the fact that, for the same applied direct strain ϵ_x the assembly's compliance diminishes with increasing L/R. The orientation (fig. 35.f), on the other hand, reflects the topological changes associated with varying L/R, and it approaches that of the

internal forces of a triangular lattice [97] as $L/R \to 1$. At this stage the problem at hand presents 6 unknowns with 3 symmetry conditions already included. From an

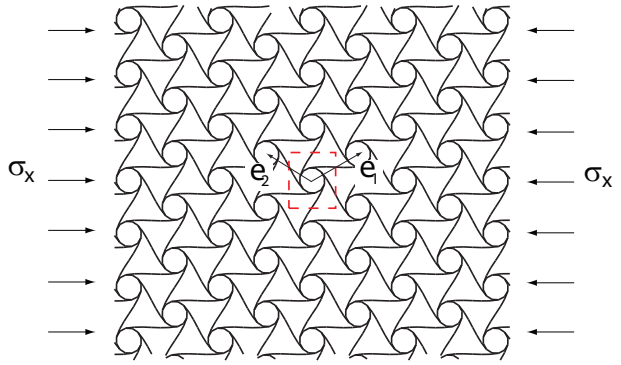

(a)

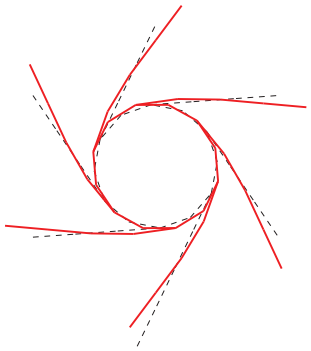

(b)

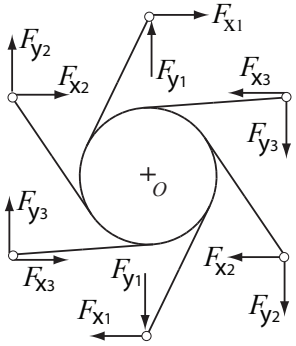

(c)

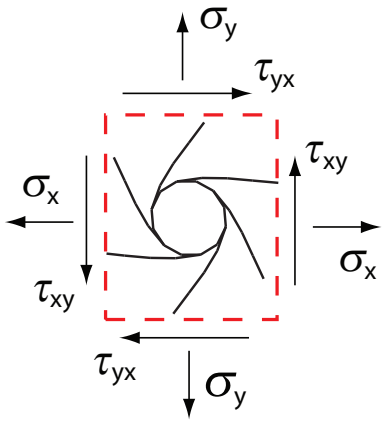

(d)

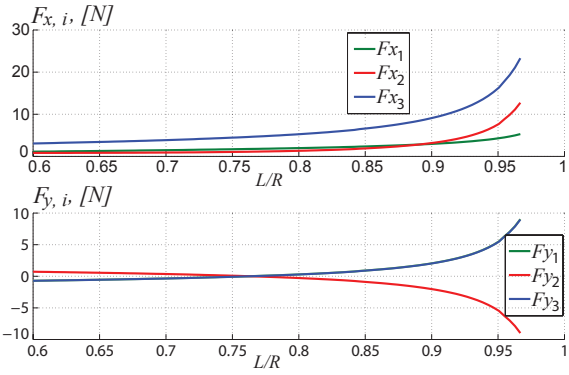

(e)

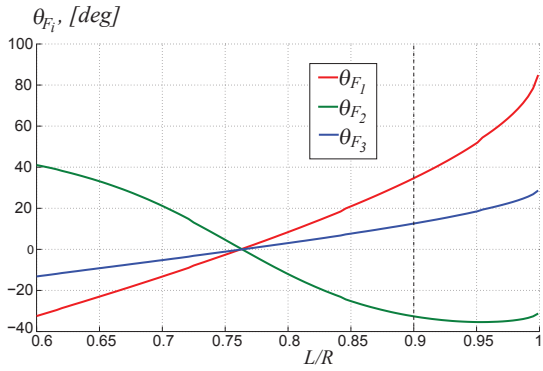

(f)

Figure 35: In-plane deformation behavior of the chiral lattice with deformable nodes due to loading in the x-direction. Loading conditions (a), resulting deformation of internal members $L/R = 0.90$ (b), resultant forces (c), resultant stresses (d), force-magnitude dependence on L/R (e) and force-orientation dependence on L/R (f)

equivalent-continuum point of view, the unit cell depicted in fig. 35.d is the smallest feature of the lattice, thus its boundaries may be utilized for a stress analysis to obtain additional equations to solve for the resultant forces F_{x_i} and F_{y_i}. Specifically, the following expressions are satisfied:

$$F_{x_2} + F_{x_3} = \sigma_x bR, \tag{48}$$

$$F_{y_2} + F_{y_3} = 0. \tag{49}$$

Eqs. (48) and (49) relate the externally applied stress σ_x to internal forces and exploit the fact that no shear stress τ_{xy} is imposed at the boundaries of the lattice. Two additional equations should be provided by the fact that neither τ_{yx} or σ_y are imposed at the boundaries of the assembly. However, both F_{x_1} and F_{y_1} are non-zero, introducing unexpected complexity in the problem at hand, which is thus hyperstatic. Furthermore, for hyperstatic problems associated with the unit-cell of a given cellular solid, it is customary to exploit the reflection symmetry of a unit cell to obtain additional equations at a central joint by taking cuts and enforcing equilibrium [97]. The chiral lattice has neither reflection symmetry nor a central joint. An additional equation is provided by considering that the sum of the moments must be zero. Then the elasto-static problem at hand yields 6 unknowns and 2 equations relating internal forces and external stress and 1 equation of equilibrium of moments, thus it presents a system degree of redundancy of 3. If the nodes are allowed to deform, moreover, no particular kinematic behavior should be assumed, as it may strongly depend upon a given topology. The elastic behavior due to loading in the y-direction as well as shear loading is investigated next, before any analyses are proposed.

The deformed state of the chiral lattice when loaded by an external, uniaxial stress σ_y is shown in fig. 36.a. Note that the deformed state of the circle resembles an ellipse (fig. 36.b) with its major axis now aligned with $\boldsymbol{e}_1$, while for loading in the x-direction the circle's deformation was aligned along $\boldsymbol{e}_2$ (fig. 35.b). The variation

of force-component magnitude and force orientation are shown in fig. 36.c and 36.d respectively. As for loading along the x-direction, the case at hand produces 6 dis-

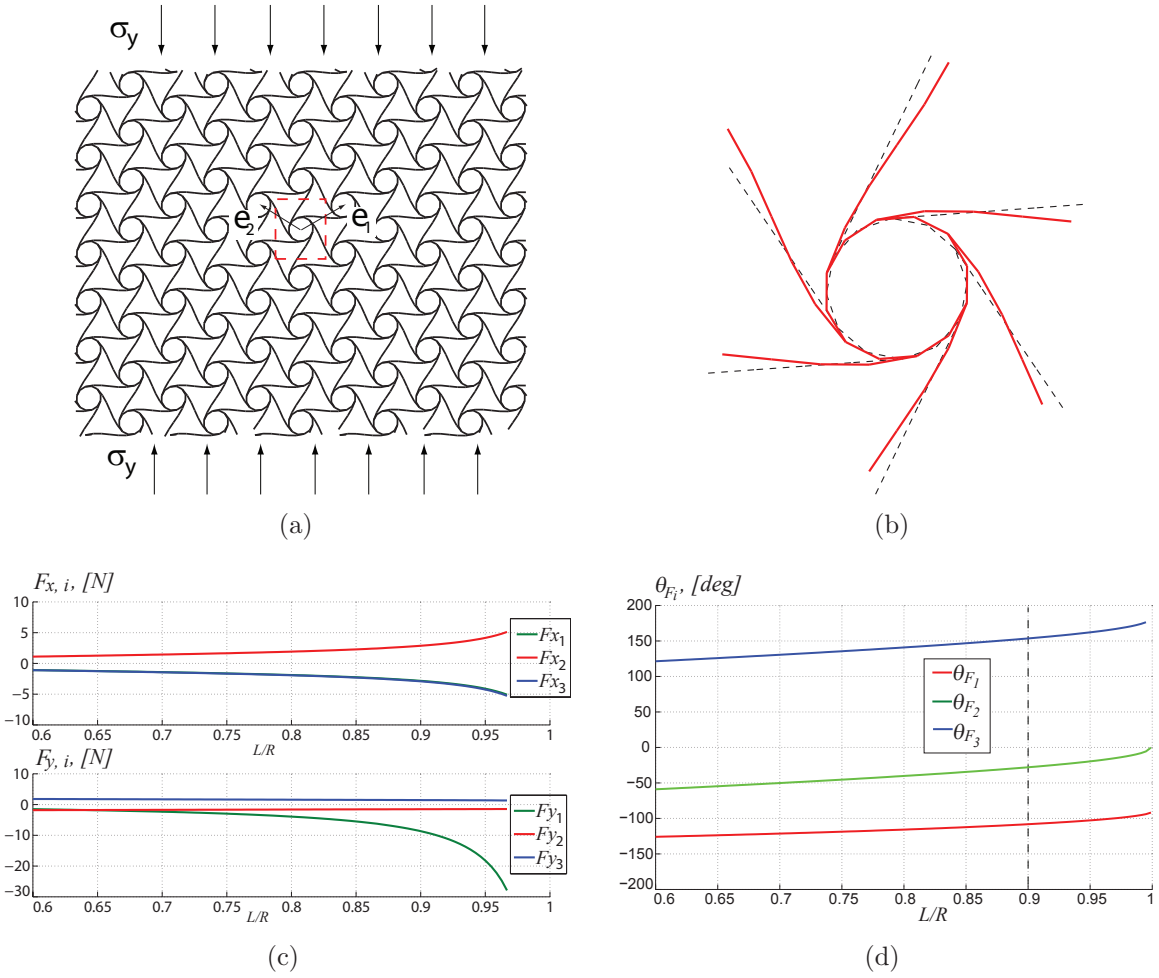

Figure 36: In-plane deformation behavior of the chiral lattice with deformable nodes due to loading in the y-direction. Loading conditions (a), resulting deformation of internal members $L/R = 0.90$ (b), force-magnitude dependence on L/R (c) and force-orientation dependence on L/R (d)

tinct reaction-force components that respect the hexagonal symmetry of the lattice (fig. 36.c). Internal forces for loading in the y-direction satisfy the following relation:

$$F_{x_2} + F_{x_3} \quad = \quad 0. \tag{50}$$

Once again, the stress state of the unit cell is peculiar. It is reasonable, in fact, to expect that $F_{x,1} = 0$ and $F_{y,1} = -\sigma_y bR\cos\theta$, since no shear stress τ_{yx} or τ_{xy} is

applied (fig. 36.a). However the macro-lattice, FE model yields $F_{x,1} \neq 0$ and $F_{y,1} \neq -\sigma_y bR\cos\theta$. As before, an additional equation is obtained by enforcing equilibrium of moments. For loading in the y-direction the problem is hyperstatic with a system degree of redundancy of 4.

The deformed state of the chiral lattice resulting from shear loading is shown in fig. 37. For the current loading conditions, the circles appear more deformed than the ligaments (fig. 37.b), and for this case hence neglecting node deflections leads to poor estimates for the Poisson's ratio, previously derived in terms of ligament deformations only (sec. 3.3). As for externally applied σ_x and σ_y, isolating one unit cell from the lattice subject to an applied stress τ_{xy}, τ_{yx} shows the presence of 6 distinct resultant-force components which respect the hexagonal symmetry of the lattice. The stress state of the unit cell is hard to predict as for the other loading cases. The internal stress must be in equilibrium with with externally applied stress τ_{xy}, τ_{yx}. The following must hold:

$$F_{x_2} + F_{x_3} = 0, \tag{51}$$

$$F_{y_2} + F_{y_3} = \tau_{xy} bR. \tag{52}$$

Furthermore, it is reasonable to suppose that $F_{x,1} = -\tau_{yx} bR\cos\theta$ and $F_{y,1} = 0$, since no stress σ_y is applied (fig. 37.a), however the macro-lattice, FE model yields $F_{y,1} \neq 0$ and $F_{x,1} \neq -\sigma_{xy} bR\cos\theta$. The force-component magnitude and resultant-force orientation are shown in fig. 37.c and 37.d respectively, and are equally complex as the same values for loading in the x and y-directions. For the case of shear loading, the problem presents 6 unknowns and 3 equations including equilibrium of moments, so that the system degree of redundancy of 3.

Hyperstatic problems, however, are solved routinely in the field of structural engineering. A number of methods allow the determination of additional equations to

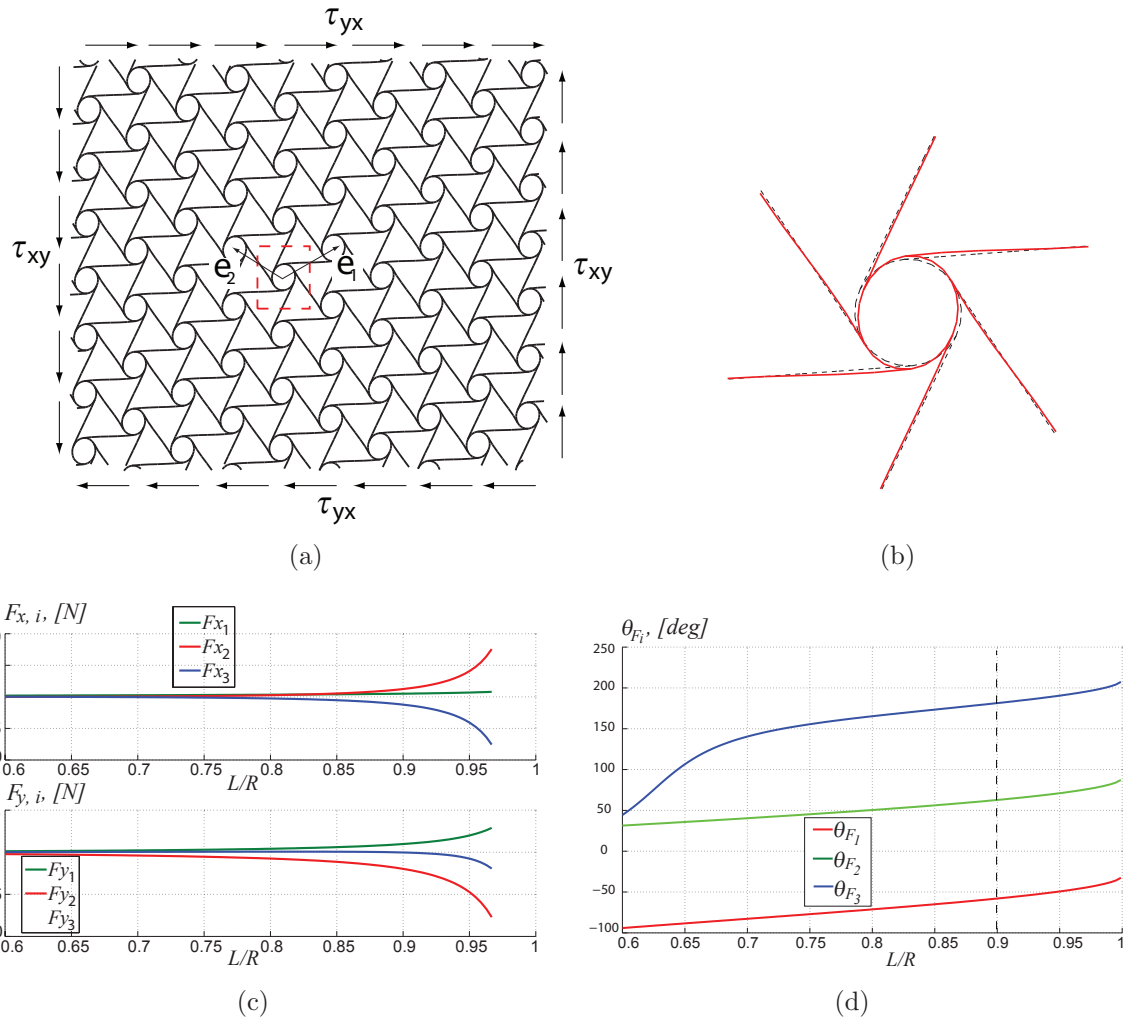

Figure 37: In-plane deformation behavior of the chiral lattice with deformable nodes due to shear loading. Loading conditions (a), resulting deformation of internal members $L/R = 0.90$ (b), force-magnitude dependence on L/R (c) and force-orientation dependence on L/R (d)

uniquely establish the relation among forces acting on a body. Employing the flexibility method for example, one may cut the system in as many locations as the degree of redundancy and define a single relative displacement for each of the cuts. Using constitutive laws, strain-displacement relationships and imposing that the assumed displacements at the cuts vanish, additional equations are obtained. Other methods such as Castigliano's Theorems may be employed for the task at hand [8]. An additional problem is given by the boundary conditions, as a unit cell is constrained

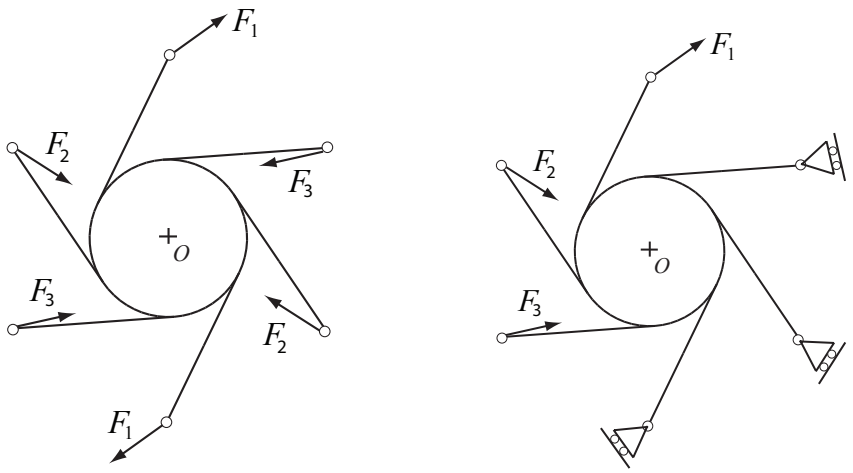

Figure 38: Unit-cell internal force orientation ($L/R = 0.90$) for loading in the x-direction (a), and possible boundary conditions (b)

by elastic supports (other unit cells). This shortcoming may be circumvented by employing the boundary conditions shown in fig. 38, which would reproduce symmetry conditions. The orientation of the roller-like supports, however, is a function of L/R introducing additional complexity in derived analytical expressions. However, attempts to resolve the mere internal forces of the node after cutting the chiral unit cell lead to intractable equations. For this reason, the elastic constants of the chiral lattice are estimated through the macro-lattice FE model. An approximate expression for Poisson's ratios and Young's moduli is established based on the formulae derived neglecting node deformations (Table 2) as they already provide a qualitatively reasonable model for in-plane stiffness. In particular, these analytical expressions provide a very good guess to fit the results of FE simulations.

3.5 Results and comparison of cases 1 and 2

Firstly, the estimated values of $E_{x,U}$ and $E_{y,U}$ differ from each other by at most 2.8%, as indicated by figs. 39.a and 39.b. It is then reasonable to conclude that

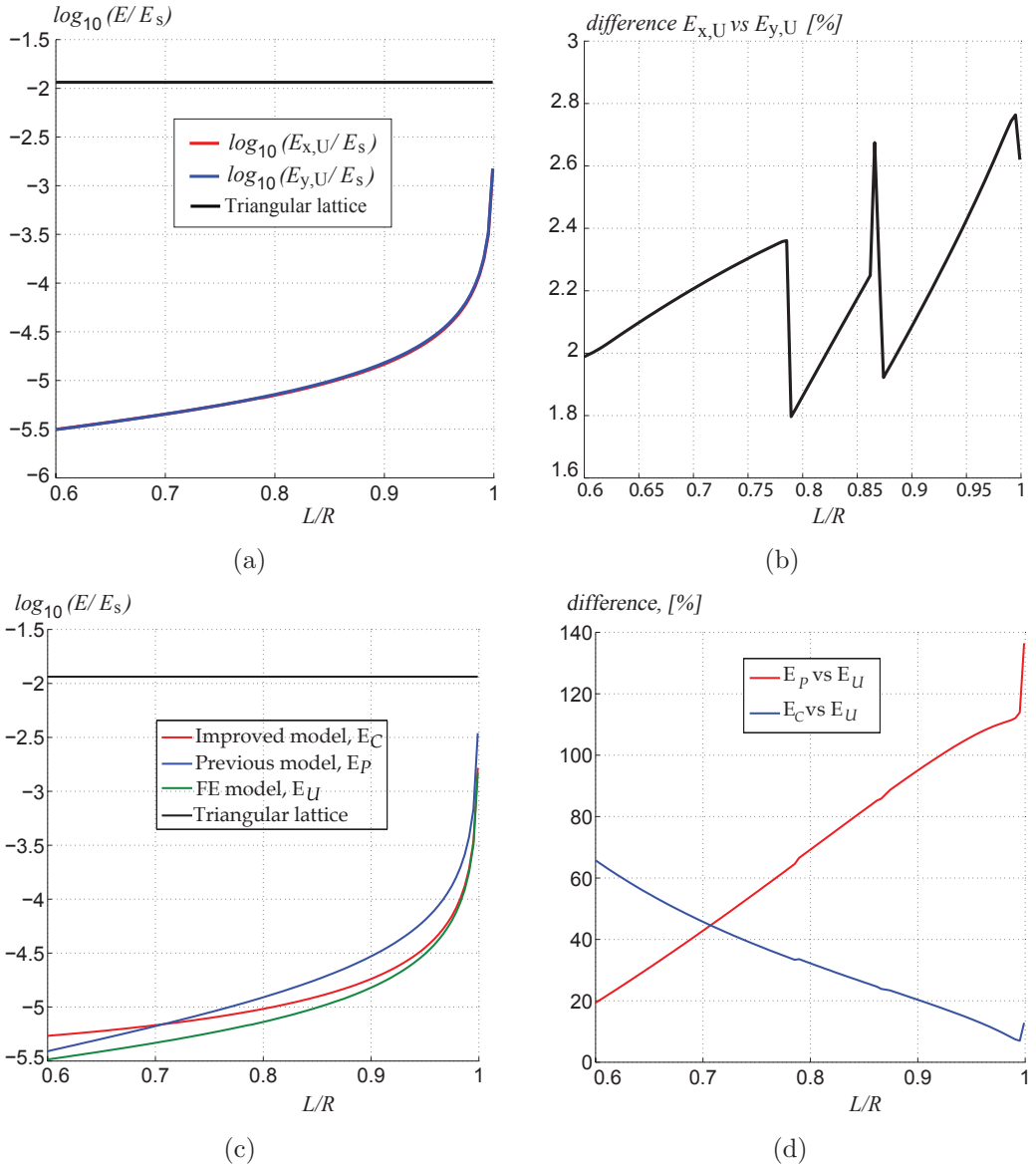

Figure 39: Young's moduli estimated from macro-lattice analysis $E_{x,U}, E_{y,U}$ (a), pecent difference between $E_{x,U}$ and $E_{y,U}$ (b). Comparison of improved estimates from case 1 E_C, the one suggested by [76] E_P and E_U (c), and relative percent difference (d)

the elasto-static behavior of the chiral lattice is transversally isotropic, or isotropic in plane. Fig. 39.a further validates the asymptotic relation between E_C and L/R discussed in sec. 3.4.2. Estimated values of E_U increase very rapidly with respect to the topology parameter L/R (fig. 39.a), approaching an asymptotic behavior as

$L/R \to 1$. The upper limit is the Young's modulus of the triangular lattice (obtained from [97]), also presented in fig. 39.a. As L/R approaches 1, in fact, $r \to 0$ and the chiral lattice becomes identical to the triangular lattice (fig. 18.d). The suggestion set forth by [76] indicating isotropic mechanical behavior is thus confirmed even when the nodes are allowed to deform. A comparison of both previous investigations (E_P) and the improved model of case 1 (E_C) with values of Young's modulus computed with FE macro-lattice models (E_U) is portrayed in fig. 39.c, where the improved model reasonably agrees with E_U as $L/R \to 1$. For low values of L/R, however, E_C and E_U present a marked discrepancy likely due to the deformation of the nodes. As shown in fig. 39.d, the difference between the two for $L/R = 0.60$ is greater than 60%. An additional characteristic portrayed by fig. 39.c is the asymptotic-like relation between E_C, E_U and E_P and the topology parameter L/R. In both eq. (25) and Table 2 in fact the equivalent stiffness is related to a given topology as $E_C/E_s \propto (L/r)^2$. The same is found in sec. 3.3. Recalling that $\cos\beta = L/R$ and $\tan\beta = 2r/L$ (from eq. (4)), it is important to note that as L/R increases linearly, L/r increases as $2/\tan\beta$. This reinforces the suggestion that the mechanical behavior of the chiral lattice can be significantly altered or tailored simply by varying a single parameter, namely the topology parameter.

Additional confirmation of isotropic behavior comes from the estimated values of ν_{xy} and ν_{yx} shown in fig. 40.a, obtained via the macro-lattice analysis presented above (sec. 3.4.3). Their relative difference, in fact, is within 1% (fig. 40.b). Furthermore, estimated values of G_U from the analysis of case 2 agree with the relation $G_U = E_U/\left(2\left(1+\nu_U\right)\right)$, as shown in fig. 40.c and 40.d. The difference between estimates of G_U obtained by quantifying the lattice's response to an applied shear stress τ_{xy} and those obtained from the the relationship between G and E, ν for an isotropic material is within 5.5% (fig. 40.d). Finally, in-plane Poisson's ratio is characterized

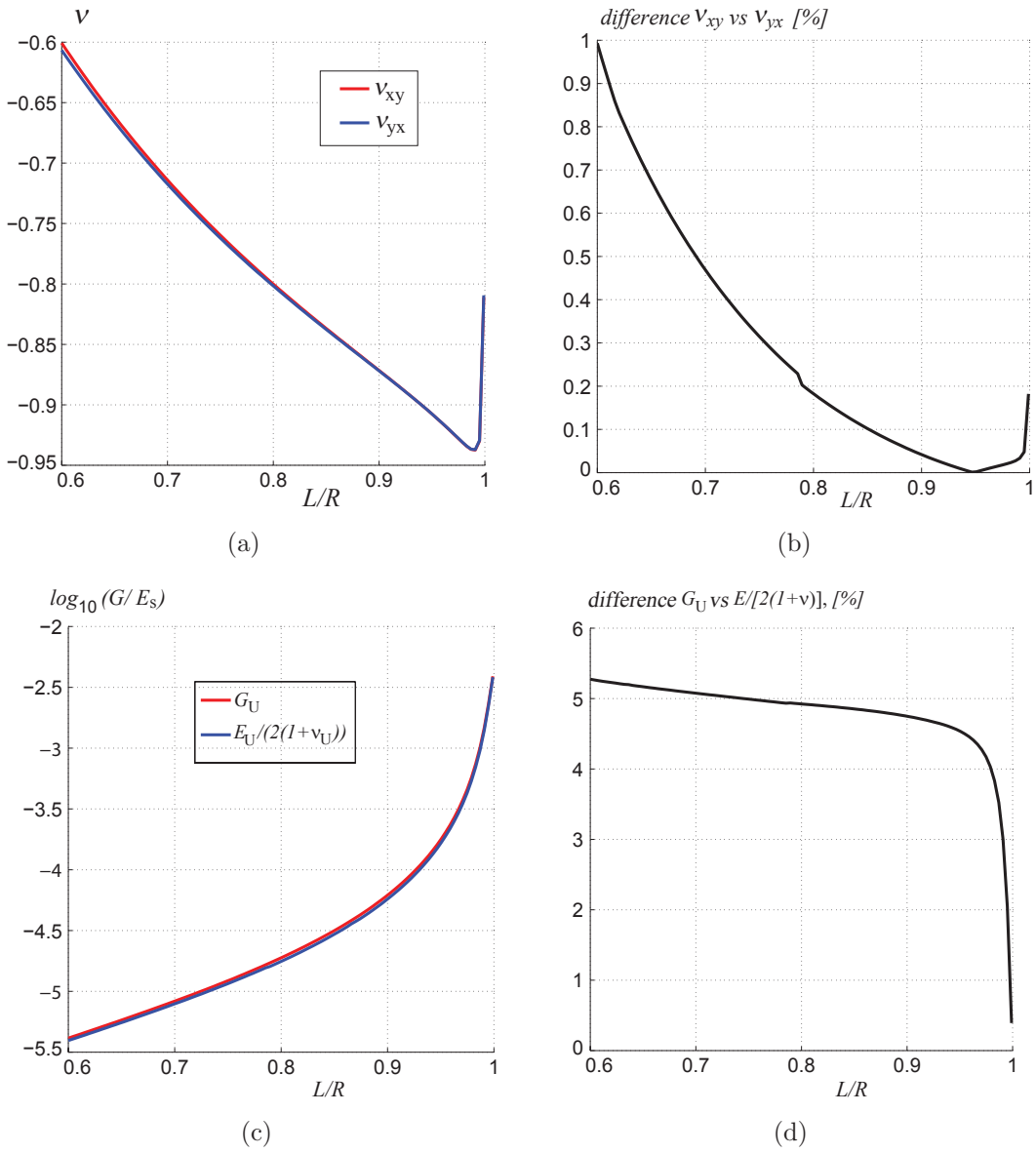

Figure 40: Poisson's ratios ν_{xy}, ν_{yx} obtained from macro-lattice analysis (a) and their relative difference (b); comparison of shear modulus G_U with the relation $G = E/[2(1+\nu)]$ from macro-lattice model (c) and their relative difference (d)

by a boundary-layer-like relation with respect to L/R; that is it approaches its minimum value (≈ -0.938 at $L/R = 0.991$) quasi-linearly. As L/R is increase beyond 0.991 the Poisson's ratio asymptotically increases toward the value of the triangular lattice or 1/3, not shown in fig. 40. As the circles become smaller in fact, the moments arising from non-central forces diminish, and the deformation behavior of the

ligaments shifts from one dominated by bending to one dominated by axial deformations. This phenomenon, moreover, justifies the rapid increase of E_U with respect to L/R. Bending-dominated structural lattices feature a dependency between in-plane Young's modulus and wall thickness as $E \propto \left(\frac{t}{L}\right)^3$, while axially-dominated lattices feature $E \propto \left(\frac{t}{L}\right)$. This is a known fact, suggested in both [40] and [97] among others.

At this stage, one would like to express the relation between Young's modulus, including deformations of the node and well as forces perpendicular to the applied stress, in terms of geometric parameters. Firstly, the computed in-plane Poisson's ratios ν_{xy} and ν_{yx} depicted in fig. 40.b differ by at most 1% for the values of topology parameter considered (fig. 40.a and 40.a). Moreover $E_{x,U}$ and $E_{y,U}$ depicted in fig. 39.a are within 2.8% of each other. This suggests that an approximate relation between E_U and geometric parameters may be formulated by exploiting the following reciprocity relationship [40, 64]:

$$E_x \nu_{xy} = E_y \nu_{yx}. \tag{53}$$

Drawing inspiration from the case of hexagonal lattices, for which $E_x \nu_{xy} = E_y \nu_{yx} = E_s \left(\frac{t_b}{L}\right)^3 \frac{1}{\sin\theta \cos\theta}$, where $\theta = 30°$, a similar relation for the chiral lattice is sought. Since the chiral lattice is bending dominated and exhibits hexagonal symmetry, just as hexagonal lattices, a similar expression should lead to relating ν_{xy} to geometric and material parameters. A possible approximation for $E_x \nu_{xy}$ is found to be:

$$E_x \nu_{xy} \approx -E_s \left(\frac{t}{L}\right)^3 \frac{\cos^2\beta\,(11 + 3\sin\beta)}{4\sin^2\beta}, \tag{54}$$

which is within 2% of the values estimated from the unit-cell analysis for $L/R \in [0.6, 0.97]$ and increases to 10% for $L/R \in (0.97, 0.999]$. A possible description of ν_{xy} based on the formula for E_C (from Table 2) in place of E_x in eq.(54) may then be:

$$\nu_{xy} = \nu_U^* \approx -\frac{\sqrt{3}(t^2 + 4r^2)\,(11 + 3\sin\beta)}{6\tan^2\beta\sin^2\beta\,[4r^2\,(1 + 1/\cos^2\beta) + L^2]\,(L/r)^2} \frac{1 + \frac{1}{(L/R)^{1.5}}}{1.78}, \tag{55}$$

where the superscript $(\,)^*$ denotes approximate values obtained by correcting the results of case 1 with respect to those of case 2. Predictions of in-plane Young's

modulus based on the assumption of rigid circles (E_C), furthermore, are compared to those obtained allowing the circles to deform (E_U). As expected, rigid circles lead to an overestimation of E as shown in fig. 39.b, while the model suggested by [76] (E_P), reported in eq. (25), yields poor results even as $L/R \to 1$. Finally, an approximate relationship between in-plane Young's modulus and L/R is formulated starting from the expression obtained assuming rigid circles. In particular, it is clear from fig. 39.a that such estimate is reasonable as $L/R \to 1$; a factor that vanishes as $L/R \to 1$ is then employed to obtain:

$$\frac{E_U^*}{E_s} = \sin^2\beta \, \frac{[4r^2\,(1+1/\cos^2\beta)+L^2]}{2(t^2+4r^2)}\sqrt{3}\left(\frac{L}{r}\right)^2\left(\frac{t}{L}\right)^3 \frac{1.78}{1+\frac{1}{(L/R)^{1.5}}}. \qquad (56)$$

The absolute difference between eq. (56) and E_U is within 6.5% as shown in fig. 41.

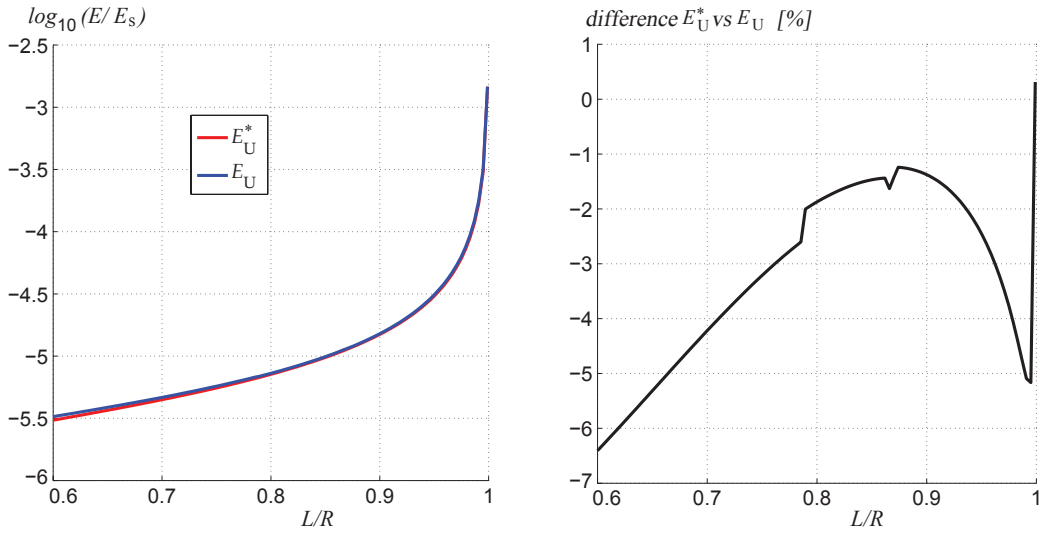

(a) (b)

Figure 41: Comparison of E_U^* from eq. (56) and that obtained from the macro-lattice FE model (a), and their relative difference (b)

The shear stiffness G_U^* is obtained from eqs. (55) and (56) by enforcing that $G_U^* = E_U^*/[2(1+\nu_U^*)]$.

3.6 Comparison of the elastic properties of chiral and common lattices

In order to gain a perception of the mechanical behavior of the chiral lattice uncovered above, it is helpful to compare it to that of other periodic cellular solids. In particular, square, triangular and hexagonal lattices are common topologies encountered in engineering applications and have been investigated for their superior specific (mass-normalized) properties [21, 40, 96, 97]. As reported in [40, 97], the equivalent mechanical properties on the aforementioned topologies in terms of geometric parameters are listed in Table. 3. The results reported in sec. 3.4.3 have been obtained

Table 3: Mechanical properties of common lattice topologies

topology	relative density $\bar{\rho}$	E/E_s	G/E_s	ν
square	$\frac{2t}{L}$	$\frac{1}{2}\bar{\rho}$	$\frac{1}{16}\bar{\rho}^3$	$\frac{1}{2}\nu_s\bar{\rho}$
triangular	$2\sqrt{3}\frac{t}{L}$	$\frac{1}{3}\bar{\rho}$	$\frac{1}{8}\bar{\rho}$	1/3
hexagonal	$\frac{2}{\sqrt{3}}\frac{t}{L}$	$\frac{3}{2}\bar{\rho}^3$	$\frac{3}{8}\bar{\rho}^3$	1.0

by considering the wall thickness $t = 0.01\ m$, the ligament length $L = 1\ m$. For a topology parameter $0.6 \leq L/R \leq 0.999$ and the specified wall thickness and ligament length, the resulting relative density $\bar{\rho}$ for the chiral lattice, described by eq. (10) (sec. 2.7), is shown in fig. 42. With the relative density at hand, it is possible to compare the mechanical properties of the chiral lattice with those of square, triangular and hexagonal lattices. In particular, the Young's modulus for the aforementioned lattices is presented in fig. 43.a. Quite interestingly, the chiral lattice features the lowest Young's modulus for $0.6 \leq L/R \leq 0.98$, while the square lattice is the least compliant. Regarding shear deformations, in contrast, the square lattice features the

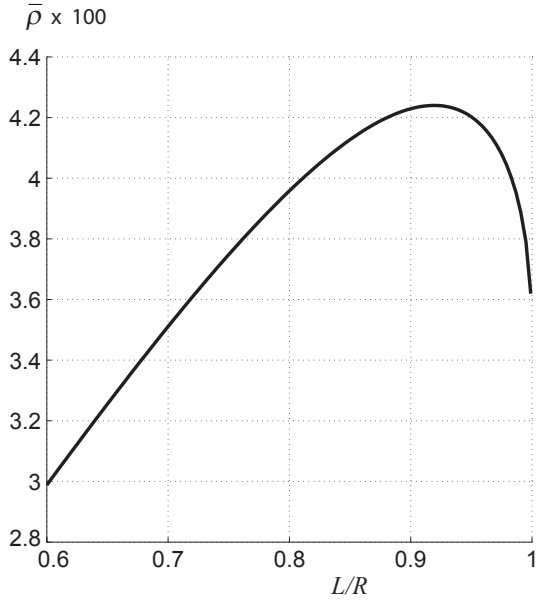

Figure 42: Relative density $\bar{\rho}$ for the chiral lattice given $0.6 \leq L/R \leq 0.999$, $t = 0.01$ m and $L = 1$ m

lowest shear modulus, and the triangular lattice the highest. The chiral lattice performs better in shear than square and hexagonal lattices for $L/R > 0.83$ and its shear modulus approaches that of the triangular topology as $L/R \to 1$, in agreement with the earlier findings of secs 3.4.2 and 3.4.3.

3.7 Summary

The analyses presented in this chapter are devoted to establishing the elasto-static behavior of the chiral lattice. This endeavor was began by the seminal work in [76] concluding strong influence of the topology parameter L/R on the mechanical behavior, and a negative Poisson's ratio. These characteristics instilled curiosity and motivated the research presented herein. The findings in [76], moreover, propose that chiral lattice is isotropic and it is characterized by a Poisson's ratio of exactly -1 indicating an assembly that transversally expands when stretched and transversally contracts when compressed. Such elastic properties suggest an unusual mechanical behavior and attracted the interest of various researchers, such as [10, 44], seeking

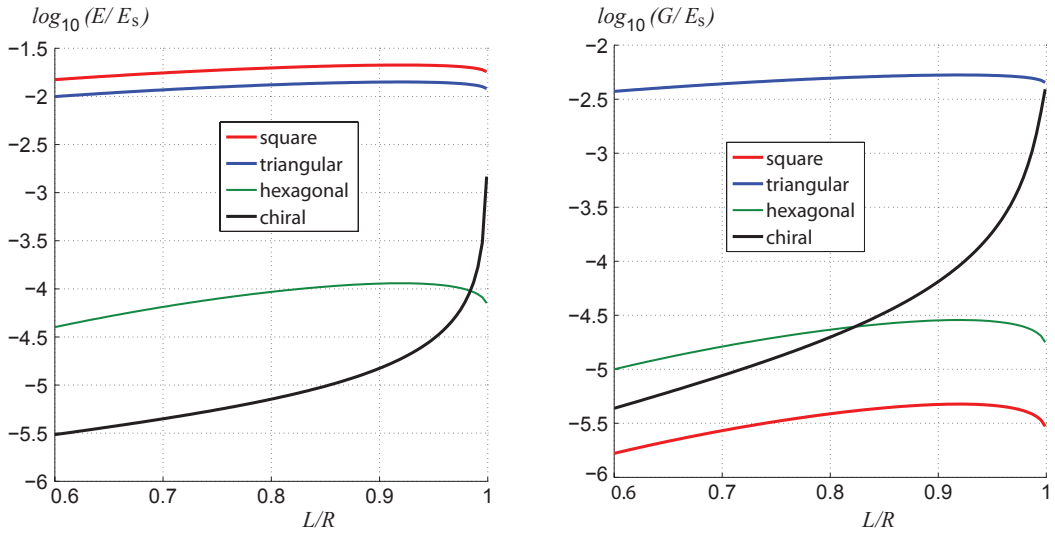

(a) (b)

Figure 43: Comparison of Young's modulus (a) and shear modulus (b) for various periodic topologies

cellular solids with superior performance. In the literature on auxetic materials, in fact, it is often indicated that a negative Poisson's ratio leads to a high shear stiffness [44, 76, 37, 58, 86]. The combination of isotropy and a Poisson's ratio $\nu = -1$ however hindered any attempt to evaluate the applicability of chiral geometries for various engineering applications via equivalent-continuum models owing to a singular constitutive matrix.

The unique geometry of the chiral lattice, not symmetric to its mirror image, and the lack of a central joint at which internal members meet provides significant challenges with respect to employing existing analytical methods to determine the equivalent-continuum elastic constants based on unit-cell analyses. In order to establish more accurate values of Young's modulus and Poisson's ratio, a two-phase study is carried out. In the first step, the suggestion made in [76] to neglect internal-force components perpendicular to externally-applied stresses is relaxed and improved expressions for Young's modulus are derived. Moreover, axial and shear deflections,

previously not considered, are included in the investigations, while the circular members of the lattice are maintained rigid as was true in [76]. Instead of determining displacements arising from imposed loads, deformations based on experimental measurements in [76] are imposed, leading to a Poisson's ratio of -1. Accordingly, the shear stiffness is not addressed in the first phase. In a second approach, no restrictions on internal-force components or the deformations of the nodes are imposed. The high degree of redundancy of the unit cell, however, leads to intractable analytical expressions. A macro-lattice FE model is instead used to obtain numerical values of Young's modulus, Poisson's ratio and shear stiffness, which indicates that the deformations of the nodes are not negligible, and for shear loading the dominant feature.

The mechanical behavior of the chiral lattice is found to be isotropic denoted for strong influence of topology parameter L/R. In particular, the Young's modulus increases by 3.5 orders of magnitude as L/R is varied from 0.6 to 0.999, while the Poisson's ratio decreases to a minimum of -0.94 and subsequently increases asymptotically to 1/3. The shear modulus, also increases significantly as L/R increases. All three elastic constants approach the values of those of the triangular lattice, in compliance with the fact that the chiral lattice approaches a triangular configuration as $L/R \rightarrow 1$. If compared to common lattices such as square, triangular and hexagonal geometries with equal relative density, the chiral lattice features the lowest Young's modulus for $L/R < 0.99$, while the shear stiffness is the highest for $L/R \geq 0.83$ except for the triangular lattice.

CHAPTER IV

OUT-OF-PLANE MECHANICAL PROPERTIES OF THE CHIRAL LATTICE

4.1 Introduction

Honeycomb-core sandwich panels are common structural components first adopted by the aeronautical industry [47, 48, 102] but have since become less expensive and common components for the construction, naval, automotive and wind-turbine industries, to name a few [102]. The most commonly utilized core is that of the hexagonal honeycomb whose mechanical properties have been investigated and reported in a significant number of publications, eloquently summarized in [40]. While the manufacturing of planar sandwich-panels has reached significant maturity, curved panels still pose challenges, mainly due to Poisson's ratio effects. The hexagonal honeycomb, in fact, features a Poisson's ratio of ≈ 1 which corresponds to sandwich panels with anticlastic curvature (saddle-shaped) whenever unidirectional moments are applied at their boundaries. Honeycombs with square topology on the other hand feature an in-plane Poisson's ratio of ≈ 0 allowing the manufacturing of singly-curved (cylinder-like) panels. Core topologies featuring a negative Poisson's ratio yield a doubly-curved (dome-shaped) sandwich panel whenever unidirectional moments are applied at their boundaries [102]. This characteristic is one of the motivations for the research presented in this chapter since the chiral lattice displays auxetic behavior.

If the chiral lattice is to be proposed as a honeycomb core for sandwich panels as the one depicted in fig. 44, out-of-plane mechanical properties are needed. With the in-plane Young's modulus $E_x = E_y$ and Poisson's ratio $\nu_{xy} = \nu_{yx}$ known, three more elastic constants are sought: namely the out-of-plane Young's modulus E_z, shear

modulus $G_{xz} = G_{yz}$ and Poisson's ratio $\nu_{xz} = \nu_{yz}$. One can say that $G_{zx} = G_{zy}$ and $\nu_{xz} = \nu_{yz}$ even before embarking in a detailed analysis, since as indicated by [64] and presented in chapter 2, in-plane hexagonal symmetry requires five elastic constants to uniquely define the strain energy function. Since two elastic constants have been uncovered, three more are needed to fully characterize the mechanical behavior of a chiral honeycomb.

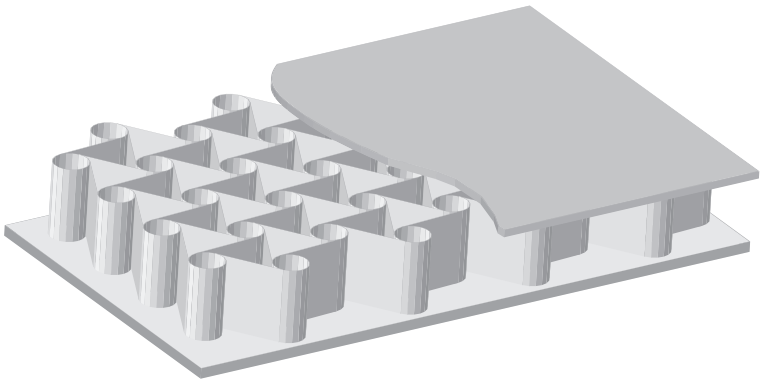

Figure 44: Sandwich panel with chiral-honeycomb core

The analysis of the out-of-plane elastic properties will proceed with an overview of available analytical methods (sec. 4.2), while secs. 4.3 and 4.4 will address the out-of-plane Poisson's ratios and Young's modulus E_z respectively. Analytical expressions for the shear stiffness are presented in sec. 4.5, while sec. 4.6 is devoted to the refinement of analytical expressions with the aid of a unit-cell, FE model. Finally, sec. 4.7 compares the shear stiffness of chiral and hexagonal honeycombs to assess the out-of-plane performance of the former with respect to common topologies.

4.2 Overview of methods to determine the out-of-plane properties of honeycomb cores

The out-of-plane shear moduli of honeycomb cores are the most difficult elastic constants to derive [40]. A number of elastic phenomena in the core corresponding to externally-applied shear stresses in fact need to be disregarded in order to obtain

tractable analytical expressions. Nonetheless, insightful publications by [18, 29, 40, 53, 74] have offered a number of methods to analyze out-of-plane shear stress. The simplest method, proposed by Chang [18], enforces compatibility of strain and associates the latter to equivalent loads through the relation $P = GA\gamma$. A load for each component of the unit cell is computed and summed to obtain the external shear stress acting on the core. The ratio of effective shear stress and assumed strain produces a formula for G. A similar procedure is also proposed by Penzien [74], where in addition, the effect of warping of the core members is analyzed and found to be negligible provided that b/L be large. The most comprehensive and insightful analysis is provided by Kelsey [53], where the Unit Load and Unit Displacement methods are employed to obtain upper and lower-bound estimates of the shear modulus in terms of geometric parameters, by enforcing that an assumed stress state in the core be in equilibrium, and an assumed strain state be compatible respectively. The method proposed in [53], moreover, finds that estimates of the shear modulus via the Unit Load Method represent a lower bound, while those obtained with the Unit Displacement Method yield an upper bound. In [40], the method proposed by Kelsey [53], which requires the evaluation of stiffness and flexibility matrices, is simplified by substituting the Principle of Virtual Displacements and the Principle of Virtual Forces with the Theorem of Minimum Total Potential Energy and the Theorem of Complementary Potential Energy respectively.

The analysis presented in [40] is reported herein to illustrate the procedure that will be employed in the next sections for the chiral honeycomb. In the case of the hexagonal lattice of fig. 45.a, the following simplifications are considered:

- ◇ only three topologically-distinct components of the unit cell, namely the walls f, g and h, are included in the analysis (fig. 45.b);
- ◇ the strain energy only accounts for shear deformations and bending of the walls is neglected;

◇ t/L are small, while b/L is large;

◇ small deformations/deflections.

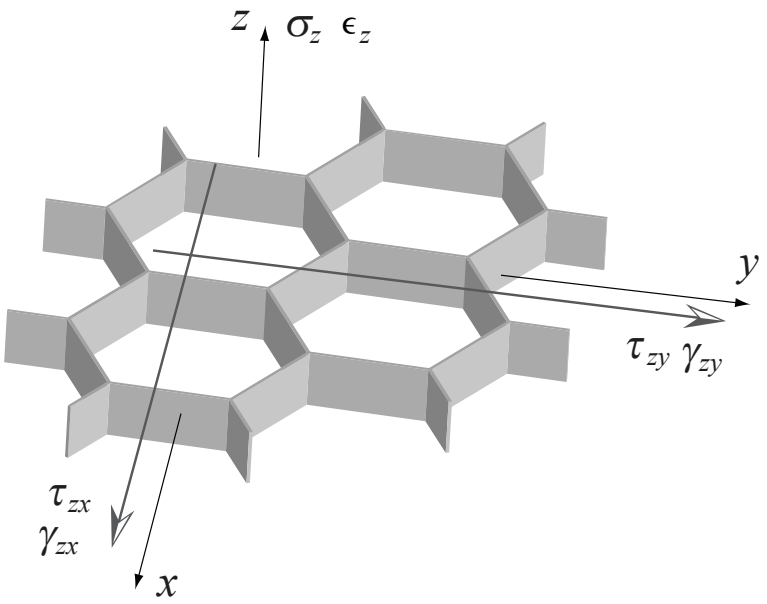

(a)

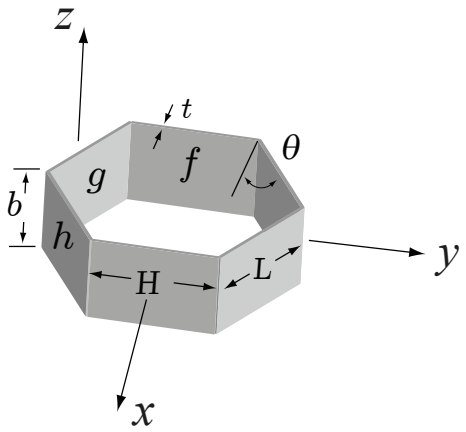

(b)

Figure 45: Hexagonal honeycomb with shearing stresses and strains normal to z (a), and unit cell (b). Reproduced from [40]

The Theorem of Minimum Total Potential Energy is used to obtain an upper bound of the shear moduli by enforcing compatibility of displacements with external boundary

conditions. For loading in the x-direction, the shear strains in walls f, g and h are:

$$\begin{aligned} \gamma_f &= 0 \\ \gamma_g &= \gamma_{xz} \cos\theta \\ \gamma_h &= \gamma_{xz} \cos\theta, \end{aligned} \tag{57}$$

where γ_f, γ_f, γ_f denote shear strain in walls f, g, h, while γ_{xz} is the applied shear strain. The angle θ determines the topology of the honeycomb, which in this case is 30° (fig. 45.b). For an imposed shear strain γ_f wall f is expected to bend, and thus in compliance with the assumptions set forth above, its deformations are neglected. The Theorem of Minimum Total Potential Energy may be expressed as an inequality as follows [40]:

$$\frac{1}{2} G_k \gamma_k^2 V \leq \frac{1}{2} \sum_i \left(G_s \gamma_i^2 V_i \right), \tag{58}$$

where $k = xz, yz$, G_s is the shear modulus of the constituent material and V_i is the volume of each wall. For wall f for example $V_f = Htb$. The other two values are computed in the same manner. For loading in the y-direction the shear strains in the walls are:

$$\begin{aligned} \gamma_f &= \gamma_{yz} \\ \gamma_g &= \gamma_{yz} \sin\theta \\ \gamma_h &= \gamma_{yz} \sin\theta. \end{aligned} \tag{59}$$

With the shear strains in each wall (eqs. (57) and (59)) and their respective volume, eq. (58) is used to obtain the relation between G_k and the honeycomb's geometric parameters.

In order to obtain a lower bound of the shear moduli, equilibrium of internal stresses τ_i's with external boundary conditions is enforced. The Theorem of Complementary Potential Energy is applied. For loading in the x-direction, symmetry

considerations impose the following relation [40]:

$$\tau_g = \tau_h. \tag{60}$$

Equilibrium with external loads requires that:

$$2\tau_{zx} L \left(H + L\sin\theta\right) = \tau_g t L \cos\theta. \tag{61}$$

For loading in the y-direction, symmetry considerations impose the same relation as eq. (60) ([40]). Equilibrium in the z-direction at locations where walls meet requires that:

$$\tau_f = \tau_g + \tau_h = 2\tau_g, \tag{62}$$

while equilibrium with external loads yields:

$$2\tau_{yz} L \left(H + L\sin\theta\right)\cos\theta = 2\tau_g t L \sin\theta + \tau_f H t. \tag{63}$$

The Theorem of Complementary Potential Energy may be expressed as [40]:

$$\frac{1}{2}\frac{\tau_k^2}{G_k} V \leq \frac{1}{2}\sum_i \left(\frac{\tau_i^2}{G_s}, V_i\right) \tag{64}$$

where τ_i is the shear stress in each wall ($i = f, g, h$).

With expressions for the stress in each of the walls, eq. (64) is evaluated to obtain lower-bound estimates of G_k. It is important to note that both upper and lower-bound estimates of G_k are derived based upon a 2-D analysis, hence phenomena related to the out-of-plane thickness b are so far neglected. In this case, according to [42, 43], a numerical fitting based on FE models can obviate such shortcoming. This is a common procedure for honeycombs [40, 42, 43] for which the effective out-of-plane shear modulus may be expressed as:

$$G_k = G_k^L + \frac{\alpha}{b/L}\left(G_k^U - G_k^L\right), \tag{65}$$

where the superscripts $(\ )^U$ and $(\ )^L$ indicate upper and lower-bound estimates respectively obtained from eqs. (58) and (64). For regular hexagonal honeycombs it is

found that $\alpha = 0.787$ well describes the out-of-plane shear stiffness for $b/L \in [1, 10]$ as reported in [40, 42, 43].

The same procedure elucidated above will be employed to uncover out-of-plane mechanical properties of the chiral honeycomb.

4.3 Out-of-plane Poisson's ratio

Given the in-plane, hexagonal symmetry of the chiral honeycomb, $\nu_{xz} = \nu_{yz}$ relates direct strains in the x and y-direction to that in the z. It is however instructive to demonstrate the reasons for this. The out-of-plane Poisson's ratios can be determined by utilizing the following reciprocal relations [40, 64]:

$$\frac{\nu_{xz}}{E_x} = \frac{\nu_{zx}}{E_z} = -S_{xz}, \tag{66a}$$

$$\frac{\nu_{yz}}{E_y} = \frac{\nu_{zy}}{E_z} = -S_{yz}, \tag{66b}$$

where S_{xz} and S_{yz} are components of the compliance matrix (eq. (6), sec. 2.5) relating the direct strain ϵ_z to direct stresses σ_x and σ_y respectively. Since the chiral honeycomb is isotropic in plane, from eq. (66), $\nu_{xz} = \nu_{yz}$. Furthermore, it is expected that $E_z \gg E_x$ as an applied stress along z would be resisted by axial deformations, while applied direct stresses in plane yield bending-dominated deformations of the lattice's internal members. As discussed in chapter 3 in fact, periodic cellular solids with axially-dominated, deformation mechanisms are characterized by equivalent elastic-constants that are proportional to the relative density while bending-dominated deformation mechanisms lead to elastic properties proportional to $\bar{\rho}^3$. So from eq. (66a) $\nu_{xz} = \nu_{zx}E_x/E_z \approx 0$ and likewise from eq. (66b) $\nu_{yz} = \nu_{zy}E_y/E_z \approx 0$. Poissons's ratios ν_{zx} and ν_{zy} relating direct strains in the plane to the direct strain in the z-direction are [40]:

$$\nu_{zx} = \nu_{zy} = \nu_s, \tag{67}$$

where ν_s is the Poisson's ratio of the core material.

4.4 Out-of-plane Young's Modulus

The out-of-plane Young's modulus E_z can be estimated by considering stress-strain relationships for an elastic continuum. For transversely-isotropic materials in particular the stress σ_z is related to strain components as [64]:

$$\sigma_z = \frac{\nu_{xz}}{1 - \nu_{xy} - 2\nu_{xz}\nu_{zx}} E_z \left(\epsilon_x + \epsilon_y\right) + \frac{1 - \nu_{xy}}{1 - \nu_{xy} - 2\nu_{xz}\nu_{zx}} E_z \epsilon_z. \tag{68}$$

Substituting the findings of the previous section, i.e. $\nu_{xz} = \nu_{yz} \approx 0$, eq. (68) simplifies as follows:

$$\sigma_z = E_z \epsilon_z, \tag{69}$$

where, both σ_z and E_z represent equivalent homogenized values, stress and Young's modulus in the z-direction specifically. The stress acting on the area occupied by a unit cell (fig. 46.a) is expressed as $\sigma_z = P/A$, where P is the applied load. Recalling

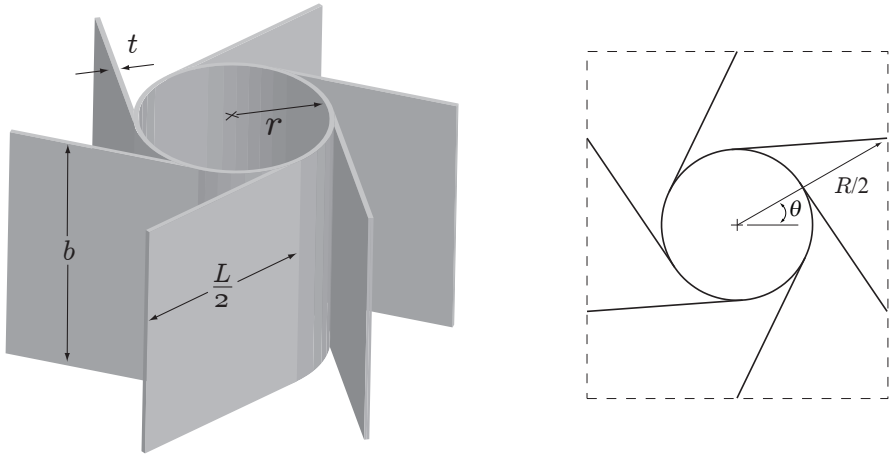

Figure 46: Chiral-honeycomb unit cell with characteristic geometric parameters (a) and equivalent-continuum area (b)

from sec. 2.5 that $\theta = 30°$, the distance between node centers is R and that the chiral topology is symmetric about 2θ rotations, the loaded area (fig. 46.b) is $A = R^2 \cos\theta$. The strain ϵ_z resulting from an applied load is related to the axial stiffness of the unit

cell as follows:

$$P = E_s \; A_w \; \epsilon_z = E_s \; (2\pi r + 3L)t \; \epsilon_z, \tag{70}$$

where A_w is the surface provided by the honeycomb's walls (fig. 46.a). The resulting equivalent stiffness in the z-direction is then:

$$\frac{E_z}{E_s} = \frac{2\sqrt{3}\;(2\pi r + 3L)\;t}{3\;R^2} = \frac{\rho^*}{\rho_s} = \bar{\rho}. \tag{71}$$

4.5 Out-of-plane Shear Moduli

The shear-moduli estimation is based on the following set of assumptions:

- ◇ the ratio t/L is small;
- ◇ the ratio b/L is large so that warping of the cell walls ca be neglected;
- ◇ circles are approximated as hexagons;
- ◇ shear stress is constant in each component of the unit cell;
- ◇ the wall thickness is equal for all unit-cell elements so that $t_b = t_c = t$;

4.5.1 Upper-bound estimate

Employing the Theorem of Minimum Total Potential Energy to obtain an upper bound of the shear moduli, compatibility of displacements with external boundary conditions is enforced. For an externally applied γ_{zx} (fig. 47.a) the internal shear components are assumed constant in each unit-cell internal component of volume V_i.

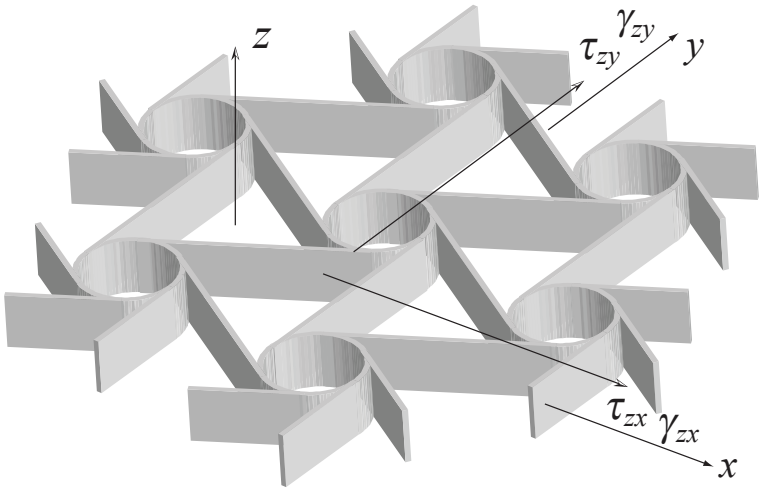

(a)

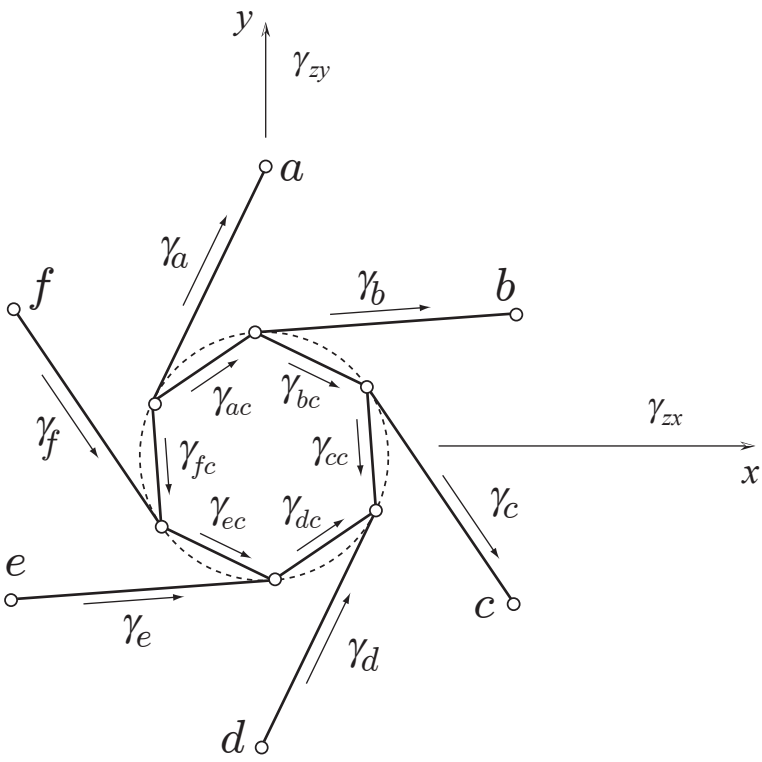

(b)

Figure 47: Chiral honeycomb with shearing stresses and strains normal to z (a), and unit cell with shear-strain components (b)

For loading in the x-direction, the shear strains (fig. 47.b) are:

$$\begin{aligned}
\gamma_a &= \gamma_{zx} \cos 3\theta - \beta \\
\gamma_b &= \gamma_{zx} \cos(\theta - \beta) \\
\gamma_c &= \gamma_{zx} \cos(-\theta - \beta) \\
\gamma_d &= \gamma_{zx} \cos(-3\theta - \beta) \\
\gamma_e &= \gamma_{zx} \cos(-5\theta - \beta) \\
\gamma_f &= \gamma_{zx} \cos(-7\theta - \beta) \\
\gamma_{ac} &= \gamma_{zx} \cos(2\theta - \beta + \pi) \\
\gamma_{bc} &= \gamma_{zx} \cos(-\beta) \\
\gamma_{cc} &= \gamma_{zx} \cos(-2\theta - \beta) \\
\gamma_{dc} &= \gamma_{zx} \cos 2\theta - \beta \\
\gamma_{ec} &= \gamma_{zx} \cos(-\beta) \\
\gamma_{fc} &= \gamma_{zx} \cos(-2\theta - \beta)\,.
\end{aligned} \tag{72}$$

The volume occupied by a ligament (fig. 47.b) is $V_i = Ltb/2$, while that of a component of the inner hexagon is $V_{i,c} = rtb/2$, where the subscript $(\ )_c$ indicates components belonging to the circle. The volumes occupied by the remaining elements are computed in the same manner. Substituting eqs. (72) into eq. (58), and noting that the sign of the assumed shear strain in each element is irrelevant (eq. (58)), one obtains an upper bound estimate as:

$$\frac{G^U_{zx}}{G_s} = \sqrt{3}\,(\sin\beta + \cos\beta)\cos^3\beta,\,\frac{t}{L} \tag{73}$$

where the superscript $(\ )^U$ denotes an upper-bound estimate. For an externally applied γ_{zy} (fig. 47.a), the shear-strain components within the unit-cell are:

$$\begin{aligned}
\gamma_a &= \gamma_{zy} \sin(3\theta - \beta) \\
\gamma_b &= \gamma_{zy} \sin(\theta - \beta) \\
\gamma_c &= \gamma_{zy} \sin(-\theta - \beta) \\
\gamma_d &= \gamma_{zy} \sin(-3\theta - \beta) \\
\gamma_e &= \gamma_{zy} \sin(-5\theta - \beta) \\
\gamma_f &= \gamma_{zy} \sin(-7\theta - \beta) \\
\gamma_{ac} &= \gamma_{zy} \sin(2\theta - \beta + \pi) \\
\gamma_{bc} &= \gamma_{zy} \sin(-\beta) \\
\gamma_{cc} &= \gamma_{zy} \sin(-2\theta - \beta) \\
\gamma_{dc} &= \gamma_{zy} \sin(2\theta - \beta) \\
\gamma_{ec} &= \gamma_{zy} \sin(-\beta) \\
\gamma_{fc} &= \gamma_{zy} \sin(-2\theta - \beta)\,.
\end{aligned} \tag{74}$$

Substituting eqs. (74) into eq. (58) now adapted for G_{zy}, and noting that the component volumes are unchanged, one obtains:

$$\frac{G^U_{zy}}{G_s} = \sqrt{3}\,(\sin\beta + \cos\beta)\cos^3\beta \frac{t}{L}. \tag{75}$$

Eqs. (73) and (75) are identical indicating that the chiral honeycomb is transversally isotropic.

4.5.2 Lower-bound estimate

The assumption that the strain energy is to be attributed to shear deformations, while bending of the unit-cell components is neglected simplifies the analysis for the hexagonal honeycomb. In the case of the chiral honeycomb, the same simplification can be made for certain topologies such as the one depicted in fig. 48.a for which

$L/R = 0.90$, but not for $L/R = 0.60$ of fig. 48.b, as the orientation of unit-cell components varies with L/R. Since the objective of this chapter is to derive estimates for the out-of-plane shear moduli applicable to topologies with $0.60 \leq L/R < 1$, no assumption regarding wall bending is made.

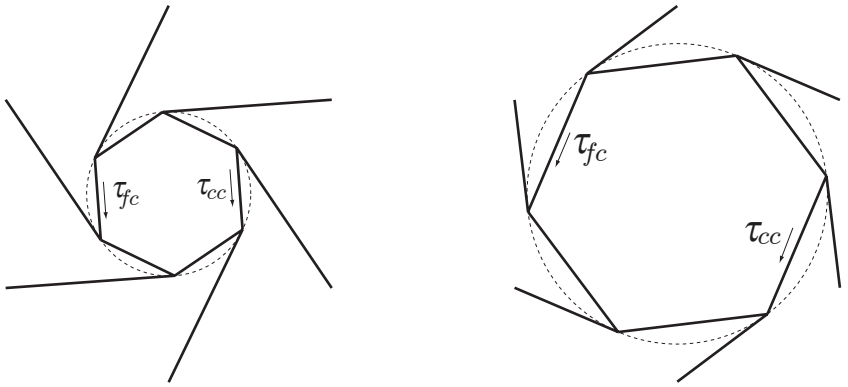

(a) $L/R = 0.90$ (b) $L/R = 0.60$

Figure 48: Orientation of internal shear-stress components

Fig. 49.a illustrates the assumed direction of shear stress within each unit-cell component. Specifically, the shear-stress components τ_i $(i = a, ac, b, bc, \cdots, f, fc)$ are assumed constant yielding 12 unknowns. Given the hexagonal symmetry of the chiral topology, the following relations for the ligaments are enforced:

$$\begin{aligned} \tau_a &= \tau_d \\ \tau_b &= \tau_e \\ \tau_c &= \tau_f. \end{aligned} \tag{76}$$

As shown in fig. 49.b, moreover, cutting the structure where the ligaments meet the node (hexagon), and noting that all unit-cell elements feature the same height b and

wall thickness t, the following relations must hold:

$$\begin{aligned} \tau_b + \tau_{bc} &= \tau_{ac} \\ \tau_a + \tau_{ac} &= -\tau_{fc} \\ \tau_f + \tau_{fc} &= \tau_{ec} \\ \tau_d + \tau_{dc} &= -\tau_{cc} \\ \tau_c + \tau_{cc} &= \tau_{bc}. \end{aligned} \tag{77}$$

It is important to note that there are 6 possible cuts that provide equilibrium relations among the stress components, but only 5 such equations are independent as a result of enforcing symmetry for the ligaments. The internal stress components must be in equilibrium with the externally-applied shear stress τ_{zx}, τ_{zy}. For shear loading in the x-direction, the following must hold:

$$\begin{aligned} \rightarrow \sum_i F_i &= (\tau_a + \tau_d)\frac{Lt}{2}\cos(3\theta-\beta) + (\tau_{ac}+\tau_{dc})\,rt\cos(2\theta-\beta) \\ &\quad + (\tau_b+\tau_e)\frac{Lt}{2}\cos(\theta-\beta) + (\tau_{bc}+\tau_{ec})\,rt\cos(-\beta) \\ &\quad + (\tau_c+\tau_f)\frac{Lt}{2}\cos(-\theta-\beta) + (\tau_{cc}+\tau_{fc})\,rt\cos(-2\theta-\beta) \\ &\quad = \tau_{zx}R^2\cos\theta, \end{aligned} \tag{78a}$$

$$\begin{aligned} \uparrow \sum_i F_i &= (\tau_a + \tau_d)\frac{Lt}{2}\sin(3\theta-\beta) + (\tau_{ac}+\tau_{dc})\,rt\sin(2\theta-\beta) \\ &\quad + (\tau_b+\tau_e)\frac{Lt}{2}\sin(\theta-\beta) + (\tau_{bc}+\tau_{ec})\,rt\sin(-\beta) \\ &\quad + (\tau_c+\tau_f)\frac{Lt}{2}\sin(-\theta-\beta) + (\tau_{cc}+\tau_{fc})\,rt\sin(-2\theta-\beta) = 0. \end{aligned} \tag{78b}$$

At this stage, however, eqs. (76-78) only provide 10 relations, while 12 unknowns are present, rendering the problem at hand under-determined with a system degree of redundancy 2. The internal components of shear stress in terms of two unknowns are reported in Table 4. As discussed in sec. 4.2, a lower-bound estimate of the out-of-plane, shear stiffness is obtained by enforcing that state of stress within a periodic cellular solid be compatible with externally-applied loads. Neither the constitutive

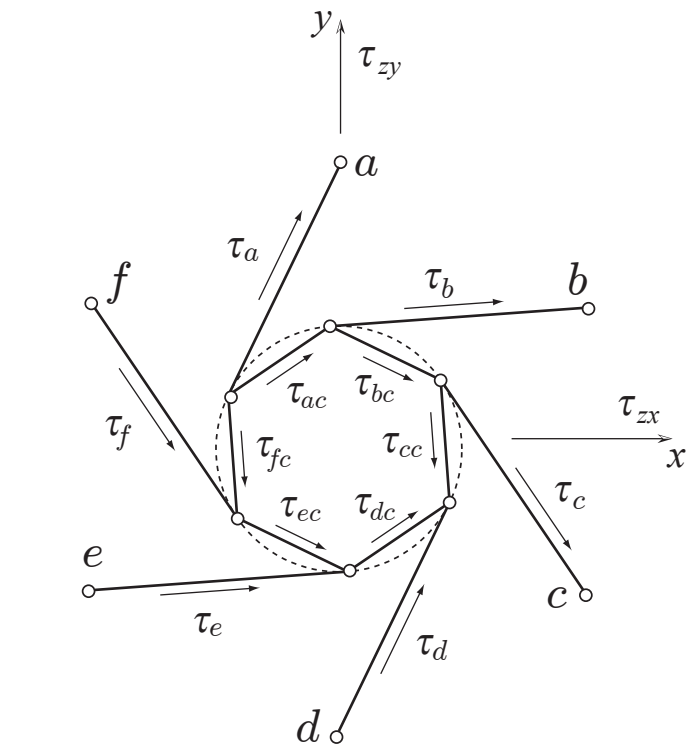

(a)

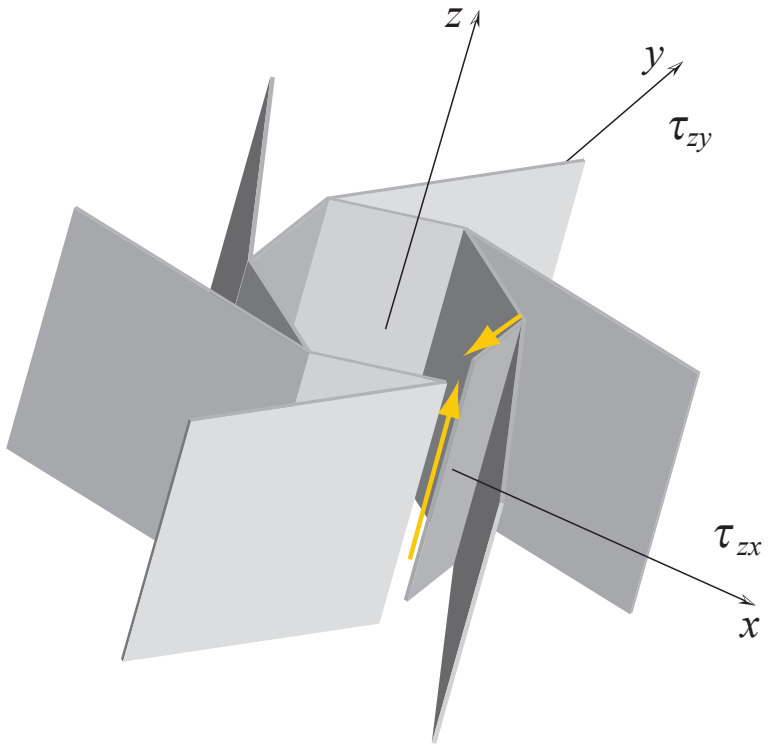

(b)

Figure 49: Unit-cell with shear-stress components (a) and method to enforce equilibrium of shear-stress components (b)

Table 4: Internal stresses resulting from externally applied τ_{zx}

τ_a	$-\tau_{cc} - \tau_{fc} - \frac{\cos(\beta)\tau_{zx}R^2}{Lt}$
τ_{ac}	$\tau_{cc} + \frac{\cos(\beta)\tau_{zx}R^2}{Lt}$
τ_b	$\tau_{cc} + \tau_{fc} + \frac{3\cos(\beta)\tau_{zx}R^2}{2Lt}$
τ_{bc}	$-\tau_{fc} - \frac{\cos(\beta)\tau_{zx}R^2}{2Lt}$
τ_c	$-\tau_{cc} - \tau_{fc} - \frac{\cos(\beta)\tau_{zx}R^2}{2Lt}$
τ_{cc}	τ_{cc}
τ_d	$-\tau_{cc} - \tau_{fc} - \frac{\cos(\beta)\tau_{zx}R^2}{Lt}$
τ_{dc}	$\tau_{fc} + \frac{\cos(\beta)\tau_{zx}R^2}{Lt}$
τ_e	$\tau_{cc} + \tau_{fc} + \frac{3\cos(\beta)\tau_{zx}R^2}{2Lt}$
τ_{ec}	$-\tau_{cc} - \frac{\cos(\beta)\tau_{zx}R^2}{2Lt}$
τ_f	$-\tau_{cc} - \tau_{fc} - \frac{\cos(\beta)\tau_{zx}R^2}{2Lt}$
τ_{fc}	τ_{fc}

relation between stress and strain or any strain-compatibility equations are included in the analysis. This simplification allows the use of the Principle of Least Work, which states [8]:

> *Among all statically admissible stress fields, the actual stress field that corresponds to the compatible deformations of a rigidly-held body makes the total stress energy an absolute minimum.*

The total complementary energy Π' can be expressed as:

$$\Pi' = \sum_i \left(\frac{\tau_i^2}{G_s} V_i \right). \tag{79}$$

Employing the Principle of Least Work and choosing τ_{fc} and τ_{cc} as redundant, two additional equations are obtained by letting:

$$\begin{aligned} \frac{\partial \Pi'}{\partial \tau_{cc}} &= 0 \\ \frac{\partial \Pi'}{\partial \tau_{fc}} &= 0. \end{aligned} \tag{80}$$

Given the internal-stress components of Table 4 and eqs. (79) and (79), the redundant stresses τ_{cc} and τ_{fc} are found to be:

$$\tau_{cc} = \frac{\cos(\beta)\tau_{zx}R^2}{2Lt} \tag{81}$$

$$\tau_{fc} = \frac{\cos(\beta)\tau_{zx}R^2}{2Lt}. \tag{82}$$

With all internal stresses at hand and the internal volumes V_i defined in sec. 4.5.1, eq. (64) yields:

$$\frac{G_{zx}^L}{G_s} = \frac{\sqrt{3}}{(\tan(\beta)+1)} \left(\frac{t}{L} \right), \tag{83}$$

where the superscript $(\ )^L$ indicates a lower-bound estimate.

For loading in the y-direction, the hexagonal symmetry of the chiral honeycomb is enforced using eq. (76), and equilibrium of internal stresses among themselves is

imposed via eq. (77). Equilibrium with respect to an externally-applied stress τ_{zy} leads to the following:

$$\begin{aligned}
\rightarrow \sum_i F_i = {} & (\tau_a + \tau_d)\,\frac{Lt}{2}\cos(3\theta-\beta) + (\tau_{ac}+\tau_{dc})\,rt\cos(2\theta-\beta) \\
& + (\tau_b+\tau_e)\,\frac{Lt}{2}\cos(\theta-\beta) + (\tau_{bc}+\tau_{ec})\,rt\cos(-\beta) \\
& + (\tau_c+\tau_f)\,\frac{Lt}{2}\cos(-\theta-\beta) + \\
& (\tau_{cc}+\tau_{fc})\,rt\cos(-2\theta-\beta) = 0,
\end{aligned} \tag{84a}$$

$$\begin{aligned}
\uparrow \sum_i F_i = {} & (\tau_a + \tau_d)\,\frac{Lt}{2}\sin(3\theta-\beta) + (\tau_{ac}+\tau_{dc})\,rt\sin(2\theta-\beta) \\
& + (\tau_b+\tau_e)\,\frac{Lt}{2}\sin(\theta-\beta) + (\tau_{bc}+\tau_{ec})\,rt\sin(-\beta) \\
& + (\tau_c+\tau_f)\,\frac{Lt}{2}\sin(-\theta-\beta) + (\tau_{cc}+\tau_{fc})\,rt\sin(-2\theta-\beta) \\
& = \tau_{zy}R^2\cos\theta.
\end{aligned} \tag{84b}$$

The internal components of shear stress in terms of two unknowns are reported in Table 5. With the aid of eqs. (79) and (80) and the relations of Table 5, the redundant shear-stress components τ_{fc} are found to be:

$$\tau_{cc} = \frac{\cos(\beta)\tau_{zy}R^2}{6Lt}, \tag{85}$$

$$\tau_{fc} = \frac{\cos(\beta)\tau_{zy}R^2}{6Lt}. \tag{86}$$

With all internal stresses at hand, eq. (64) yields:

$$\frac{G^L_{zy}}{G_s} = \frac{\sqrt{3}}{(\tan(\beta)+1)}\left(\frac{t}{L}\right). \tag{87}$$

The expressions for G^L_{zx} and G^L_{zy} are identical as for the upper-bound counterparts of eqs. (73) and (75). Once gain, this is confirmation that the chiral honeycomb is transversally isotropic.

4.6 Influence of gage thickness

The estimation of out-of-plane shear modulus is refined to include the influence of the out-of-plane thickness b with the aid of a FE model. Given the assumption of thin

Table 5: Internal stresses resulting from externally applied τ_{zy}

τ_a	$-\tau_{fc} - \tau_{cc}$
τ_{ac}	τ_{cc}
τ_b	$\tau_{cc} + \tau_{fc} + \frac{\cos(\beta)\tau_{zy}R^2}{2Lt}$
τ_{bc}	$-\tau_{fc} - \frac{\cos(\beta)\tau_{zy}R^2}{2Lt}$
τ_c	$-\tau_{cc} - \tau_{fc} - \frac{\cos(\beta)\tau_{zy}R^2}{2Lt}$
τ_{cc}	τ_{cc}
τ_d	$-\tau_{fc} - \tau_{cc}$
τ_{dc}	τ_{fc}
τ_e	$\tau_{cc} + \tau_{fc} + \frac{\cos(\beta)\tau_{zy}R^2}{2Lt}$
τ_{ec}	$-\tau_{cc} - \frac{\cos(\beta)\tau_{zy}R^2}{2Lt}$
τ_f	$-\tau_{cc} - \tau_{fc} - \frac{\cos(\beta)\tau_{zy}R^2}{2Lt}$
τ_{fc}	τ_{fc}

walls, shell elements (SELL181 [2]) featuring both membrane and bending capabilities are employed. Such element, suitable for analyzing thin to moderately-thick shell structures, is a 4-node element with six degrees of freedom per node, which include translations in the x, y, and z directions, and rotations about the x, y, and z axes [2]. The discretized unit cell is assumed clamped at the bottom (red nodes in fig. 50.a), while the top surface is constrained to displace along the x or y-direction as if it were perfectly bonded to the face sheets of a sandwich panel (yellow nodes in fig. 50.b). Symmetry conditions are imposed at the extremities of each ligament to reproduce the conditions of a honeycomb of infinite extent in the x-y plane (fig. 50.b.) This is achieved by selecting a set of master nodes and a set of slave nodes and eliminating the latter set from the equation system. In-plane symmetry is enforced by imposing

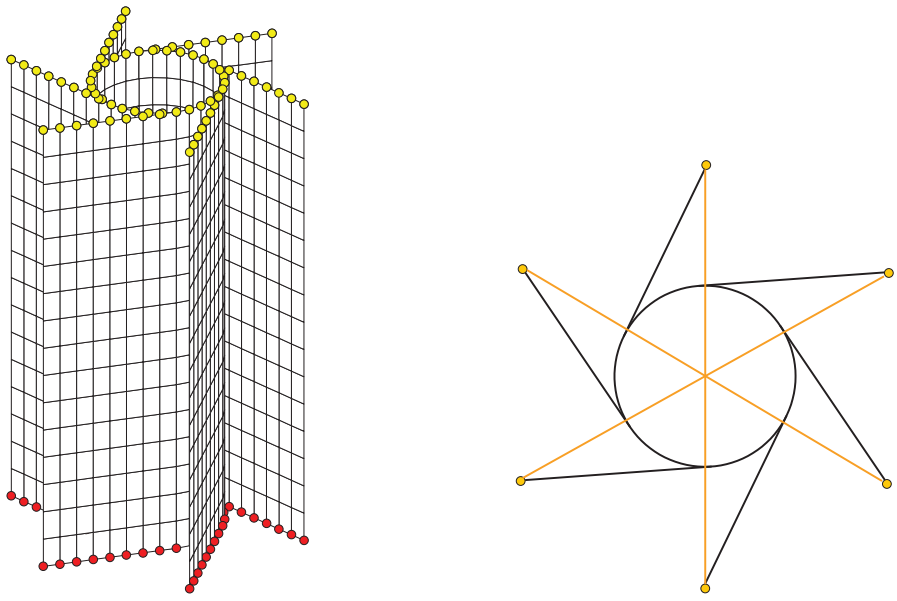

(a) (b)

Figure 50: Unit-cell FE model: (a) constrained nodes, (b) symmetry conditions

the following:

$$\sum_{i=1}^{N} c_i u_i = 0, \tag{88}$$

where N is the number of nodal locations to relate, $c_i = [-1, 1]$, and u_i are the displacements to be coupled [2]. Finally, small deformations are assumed, and thus a linear solution procedure is used.

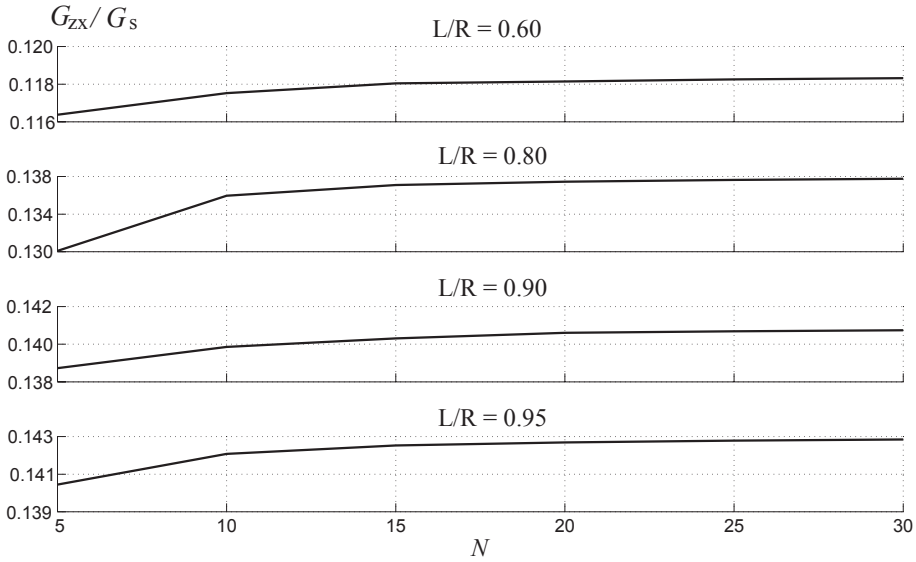

Figure 51: Shear analysis convergence study

In order to establish a proper level of discretization of the unit cell, a convergence study is carried out. Geometric and material properties used both for convergence studies and for subsequent estimation of out-of-plane shear stiffness are reported in Table 6. Given the outcome of the convergence study shown in fig. 51 for which b is set

Table 6: Base configuration parameters of unit cell FE model

Geometric properties:	
L	1 cm
t	1 mm
b	$1 - 10$ cm
L/R	$0.60 - 0.999$
Material properties, Aluminum:	
E_s	71 GPa
ν_s	1/3

to 2 cm, and where N denotes the number of elements per ligament, a discretization

with $N = 20$ is selected, yielding the configuration shown in fig. 50.a.

The computed shear moduli G_{zx}^{FE} and G_{zy}^{FE} (the superscript $(\ )^{FE}$ is used to indicate results obtained from the FE model) for varying out-of-plane thickness ratio $1 \leq b/L \leq 10$ (19 intervals) and topology parameter $0.60 \leq L/R \leq 0.999$ (19 intervals) are shown in fig. 52.a and 52.b. Their difference is within 1×10^{-8} % for all considered values of the topology-parameter and out-of-plane thickness values, thus further consolidating the conclusion of transverse isotropy suggested in secs. 4.5.1 and 4.5.2. Upper and lower-bound expressions from eqs. (73) and (83) are illustrated in dashed red and black lines respectively. The computed values G_{zx}^{FE} decrease with increasing b/L as a result of the fact that bending deformations of the walls become the dominant deformation mechanism. The relation between the computed values G_{zx}^{FE} and L/R on the other hand appears to scale with the relative density for $b/L < 2$. For $0.60 \leq L/R \leq 0.999$ the resulting relative density is reported in fig. 42. For higher values of b/L the behavior of G_{zx}^{FE} is not easily attributed to any specific geometric-parameter changes. The agreement between G_{zx}^{L}, G_{zx}^{U} and the FE-model estimates is satisfactory. The lower-bound analytical expression in particular provides a good approximation for $L/R > 0.90$, while for lower values of topology parameter circles are the dominant topological feature of the assembly (fig. 48) and thus the approximation of the chiral-honeycomb's circles as hexagons introduces some discrepancy.

The computed values of G_{zx}^{FE} and G_{zy}^{FE} are presented as a function of b/L in fig. 53, along with upper and lower-bound estimates in dashed red and black line respectively. One peculiar aspect of fig. 53.a and 53.b is the fact that the maximum value of G_{zx}^{FE} and G_{zy}^{FE} coincides with $L/R = 0.955$ and $b/L = 1$. This indicates that the chiral honeycomb is stiffer in shear than a triangular honeycomb for which L/R would be 1. The assumption that the chiral lattice inner circles may be modeled as hexagons, as shown in fig. 49.b, is reasonable since the difference in out-of-plane

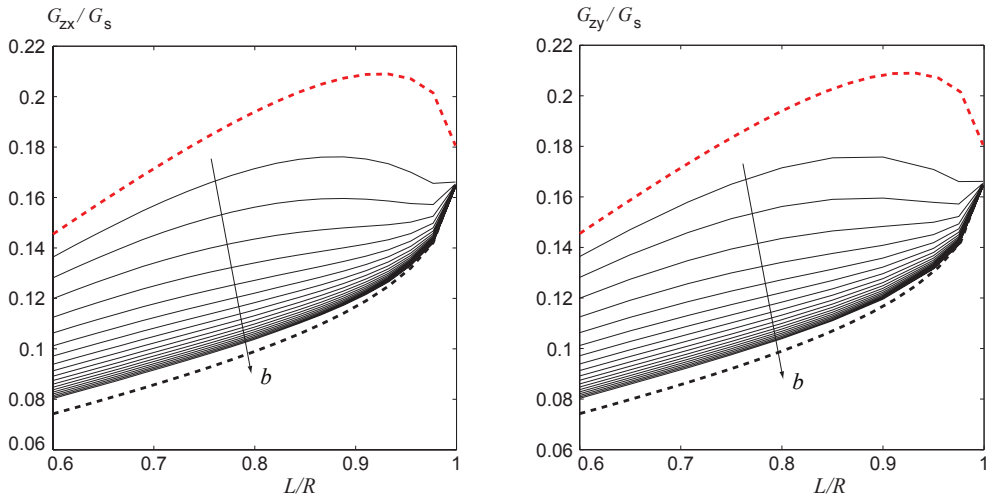

(a) (b)

Figure 52: Computed shear moduli G_{zx}^{FE} (a) and G_{zy}^{FE} (b) with unit-cell FE model. Upper-bound G_{zx}^{U} – – – and lower-bound G_{zx}^{L} – – –

shear modulus between the model shown in fig. 50.a and one with the inner circle replaced by a hexagon is within 4.5 % as reported in fig. 53.d. While some discrepancy between the chiral-honeycomb model featuring circular nodes and the model featuring hexagonal nodes is present, particularly for $L/R < 0.90$, the simplifications afforded by such geometric-model reductions greatly facilitated the analytical investigations of sec.'s 4.5.1 and 4.5.2.

At this stage, it is important to include the influence of out-of-plane thickness b into the upper and lower-bound analytical estimates of eqs. (75) and (87). Employing eq. (65) and letting $M = G_{zx} - G_{zx}^{L}$ and $K = G_{zx}^{U} - G_{zx}^{L}$, where the rows of M and K correspond to the considered values of L/R while their columns correspond to the values of b, one obtains:

$$M = \Phi(L/R, b/L)K. \tag{89}$$

The dependency of the shear modulus G_{xz} on topology parameter L/R and out-of-plane thickness b, illustrated in figs. 52 and 53.a, is much more complicated than hexagonal honeycombs [42, 43]. Attempts to characterize $\Phi(L/R, b/L)$ simply as

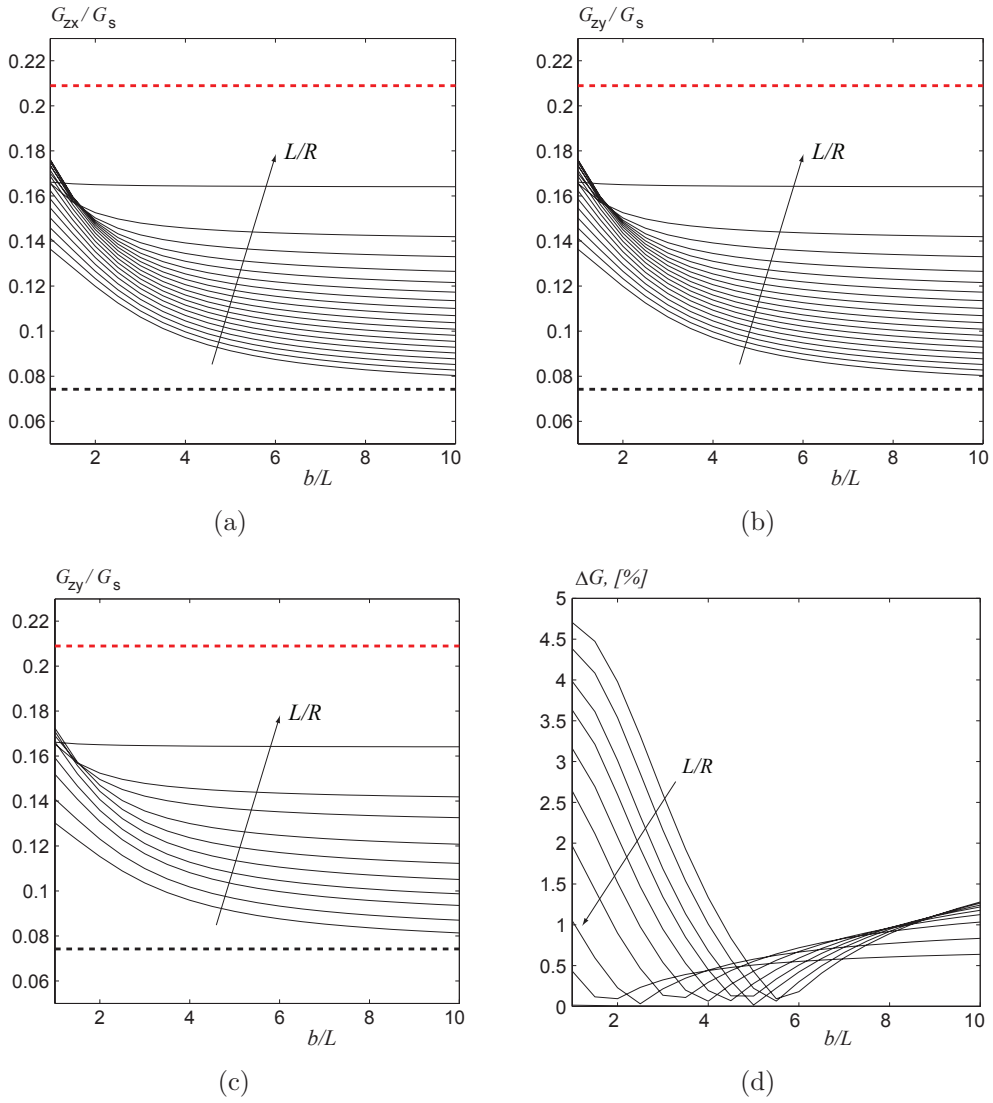

Figure 53: Estimated shear modulus: (a) G_{xz}, (b) G_{yz}, (c), G_{xz} for the simplified cell shown in fig. 49.b, percentage difference between simplified and actual chiral models (d)

$k/(b/L)$, where k is a constant, yields very poor estimates. Based on the dependency of upper and lower-bound estimates provided by eqs. (75) and (87) and shown in fig 52, $\Phi(L/R, b/L)$ is approximated employing a complete bivariate polynomial of order 8. Specifically, the interpolating polynomial takes the form:

$$\Phi(L/R, b/L) = \sum_{i,j} a_{i,j} \, (L/R)^{i-1} \, (b/L)^{j-1} \, , \tag{90}$$

where $i, j = 1, 2, \ldots, 5$. The resulting coefficients are reported in Table 7. The surface to be interpolated as well as the polynomial $\Phi(L/R, b/L)$ (red dots) are shown in fig. 54. The computed and approximated values of G_{zx} via eq. (89) are shown in fib. 55.a while fib. 55.b reports the percentage error associated with the interpolating polynomial, which is satisfactorily within 3.5 % of the FE values. The shear-stress

Table 7: Coefficients of bivariate polynomial $\Phi(L/R, b/L)$

a_1	-122.9	a_{14}	18.40
a_2	64.29	a_{15}	-0.7109
a_3	-15.97	a_{16}	1177
a_4	1.715	a_{17}	-613.6
a_5	-0.06621	a_{18}	152.1
a_6	665.9	a_{19}	-16.33
a_7	-346.0	a_{20}	0.6311
a_8	85.69	a_{21}	-388.2
a_9	-9.189	a_{22}	202.9
a_{10}	0.3548	a_{23}	-50.31
a_{11}	-1332	a_{24}	5.400
a_{12}	6922	a_{25}	-0.2086
a_{13}	-171.5		

τ_{zx} resulting from an applied displacement on the top portion of the unit-cell, FE model along the x-direction, reported in fig. 56, reveals that approximating circles as hexagons is reasonable, as for the agreement of upper and lower-bound estimates compared to the FE model of figs. 52 and 53. The stress within the ligaments for both the actual chiral-cell model and the simplified model appears quantitatively

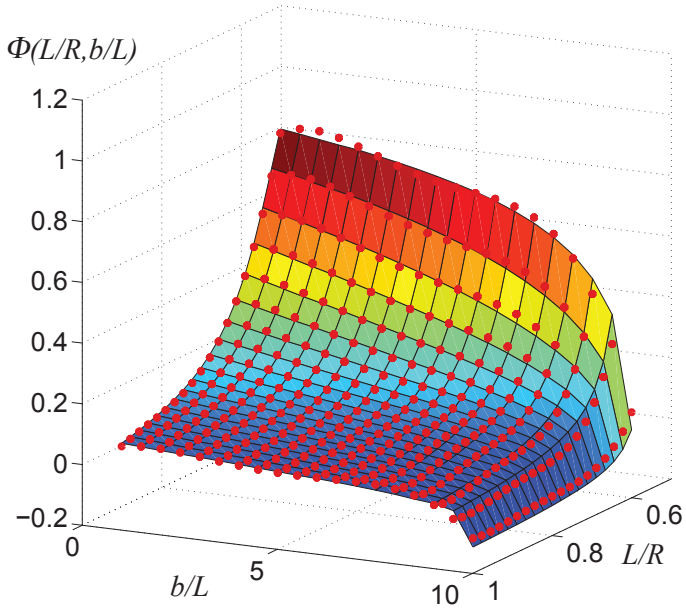

Figure 54: Bivariate polynomial $\Phi(L/R, b/L)$ (red dots) and target surface for interpolation

similar, while the circle and hexagon display at least a qualitative agreement. The most important difference, in fact, is the absence of high stress concentration at locations where ligaments tangentially meet the circle. The most important deviation from the simplifying assumptions, however, consists in the fact that the shear-stress distribution within ligaments and circles is not constant, as shown in fig. 56. While the analysis proposed in sec. 4.5 is certainly extendible to including non-constant shear stress within each of the assembly's components, the resulting lower-bound estimates would be intractable.

4.7 Comparison of shear moduli of chiral and hexagonal honeycombs

The assumption made in sec. 3.2 that shear stress is constant over the walls of the hexagonal honeycomb facilitates analytical investigations. In order to establish the validity of this, a FE model of the same honeycomb is used to compute the response of a unit cell to applied displacements of the top portion in the x-direction. The

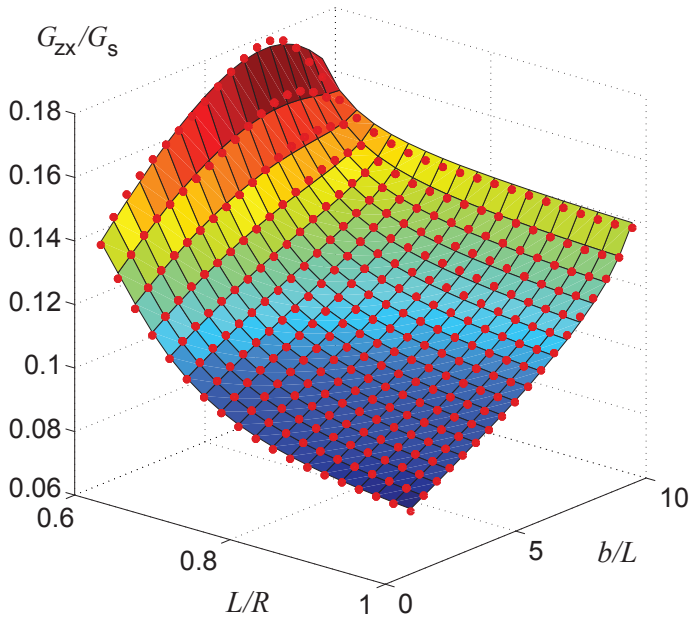

(a)

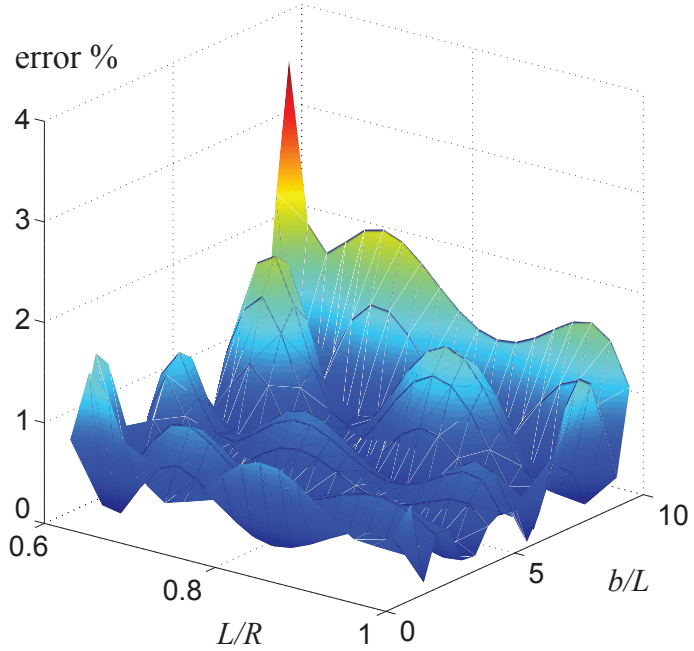

(b)

Figure 55: Comparison of G_{zx}^{FE} computed from unit-cell FE (surface) and analytical models $\cdots$ (a) and percentage error between the two estimates (b)

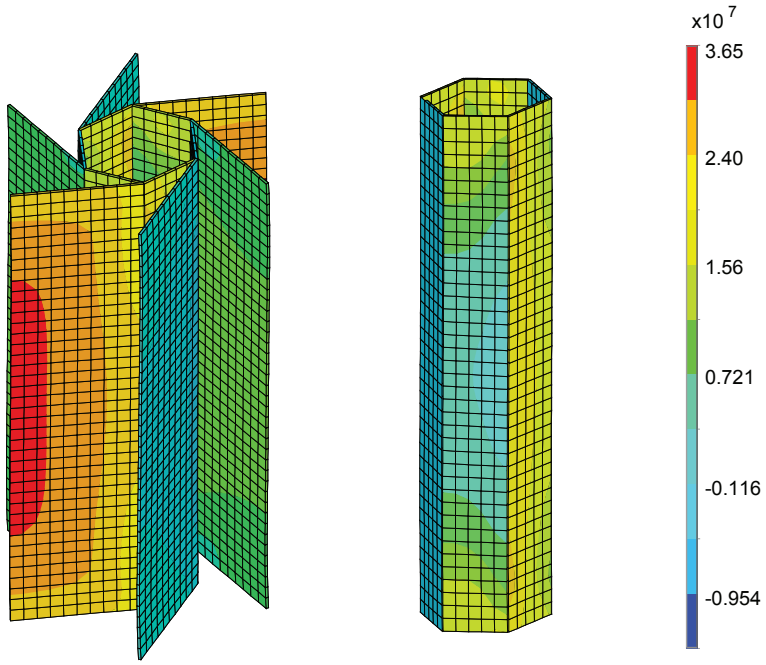

(a)

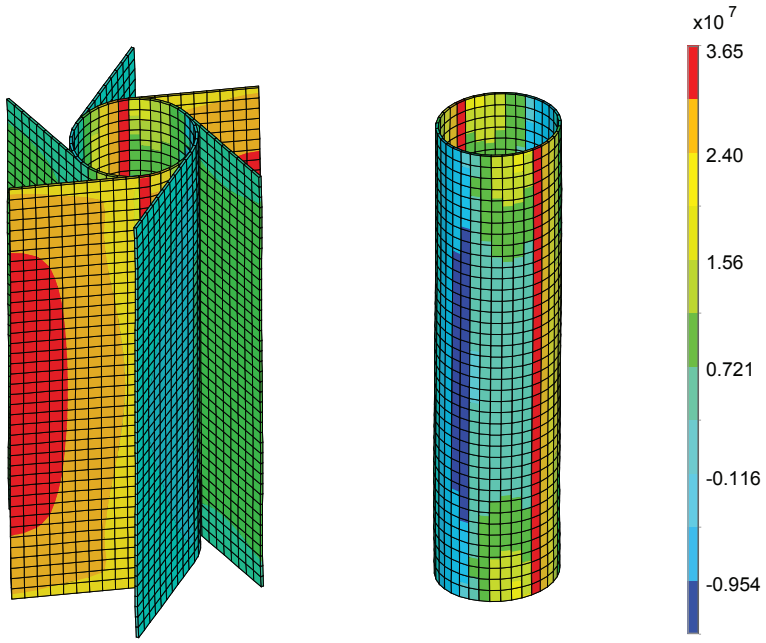

(b)

Figure 56: Shear stress τ_{zx} (Pa) resulting from an imposed displacement of the upper nodes along the x-direction. Simplified model (a), chiral cell (b)

outcome is shown in fig. 57, which confirms the applicability of the constant shear-stress assumption as well as the simplification provided by regarding the contribution to the strain energy of walls perpendicular to the loading direction as negligible.

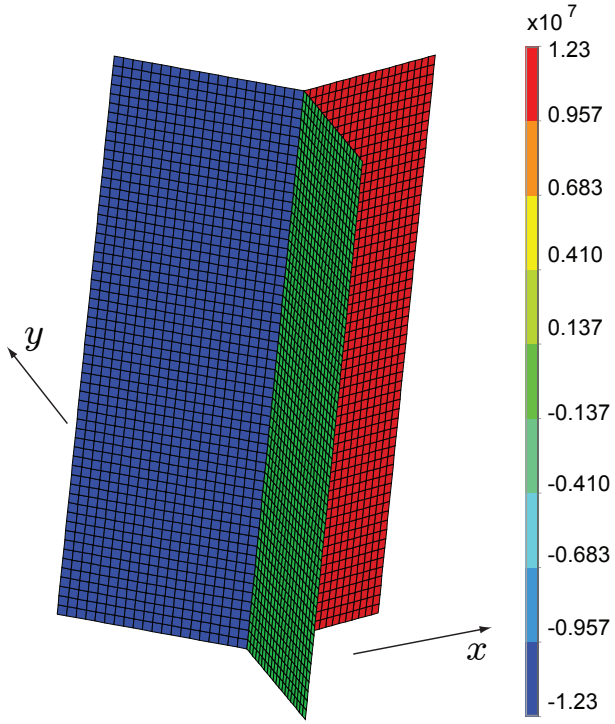

Figure 57: Shear stress τ_{zx} (Pa) resulting from an imposed displacement of the upper nodes along the x-direction for the hexagonal honeycomb

According to [40], the lower-bound, out-of-plane shear stiffness of a regular hexagonal honeycombs ($\theta = 30°$, fig. 45.b) is:

$$\frac{G^L_{zx}}{G_s} = \frac{G^L_{zy}}{G_s} = 0.577 \left(\frac{t}{L}\right). \tag{91}$$

The upper bound is [40]:

$$\frac{G^U_{zx}}{G_s} = \frac{G^U_{zy}}{G_s} = \frac{\sqrt{3}}{3} \left(\frac{t}{L}\right), \tag{92}$$

which is identical to eq. (91). The expression of eq. 92 is then exact within the assumptions made (sec. 3.2), and thus the refinement proposed by [42] is not needed. As presented in sec. 3.6, the relative density of the regular hexagonal honeycomb is

$\bar{\rho} = 2/\sqrt{3}(t/L)$. The shear stiffness may then be recast as:

$$\frac{G_{zx}}{G_s} = \frac{1}{2}\bar{\rho}. \tag{93}$$

For the chiral honeycomb, the relative density (from sec. 2.7) is $\bar{\rho} = \frac{2\ \sqrt{3}\ (2\pi r+3L)\ t}{3\ R^2}$. Utilizing the relations of geometric parameters of sec. 2.5, the upper-bound estimate of eqs. (73) may then be recast as:

$$\frac{G^U_{zx}}{G_s} = \sqrt{3}\,(\sin\beta + \cos\beta)\cos^3\beta\frac{t}{L} = \frac{3\,(\sin\beta + \cos\beta)\cos\beta}{2\,(2\pi\tan\beta + 3)}\bar{\rho}. \tag{94}$$

The lower-bound estimate of eq. (83) is recast as:

$$\frac{G^L_{zx}}{G_s} = \frac{\sqrt{3}}{(\tan(\beta)+1)}\left(\frac{t}{L}\right) = \frac{3}{2\cos^2\beta(2\pi\tan\beta+3)(\tan\beta+1)}\bar{\rho}. \tag{95}$$

Using eqs. (65) and (89) a comparison between the two topologies is shown in fig. 58. The shear stiffness of the hexagonal is within 5 % of the upper-bound estimate for the chiral honeycomb.

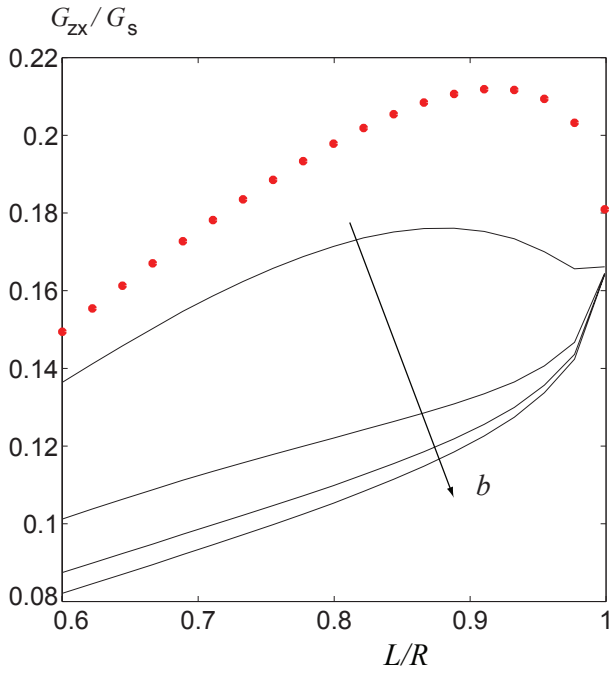

Figure 58: Shear stiffness G_{zx} for the chiral honeycomb (black lines) and hexagonal honeycomb (red dots)

4.8 Summary

The analyses presented in this chapter are devoted to establishing the out-of-plane mechanical behavior of a honeycomb with chiral topology, motivated by the possibility of manufacturing double-curved (dome-shaped) sandwich panels owing to a negative in-plane Poisson's ratio (chapter 3). Given the isotropic nature of the chiral lattice, chiral honeycombs are expected to be transversally isotropic.

The out-of-plane stiffness E_z is found to be linearly proportional to the relative density $\bar{\rho}$, as for all other honeycombs. The Poisson's ratios ν_{xz} and ν_{yz} are estimated to be approximately zero owing to the out-of-plane stiffness being significantly higher than that in plane.

The derivation of shear moduli takes advantage of existing techniques used for hexagonal honeycombs, which are based on a 2-D representation of the unit cell. The circular components of the chiral geometry are approximated as hexagons and both internal strain and stress components are assumed constant within each member without introducing significant error. In particular, an upper-bound expression is obtained via the Theorem of Minimum Total Potential energy, whereby a compatible strain state with boundary conditions is enforced neglecting stresses within the honeycomb core. A lower-bound estimate on the other hand is obtained by employing the Theorem of Minimum Complementary Energy, whereby equilibrium of internal stress components with boundary conditions is enforced neglecting compatibility of strain within the honeycomb core. It is found that $G^L_{zx} = G^L_{zy}$ and $G^U_{zx} = G^U_{zy}$, confirming that the chiral honeycomb is transversally isotropic, and both bounds are in agreement with values computed with a unit-cell, FE model. The analytical model for shear stiffness is refined with the aid of same unit-cell, FE model to include effects of out-of-plane thickness. Finally, a comparison between the out-of-plane shear stiffness of hexagonal and chiral honeycombs reveals that the former topology is stiffer for all considered values of out-of-plane thickness.

CHAPTER V

STATIC MORPHING OF CHIRAL-CORE AIRFOILS

5.1 Introduction

The unique set of mechanical properties offered by the chiral topology can be exploited for the design of airfoils with morphing capabilities. In particular, the chiral structure can be accommodated within an airfoil, so that its compliant characteristics can be used to achieve chordwise bending. The unique deformation mechanisms of structural chiral layouts allow large continuous deformations of the airfoil to occur with all the individual structural members undergoing deformations within the linear range of the material. The ability to sustain large deformations without exceeding yield conditions is required to achieve repeatability, while smooth deformations are required to obtain aerodynamic efficiency.

The application of the chiral geometry for airfoil morphing has already been investigated in [10], where it is applied to the design of a race-car spoiler with auto-adaptive characteristics. The race-car wing proposed in [10] features a core as homogeneous material having the equivalent homogenized in-plane properties of chiral honeycombs. Pressure distributions resulting from an increase in the car speed cause the mean camber line to be passively modified in order to obtain an equivalent reduction of the tab angle at the trailing edge. The corresponding elastic deformation is recovered when the speed of the car decreases, thus causing the wing tip to move upward. This passive morphing behavior results in better performance both in terms of maximum speed and handling for steep bends. Simulations were performed to predict the chordwise deflection of the airfoil when it is subjected to free-stream flow of 83 m/s, with an initial negative angle of attack of $-15°$. The pressure distribution over the airfoil

induces a deformation field over the airfoil structure, which results in a downward displacement for the trailing edge. The deformation is achieved through the flexibility provided by an isotropic chiral structure in an internal airfoil layout. No optimization was performed in order to take advantage of other anisotropic configurations of the chiral honeycomb and/or the skin. However, the change in camber obtained in [10] was considered significant and very promising.

In the following treatment, both numerical studies as well as experimental measurements are presented to support the viability of a chiral, truss-core airfoil. Numerical investigations are employed to determine advantageous configurations producing de-cambering deformations within the linear regime of the constituent material, while experimental measurements are carried out to confirm the capabilities set forth in [10] and arising from the aforementioned numerical investigations. In particular, results obtained from the model depicted in fig. 59.a lead to a simplified configuration, shown in fig. 59.b. Building upon promising experimental results obtained from aluminum truss-core airfoils, a simplified manufacturing method to produce truss-core airfoils made of fiber-composite materials is proposed. Composite chiral-core samples are investigated to confirm the mechanical behavior presented in chapter 3, and numerical models of composite, chiral-core airfoils are compared to all-aluminum configurations. Finally, a number of active-morphing strategies are presented to demonstrate the capabilities of chiral-core airfoils in withstanding concentrated applied torque and resulting camber-wise deformations.

5.2 Macrostructural Truss-core Configuration

As opposed to the design presented in [10], the considered configuration features a truss-type structure hosted within the airfoil to generate a truss-core configuration [91]. Schematics of the proposed configurations are shown in fig. 59. The particular airfoil section is an *Eppler 420* profile as in [10]. Such highly cambered airfoil is

chosen to demonstrate the compliance of the proposed assembly, which constitutes a system with theoretically high lift at low free-stream velocity, responsible for camber deformations. As the free-stream velocity is increased, the system would tend to a structurally stable low-camber, low-induced-drag configuration. Structural stability, or a finite de-cambering event, is guaranteed by a faster growth of elastic loads than their aerodynamic counterparts.

The performance of the considered configurations is first investigated numerically, through weakly coupled structural and computational-fluid-dynamics (CFD) models. Numerical results are used to identify selected configurations to be manufactured and tested under assigned loading conditions.

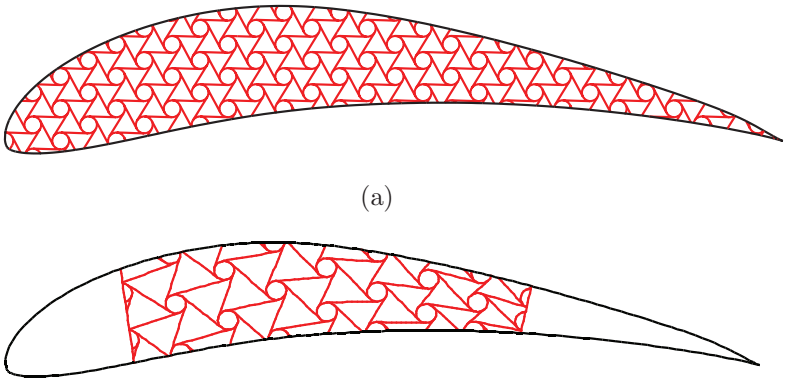

(a)

(b)

Figure 59: Proposed truss-core configurations

5.3 Numerical analysis of static aeroelastic performance

The performance of the considered airfoil is investigated through weakly coupled structural and (CFD) models. The weak coupling is justified by the limited requirement of evaluating the deformed configuration of the airfoil resulting from steady aerodynamic loads produced by specified flow conditions. Within such assumptions, the structural displacements can be predicted through an iterative process where air loads and corresponding displacements are iteratively passed to the structural and

fluid models until convergence is obtained.

5.3.1 Structural Model

The static equilibrium state of the proposed airfoil configuration is predicted by a two-dimensional FE model, whereby beam and plane elements are used to discretize the structural system. In particular, the model shown in fig. 59.a is analyzed using beam elements only, while the model shown in fig. 59.b requires the use of both beam and planar elements, as part of the leading and trailing edge regions are composed of a continuum material. The airfoil profile and chiral core are hence analyzed as a frame structure, with beam elements featuring both axial and transverse degrees of freedom (DOF). Transverse shear deformations are also included according to the formulation presented in [19], in order to avoid inaccuracies derived from the presence of non-slender elements. Classical isoparametric planar elements are employed to model the leading and trailing edge regions, where it is assumed that a homogeneous material is utilized. The mesh employed for such regions includes both triangular and quadrilateral elements of the kind shown in fig. 60. The quadrilateral elements are of the bilinear kind, developed according to the formulation denoted as $Q6$ in [19], while the planar triangular elements are constant strain elements. Both triangular and quadrilateral elements feature "drilling" DOF's, which allow their coupling with the beam elements used for the chiral core and skin discretization.

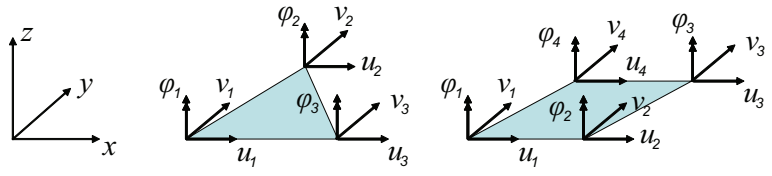

Figure 60: Isoparametric planar elements

5.3.2 Computational fluid dynamics model

As relatively large deformations of the airfoil are to be investigated, no assumption regarding the linearity of the flow field, or resulting aerodynamic loads, is made. Rather, the entire flow field is resolved using the finite-volume Galerkin program NSC2KE [68]. The fluid region is discretized with the unstructured triangular mesh depicted in fig. 61. While the program NSC2KE offers a variety of viscous flow and boundary layer models, their use is beyond the scope of the current work, which aims at investigating static aeroelastic deformations due to lift and not drag. Nonetheless, the entire flow field is analyzed using an inviscid flow Euler model [68]. The mesh of elements in contact with the airfoil profile is selected to feature minimum element side length at the trailing and leading edges equal to $1 \times 10^{-3} \cdot c$, with c denoting the airfoil chord. The element size over the rest of the airfoil profile is linearly relaxed by a factor of 5 (fig. 61.b), since particularly unfavorable pressure gradients are not expected. This results in triangular elements in contact with the airfoil whose maximum side length varies from $10^{-3} \cdot c$, at the trailing and leading edges, to $5 \times 10^{-3} \cdot c$ at the mid curvilinear length along the top and bottom portions of the airfoil. The relaxation of the element size in the direction normal to the airfoil is not directly controlled; instead the inflow and outflow boundaries are represented by 30 elements whose maximum side length is at a minimum at mid curvilinear length of each boundary, and linearly relaxed otherwise. The wake region is also discretized with the same logic as the airfoil boundaries: wake elements near the trailing edge of the wing profile share the same size imposed to elements on the airfoil boundary. Wake element size is then increased linearly up to the outflow boundary (fig. 61.a). External forces such as gravitational forces are neglected as the inertial frame of reference is assumed to be at rest. An implicit Euler local time stepping procedure is employed as the sought solution is assumed to be steady-state. The number of iterations required to resolve the flow field has been selected based on the considered mesh (fig. 61). In particular, both the

residual's norm and the lift coefficient have been analyzed. Figure 62.a suggests that

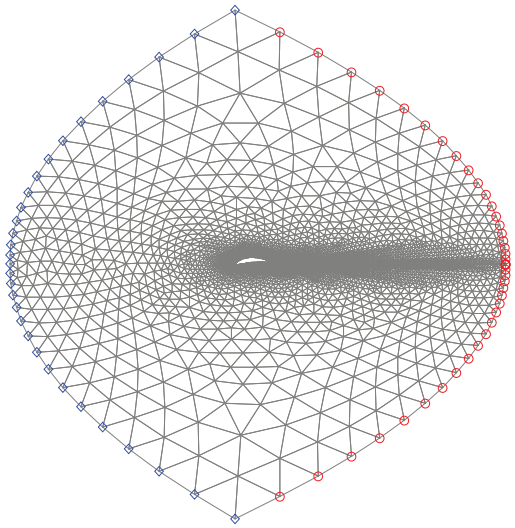

(a) ◇ inflow points; o outflow points.

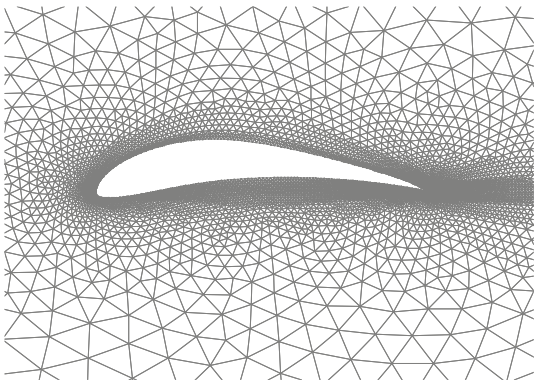

(b) detailed view of airfoil boundary

Figure 61: Unstructured Euler grid

reasonable results can be obtained with $\sim$ 4000 to 5000 iterations. Figure 62.b, on the other hand, suggests that the normalized L_2 norm is reduced by four orders of magnitude with 8000 iterations. The latter number is then used as the current static aeroelastic investigation requires the pressure distribution around the airfoil to then evaluate structural deformations, as opposed to investigating the global lift coefficient only.

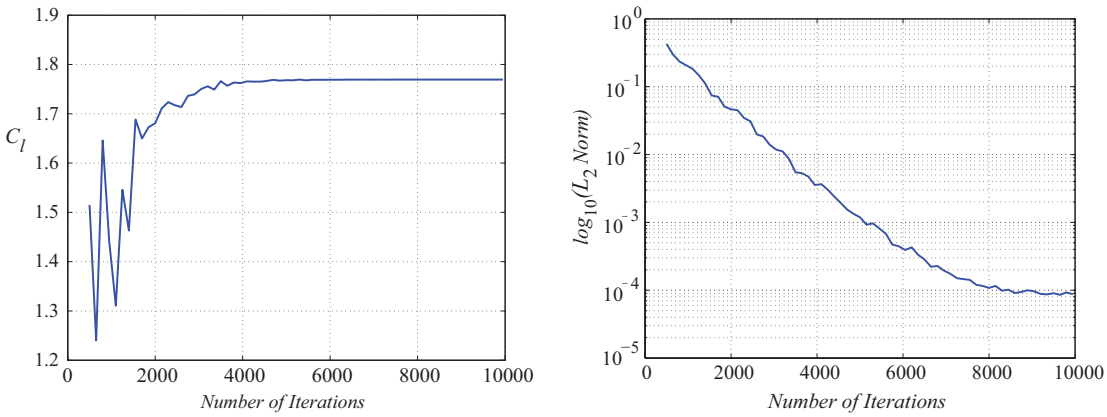

(a) (b)

Figure 62: Result convergence in terms of C_l and L_2 norm

5.3.3 Fluid-structure interaction and convergence

Coupled-field analyses may be carried out according to the sequential and direct methods. In the case of the direct method a coupled-field element type containing all necessary degrees of freedom is used. In the case of the sequential method, solutions for the fluid and solid analyses are carried out separately. Given the need for analyzing relatively large structural deformations, and thus potentially substantial changes in the flow field, a sequential method is used, whereby the static aeroelastic solution is obtained through an iterative process based on convergence of fluid and structural solutions. The computed gauge pressure at the fluid-airfoil boundary is applied as a distributed load on the structural model. Equilibrium is then imposed, and the resulting deformed configuration is used to obtain a newly meshed fluid region. The process is repeated until $\Pi_i - \Pi_{i-1} < 1 \times 10^{-4}$, where Π is the total strain energy of the truss-core airfoil, and i is the iteration number. The flow chart depicting the iterative procedure considered for the sequential method is shown in fig. 63. Typically, convergence is achieved after 3 or 4 iterations. An example of pressure distribution upon convergence of the flowfield model, is shown in fig. 64.a, while the associated pressure coefficient (C_p) over the airfoil boundary is depicted in fig. 64.b.

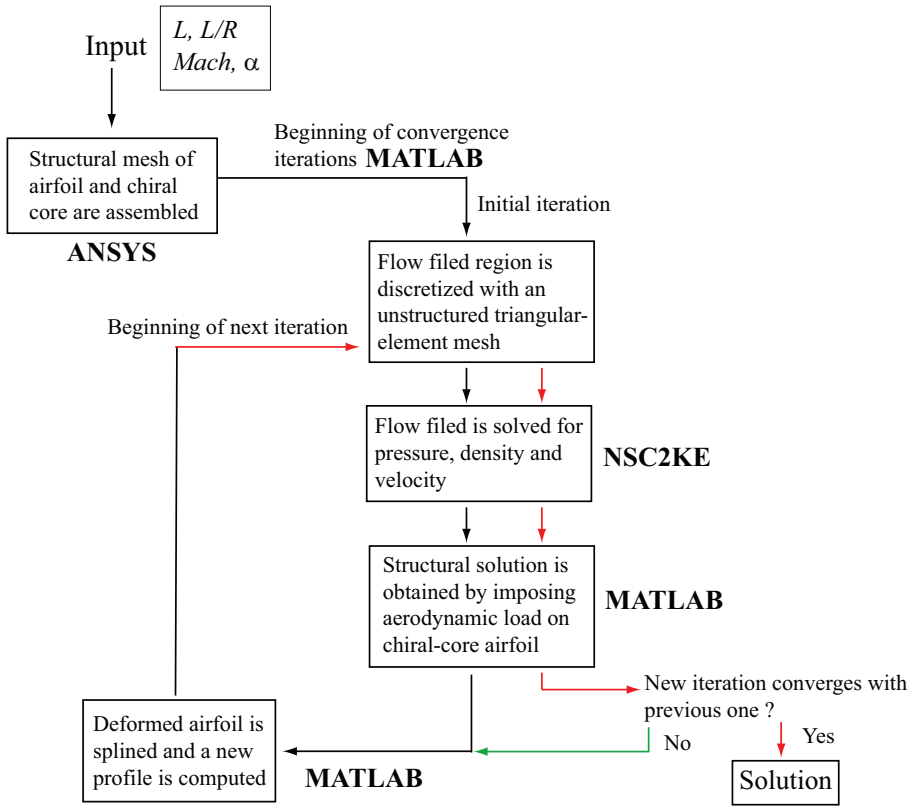

Figure 63: Schematic of static, aeroelastic convergence model

No particular corrugations over the upper portion of the airfoil profile are observed as the C_p distribution depicted in fig. 64.b does not present any pressure discontinuities, which would indicate corrugation of the airfoil profile.

5.4 Design configuration 1

Initial investigations are carried out on the configuration shown in fig. 59.a. The design is obtained by fitting a regular, periodic chiral layout into the airfoil shape of an *Eppler 420* of chord $c = 1$ m, as shown in Figure 65.a. Fig. 65.b shows the resulting truss-core airfoil. The leading edge is considered clamped, and the out-of-plane depth of the assembly is 2.54 cm. The core is aluminum (Young's Modulus $E = 7.1 \times 10^{10}$ N/m^2, density $\rho = 2700$ kg/m^3, Poisson's ratio $\nu = 0.33$) with a wall thickness $t = 0.8$ mm, while the outer skin is modeled as a softer material (Young's

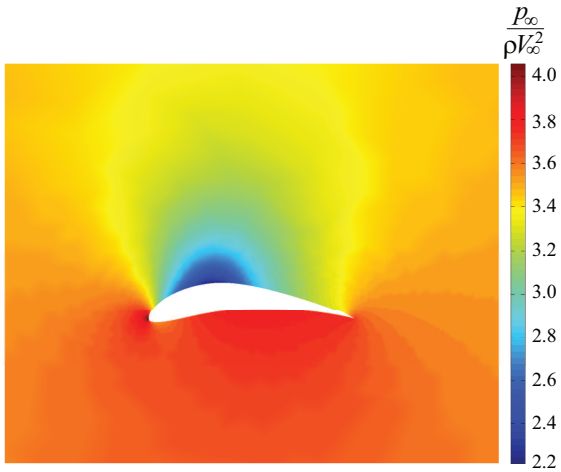

(a)

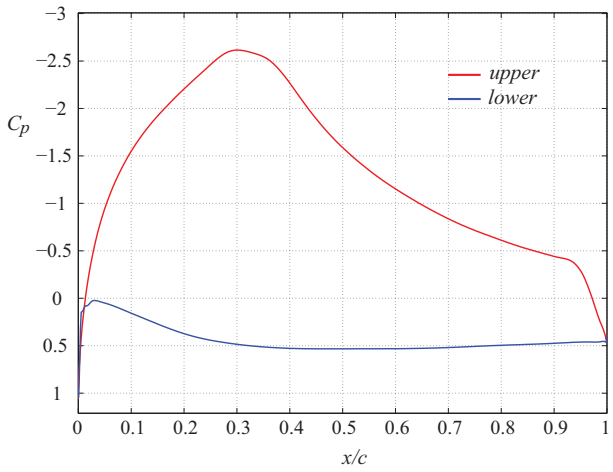

(b)

Figure 64: Gauge pressure and C_p distributions upon convergence of the CFD model

Modulus $E = 9 \times 10^9$ N/m^2, density $\rho = 2700$ kg/m^3, Poisson's ratio $\nu = 0.33$) with a wall thickness $t = 0.4$ mm. The softer skin is chosen to promote axial deformations due to chordwise bending of the wing profile. Free-stream properties are assumed to be those at sea-level, with a Mach number of $M = 0.45$, and an angle of attack $\alpha = 2°$. Such free-stream conditions produce the pressure distribution shown in fig. 64.a. The resulting deformed configurations of airfoils of different core designs are presented in fig 66. The first core design features an upward deflection approximately equal to

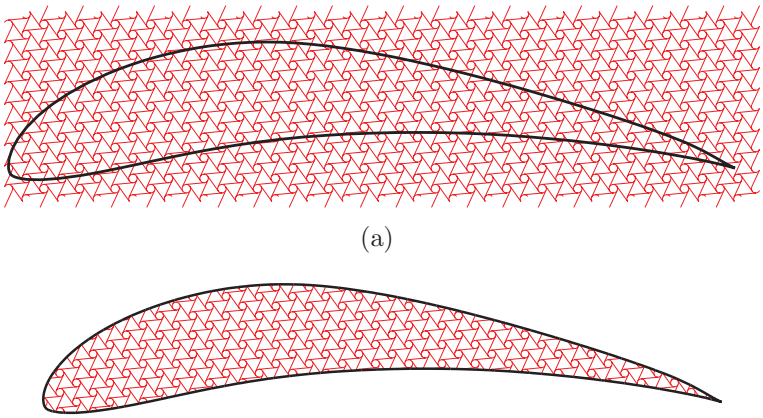

(a)

(b)

Figure 65: Eppler airfoil superimposed to regular, periodic chiral layout (a), and resulting truss-core airfoil (b)

2.75 cm, while the second core is significantly stiffer, as the tip displacement under the same conditions is more than one order of magnitude lower ($\simeq 0.22$ cm). Such a difference in compliance is obtained by only varying a single parameter, i.e. L/R, while maintaining material and geometric parameters constant. Such capabilities demonstrate the sensitivity of the considered design to small changes in the core configuration, which may be optimized to achieve the desired compliance, or in general the required functionality. In principle, this potentially simplifies the optimization of the core configuration. These results also suggest that ribs of the kind here considered may be manufactured to obtain different levels of compliance at different locations along the wing. The deformed configuration depicted in fig. 66.a, for $L/R = 0.60$, corresponds to the distribution of axial strain shown in fig. 67. It is interesting to observe how the maximum strain levels in the core are of the order of 1×10^{-4}, and therefore can be considered safely within the linear-elastic region of the constituent material.

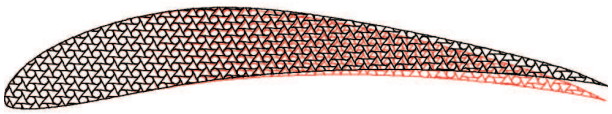

(a) $L/R = 0.60$

(b) $L/R = 0.80$

Figure 66: Deformed configurations obtained with two core designs

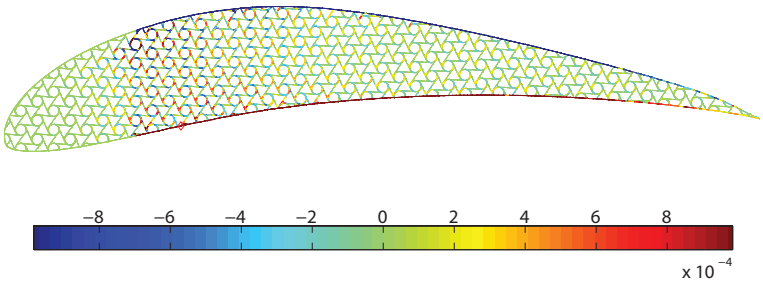

Figure 67: Axial strain distribution corresponding to the configuration shown fig. 66.a

5.5 Design configuration 2

The information obtained from the strain distribution for deformed configurations of design 1 is used to simplify the design of chiral truss-core airfoils. Fig. 67 shows that the highest strain levels due to chordwise bending only occur within a limited portion of the airfoil. Based on this observation the design is modified according to the configuration shown in fig. 59.b. This choice also facilitates the meshing process and simplifies the manufacturing of the assembly. A schematic of the process for the generation of this modified layout is shown in fig. 68. The core configuration is defined by assigning the parameters of the chiral topology (L/R) in the undeformed configuration, and the number of cells along the longitudinal and transverse directions r, s. The resulting regular, periodic configuration is then mapped into the curved geometry of the airfoil through a change of coordinates. The following wing

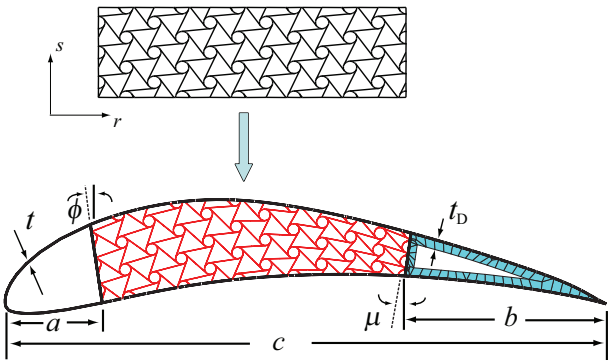

Figure 68: Mapping of chiral layout into airfoil profile

dimensions are selected based on manufacturing constraints: chord $c = 0.7$ m, angle $\phi = 8.58°$, angle $\mu = 8.0°$, lengths a and b respectively equal to 11 and 23.5 cm, and wall nominal thickness of core structure and airfoil profile $t = 0.76$ mm. Finally, the out-of-plane thickness of the structure is 1.9 cm. The shaded area in the trailing-edge region (fig. 68) is obtained by offsetting the trailing-edge profile by 2.54 cm. The resulting thickness on the upper and lower trailing-edge boundaries, t_D is then 2.54 cm.

The performance of this second design is evaluated for the same free-stream conditions previously considered. The choice of the chord length is driven by limitations imposed by manufacturing considerations. The core and the top part of the skin are made of aluminum, while the lower section of the skin is modeled as a softer material to facilitate the desired bending deformations. A summary of the considered airfoils' performance is presented in fig. 69 where the displacement of the trailing edge for assigned flow conditions and various core configurations is plotted versus L/R. Results are presented for different number of cells across the thickness of the airfoil, namely 2, 3, and 4, and for various values of the lower skin's Young's modulus. Figs. 69 confirm that large nodes resulting from low numbers of cells through the thickness yield greater compliance. Another parameter that clearly has great influence on the airfoil performance is the skin stiffness, as dictated by the Young's modulus of the constitutive material. As the results show, and as expected, the lower the skin's Young's modulus the higher the compliance. The lower limit considered in the investigations corresponds to the smallest possible values to prevent significant bulging deformations due to aerodynamic loads.

5.6 Experimental investigations of airfoil compliance

The main objective of the following studies is to investigate the properties of the chiral core airfoil experimentally, and confirm the findings of the previous section. While in sec. 5.3, the loads applied to the FE models are distributed pressures of aerodynamic nature, experimental tests on the manufactured airfoil samples involve a simplified scenario whereby mechanical point-loads are employed to promote bending. Specifically, the de-cambering deformations of the airfoil as a result of increasing mechanical loads are measured while monitoring the strain at selected locations. The purpose of the tests is to verify the strong influence of core design on airfoil compliance and to estimate maximum deflections achievable in the elastic range of the material. The

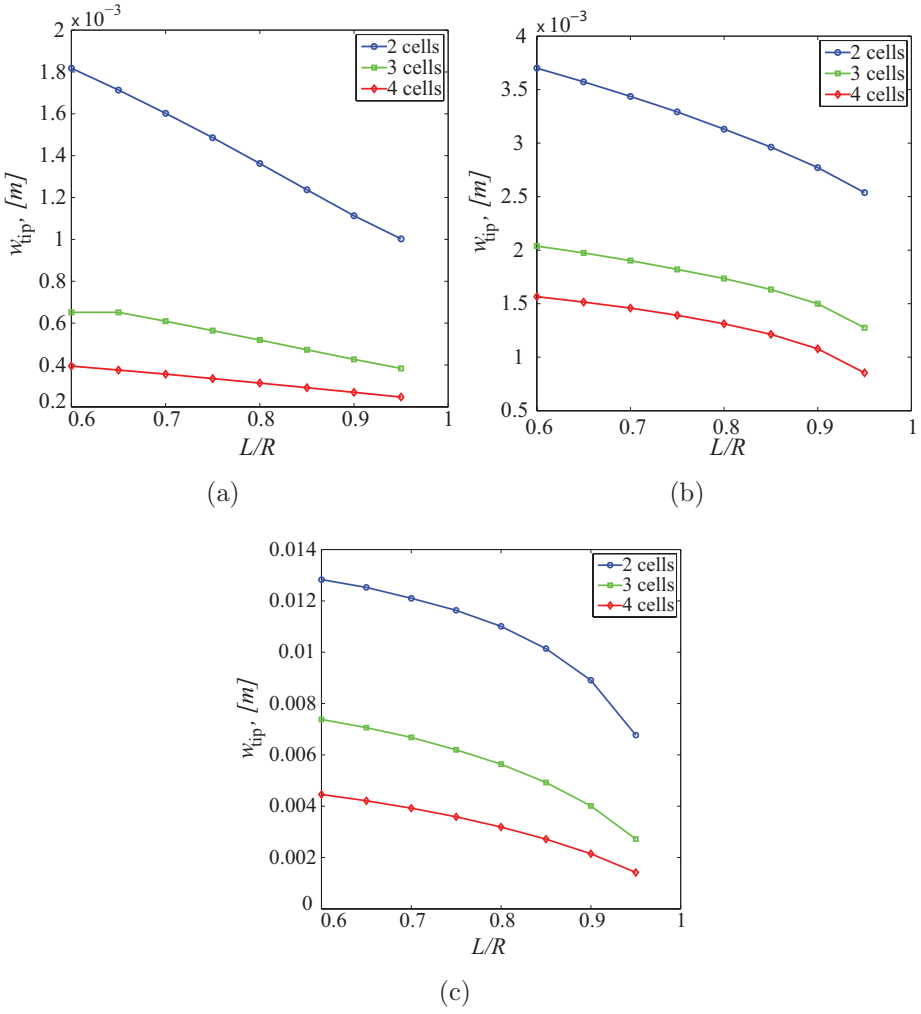

Figure 69: Trailing edge tip displacement for various values of bottom skin Young's modulus: (a) $E_s = 7.1 \times 10^{10}$ Pa, (a) $E_s = 7.1 \times 10^{9}$ Pa, and (c) $E_s = 7.1 \times 10^{8}$ Pa

tests are guided by a numerical model, which is used to predict load values to be considered in the experiments. The model is significantly different from the one used in sec. 5.3. First, material non-linearities are introduced to enable the prediction of loads causing the material to enter the plastic range, and secondly geometric stiffening due to large deformations is included. In addition, the geometry of the structure is modified to reflect variations from the ideal geometry due to the water jet manufacturing process employed for the fabrication of the samples. In particular, a perfect tangency condition between nodes and ligaments cannot be reproduced. Fillets between nodes and ligaments are included in the FE model in an attempt to reproduce the geometry of the test specimens. The presence of fillets is important as it may in fact modify the bending behavior of the ligaments, which is the leading mechanism of deformation of the chiral structure [76] (chapter 3).

5.6.1 Numerical results

The following analysis focuses on the structural deformations of the proposed airfoil assembly, without considering the effects of aerodynamic loading. The deformations of the wing profile are induced by a concentrated mechanical load applied at upper left corner of the trailing edge void shown in fig. 68. This loading configuration reproduces the one considered experimentally. A structural FE model is utilized to investigate the ability of the airfoil assembly to undergo large chord-wise deformations while within the linear behavior of the constitutive material. Hence the ability to predict the onset of non-linear stresses is needed. For this purpose a static, large-deformation, non-linear-FE model is employed to predict stresses and strains resulting from the applied loads. The commercially available software ANSYS® is used for this purpose. In the model, the material behavior is described by a bilinear stress-strain curve, whose slopes are defined by the Young's modulus (69 GPa) of the material, and beyond the specified yield stress ($\sigma_y = 276$ MPa), by the tangent modulus (100

MPa). Such constitutive model represents a reasonable approximation of the stress-strain curve, as given by [45], for the selected material (Aluminum 6061 $T651$), since only the onset of plasticity is sought.

The truss-core wing dimensions are identical to those presented in sec. 5.5. Manufacturing constraints imposed the presence of fillets at the locations where ligaments join with nodes. The radius of such fillets was estimated to be of the order of 0.13 mm. In addition, the thickness of the ligaments, nominally designed to be 0.76 mm, was found upon measurement to vary between 0.66 and 0.80 mm. In the non-linear FE model thus, the wall thickness of the core elements is randomly assigned to each element varying from 0.66 to 0.80 mm, and plane elements are added in regions where ligaments join the nodes to simulate the presence of fillets, as shown in fig. 70.

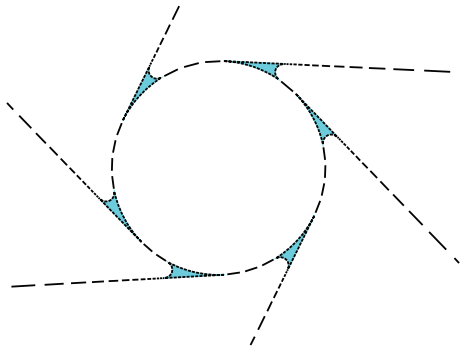

Figure 70: Detail of core discretization with fillets at the nodes/ligaments joints

The results presented in sec. 5.5 show that the airfoil compliance strongly depends upon the core configuration. In particular, the number of cells in the chordwise direction and across the thickness, and the nominal topology parameter L/R are the parameters which affect the airfoil performance the most. In an attempt to maximize deflections and evaluate the performance of the chiral core for large deformations, the lower skin of each airfoil configuration has been cut at the locations indicated by arrows in fig. 71. In the proposed design, the skin has been found to act as an obstacle to the de-cambering deformation. Moreover, the ability to carry shear loads and the

potential torsional rigidity of the chiral layout due to its negative Poisson's ratio suggest that the classic closed section with stressed-skin may not be necessary. prova71

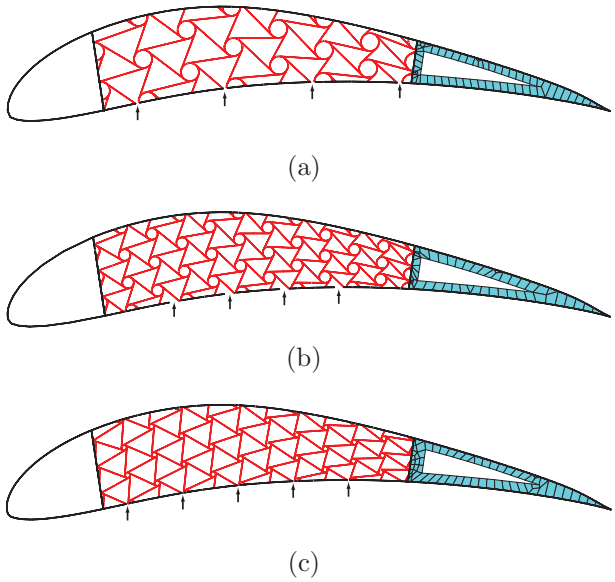

Figure 71: Mapped chiral-core configurations and locations of lower skin cuts

The configurations considered for the analysis are depicted in fig. 71. Such geometries, selected on the basis of of results reported in sec. 5.5 are respectively defined by 2 cells across the thickness and $L/R = 0.60$ (configuration a) (fig. 71.a), 3 cells across the thickness and $L/R = 0.60$ (configuration b) (fig. 71.b), and 3 cells across the thickness and $L/R = 0.94$ (configuration c) (fig. 71.c). The compliance of these truss-core airfoils is assessed by applying increasing loads at the upper left corner of the trailing edge void, and by recording the corresponding trailing edge vertical displacement. Load/displacement curves, obtained from the non-linear FE model, for the three configurations are plotted in fig. 72, which demonstrates, in adherence with the previous predictions, that configuration a is the most compliant, while configuration c is the least compliant. Fig. 73 shows the Von Mises stress distribution immediately before the onset of plastic deformations. In all cases, the highest stresses appear within the core, and in particular, where ligaments join nodes. It is worth

noting that the locations of highest stress are different for each configuration. Such disparities may be attributed to the different deformation mechanisms that arise by varying the geometry of the core.

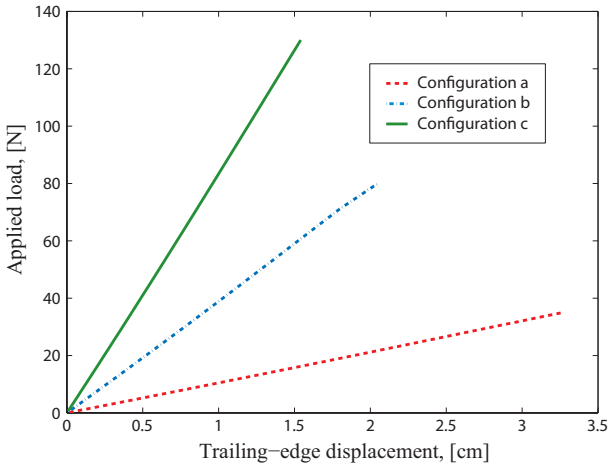

Figure 72: Load, trailing-edge displacement relationship for the considered configurations

5.6.2 Manufacturing and experimental set-up

Three truss-core airfoils matching the configurations shown in fig. 71 have been manufactured to validate numerical predictions presented above. An OMAX® water-jet machine was used to cut the airfoils out of a plate of aluminum 1.9 *cm* thick. The manufacturing process is depicted in fig. 74, and the completed chiral, truss-core airfoils are shown in fig. 75.

The experimental setup consists of a linear variable displacement Transducer (LVDT) from RDP® (Model DCTH) and associated power supply (Agilent®, Model E3641A), to measure the trailing edge deflection, as depicted in fig. 76. The strain in selected structural members is measured by a set of strain gages (VISHAY® CEA-13-125UN-120), which are applied to the ligaments within the truss core and on the airfoil profile based on the stress distribution provided by the numerical simulations presented in sec. 5.6.1. The selected locations for the strain gages are depicted in

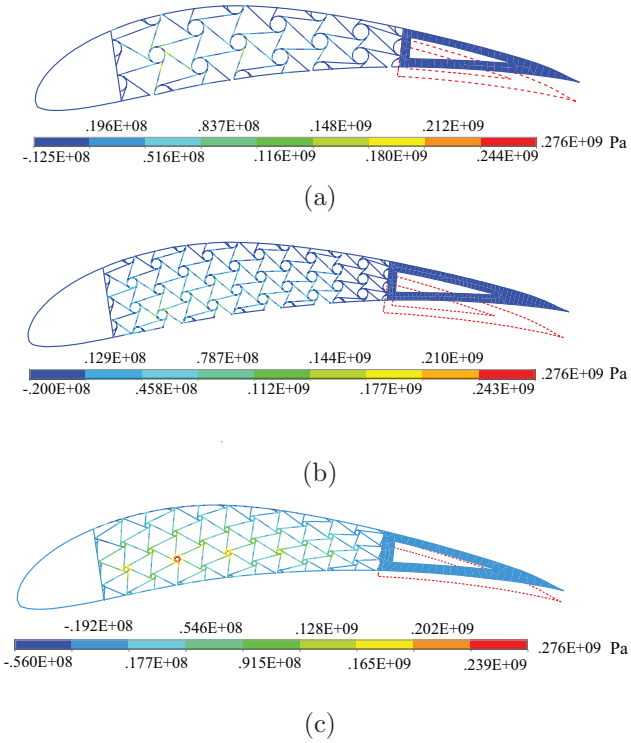

Figure 73: Von Mises stress distribution of considered configurations

fig. 77, which also shows the point of load application and location of the LVDT. The stress distribution within a ligament can be estimated from the simple linear-elastic deformation mechanism proposed by [76] outlined in sec. 3.3. Loading of the chiral core causes rotation of the nodes and bending of the ligaments as depicted in fig. 25. Neglecting shear deformations, the resulting axial strain distribution within a ligament varies linearly along the length from a negative to a positive value, so that, at mid span, the axial strain is approximately 0. The highest axial strain is then expected at the location where ligaments join nodes in a tangential fashion. Consequently, the strain gages are placed on the ligaments, as close to the nodes as possible.

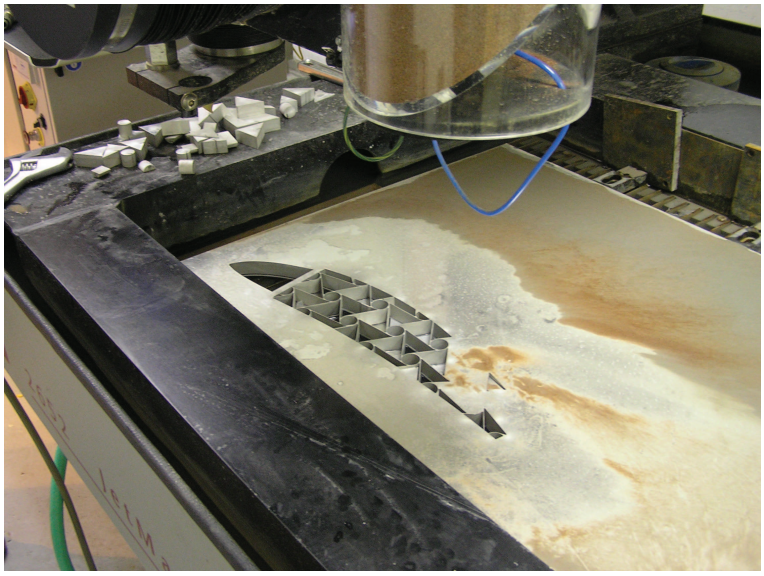

Figure 74: Experimental setup

5.6.3 Experimental results and comparison with numerical predictions

In the experiments, each specimen is subjected to a loading/unloading cycle to observe deviations from linearity, hysteresis and the presence of residual deformations upon unloading. To preserve the integrity of the manufactured truss-core airfoil samples for future tests, the maximum applied load is maintained below the value which numerical results indicate capable of producing plastic deformations. The employed numerical analysis in certain circumstances, however, underestimates stress concentrations where ligaments are tangent to the nodes, even with very refined meshes.

The load/trailing-edge-displacement variation for configuration a is shown in fig. 78, which directly compares experimental measurements and numerical predictions. The plot shows good agreement and indicates the presence of some hysteresis in the experiments. Such hysteresis can be associated to friction at the airfoil/LVDT contact region, and internal to the LVDT itself. In addition, a residual displacement is observed experimentally upon unloading. The evidence of residual deformations can be also observed from the strain gage measurements. The strain recorded at location

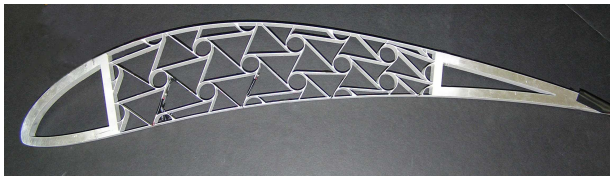

(a)

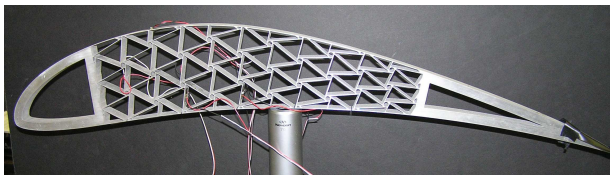

(b)

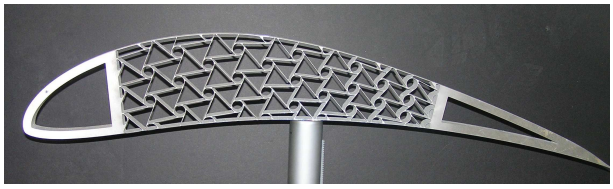

(c)

Figure 75: Manufactured samples with *Eppler 420* profile: 2 cells across the airfoil maximum thickness and $L/R = 0.60$ (a), 3 cells and and $L/R = 0.60$ (b) and 3 cells and and $L/R = 0.94$ (c)

5 (see fig. 77) shown in fig. 79 also indicates the presence of a residual strain upon unloading. For completeness, the strain predicted at location 4 is also shown in the figure. The discrepancy between numerical and experimental strain may be attributed to the fact that strain gages may not have been placed exactly at the location of maximum strain, and by the fact that the strain measured by strain gages is averaged over the gage area, while a point, nodal strain is extracted from the finite-element results.

Results for configuration b presented in fig. 80 show excellent agreement between measurements and numerical predictions. As opposed to the case of configuration a, no residual displacement is observed, indicating that, for configuration b, the trailing edge displacement is recovered upon unloading. The absence of plastic deformations in the material is confirmed by the strain variation at location 5 (see fig. 77) shown in fig. 81. The strain variation at another location (location 2) does not show the same level of agreement, but confirms the absence of residual strains. It should be

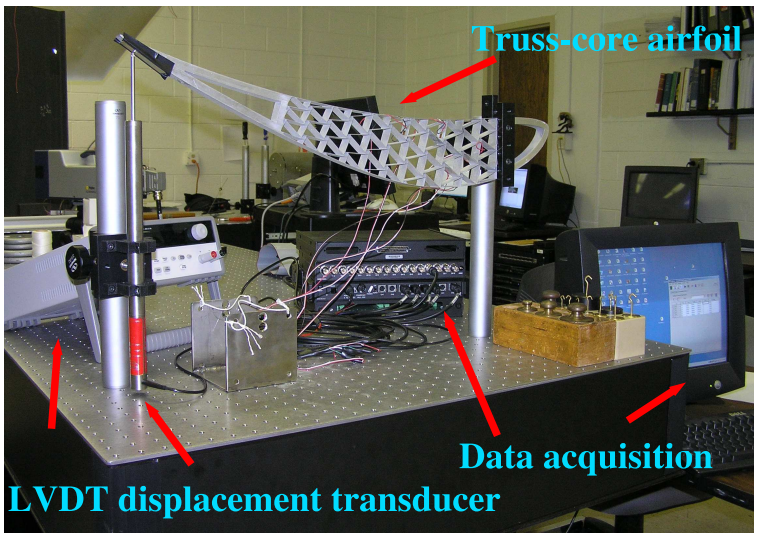

Figure 76: Manufacturing process of chiral truss-core airfoils

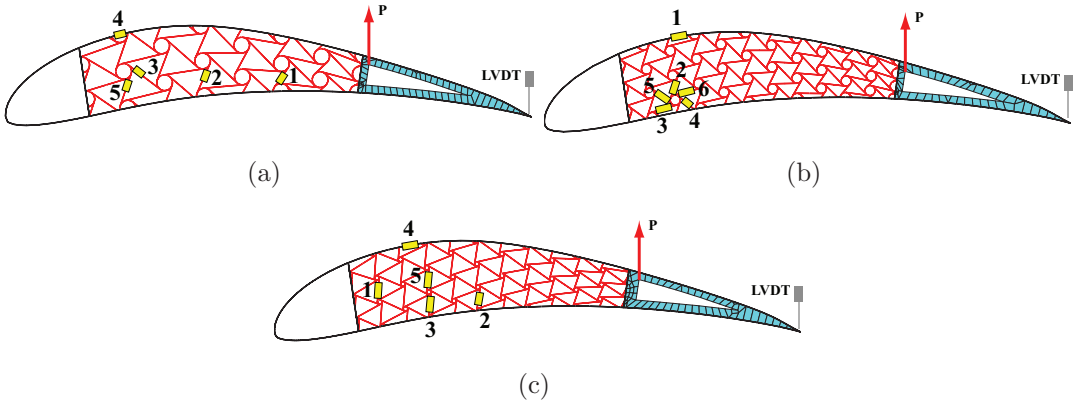

Figure 77: Strain gage, load and LVDT locations

observed that the application of strain gages on configuration b was more difficult due to the smaller size of the unit cell and correspondingly of the ligaments on which strain gages are applied. Similarly to configurations a and b, the numerical model for configuration c is able to capture the trailing edge displacement variation for increasing applied loads (fig. 82). As in the case of configuration b, no residual displacements are observed. Variations of strain clearly confirm the absence of non-linear behavior, and of residual strains upon unloading (fig. 83). As in the case of configuration b, no residual displacements are observed. Variations of strain at selected locations do

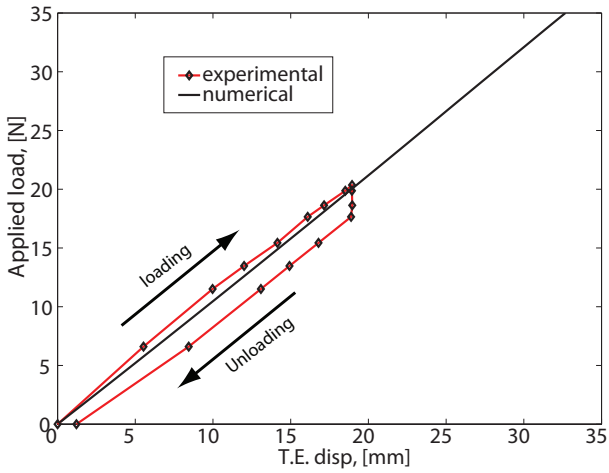

Figure 78: Numerical and experimental trailing-edge displacement for configuration *a*

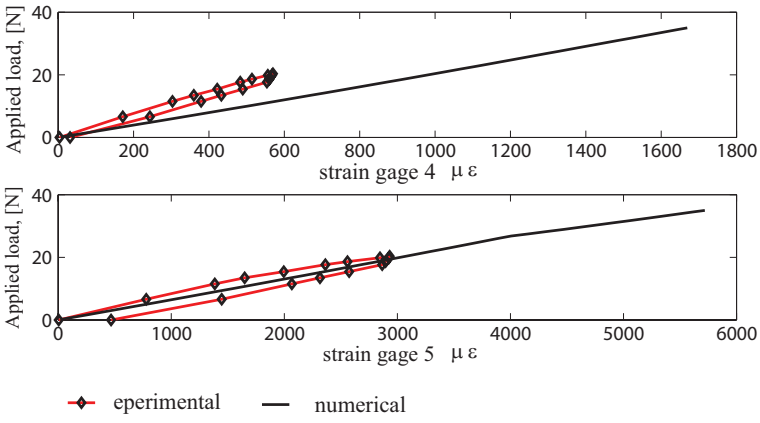

Figure 79: Numerical and experimental strain for configuration *a*

not show as good of an agreement as in the previous two cases, but clearly confirm the absence of non-linear trends in the curve, and of residual strains upon unloading. The lack of agreement on strains in this and in the previous two cases may indicate shortcomings in the FE model, and a lack of accuracy in the strain gage positioning. Experimental results, indeed, confirm the strong dependence of the airfoil compliance on the core configuration. Direct comparison of trailing edge displacement versus load, both numerical and experimental, for the three configurations is presented in fig. 84, confirming that configuration *a* provides the highest compliance of the airfoil,

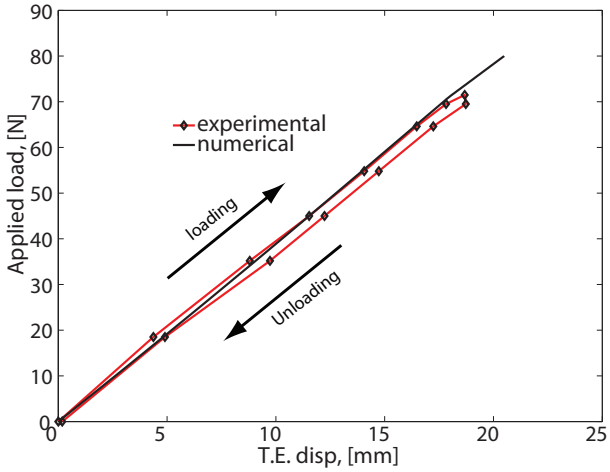

Figure 80: Numerical and experimental trailing-edge displacement for configuration *b*

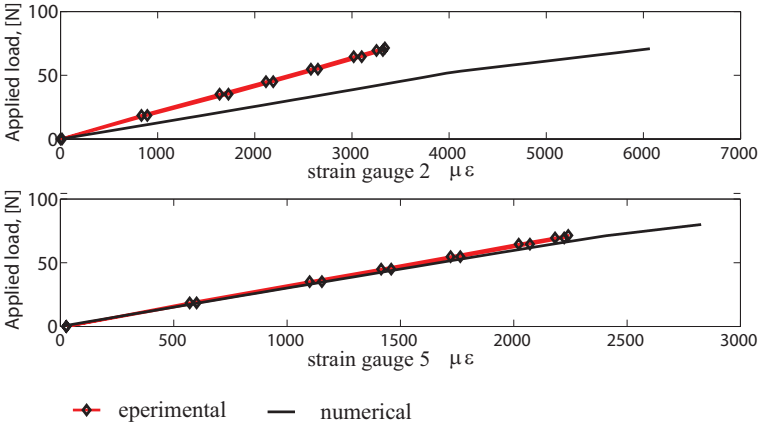

Figure 81: Numerical and experimental strain for configuration *b*

while configurations *b* and *c* are much stiffer designs.

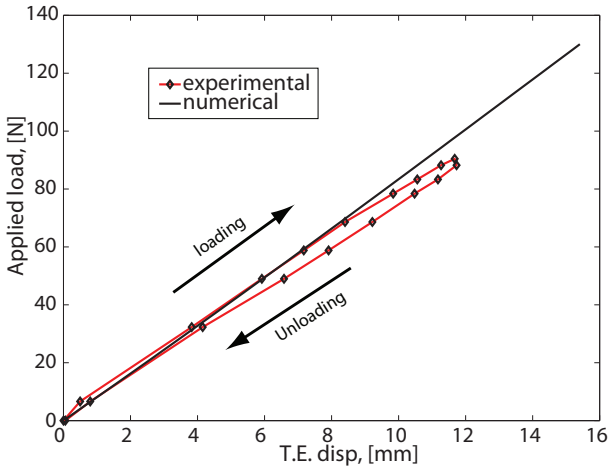

Figure 82: Numerical and experimental trailing-edge displacement for configuration *c*

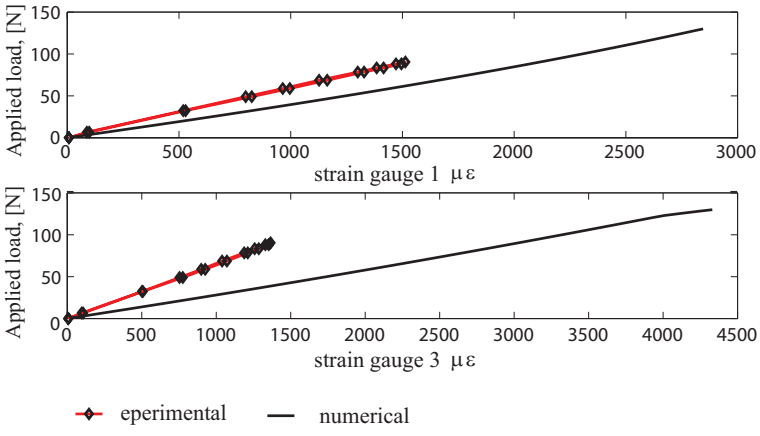

Figure 83: Numerical and experimental strain for configuration *c*

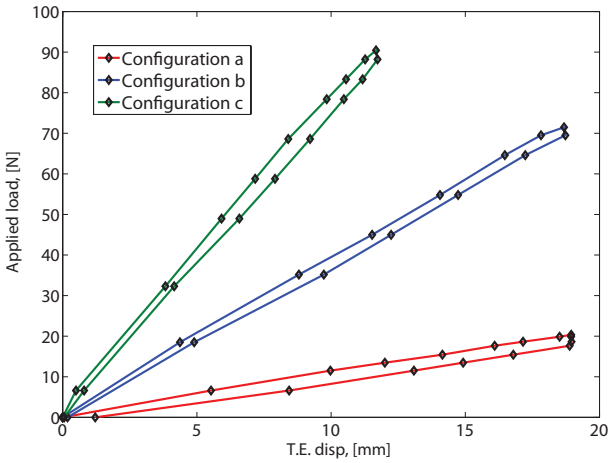

Figure 84: Comparison of trailing-edge displacement for the three considered configurations

5.7 Fiber-Composite Chiral Honeycomb

While water-jet cutting produced satisfactory truss-core airfoil samples, such manufacturing process is limited to homogeneous materials not sensitive to water exposure such as aluminum. Furthermore, the out-of-plane thickness achievable with water-jet cutting is limited as the high-pressure water jet becomes distorted upon contact with the metal slab, and such distortion increases with slab thickness. If deep truss-core wing sections are desired, water-jet cutting is not a feasible process to obtain monolithic samples. In order to circumvent such obstacles and to explore the use of other materials, a new manufacturing process is has been investigated by a research group at the Politecnico di Milano, Italy, with which a collaboration has been established. The application of a fiber-composite-winding process permits the assembly of truss-core airfoils with large out-of-plane depth and different fiber lay-ups to obtain configurations that may perform better than those made of aluminum.

Fiber-composite materials, however, may feature significant elastic anisotropy, which in turn may alter the deformation mechanism investigated in chapter 3. In order to contemplate the employment of anisotropic materials and validate the new manufacturing method, experimental analyses of a chiral cell are carried out to study the mechanical behavior arising from the considered composite materials, and a comparison based on numerical models is utilized to determine possible advantages produced by alternative materials used for truss-core airfoils.

5.7.1 Manufacturing Procedure: Fiber-Composite Winding

The set up of a feasible technological process to manufacture truss-core airfoils has driven the production method of a chiral macro-cell, which has been devised by the Aerospace Department at the Politecnico di Milano, Italy, and documented in [9]. Based upon previous manufacturing experience by the researches in Italy, the assembly of ligaments and cylinders has been accomplished by means of classical lamination,

by using a vacuum-bag process. Fig. 85.a shows the mould prepared to cure the parts of the chiral structure subsequently assembled. The minimum dimension of the elements that can be manufactured in such a way depends upon a trade-off between the drapeability of the pre-preg material and minimum curvature radii desired. The assembly of the chiral cells is obtained by a second curing process to bond the pre-cured parts with a structural adhesive film, shown in fig. 85.b. In the final version of the devised process, cylinders are obtained by superimposing the curved portion of the ligaments during the assembly. It should be observed that the strength of the obtained chiral core strongly depends upon the quality of the adhesion between its parts. To overcome such difficulty, a specific mould has been conceived for the cell

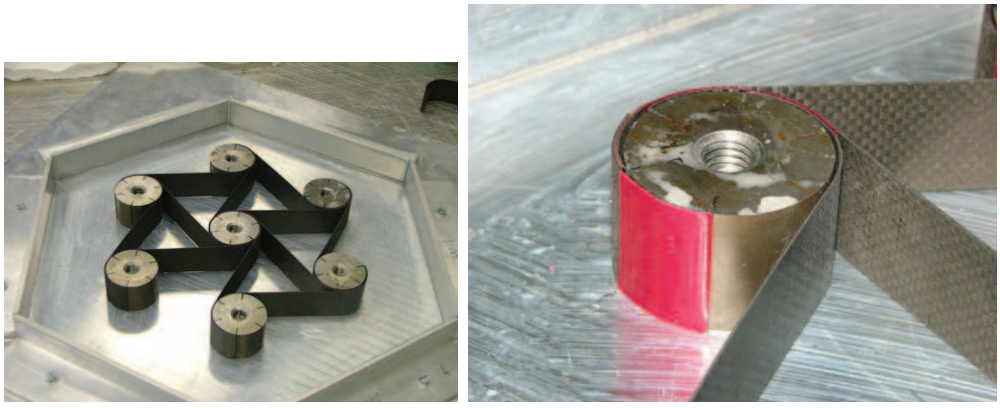

(a) (b)

Figure 85: Manufacturing procedure of a composite chiral cell: mould (a) and detail of circle construction with adhesive layer (b)

assembly. The hexagonal mould, shown in fig 85.a, has a series of metallic cylinders fixed to its lower base to proper position the pre-cured ligaments. The ligaments are positioned introducing the adhesive films between the superimposing curved parts (fig 85.b). The assembled mould is then introduced in a vacuum bag and cured in an autoclave. The geometric dimension and the material selection is based on a trade-off between numerically evaluated performance and the practicality of the manufacturing process. It has been opted to avoid excessively small dimensions and curvature

radii so as to reduce difficulties in the pre-curing of the ligaments as well as in handling the elements during the final assembly. A nominal topology parameter L/R of 0.90 characterizes the constructed sample, leading to a cylinder radius $r = 18$ mm. Plain-weave fabric plies with a relatively low cured ply thickness of 0.1 mm have been selected to exploit the drapeability of fabric without leading to excessively thick laminates. The elastic constants of such fabric materials, evaluated in previous works, are the ones provided in Table 8. Ligaments have been manufactured using a lay-up

Table 8: Material properties of employed fiber-composite material

Carbon-Fiber CC90 ET443 SEAL:	
E_{xx}	56.55 GPa
E_{yy}	56.55 GPa
ν_{xy}	0.0514
G_{xy}	4.043 GPa
σ_{yield}	565.5 MPa
$\epsilon_{11_{max}}$	0.01

sequence f ($[0]_5$) (i.e. 5 plies all oriented in the 0-direction), with each ply of thickness 0.1 mm, yielding laminates 0.5 mm thick. $AFK - 163 - 2K$ adhesive film has been used to bond the different components as shown in fig. 85.b. The overall size of the cells, measured as the distance between two opposite cylinders is approximately 168 mm. In the next sections, results of experiments carried out by researches at the Politecnico di Milano are reported for completeness.

5.7.2 Experimental evaluation of chiral-cell strength

Tests have been performed at the Politecnico di Milano with the objective of confirming the deformation characteristics of the chiral lattice, and furthermore, the capability of chiral cells to undergo large displacement without experiencing permanent deformation, degradation or failure.

To accomplish such objective, a simple test lay-out has been adopted. Two of the

cylinders of the chiral cell have been respectively connected to the moveable and the fixed cross head of an MTS 858 Static Test System, as shown in fig. 86.a. The pins have been inserted in rings having the outer diameter matching the inner diameter of the cylinders and can freely rotate about their axis. Each one of the three cells has been subjected to a different loading-unloading cycle, according to the displacement schedule reported in fig. 86.b. The cross head speed has been set to 2 mm/min.

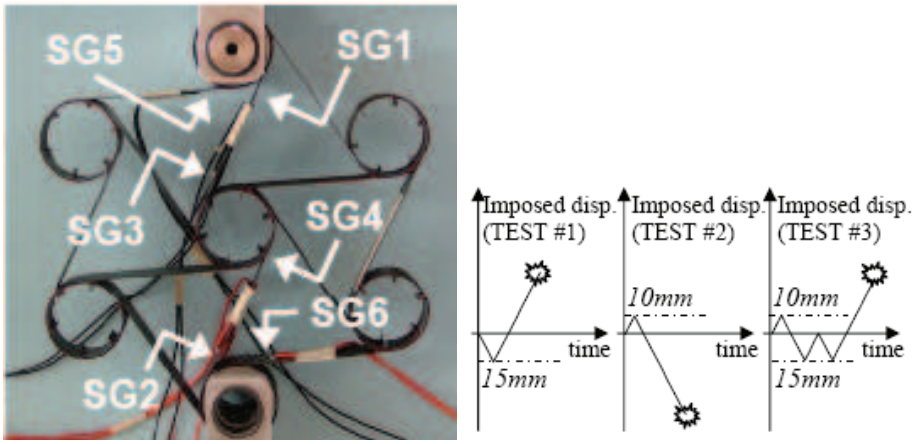

(a) (b)

Figure 86: Experimental setup (a) and imposed displacement schedule for each of three tests (b)

The imposed displacement schedule is chosen to detect possible stiffness degradation or permanent deformation occurring after the first loading-unloading cycle. Tensile and compressive failure have been triggered to quantify the cell strength as well as to identify the actual critical locations of the assembled structure. Six strain gauges have also been mounted on each of the manufactured composite chiral cells, the locations of which are reported in fig. 86.a.

5.7.3 Results and Discussion

Force-versus-displacement response obtained in the three performed tests show a markedly non-linear behavior, with a clear tendency to soften in compression and to stiffen in tension as depicted in fig. 87. One and two loading-unloading compressive

cycles have been carried out in test ♯1 and test ♯3, respectively, before the tensile test ♯2. The imposed compressive displacement of 15 mm corresponds to about 9% of the cell dimensions. The first tensile cycle, performed in test ♯2 and displayed in fig. 87,

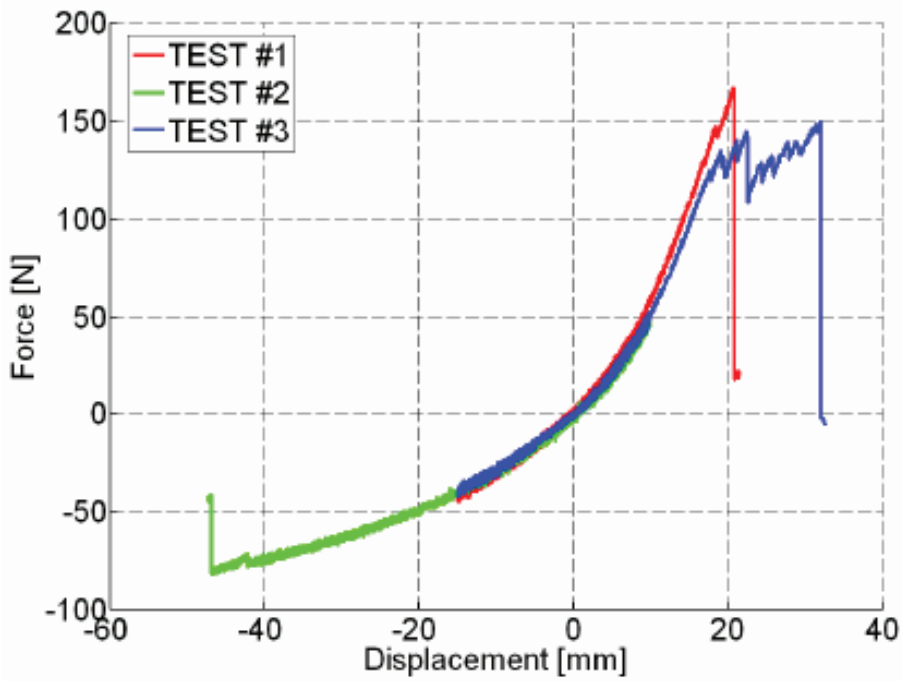

Figure 87: Force-displacement history for the performed tests

shows that the compressive cycles did not induce significant permanent deformation as well as stiffness degradation in the cell. Analogously, the tensile loading-unloading cycle, first performed on the cell used in test ♯2, did not induce significant differences in the compressive response, with respect to test ♯1 and test ♯3. In such case, the imposed tensile displacement of 10 mm corresponds to about 6% of the cell dimension. Failure occurred in tension due to de-bonding of the ligaments at the upper cylinder as a result of an imposed displacement of 20 mm, about 12% of the cell dimension, shown in fig. 88.

Fig. 89.a shows the strain recorded by the gages SG2, SG4 and SG6 as a result of imposed displacement in test ♯1. The behavior of the SG1, SG3 and SG5 signals demonstrate symmetry in the mechanical behavior of the manufactured chiral cells.

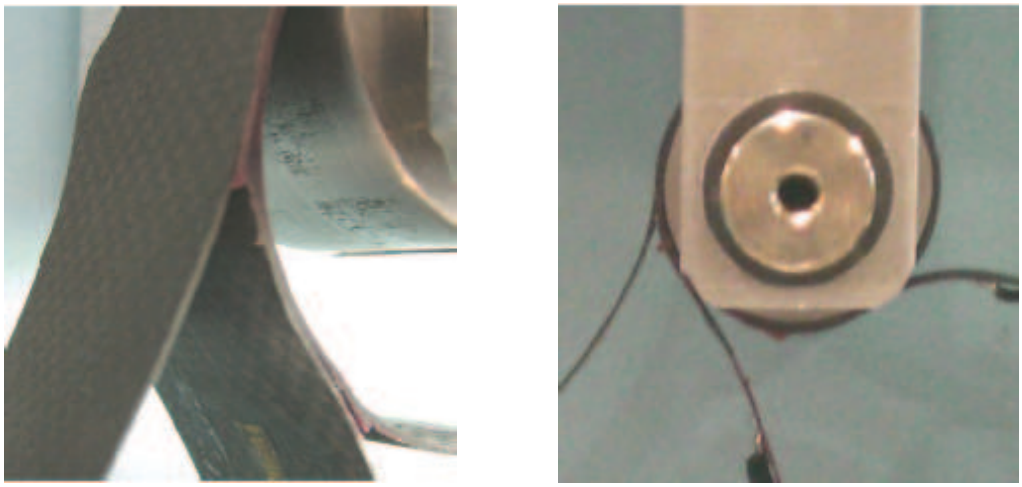

(a) (b)

Figure 88: Tensile failure: test ♯1 (a) and test ♯3 (b)

In tension, the strain levels SG2 and SG6 on the compressed side of the two ligaments converging on the constrained cylinders are similar and are about three times the strain recorded near the central cylinder. If a maximum admissible strain in compression of 0.01 for the fiber composite material is considered, the strain signals indicate that the compressive failure of ligaments would be achieved with a relatively small increment of the imposed displacement. Hence, although the presented results indicate that bonding is the actual weak point of the manufactured structure in tension, their strength appears adequate to exploit almost the whole in-plane compressive strength of the composite ligaments. As far the compressive failure is concerned, the force-versus-displacement curve of test ♯2 indicates that failure occurs for an imposed displacement of almost -50 mm, corresponding to about 30% of the cell dimension. Fig. 89.b reports the strain recorded in test ♯2 by SG2, SG4, SG5 and SG6. Strain gauges SG5 and SG6, located on the tensed side of the failed ligaments, experienced the highest strain levels among the recorded ones. The failure of the ligaments occurred in correspondence of strain levels between 13000 and 14000

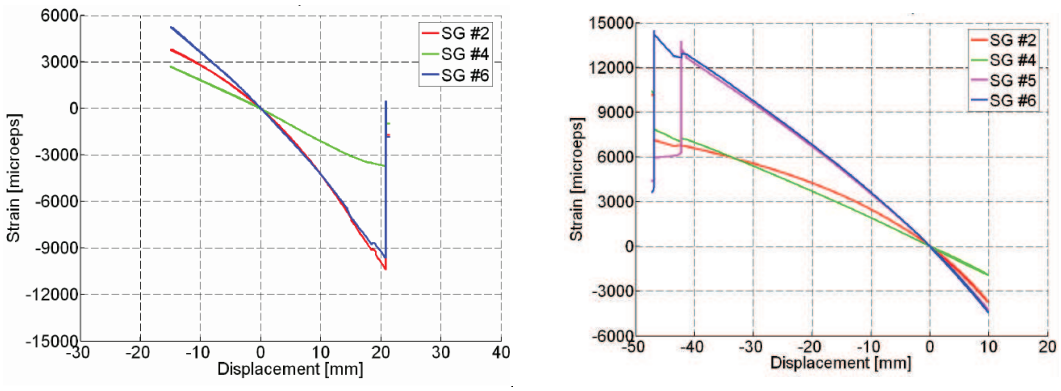

(a) (b)

Figure 89: Strain versus displacement history: test ♯1 (a) and test ♯2 (b)

$\mu\epsilon$. Compression appears less critical than tension as far as the cell strength is concerned. In such case, the failure-triggering factor appears to be the bending strength of composite ligaments. A detailed non-linear FE analysis capable of reproducing the failure mechanisms discussed above and confirming the findings of experimental measurements is presented in [9]. The agreement between the non-linear model presented in [9] and experimental measurements is encouraging as such numerical model will be employed to asses capabilities and feasibility of future configurations of truss-core airfoils.

The ability to realistically manufacture deep chiral truss-core wing-sections may thus be provided by ligament winding of carbon-fabric plies onto a jig. Encouraging experimental measurements, moreover, demonstrate the dominant deformation mechanism to be very similar to that observed in aluminum configurations. An additional concern deriving from the use of adhesively-bonded carbon-fiber plies is the failure mechanism and its influence on the overall strength of chiral configurations. The failure mechanisms observed in experiments however allow the allowable loads to span the large deformations within the linear regime of the constituent material afforded by the chiral topology.

5.8 A comparison of Aluminum and Fiber-Composite Truss-Core Airfoils

The promising features presented in the previous section may be employed to obtain truss-core airfoils capable of sustaining larger deformations than their aluminum counterparts. In the following numerical simulations, the influence of manufacturing limitations as well as the advantages offered by carbon-fiber components are quantified.

In the following analyses, fillets are not included for either the aluminum model or for the composite model. The manufacturing process presented in sec. 5.7.1, in fact, provides the ability of assembling ligaments and nodes without any fillets. This is advantageous as it does not produce significant deviations from the nominal model. The overlay of carbon-fabric ligaments to obtain nodes or circles, however, yields circles with higher wall thickness than the ligaments themselves, and accordingly, this deviation from the nominal material distribution within the core is modeled as depicted in fig. 90. In particular, $t_b = 0.8$ mm (4 plies) and $t_c = 1.4$ mm (14 plies)

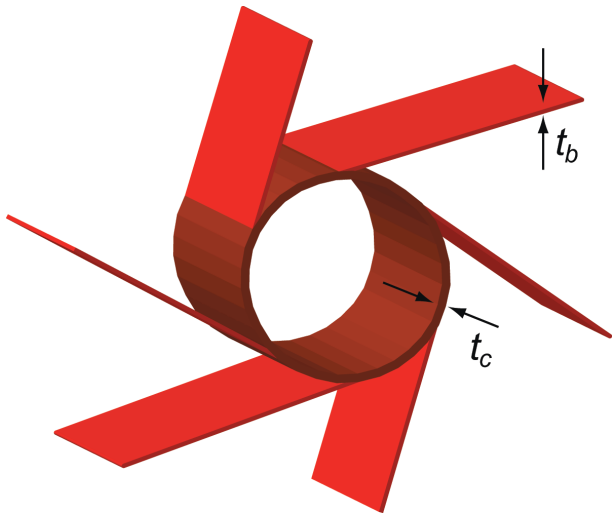

Figure 90: Detail of fiber-composite airfoil core

as for the chiral-cell sample discussed in sec. 5.7.3. The nominal topology parameter (before mapping of the core) is $L/R = 0.60$. The envisioned composite-truss-core

airfoil is the one depicted in fig. 91, where the light/dark grey portions represent aluminum 6061 T051, the red portion the considered carbon-fiber material while the green portion indicates a softer material to promote de-cambering deformations. As for the non-linear FE model discussed in sec. 5.6.1, a bilinear-isotropic material model is employed to detect deviations from the elastic regime of the carbon-fiber material. For the elastic regime, the material properties indicated in Table 8 are employed. For the plastic regime, tangent moduli $E_{xx_t} = E_{yy_t} = 56.55$ MPa are assumed. The soft-

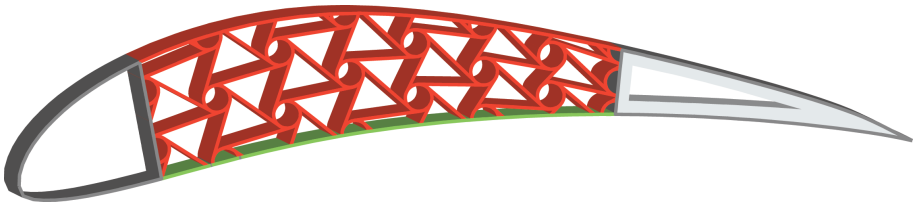

Figure 91: Fiber-composite truss-core airfoil: light/dark gray aluminum 6061 T051, red carbon fiber and green soft material

material portion shown in green in fig. 91 features elastic moduli $E_{xx} = E_{yy} = 565.5$ MPa, yield stress $\sigma_{yield} = 565.5$ MPa and tangent moduli $E_{xx_t} = E_{yy_t} = 0.566$ MPa. The considered loading and boundary conditions are the same as those employed previously for the all-aluminum model of sec. 5.6.1 and depicted in fig. 77.

The influence of core material as well as core density on airfoil de-cambering compliance is depicted in figs. 92. The low core density associated with the 2-cell configuration of fig. 92.a expectedly yields the highest compliance while the 4-cell configuration yields the highest stiffness (fig. 92.c). Interestingly, employing carbon fiber as the core material affords a trailing-edge displacement generally twice as large as that obtained with aluminum at the onset of plasticity. Of note is also the non-linear behavior of the 2-cell configuration with carbon-fiber core even before the onset of plasticity (fig. 92.a). This phenomenon should clearly be attributed to the non-linear response associated with geometric stiffening/softening of the core components. While the dependency of trailing-edge displacement upon core density and material

is intuitive, the stress distribution resulting from the adoption of carbon fiber is not equally so. In particular, the stress distribution for the 2-cell configuration made of aluminum depicted in fig. 93.a appears confined at the lower portion of the chiral core, while the same configuration with carbon-fiber core features highest axial stress of the ligaments on the upper section of the airfoil profile and ligament closest to the leading edge (fig. 93.b). As for the findings in [90], the core nodes exhibit much lower stress than the ligaments. The 3-cell configuration also features a significant difference in core axial stress between the aluminum and carbon-fiber configurations (figs. 93.c and 93.d). The discrepancy in axial stress distribution may be attributed to the larger deformations afforded by the composite material, as well as a low relative density of the truss core. The axial-stress distribution for 4-cell configurations made of aluminum and carbon fiber, in fact, does not differ as markedly as for the 2-cell and 3-cell models. Despite the large de-cambering deformations depicted in figs. 93.e and 93.f, in fact, core components do not deform as much as for the 2 and 3-cell configurations, likely due to higher relative density of the truss-core.

In summary, the employment of carbon-fiber composites not only allows the manufacturing of deep truss-core airfoils or wings, but it also permits significantly larger de-cambering deformations while within the elastic regime of the material. Improvements in performance may also be obtained by the tailoring capabilities offered by composites. Future studies, however, are needed to establish the repeatability of such large deformations as well as to better understand failure mechanisms that could be detrimental to the integrity of the wing assembly.

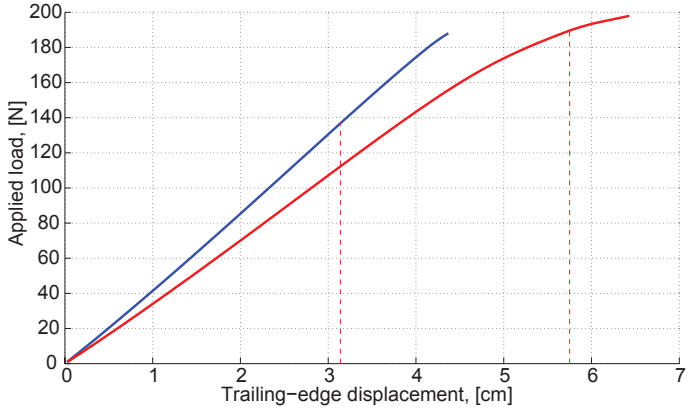

(a)

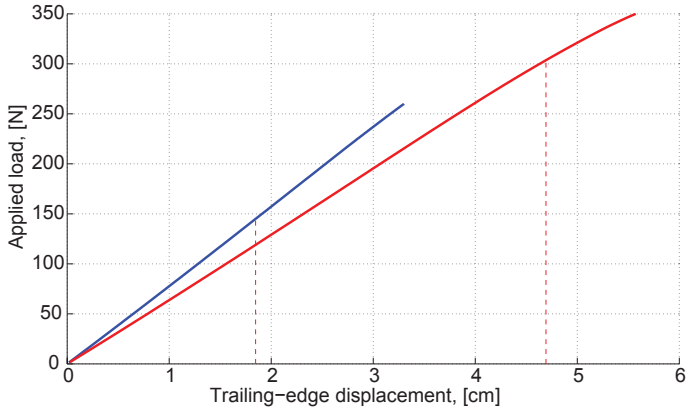

(b)

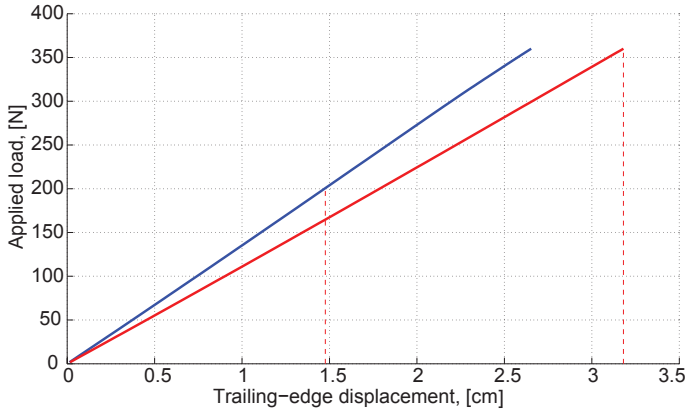

(c)

Figure 92: Airfoil trailing-edge displacement versus applied load: 2-cell (a), and 3-cell (b) and 4-cell configuration (c). Blue line, aluminum core, red line carbon-fiber core. Red dashed line, plasticity onset

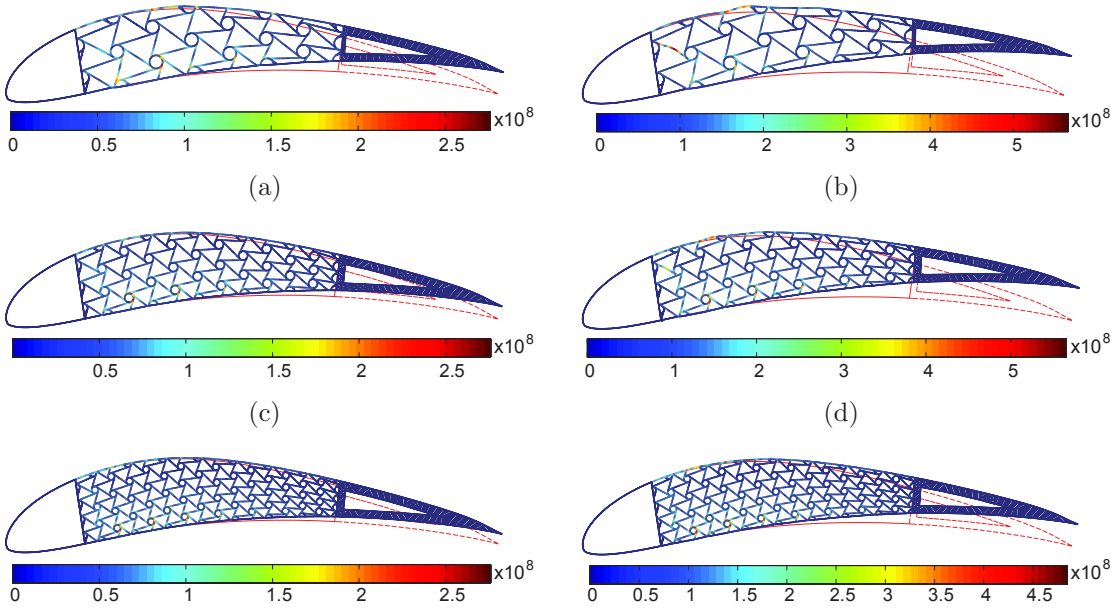

Figure 93: Axial stress intensity at the onset of plasticity (MPa), for aluminum models, 2-cell (a), 3-cell (c), 4-cell (e) and composite models, 2-cell (b), 3-cell (d), 4-cell (f). Red dashed lines indicate the undeformed configuration

5.9 Active Morphing of composite chiral-core airfoils

5.9.1 overview

In recent years, significant effort has been devoted to investigating structural concepts with morphing capabilities. The introduction of smart structures and adaptive technologies in the aerospace field offers exciting opportunities to implement previously inaccessible structural morphing concepts [67]. According to [11], morphing in the engineering sense can be generally defined as "a set of technologies that increases a vehicle's performance by manipulating certain characteristics to better match the vehicle state to the environment and task at hand". Particularly to the aerospace field, the typical objective of a morphing concept is to provide airfoils with continuous deformations, and to eliminate the need for flap-type mechanisms. In this sense, a variety of solutions have been recently proposed to provide aircraft wings and helicopter rotor blades with adaptive capabilities. Methods to generate both chord-wise and span-wise camber variations are of particular interest, with the goal of controlling aeroelastic and structural performance of wings and blades in response to changing fight conditions. The belt rib concept, for example, is an interesting solution proposed by [17]. Continuous camber variation is achieved by transferring the stroke of an actuator into a geometric change of the airfoil shape through a closed belt and an internal network structure. A similar, remarkable solution for camber variation is the finger concept presented by [69], where the airfoil features a flexible rib composed of plate-like elements connected through revolute joints. The rotation of the driven element is transferred gradually from element to element thus providing the desired deformed profile. Tension-torsion coupling has been employed as an effective mean to actively control camber variations in helicopter blades [13]. Moreover, recent design solutions have considered inflatable airfoil structures [16], variable-span morphing wings [4, 95], and hingeless, flexible leading and trailing edges actuated using shape memory alloys [56].

The compliance associated with de-cambering deformations demonstrated by chiral, truss-core airfoils as a result of aerodynamic loads (sec. 5.5), and performance improvements derived from the used of composite materials (sec. 5.8) further offer the opportunity to easily morph a given truss-core airfoil into a desired shape. In particular, the unique deformation mechanism characteristic of chiral frame structures (chapter 3) features rotation of the circular components as well as bending of the ligaments. A relatively simple strategy to obtain global deformations then may be the application of concentrated moments at various node locations to obtain camber-wise deformations.

5.9.2 Examples of actively induced camber-wise morphing

A possible objective of active morphing, in the aerospace field in particular, may be to deform a lifting surface, for example, to best adapt to a given flight regime. While passive morphing would provide a very efficient way to adapt to given flight conditions, its scope and applicability are limited to the inherent capabilities of the underlying system. Active morphing on the other hand may expand the possibly limited capabilities of a compliant system, able to withstand loads, by forcing the system to assume a desired shape. In the particular case of aerospace applications, continuous deformations may be required.

To demonstrate the possibility of actively morphing chiral, truss-core airfoils, a symmetric airfoil is employed: namely the *NACA 0012* profile. This particular airfoil is chosen to illustrate to capability of inducing a symmetric profile to assume cambered configurations by loading the chiral truss-core. A relatively high-relative-density core is selected to avoid wrinkling, which is characteristic of low-core-density configurations such as the one depicted in figs. 93.a and b. In particular a 4-cell configuration is employed. The upper and lower portions of the airfoil are assumed more compliant than the core to promote camber-wise deformations. The resulting airfoil is depicted

in fig. 94. The mapping process of the chiral core into the airfoil profile is identical

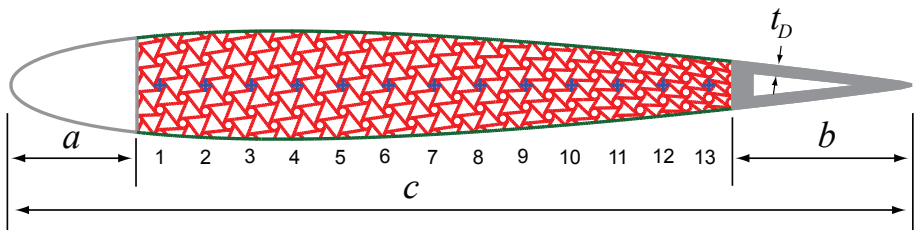

Figure 94: *NACA* 0012 with chiral core. Soft composite material (green), carbon-fiber material (red), aluminum 6061 T051 (grey), locations for torque application (blue)

to the one presented in fig. 68. The chord c is 0.70 m as for all the configurations previously considered, $a = 0.098$ m, $b = 0.14$ m, while $t_D = 8.3$ mm. The wall thickness and material properties of airfoil profile and core components are identical to those of the model of sec. 5.8 and fig. 90. Namely, ligaments and airfoil profile feature a wall thickness $t_b = 0.8$ mm, while the nodes feature a wall thickness $t_c = 1.4$ mm as in fig. 90. The out-of-plane depth is 1.9 cm. The nodes denoted by blue crosses in fig. 94 are assumed rigid and indicate locations where torque is applied. The solution procedure includes large deformations producing geometric softening/stiffening, as well as a bi-linear isotropic material model to detect the onset of plasticity.

A possible actuation strategy is to apply a torque at each of the node locations denoted by blue crosses in fig. 94. Based on preliminary simulations, it is found that a torque of 2 N-m is sufficient to deform the truss-core assemblies up to the onset plasticity, or wrinkling of the outer skin, depending on core topology. As for passive morphing, it is important to establish the influence of topology on the compliance and achievable deformed configurations of chiral, truss-core airfoils. To this end, the trailing-edge displacement for a set of configurations denoted by $L/R \in [0.60, 0.90]$ loaded in the same manner as described just above is computed. Fig. 95 suggests that, as for passive morphing, low topology parameter values, i.e. $L/R \to 0.60$, yield a compliant assembly while high topology parameter values, i.e. $L/R \to 1$, produce

stiffer configurations.

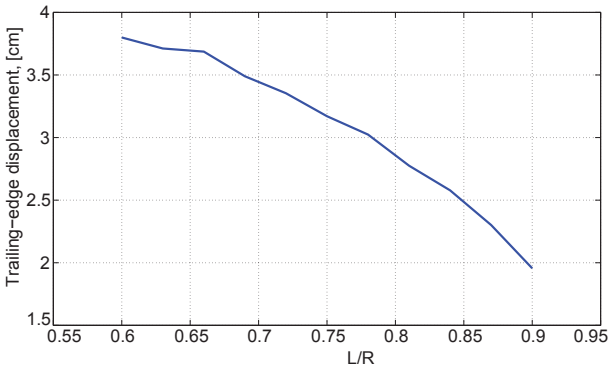

Figure 95: Trailing-edge displacement versus topology parameter L/R, given an applied torque of 2 N-m on each of the constrained nodes

The chiral core has been shown to be able to withstand aerodynamic loads (sec. 5.5), however, the internal components of the core are thin-wall elements and may not be able to withstand concentrated loads. In order to propose chiral, truss-core airfoils as useful for active morphing provided by simple actuation strategies, internal stresses resulting from applied loads need to be known. Of the considered configurations, the most compliant ($L/R = 0.60$) and the stiffest ($L/R = 0.90$) are analyzed to ensure that axial stress within each core component is within tolerable levels. For the configuration denoted by $L/R = 0.60$ and depicted in fig. 96.a, the largest achievable camber-wise deformations are limited by wrinkling of the upper-skin portion of the airfoil profile. Localized deformations of the upper-part of the wing section near the leading edge reach a maximum value of approximately 10% of the airfoil thickness or 6.7 mm. The maximum stress within the core, in fact, is approximately 190 MPa, which is well within the maximum axial stress allowed for the considered carbon-fiber material (Table 8). The axial-stress intensity resulting from applied moments for the configuration denoted by $L/R = 0.90$ is shown in fig. 96.b. For the same loading conditions, the latter configuration is much stiffer, and thus wrinkling of the airfoil profile is not present due to significantly reduced camber-wise deformations.

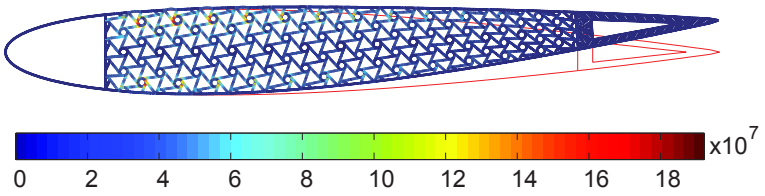

(a)

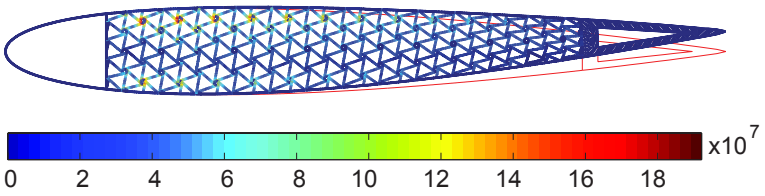

(b)

Figure 96: Axial stress intensity (MPa) due to applied concentrated moments,$L/R = 0.60$ (a) and $L/R = 0.90$

A further actuation strategy may be the application of concentrated moments of different magnitude within the truss core. Preliminary simulations aimed at investigating the feasibility of morphing to obtain complex configurations suggest that an applied torque of 10 N-m on nodes 2 through 5 and -6 N-m on nodes 10 and 11 produces the camber-wise deformations depicted in fig. 97. The axial stress intensity

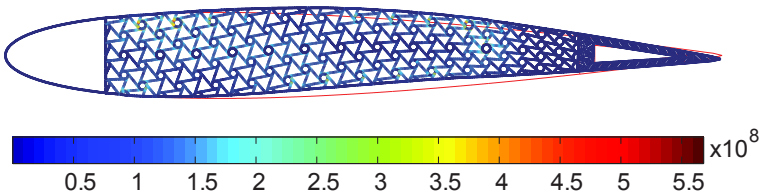

Figure 97: Axial stress intensity (MPa) due to applied concentrated moments,$L/R = 0.60$

reaches its maximum allowed level at nodes near the upper portion of the airfoil profile and near node 11 (refer to fig. 94). In this case, no wrinkling of the airfoil profile is present, and the limiting factor in achieving the deformations depicted in fig. 97 is certainly the maximum allowed axial stress for the carbon-fiber material.

5.10 summary

The unique set of mechanical properties offered by the chiral topology are exploited for the design of truss-core airfoils with morphing capabilities. Particularly, the ability of chiral lattice structures to withstand large deformations within the elastic regime of the constituent material are exploited. An initial configuration obtained by accommodating a periodic chiral lattice within a *Eppler 420* profile resulted in undue complexity as the strain resulting from aerodynamic loads is nearly confined in a small portion of the core. A second design featuring a reduced truss-core zone is proposed as an improved alternative to the first arrangement. To asses the capabilities of the improved design in allowing and withstanding de-cambering deformations, a weakly coupled static-aeroelastic numerical model is devised. The outcome of such simulations suggests the ability of chiral, truss-core airfoils to withstand aerodynamic load as well as large de-cambering displacements, on average about 2.9% of the chord at the trailing edge. Three samples have been manufactured with the intent of confirming the findings of numerical models. Good agreement, both in the strain distribution and load-trailing-edge-displacement relation is achieved between experimental measurements and numerical predictions. This is encouraging as it suggests the use of numerical models for the design of future truss-core configurations.

Limitations encountered in the production of the three aforementioned samples led to an improved manufacturing technique encompassing carbon-fabric winding that will allow the production of deep truss-core samples. The use of composite materials, moreover, will afford improved performance via fiber-orientation tailoring, large-deformation capabilities, reduced weight, and the possibility of embedding actuators in the ligaments and nodes of the core. Concerns regarding the possibly altered mechanical behavior resulting from composite materials were discredited based on experimental measurements of the kinematics of a chiral macro-cell. The same numerical models employed to investigate the onset of plasticity resulting from

large camber-wise displacements, furthermore, indicate that carbon-fiber materials may generally allow trailing-edge displacements twice as large as those obtained with all-aluminum models. Furthermore, the compliance of the chiral truss-core can be exploited to actively induce camber-wise deformations of wing-sections. Two examples are analyzed to demonstrate to ability to produce deformed configurations with single and multiple-curvature camber.

Finally, the investigations reported in the current chapter take advantage of large-deformation capabilities associated with the chiral lattice.

CHAPTER VI

DYNAMIC SHAPE CONTROL

Chapter 3 outlines the dependence of the mechanical properties of chiral honeycombs upon their geometric parameters. In particular, the Young's modulus can be directly varied by controlling the ratio L/R. The static aeroelastic response of chiral truss-core airfoils stands as a prime example. The experimental results obtained by applying a concentrated load confirm such characteristics, whereby the airfoil compliance directly depends upon the L/R ratio and upon the core relative density. Such dependency can be investigated in the dynamic regime. In [88], for example, it was observed how the ratio L/R affects the acoustic performance of chiral truss-core panels. The panels' modal density was in fact shown to depend upon the aforementioned geometric parameters, which directly influence transmission loss and sound absorption characteristics [88]. In addition, it was shown how the dynamic response of the truss-core panels changes considerably with frequency. At low frequencies, the panels deforms much like homogenous beams in global bending operational deflection shapes (ODSs). In the mid-frequency region, the wavelength of the deformations approaches the length of the core elements and the phenomenon of intra-cell resonance takes place [88]. Interestingly, at the boundary of the two frequency regions, localized deformations appear. It is presumed that such phenomena depend upon the wave propagation characteristics of the chiral honeycomb, which in fact is the subject of current research. It is therefore appealing to extend this type of dynamic analysis to truss-core airfoils to investigate their dynamic properties, and possibly extend the observations presented for truss-core panels. In particular, focus is placed on the capability of the proposed configurations to generate ODSs where deformations are

mostly localized in small regions of the structure. The ODSs correspond to excitation at the natural frequencies of the structure, so that resonance can be exploited to minimize the power required for the appearance of localized deformations, thus giving practicality to the concept. The analysis is supported by preliminary numerical and experimental investigations on a cantilever truss-core beam. The dynamic behavior of the *Eppler 420* airfoils with chiral core is then investigated both numerically, through a model developed using a commercial FE package, and experimentally.

6.1 Preliminary investigations: dynamic analysis of a truss-core beam with chiral core

The ability to obtain useful deformed configurations with low input power levels, and the authority provided by the chiral geometry offer an alternative to more traditional morphing concepts. Shape control of structural components can be achieved by employing active materials, such as electroactive polymers (EAP) [5], or mechanisms composed of actuators. In the former case, the material may not be suitable for load-carrying applications, while the latter case may be difficult to implement, as actuators usually require a control system and add significant mass. Consequently, chiral truss-core assemblies are proposed as a novel technique to obtain useful deformed configurations, as they offer a scalable geometry, and thus a scalable frequency response, low energy input requirements, and multifunctional characteristics, whereby load-carrying and dynamic shape control capabilities may be combined.

6.1.1 Numerical dynamic model using spectral elements

The dynamic behavior of each element of a truss-core cantilever beam is described through dynamic equations derived from distributed parameter models [27, 28]. This allows the accurate prediction of the dynamic response of the structure over a wide frequency range, without the need for refinement of the discretization as frequency increases. The elements are oriented in the plane of the structure x, y according to

the core topology. The dynamic behavior of each element is described in the local reference system $\mathfrak{L} = (\xi, \eta)$, rotated with respect to the global reference system $\mathfrak{G} = (x, y)$ of the angle α (see fig. 98). The model contains elements of various lengths, some of which are very small. Timoshenko beam theory is thus considered to prevent lack of accuracy in the description of relatively short members through Euler-Bernoulli theory.

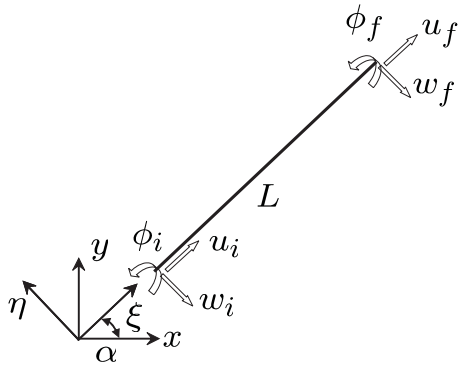

Figure 98: Global and local reference systems, with associated element degrees of freedom

6.1.2 Distributed Parameter Model in the Local Reference System

The equations of motion and boundary conditions governing the longitudinal and transverse vibrations of a beam element can be derived by applying Hamilton's principle:

$$\int_{t_1}^{t_2} \delta(T - U + W)dt = 0, \tag{96}$$

where $\delta(.)$ denotes the first variation, t_1 and t_2 are the initial and final time, T and U are respectively the kinetic and the strain energy of the beam, and W is the work done by the external forces. Each element is considered as a Timoshenko beam, and includes axial degrees of freedom. In the local reference system, the beam's strain energy can be expressed as:

$$U = \frac{1}{2} \int_0^L \left[EAu_{,\xi}^2 + EI\phi_{,\xi}^2 + \kappa AG(w_{,\xi} - \phi)^2 \right] \mathrm{d}\xi, \tag{97}$$

where E, G are the Young's and shear moduli of the beam material, A, I are the area and the second moment of area of the beam cross section, and κ is the shear coefficient. Also, in eq. (97), $u = u(\xi, t), w = w(\xi, t)$ denote the axial and transverse deflection of the beam, while $\phi = \phi(\xi, t)$ is the rotation of the cross section at location ξ and time t. Finally, the following notation $(\diamond)_{,\xi} = \frac{\partial(\diamond)}{\partial \xi}$ is used to denote partial differentiation. Finally, the kinetic energy is given by

$$T = \frac{1}{2} \int_0^L \left[\rho A (u_{,t}^2 + w_{,t}^2) + \rho I \phi_{,t}^2 \right] \mathrm{d}x, \tag{98}$$

where ρ is the density of the beam material.

6.1.3 Dynamic Stiffness Matrix formulation

In the local frame, a set of three differential equations describes the beam's longitudinal and transverse vibration. For harmonic motion at frequency ω the equations of motion can be expressed in matrix form as follows:

$$\boldsymbol{z}_{,\xi}(\xi) = \boldsymbol{A}\boldsymbol{z}(\boldsymbol{\xi}), \tag{99}$$

where $\boldsymbol{A}$ is a matrix of constant coefficients, and where

$$\boldsymbol{z} = [\ u \quad w \quad \phi \quad u_{,\xi} \quad w_{,\xi} \quad \phi_{,\xi}\ ]^T \tag{100}$$

is the state vector describing the axial and bending behavior of the considered beam element at frequency ω. In the current development, lower case bold letters indicate vectors, while capital bold case letters indicate matrices. A general solution of eq. (99) can be expressed as:

$$\boldsymbol{z}(\xi) = e^{\boldsymbol{A}\xi}\boldsymbol{z}(0) \tag{101}$$

which relates the vector $\boldsymbol{z}$ at the generic location ξ to that at $\xi = 0$. An alternative expression for the state vector can be introduced to contain generalized displacements and stress resultants at the considered location. A vector $\boldsymbol{y}$ can be defined as:

$$\boldsymbol{y} = [\ u \quad w \quad \phi \quad N \quad V \quad M\ ]^T, \tag{102}$$

where $N(\xi) = EAu_{,\xi}, V(\xi) = \kappa GA(w_{,\xi} - \phi), M(\xi) = EI\phi_{,\xi}$ are respectively the axial resultant, the shear force and the bending moment at location ξ. The vectors $\boldsymbol{y}$ and $\boldsymbol{z}$ are simply related through the following expression:

$$\boldsymbol{y}(\xi) = \boldsymbol{G}\boldsymbol{z}(\xi), \tag{103}$$

where $\boldsymbol{G}$ is the constitutive matrix containing the material and cross sectional properties of the beam element. Eqs. (101) and (103) can be used to obtain a relation between state vectors at two locations on the element:

$$\begin{aligned} \boldsymbol{y}(\xi) &= \boldsymbol{G}e^{\boldsymbol{A}\xi}\boldsymbol{G}^{-1}\boldsymbol{y}(0) \\ \boldsymbol{y}(\xi) &= \boldsymbol{T}(\xi)\boldsymbol{y}(0), \end{aligned} \tag{104}$$

where $\boldsymbol{T}(\xi)$ is the "transfer matrix" of the beam, calculated at location ξ. The transfer matrix relates generalized displacements and forces at the two ends of the element ($\xi = L$):

$$\boldsymbol{y}(L) = \boldsymbol{T}(L)\boldsymbol{y}(0). \tag{105}$$

Eq. (105) then can be expanded as follows:

$$\begin{pmatrix} \boldsymbol{u}_f \\ \boldsymbol{f}_f \end{pmatrix} = \begin{pmatrix} \boldsymbol{T}_{11} & \boldsymbol{T}_{12} \\ \boldsymbol{T}_{21} & \boldsymbol{T}_{22} \end{pmatrix} \begin{pmatrix} \boldsymbol{u}_i \\ \boldsymbol{f}_i \end{pmatrix}, \tag{106}$$

where $\boldsymbol{u}_i, \boldsymbol{u}_f$ and $\boldsymbol{f}_i, \boldsymbol{f}_f$ respectively are the generalized displacements and forces at the initial and final node. Eq. (106) can be rearranged to obtain:

$$\boldsymbol{f}_e^{\mathcal{L}} = \boldsymbol{K}_{d_e}^{\mathcal{L}}\boldsymbol{u}_e^{\mathcal{L}}, \tag{107}$$

where $\boldsymbol{f}_e^{\mathcal{L}} = (\boldsymbol{f}_i \quad -\boldsymbol{f}_f)^T$, $\boldsymbol{u}_e^{\mathcal{L}} = (\boldsymbol{u}_i \quad \boldsymbol{u}_f)^T$, and where $\boldsymbol{K}_{d_e}^{\mathcal{L}}$ is the dynamic stiffness matrix of the element, which is obtained as:

$$\boldsymbol{K}_{d_e}^{\mathcal{L}} = \begin{pmatrix} -\boldsymbol{T}_{12}^{-1}\boldsymbol{T}_{11} & \boldsymbol{T}_{12}^{-1} \\ \boldsymbol{T}_{21} - \boldsymbol{T}_{22}\boldsymbol{T}_{12}^{-1}\boldsymbol{T}_{11} & \boldsymbol{T}_{22}\boldsymbol{T}_{12}^{-1} \end{pmatrix}. \tag{108}$$

In eq. (107), the subscript e denotes vectors pertaining to the element, while superscript $\mathfrak{L}$ indicates that the expression is obtained in the local reference system $\mathfrak{L} = (\xi, \eta)$. The generalized displacements of points within the element are expressed in terms of the nodal degrees of freedom:

$$\boldsymbol{u}(\xi) = \boldsymbol{N}(\xi)\boldsymbol{u}_e^{\mathfrak{L}}, \tag{109}$$

where $\boldsymbol{N}(\xi)$ is the matrix of the dynamic interpolation functions, which is obtained from the transfer matrix formulation given above. The dynamic stiffness matrix for the element is obtained from the beam's distributed parameter model for harmonic motion at frequency ω. Within the validity of Timoshenko approximations, the model reproduces the exact displacements of the considered element. Accordingly, a single finite element is sufficient to fully characterize the response of a beam.

The components of the beam's longitudinal and transverse displacements u, w in the global reference system $\mathfrak{G} = (x, y)$ are given in terms of the rotation angle α in fig. 98. The dynamic stiffness formulation in the global reference system $\boldsymbol{K}_{de}^{\mathfrak{G}}$ is defined in terms of the stiffness matrix in local coordinates through a rotation matrix defined in term of the angle α.

Assembly for all the elements of the truss-core beam yields the discretized equation of motion for the considered structure, which has the well known form:

$$\boldsymbol{f} = \boldsymbol{K}_d\boldsymbol{u}, \tag{110}$$

where $\boldsymbol{u}, \boldsymbol{f}, \boldsymbol{K}_d$ are the vector of the degrees of freedom of the entire structure, the vector of the equivalent external nodal loads, and the assembled dynamic stiffness matrix. Solution of the equation for an assigned set of external loads at given frequency yields the amplitude of the displacements at each node. The displacements within each element can then be obtained through the general elemental solution and the dynamic interpolation functions described by eq. (109).

6.1.4 Numerical Results

The numerical model described in sec. 6.1.1 is first used to predict the dynamic response of the truss-core beam shown in fig. 99. The baseline configuration features two identical constraining layers of thickness $t_{b1} = 0.81$ mm, and a core of thickness $t_c = 6.9$ cm. The total length of the beam is $L_b = 0.5$ m. Both the core and constraining layers are made of aluminum (Young's Modulus $E = 71$ GPa, density $\rho = 2700$ kg/m^3, Poisson's ratio $\nu = 0.33$). The chiral configuration is characterized by the following parameters (see fig. 17): $R = 2.82$ cm, $r = 0.56$ cm, $L = 2.59$ cm, $\theta = 30°$, $\beta = 26.9°$. The wall thickness of the ligaments is 0.81 mm, while the wall thickness of the nodes is 0.89 mm. The beam is fixed at the right end and free at the left end. Finally, the out-of-plane thickness is 2.54 cm. The excitation configuration shown in fig. 99 is considered in the simulation. The

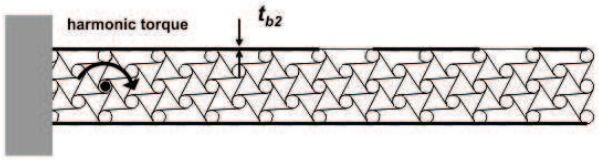

Figure 99: Truss-core beam with chiral core

excitation frequency is a harmonic torque of frequency varying from 0 to 3000 Hz, to cover a large number of structural resonances. At low excitation frequencies, the influence of the core topology is only limited to increasing or decreasing the bending stiffness of the complete assembly, and the beam approximately behaves as a homogeneous beam. Examples of the deformed configurations at low frequencies are depicted in figs. 100.a and 100.b, which respectively show the ODS's corresponding to the first two natural frequencies. The end of the low-frequency region is signaled by intra-cell resonance [80], as the wavelength becomes of the order of the core elements' length. Intra-cell resonance is here investigated as the phenomenon responsible for the

complex deformation patterns observed in this class of structures. A selection of deformed configurations featuring intra-cell resonance is shown in figs. 100.c and 100.d. In particular, at the selected frequencies local deformations appear on the constraining layers. This phenomenon then is the focus of the experimental validation, and more generally, of the current study. In particular, it is interesting to observe that the relative phase between the localized deformations can be changed by controlling the excitation frequency.

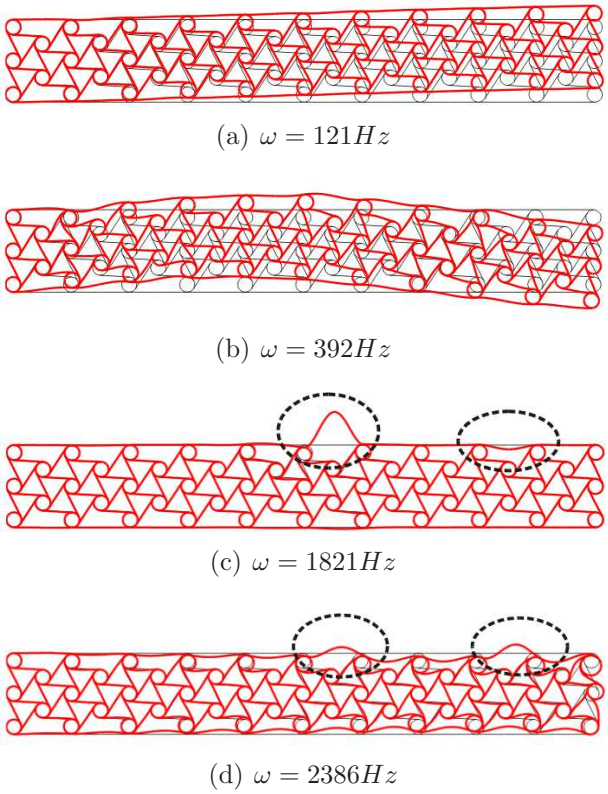

(a) $\omega = 121Hz$

(b) $\omega = 392Hz$

(c) $\omega = 1821Hz$

(d) $\omega = 2386Hz$

Figure 100: Deformed configurations at various excitation frequencies

6.1.5 Experimental set-up

A proof-of-concept truss-core beam has been built with the objective of demonstrating the particular dynamic behavior of chiral assemblies. Geometry and materials for the experimental specimen have been selected with the goal of maintaining simplicity of fabrication while utilizing off-the-shelf components. The radius r of the nodes,

the length of the ribs, and the wall thickness of both ribs and nodes are chosen to allow bending deformation of the ribs with low deformation of the nodes. This is a necessary condition to ensure the peculiar "unfolding" behavior of deformed chiral honeycombs [60, 76]. Both the core ribs and the constraining layers are fabricated from standard alloy 6061 T6 aluminum sheet (Young's modulus $E = 7.0$ GPa, density $\rho = 2700$ Kg/m^3, Poisson's ratio $\nu = 0.33$). The ribs are 2.90 cm long, and have a wall thickness of 0.81 mm, which corresponds to the standard thickness of 0.032 in in aluminum sheets. The nodes are fabricated from aluminum tubing of diameter 1.11 cm (7/16 in), with wall thickness $t = 0.89$ mm (0.035 in). The top and bottom constraining layers are 49.24 cm long and their wall thickness is equal to 0.81 mm. Finally, the out-of-plane thickness of the structure is equal to 2.54 cm. Given these dimensions and the geometry shown in fig. 99, the parameter L becomes equal to 2.59 cm, while the distance between the nodes R is equal to 2.82 cm. Due to the thickness of the ribs, the ratio L/R decreases from a nominal value of 0.919 to 0.892. The complete truss-core beam is composed of 53 nodes and 112 ribs. The overall dimensions of the structure are $L_b = 0.5$ m, and $t_c = 6.9$ cm. The experimental specimen was assembled by first constructing a wooden template to ensure correct positioning of the nodes (fig. 101.a). Finally, the constraining layers and ribs were welded to the nodes using the $\mathbf{3M}$ epoxy adhesive $DP-190$ to obtain the completed assembly shown in fig. 101.b.

The structure is constrained at one end by two vices which rigidly clamp both the core and the constraining layers. The considered measurement setup shown in fig. 102.a consists of the Polytec PSV-400 laser scanning head, the Polytec PSV-400 M2 data acquisition system and signal processing, a LDS V203 shaker, and a 10-*lb* force transducer, mounted on the shaker's stinger. In order to simulate the case of an applied torque, a threaded steel axle is inserted in one of the core nodes, and it is secured to the assembly with nuts. A solid steel plate 2.4 cm long is welded

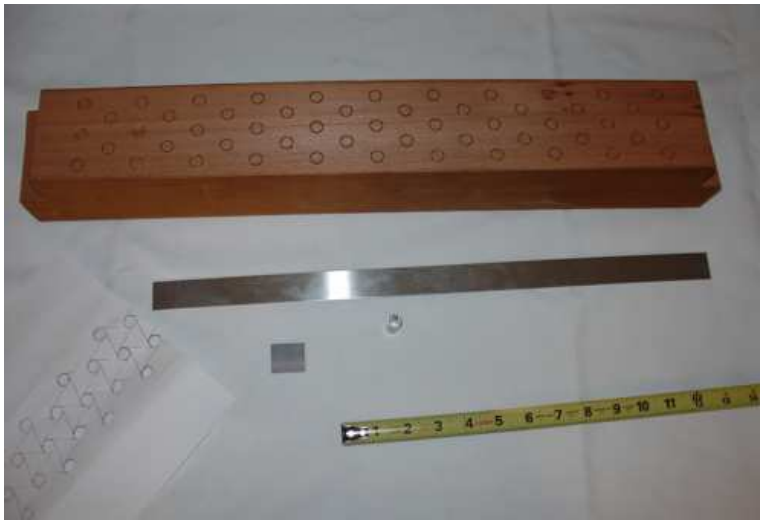

(a)

(b)

Figure 101: Wooden template (a) and completed truss-core assembly (b)

on one end of the steel axle. The shaker then applies a torque to the core of the assembly as shown in fig. 103. Finally, The vibration of the structure is characterized by measuring the velocity of points belonging to a 1281-point measurement grid on the constraining layer facing the laser head.

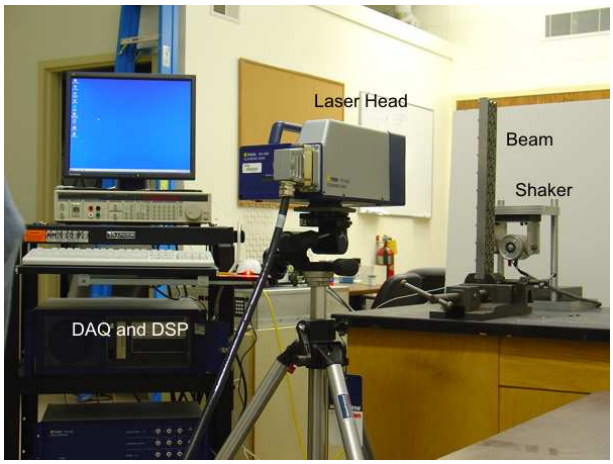

Figure 102: Experimental setup and testing equipment

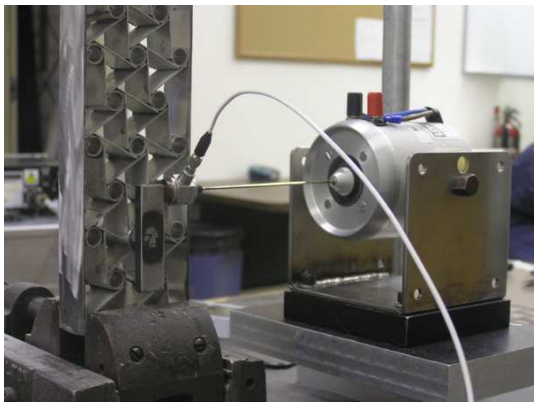

Figure 103: Mechanism for torque actuation at one node

6.1.6 Experimental results

Fig. 104 shows a comparison between measured and analytical operational deflection shapes, at frequencies belonging to the low frequency regime, while figs. 105, show deformations at high frequencies, which present very well marked localized deformations near the free end of the beam, with the rest of the constraining layers nearly

undeformed.

The unique behavior of chiral truss-core beams observed from numerical and experimental analyses shows that, when the excitation frequency is such that wavelengths become of the order of the core components' length, energy is transferred from the location of excitation to specific locations on the constraining layers, without generating global deformations, as shown in figs. 104 and 105. The onset of intra-cell resonance is determined by natural frequencies corresponding to specific geometric and constitutive parameters. This suggests that the actuation frequencies producing localized deformations may be scaled to favor particular operation deflection shapes for a given application. Finally, localized deformations on the constraining layers appear to be a dominant characteristic of the dynamic response of chiral-core assemblies, since two distinct forcing frequencies, for example, produce localized deformations (figs. 105) with opposite phase. This indicates that the onset of different types of local deformations can be simply controlled by changing the excitation frequency.

6.2 Dynamic Shape Control of a Chiral Truss-Core Airfoil

6.2.1 overview

The same FE model developed for the analysis of the static compliance of chiral truss-core airfoils presented in sec. 5.6.1 is employed to investigate the dynamic response of such unusual airfoil configurations. The analysis is however fully linear as only linear modes and related natural frequencies need to be predicted. The model however includes structural details such as fillets between ligaments and nodes which simulate the actual geometry of the manufactured samples.

The three samples depicted in fig. 75 are used for the experimental investigations. As for their corresponding numerical models, the assemblies were clamped at the leading-edge location, and were excited by a dynamic point load at the trailing edge.

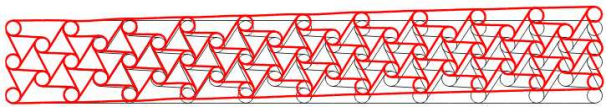

(a) $\omega = 121Hz$

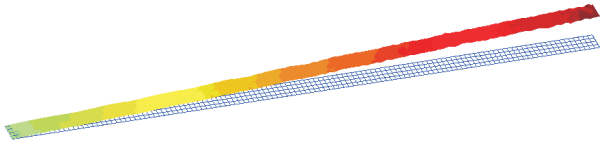

(b) $\omega = 102Hz$

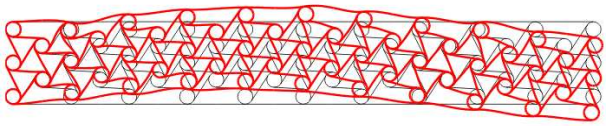

(c) $\omega = 392Hz$

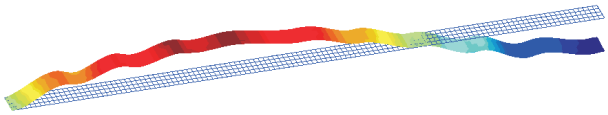

(d) $\omega = 427Hz$

Figure 104: Experimental (b,d) and numerical (a,c) operational deflection shapes

The load varies as a random signal to excite the structure over a broad frequency band. As for the truss-core beam, the scanning laser doppler vibrometer records the structural velocities and extrapolates the corresponding displacements at the top and bottom portion of the *Eppler 420* profile.

6.2.2 Numerical and experimental results

Similarly to the findings presented in [89] and sec. 6.1, the response of chiral, truss-core airfoils in the low frequency regime is characterized by global modes resembling those of a homogeneous cantilever structure. This is evident from the selection of ODSs of two of the *Eppler 420* samples, which have been chosen to illustrate the salient aspects of their dynamic response (see figs. 106 through 109). In each figure the deformed configurations on the left side depict numerical results, while those on the right side correspond to results obtained from the experiments. The first aspect that transpires

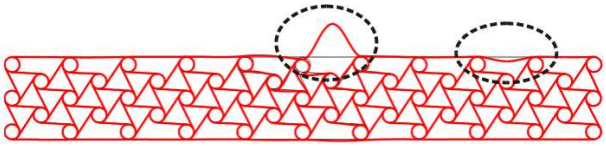

(a) $\omega = 1821Hz$

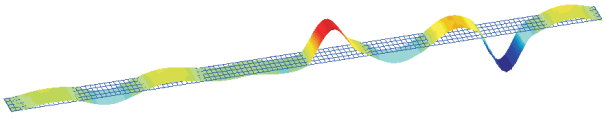

(b) $\omega = 1867Hz$

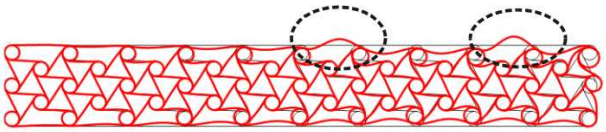

(c) $\omega = 2386Hz$

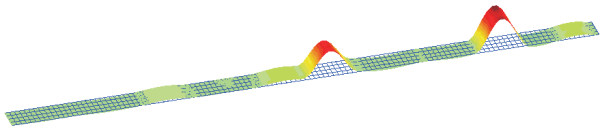

(d) $\omega = 2027Hz$

Figure 105: Experimental (b,d) and numerical (a,c) operational deflection shapes

from the results is the similarity in response corresponding to the first and second natural frequencies among the discussed configurations. All three *Eppler 420* samples demonstrate similar qualitative behavior at low frequencies whereby global deformations dominate the dynamic response. Characteristic localized deformations on the airfoil profile, stemming from the unusual dynamic behavior of the chiral honeycomb as a truss-core, are depicted in figs. 107.a and 109.a. Localized deformations appear in different locations of the airfoil profile depending on configuration and excitation frequency. Worthy of mote, figs. 107.b show clearly the phenomenon of intra-cell resonance, where the truss-core presents much larger dynamic deformations than the airfoil profile. The presented results indicate that localized ODSs are obtained by exciting the airfoil assemblies at various natural frequencies, and suggest the potential application in the field of flow control, where, for example, vortices may be controlled by dynamically exciting the airfoil. Else wave drag may be reduced by exploiting induced shock-wave coalescence as a result of "kinks" appearing on the airfoil profile.

(a) numerical model $\omega = 82.6Hz$ (left), experimental results $\omega = 69Hz$ (right)

(b) numerical model $\omega = 318.7Hz$ (left), experimental results $\omega = 305Hz$ (right)

Figure 106: First and second ODSs for configuration a with 2 cells across the airfoil thickness, and $L/R = 0.60$

(a) numerical model $\omega = 948.9Hz$ (left), experimental results $\omega = 1039Hz$ (right)

(b) numerical model $\omega = 1888.5Hz$ (left), experimental results $\omega = 1844Hz$ (right)

Figure 107: High frequency ODSs for configuration a

(a) numerical model $\omega = 84.9Hz$ (left), experimental results $\omega = 73\ Hz$ (right)

(b) numerical model $\omega = 339.6\ Hz$ (left), experimental results $\omega = 331\ Hz$ (right)

Figure 108: First and second ODS for configuration b with 3 cells across the airfoil thickness, and $L/R = 0.60$

(a) numerical model $\omega = 1528.2Hz$ (left), experimental results $\omega = 1500Hz$ (right)

(b) numerical model $\omega = 1652.7Hz$ (left), experimental results $\omega = 1794Hz$ (right)

Figure 109: High frequency ODSs for configuration b

CHAPTER VII

VIBRATIONS WAVE PROPAGATION IN CHIRAL LATTICES

7.1 Introduction

The response of cellular materials to different operating conditions, wether that be mechanical loading, thermal loading, or electromagnetic loading for example, strongly depends upon their topology or spatial arrangement, providing ample authority in the design of novel structured configurations. In the case of the chiral topology, as transpired from analyses of the static response both in plane and out of plane in chapters 3 and 4 respectively, the topology parameter L/R greatly affects the equivalent mechanical properties. This alone provides ample opportunities to select the best topology for a given task or application. Cellular solids, however, while long known and commonly exploited for disparate uses in traditional engineering applications have recently become the focus of significant research efforts to uncover their dynamic properties.

Periodic cellular materials are defined by the spatial repetition of an irreducible geometric domain or unit cell, and their topology, moreover, strongly affects the propagation characteristics of elastic waves. The periodicity or group of a given lattice, in fact, determines frequency bands within which the propagation of elastic waves is permitted (pass bands) or forbidden (band gaps or stop bands). Anisotropy in the elasto-dynamic behavior of periodic structural assemblies, furthermore, can be exploited to steer or guide waves in specific directions (beaming) [83, 75].

Significant authority afforded by structural lattices - a deterministic subclass of cellular solids - on phenomena such as band gaps and wave-beaming, owing to the

large number of possible configurations and advances in manufacturing capabilities, suggest their employment as alternatives to elastic composites with periodic mass and stiffness modulations, or phononic crystals. The selection of the periodic material distribution in phononic crystals, in particular, is based on the need to generate band gaps at specified frequencies, and/or to guide elastic waves along a desired path [77]. A thorough classification of unit cell classes of periodic cellular structures and associated elasto-dynamic behavior, already undertaken by [83, 75] for such topologies as the hexagonal, triangular, and Kagomé lattices to name a few, may provide the possibility of designing structured materials with easily selectable wave-propagation behavior.

The unique characteristics of phononic materials are currently exploited in a number of applications which include sensing devices based on resonators, acoustic logic ports, wave-guides and filters based on surface acoustic waves (SAW). Synthesis of phononic materials with desired band-gap and wave-guiding characteristics has achieved promising maturity, mostly through the application of topology and material optimization procedures [51, 85, 50]. Although very effective, such techniques may require intensive computations and may lead to complex geometries difficult to manufacture and whose performance may lack in robustness. The application of periodic structural networks as phononic materials may potentially lead to a simplified design process, where a limited number of continuously varying parameters defines the geometry of a predefined cellular topology [23]. The successful application of this approach clearly requires identifying lattice configurations that provide sufficient design flexibility, as well as with strongly dependent elasto-dynamic properties upon a limited number of geometric parameters defining the lattice configuration.

This observation motivates the investigation of the wave propagation characteristics of the chiral structural lattice considered here. The design flexibility and the unique properties of this cellular configuration, originally proposed by [76, 100], are documented in a number of recent papers by the authors [89, 90], are here evaluated

in terms of wave propagation characteristics with the intent of broadening the already promising features offered by more traditional configurations such as triangular and hexagonal lattices proposed by [83, 75]. The influence of the unit-cell configuration on band-gaps and wave-guiding properties is investigated through a numerical model constructed considering chiral cellular topologies as assemblies of beams connected to form a frame structure. Specifically, a compact description of the dynamic behavior of the chiral assembly is provided by an elasto-dynamic discretization based on Timoshenko beam elements [19]. Finally Bloch Theorem is employed to obtain dispersion surfaces, band diagrams, and to investigate the dependency of group speeds and phase velocities on frequency and direction of wave propagation. The findings presented in the following sections reveal a unique wave-propagation behavior featuring a surprisingly high band-gap density as well as strong energy focusing dependent on frequency and wavenumber. Such intriguing properties suggest the chiral topology to be a basis for the development of meta-materials gaining their properties from the targeted design of their periodic structure.

7.2 Analysis of Free Wave Propagation

7.2.1 Bloch Theorem

The characteristics of elastic wave propagation in structural lattices can be determined by employing Bloch theorem [12]. The displacement $\boldsymbol{w}$ of a point P of the reference unit cell corresponding to a wave propagating at frequency ω can be expressed as:

$$\boldsymbol{w}(\boldsymbol{r}_P) = \boldsymbol{w}_{P_0} e^{i\omega t - \boldsymbol{k}\cdot\boldsymbol{r}_P} \ , \tag{111}$$

where $\boldsymbol{w}_{P_0}$ is the wave amplitude, and $\boldsymbol{k}$ is the wave vector. According to Bloch theorem, the displacement of the point corresponding to P at location $\boldsymbol{\rho}_p(n_1, n_2)$ can

be written in terms of the displacement of the reference unit cell as follows:

$$\begin{aligned} \boldsymbol{w}(\boldsymbol{\rho}_P) &= \boldsymbol{w}(\boldsymbol{r}_P) e^{\boldsymbol{k}\cdot(\boldsymbol{\rho}_P - \boldsymbol{r}_P)}, \\ &= \boldsymbol{w}(\boldsymbol{r}_P) e^{n_1 k_1 + n_2 k_2} \ , \end{aligned} \tag{112}$$

where $k_i = \boldsymbol{k}\cdot\boldsymbol{e}_i$ with $i = 1, 2$. Bloch theorem, as described by eq. 112, states that the proportionate change in wave amplitude occurring from cell to cell does not depend on the cell location within the periodic system. The wave propagation characteristics of the periodic assembly thus can be fully identified through the analysis of the reference unit cell. In eq. (112), $k_i = \delta_i + i\epsilon_i$ $(i = 1, 2)$ is a complex number, whose real part δ_i defines the amplitude attenuation as a wave propagates from one cell to the next, and it is known as *attenuation constant*. The imaginary part ϵ_i defines the change of phase across each cell, and it is often called *phase constant*. In the analysis of wave propagation without amplitude attenuation, δ_i is typically set to 0, and attention is devoted to determining the relation between phase constants ϵ_i and temporal frequency ω.

7.2.2 Reciprocal lattice and first Brillouin zone

Given the direct lattice space defined by the lattice vector basis $\mathcal{E} = (\boldsymbol{e}_1, \boldsymbol{e}_2)$, one may define a reciprocal lattice, which is described by the basis $\mathcal{B} = (\boldsymbol{b}_1, \boldsymbol{b}_2)$, whose basis vectors are given by:

$$\boldsymbol{b}_i \cdot \boldsymbol{e}_j = \delta_{ij}, \tag{113}$$

where δ_{ij} is the Kronecker delta. The reciprocal lattice vectors for the considered periodic chiral assembly are given by:

$$\begin{aligned} \boldsymbol{b}_1^{\mathfrak{I}} &= \left(\ \tfrac{1}{2R\cos\theta}, \quad \tfrac{1}{2(R\sin\theta)} \ \right)^T, \\ \boldsymbol{b}_2^{\mathfrak{I}} &= \left(\ -\tfrac{1}{2R\cos\theta}, \quad \tfrac{1}{2(R\sin\theta)} \ \right)^T. \end{aligned} \tag{114}$$

In the reciprocal lattice, the wave vector $\boldsymbol{k} = 2\pi\boldsymbol{\lambda}$ can be expressed as:

$$\boldsymbol{k} = k_1\boldsymbol{b}_1 + k_2\boldsymbol{b}_2, \tag{115}$$

so that, according to the definition of reciprocal lattice given in eq. (113):

$$\boldsymbol{k} \cdot \boldsymbol{e}_1 = k_1. \tag{116}$$

While the direct lattice defines the spatial periodicity of the considered domain, the reciprocal lattice describes the periodicity of the frequency-wavenumber relation. This can be easily demonstrated by replacing $\boldsymbol{p}$, where $\boldsymbol{k} = 2\pi\boldsymbol{p}$, with $\boldsymbol{p}' = \boldsymbol{p} + m_1\boldsymbol{b}_1 + m_2\boldsymbol{b}_2$ in eq. (112), with m_1, m_2 integers to obtain:

$$\boldsymbol{w}(\boldsymbol{\rho}_p) = \boldsymbol{w}(\boldsymbol{r}_p)e^{n_1 k_1' + n_2 k_2'}, \tag{117}$$

where

$$k_i' = 2\pi\boldsymbol{p}' \cdot \boldsymbol{e}_i = k_i + 2\pi m_i, \quad i = 1, 2. \tag{118}$$

Eq. (118) indicates that the wavenumber in a 2-D lattice is a periodic function of the wave vector $\boldsymbol{k}$ in the reciprocal lattice. Hence, full representation of the dependency of the wave-vector upon frequency is obtained by investigating its variation over a single period. In a 2-D lattice, the period corresponds to a region in the reciprocal lattice whose area equals the area of the reciprocal lattice's unit cell, known as *first Brillouin zone*. Given the reciprocal lattice vectors, the first Brillouin zone is obtained by selecting any point in the reciprocal lattice as the origin and by connecting it to all neighboring points. The perpendicular bisectors constructed on the connecting lines, also known as *Braggs lines*, define the first Brillouin zone [12]. Fig. 110 shows the reciprocal lattice vectors and the first Brillouin zone in the cartesian frame and in the reciprocal lattice space. The symmetry of the first Brillouin zone can be utilized to identify a subregion, known as *irreducible Brillouin zone*, which is the smallest frequency-wavenumber space necessary to determine wave dispersion for a given lattice. The irreducible Brillouin zone for the chiral lattice is also highlighted in fig. 110, while the coordinates of the points OAB defining its boundaries are listed in Table 9.

Table 9: Coordinates of corner points of the irreducible Brillouin zone for chiral lattices

	Cartesian frame	*Reciprocal lattice frame*
O	(0, 0)	(0, 0)
A	$(\frac{-1}{2R\cos\theta}, 0)$	$(\text{-}\frac{1}{2}, \frac{1}{2})$
B	$(\frac{-1}{R\cos\theta}, \frac{1}{6R\sin\theta})$	$(\text{-}\frac{1}{3}, \frac{2}{3})$

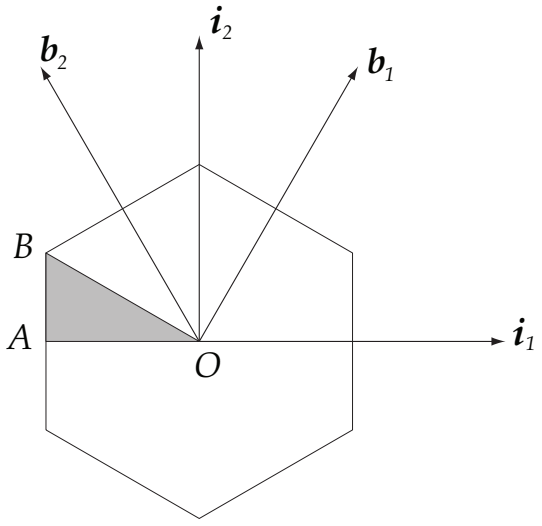

(a)

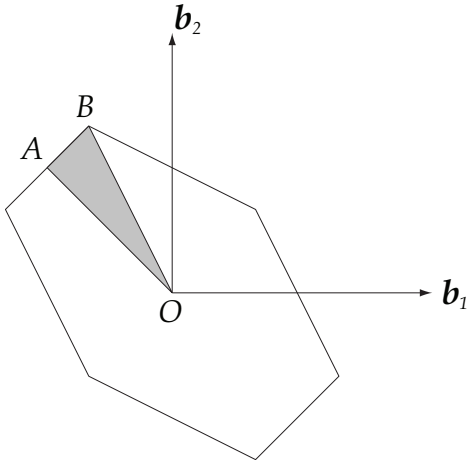

(b)

Figure 110: First and irreducible Brillouin zones and reciprocal lattice vectors in cartesian and reciprocal lattice spaces

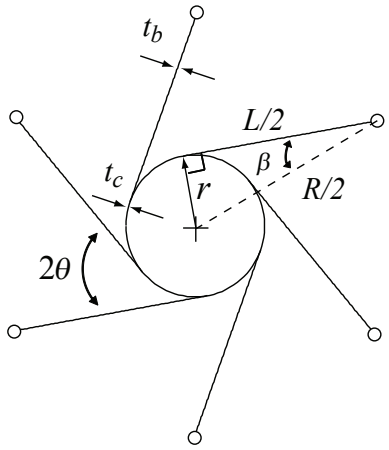

Figure 111: Chiral lattice unit cell with associated geometric parameters

7.2.3 Discretized equation of motion for the unit cell

The behavior of the unit cell can be conveniently described through a discretized equation of motion in matrix form, and by defining the cell's interaction with its neighbors (fig. 112). The unit cell depicted in fig. 111 is modeled via finite element discretization whereby components of the unit cell are treated as rigidly connected beams featuring axial, transverse, and rotational DOF's, whose behavior is governed by Timoshenko beam theory [19]. Application of standard finite-element procedures [19] yields the unit cell's equations of motion, which can be expressed as:

$$\Big(\boldsymbol{K} - \omega^2 \boldsymbol{M}\Big)\boldsymbol{u} = \boldsymbol{f}, \tag{119}$$

where ω is the frequency of wave propagation, $\boldsymbol{K}$ and $\boldsymbol{M}$ are the global mass and stiffness matrices of the cell, while $\boldsymbol{u}$, $\boldsymbol{f}$ are respectively the vectors containing generalized nodal displacements and forces of interaction of the cell with its neighbors, defined as:

$$\begin{aligned} \boldsymbol{u} &= \{\ \boldsymbol{u}_0 \quad \boldsymbol{u}_1 \quad \boldsymbol{u}_2 \quad \boldsymbol{u}_3 \quad \boldsymbol{u}_4 \quad \boldsymbol{u}_5 \quad \boldsymbol{u}_i\ \}^T, \\ \boldsymbol{f} &= \{\ \boldsymbol{f}_0 \quad \boldsymbol{f}_1 \quad \boldsymbol{f}_2 \quad \boldsymbol{f}_3 \quad \boldsymbol{f}_4 \quad \boldsymbol{f}_5 \quad \boldsymbol{0}\ \}^T. \end{aligned} \tag{120}$$

In eq. (120) the subscripts $0, 1, \cdots, 5$ follow the notation described in fig. 112, while

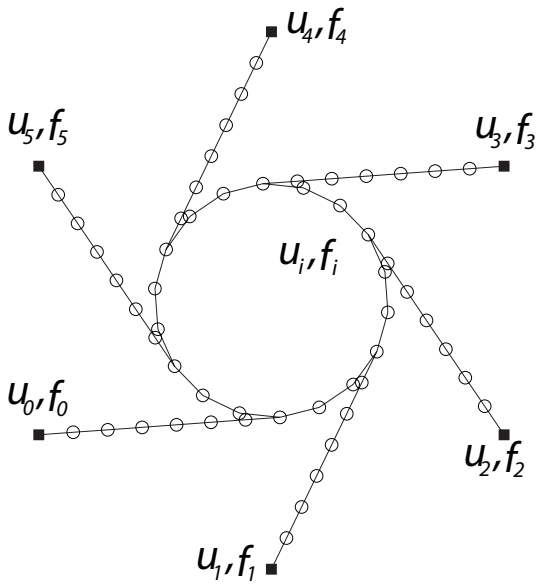

Figure 112: Unit cell discretization and detail of internal and boundary degrees of freedom and interaction forces

subscript i denotes the degrees of freedom of internal cell nodes. Fig. 112 also shows the considered unit cell discretization, highlights the internal nodes (white circles), and lists boundary nodes and forces (dark squares). The considered cell discretization approximates the circles as a sequence of straight beams, avoiding the complexity associated with a finite element discretization of curved elements [7], and has been chosen based on convergence studies performed on the dispersion relations in the frequency range considered relevant for the analysis presented in what follows. A detailed description of this convergence study is here omitted for the sake of brevity. The proposed discretization, moreover, captures up to 198 wave modes, while the current analysis only considers wave modes up to the 20^{th} thus avoiding numerical error at high-frequencies due to spatial or nodal sampling. Finally, eq. (120) relies on the assumption that no external forces are applied, and that only the interaction forces with neighboring cells appear in the cell's equation of motion.

7.2.4 Evaluation of dispersion relations

According to Bloch theorem, periodic boundary conditions relate the cell's generalized displacements, while equilibrium conditions are enforced to the generalized forces applied to consecutive cells:

$$\begin{aligned} \boldsymbol{u}_3 &= e^{k_1}\boldsymbol{u}_0, \\ \boldsymbol{u}_4 &= e^{k_1+k_2}\boldsymbol{u}_1, \\ \boldsymbol{u}_5 &= e^{k_2}\boldsymbol{u}_2, \end{aligned} \tag{121}$$

and

$$\begin{aligned} \boldsymbol{f}_3 &= -e^{k_1}\boldsymbol{f}_0, \\ \boldsymbol{f}_4 &= -e^{k_1+k_2}\boldsymbol{f}_1, \\ \boldsymbol{f}_5 &= -e^{k_2}\boldsymbol{f}_2. \end{aligned} \tag{122}$$

Eq's. (121) and (122) can be rewritten in matrix form as follows:

$$\boldsymbol{u} = \boldsymbol{T}_u\,\boldsymbol{u}_r, \tag{123}$$

$$\boldsymbol{f} = \boldsymbol{T}_f\,\boldsymbol{f}_r, \tag{124}$$

where $\boldsymbol{u}_r = \{\ \boldsymbol{u}_0 \quad \boldsymbol{u}_1 \quad \boldsymbol{u}_2 \quad \boldsymbol{u}_i\ \}^T$, and $\boldsymbol{T}_f = \boldsymbol{T}_u^T$. Substituting eq. (121) into eq. (119), and pre-multiplying the resulting equations by T_u^H, with $()^H$ denoting a complex conjugate transpose, yields:

$$\left[\boldsymbol{K}_r(k_1,k_2) - \omega^2\boldsymbol{M}_r(k_1,k_2)\right]\boldsymbol{u}_r = \boldsymbol{0}, \tag{125}$$

where $\boldsymbol{K}_r(k_1,k_2)$, $\boldsymbol{M}_r(k_1,k_2)$ are reduced stiffness and mass matrices. Eq. (125) constitutes an eigenvalue problem whose solution defines the dispersion characteristics of the lattice. Its solution requires imposing two of the three unknowns k_1, k_2, ω, and solving for the third. In the current approach, wave motion without attenuation is investigated. Accordingly, k_1, k_2 are generally imposed as imaginary numbers

$k_1 = i\epsilon_1$, $k_2 = i\epsilon_2$ which vary within the first Brillouin zone. The solution of eq. (125) yields the frequency of wave propagation, corresponding to the assigned pair k_1, k_2. Solutions obtained for k_1, k_2 spanning the entire first Brillouin zone define the dispersion surfaces of the lattice, here denoted as $\omega = \omega(k_1, k_2)$. The number of surfaces obtained corresponds to the dimensions of the eigenvalue problem in eq. (125), which in turn, is defined by the number of reduced DOF's $\boldsymbol{u}_r$. Each surface describes the wavenumber-frequency relation for the corresponding wave mode.

7.2.5 Phase speeds and group velocities.

Dispersion surfaces allow the evaluation of phase and group velocities and their dependency on frequency and direction of propagation. The wave vectors in the reciprocal and geometric space are respectively expressed as:

$$\boldsymbol{k} = k_1\boldsymbol{b}_1 + k_2\boldsymbol{b}_2 = \xi_1\boldsymbol{i}_1 + \xi_2\boldsymbol{i}_2.$$

The phase velocity at a given frequency ω is given by:

$$\boldsymbol{c}_{ph} = \frac{\omega}{k}\boldsymbol{u}, \tag{126}$$

where $k = |\boldsymbol{k}|$ and $\boldsymbol{u}$ is a unit vector in the direction of the wave vector ($\boldsymbol{u} = \boldsymbol{k}/k$). The information provided by the phase velocity is essentially the same as that obtained from constant-frequency contours of the dispersion surfaces. In fact, for non-dispersive media, the two representations can be combined in the form of *slowness curves* [3]. In the case of periodic lattices, useful information is provided by direct representation of the phase speed. Such description elucidates the increasingly dispersive and orthotropic nature of wave propagation as frequency ω increases. The phase speed c_{ph} is evaluated by selecting iso-frequency contours from dispersion surfaces at a desired frequency value. The angular range spanned by the corresponding set of wavenumbers is then computed to obtain the angular variation of the phase speed in terms of direction. For a general non-dispersive, isotropic medium, this operation yields a circle whose radius is independent of frequency.

Important indications regarding the energy flow associated with the propagation of wave packets within the lattice are provided by the group velocity, which can be evaluated as follows:

$$\boldsymbol{c}_g^{\mathcal{I}} = \left(\begin{array}{cc} \frac{\partial \omega}{\partial \xi_1}, & \frac{\partial \omega}{\partial \xi_2} \end{array} \right)^T. \tag{127}$$

The group velocity defines the direction of energy flow within the structure, and can be used to identify preferential or forbidden directions of wave propagation [83]. Such forbidden propagation zones are the result of interference phenomena resulting from the propagation of waves at the same frequency and different wave-vector directions, and can be observed over a broad range of frequencies in anisotropic materials and structures [101]. Results presented in the following sections will show how dispersion and anisotropy in chiral lattices strongly influence the characteristics of wave propagation particularly as frequency increases.

7.3 Results

Results reported in the current and following sections consider a lattice made of aluminum (Young's modulus $E = 71$ GPa, Poisson's ratio $\nu = 0.33$, and density $\rho = 2700$ Kg/m^3). A reference configuration defined by the geometric dimensions listed in Table 10 is first employed to present salient characteristics of wave propagation in a chiral lattice. The same reference configuration is also employed in subsequent parametric studies to highlight the influence of geometric arrangement on wave propagation characteristics of chiral lattices. Results are presented in terms of the non-dimensional frequency Ω:

$$\Omega = \frac{\omega}{\omega_0}, \tag{128}$$

where:

$$\omega_0 = \pi^2 \sqrt{\frac{E t_b^2}{12 \rho L^4}}, \tag{129}$$

corresponds to the first flexural frequency of a ligament of length L assumed in a simply supported configuration. Although simple supports do not reproduce the

Table 10: Reference lattice dimensions

Parameter	*Value*
Ligament length	$L = 26.4$ mm
Ligament wall thickness	$t_b = 0.5$ mm
Node radius	$r = 6.4$ mm
Node wall thickness	$t_c = 0.5$ mm
Slenderness ratio	$t_b/L = 1/52$
Topology parameter	$L/R = 0.90$

actual boundary conditions on the ligaments, the expression of ω_0 has been selected as a reference measure of frequencies at which the internal members of the lattice undergo resonance, and for which the dynamic deformations of the lattice are dominated by local behavior.

7.3.1 Dispersion surfaces

Fig. 113 presents contours of dispersion surfaces corresponding to the first four wave modes of the lattice defined by the dimensions in Table 10. The first Brillouin zone, represented in fig. 113 is superimposed to the iso-frequency contours to highlight the correctly captured periodicity of the frequency-wavenumber spectrum. Furthermore, the irreducible Brillouin zone, depicted in fig. 113 as a shaded gray area, effectively describes all the characteristics of dispersion by taking advantage of the symmetry present in the the first Brillouin zone.

The hexagonal symmetry of the chiral lattice clearly transpires in the elasto-dynamic response represented in fig. 113, where six-lobed contour curves denote the dispersion relations of all considered wave modes, a feature that becomes more apparent as frequency increases. A very interesting attribute of the first two wave modes, moreover, is provided by the "leveling-off" of the dispersion surfaces which appear to change rapidly at low frequencies, and become virtually flat as frequency increases. This behavior is indicated by the presence of a large number of iso-frequency contour lines at low wavenumbers, and by their much lower density towards the edges of the

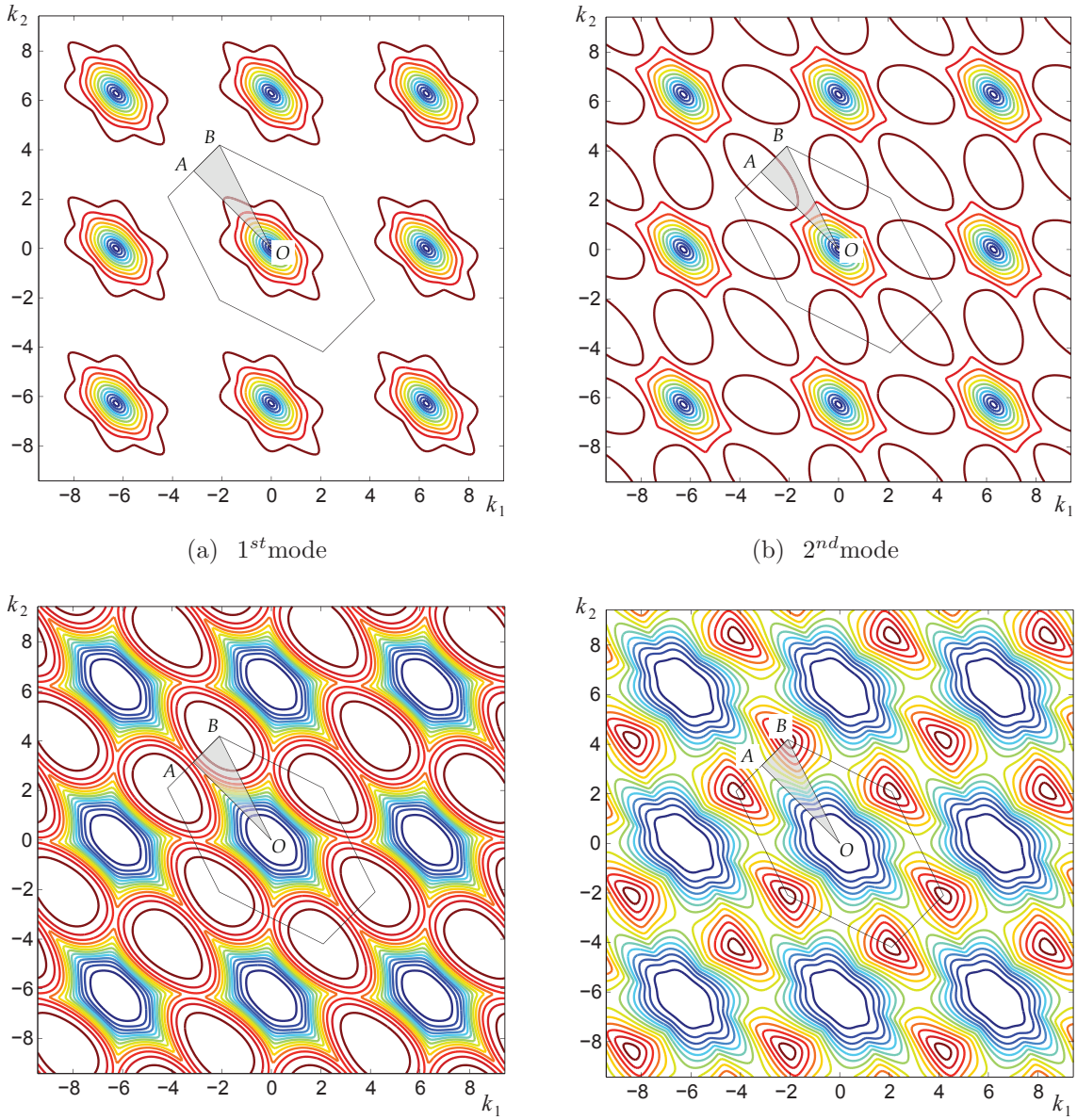

(a) 1^{st}mode

(b) 2^{nd}mode

(c) 3^{rd}mode

(d) 4^{th}mode

Figure 113: Iso-frequency contours of the dispersion surfaces and detail of first and irreducible Brillouin zone

first Brillouin zone (see figs. 113.a and b). The opposite happens for the third and fourth modes, which are characterized by rapid changes at high wavenumbers and almost flat surfaces around $k_1, k_2 \approx 0$ (see figs. 113.c and d). This implies that the wave speeds associated with wave modes 3 and 4 change significantly within the first Brillouin zone. The low wavenumber behavior of the dispersion surfaces is illustrated in fig. 114, which presents dispersion relations in terms of the wave-vector components in the cartesian frame ξ_1, ξ_2. As previously noted for the reciprocal lattice space (fig. 113), the same information displayed in a cartesian frame (fig. 114) confirms the hexagonal symmetry of the considered geometry. Finally, the circular iso-frequency contour curves associated with low frequency and wave number depicted in figs. 114.a and 114.b. suggest isotropic elasto-dynamic behavior of the chiral lattice in the first and second wave-modes.

7.3.2 Band diagrams

A convenient representation of the chiral lattice dispersion characteristics is provided in the form of band diagrams, whereby the frequency of wave propagation is plotted against the amplitude of the wave vector as it varies along the contours of the irreducible Brillouin zone. Fig. 115 compares the band diagram for the reference lattice specified in Table 10 with that of a lattice defined by a topology parameter $L/R = 0.60$ (see fig. 18). The remaining parameters are retained as for Table 10. In order to maintain the ligament length L unchanged, variations in the topology parameter are made to coincide with variations in the distance between the node centers R, and node radius r.

The band diagram associated with topology parameter $L/R = 0.90$ (fig. 115.a) highlights very interesting characteristics, some of which confirm the conclusions made from the analysis of the dispersion surfaces. Namely, the curve corresponding to the third mode appears almost flat, which implies that wave packets of this particular

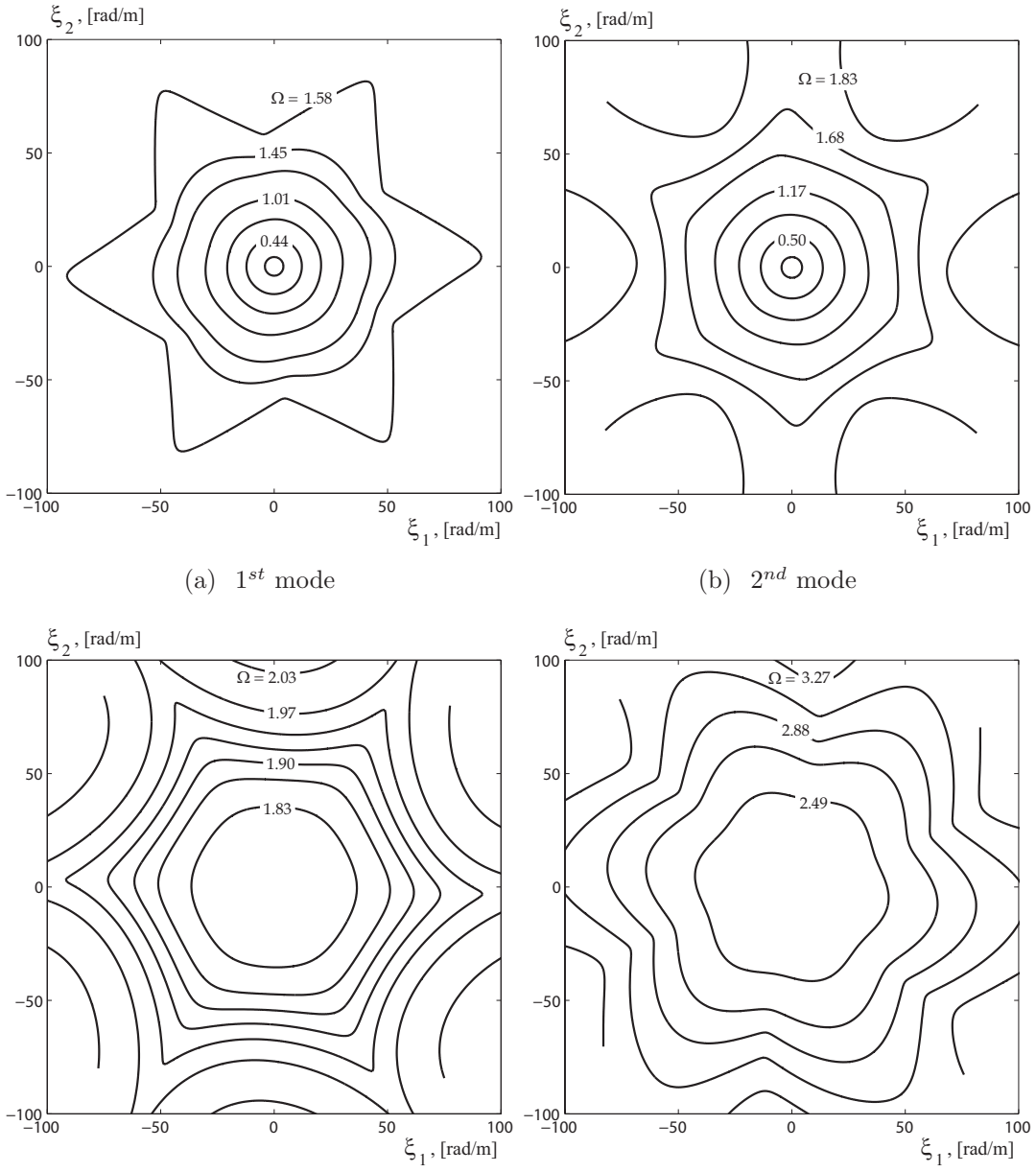

(a) 1^{st} mode

(b) 2^{nd} mode

(c) 3^{rd} mode

(d) 4^{th} mode

Figure 114: Low frequency detail of the dispersion surfaces represented in terms of wavenumbers in the cartesian space

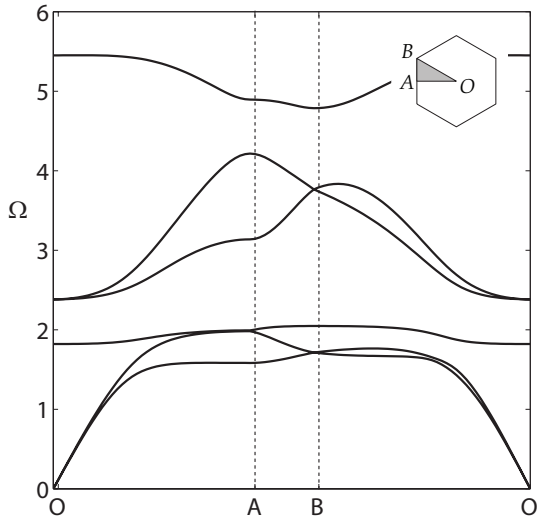

(a) $L/R = 0.90$

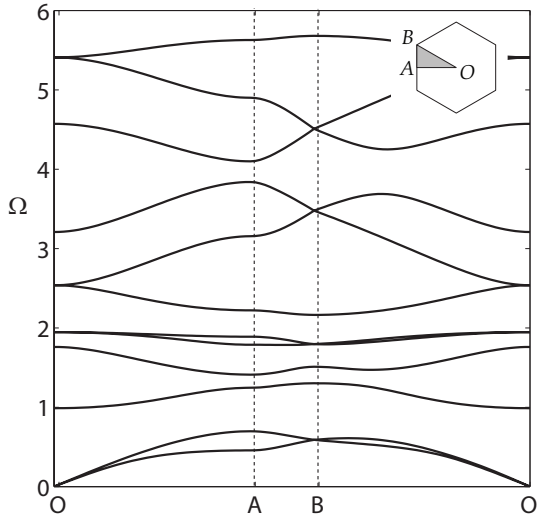

(b) $L/R = 0.60$

Figure 115: Band diagrams for $L/R = 0.90$ and $L/R = 0.60$ lattices

polarization propagate very slowly within the lattice, and may have a behavior which is closer to that of standing waves over most of the wavenumber spectrum. The two lowest modes, typically associated to P (longitudinal) and S-polarized (transverse) modes in solid materials, are approximately non-dispersive up to $\Omega \approx 1$. This is common in most cellular structures, and it is often used as the basis for the quasi-static approximation of their equivalent mechanical properties [75, 41]. In [75], for example, it is shown how the equivalent shear and bulk moduli for hexagonal and triangular lattices can be obtained through the following relations:

$$c_P = \sqrt{\frac{G^* + K^*}{\rho^*}}, \quad c_S = \sqrt{\frac{G^*}{\rho^*}}, \tag{130}$$

where c_P, c_S respectively denote the long-wavelength approximations of the phase speeds of P and S waves, while G^*, K^*, ρ^* are the equivalent shear and bulk moduli, and equivalent density of the lattice. These relations are based on the expressions of the phase speeds of an isotropic elastic medium in plane stress. In fig. 115.a., the first two modes within the non-dispersive range appear practically overlapped, which indicates that the two modes propagate virtually at the same phase speeds, i.e. $c_P \approx c_S$. The assumption that in the low frequency range the chiral lattice behaves according to the laws of two-dimensional elasticity for an isotropic medium would lead to the conclusion that $G^* >> K^*$, which would seem to confirm the results from previous investigations predicting an in-plane Poisson's ratio $\nu \approx -1$ [76]. It is however important to underline that, due to the lattice topology producing non-central forces [60] as well as rotation of the nodes or circles, the two-dimensional equations of elasticity for isotropic materials in plane stress may not accurately describe the equivalent behavior of the lattice, even at long wavelengths. The consideration of higher order elasticity models, such as micropolar continuum theories, may be needed in order to capture nodal rotations and their effect on the mechanical properties of the structure [60]. Homogenized mechanical properties for chiral lattice configurations similar to the one analyzed in the current work have been analyzed in [44] using

flexural-hinging-stretching models based on the approach formulated by [66]. Chiral lattices considered by [44] present a transversely isotropic, elasto-static behavior, confirming that structural chirality has no effect on the elasto-static properties of a material [60]. In-plane orthotropic, elasto-static properties, however, also characterize chiral tessellations of order n, where n denotes the number of ligaments connecting nodes or circles [44]. In contrast to analytical analyses appeared in the literature so far [44, 76], the current FE model features nodes or circles with in-plane flexural and axial deformation behavior capturing anisotropic elasto-static/dynamic behavior related to the first-order moduli of elasticity [10]. The identification of equivalent mechanical properties for the lattice through the asymptotic analysis of the dispersion relations goes beyond the scope of the present work and is the subject of current investigations.

An additional feature of the chiral lattice defined by $L/R = 0.90$ transpiring from the band diagram of fig. 115.a is the presence of two large band gaps, centered approximately at $\Omega = 2.1$ and $\Omega = 4.5$, which suggests the considered lattice configuration as a superior phononic meta-material than what would be possible by employing other known geometries. Among the configurations investigated by [75], in fact, the triangular lattice was the only arrangement to feature a band gap at low frequencies. The chiral lattice, hence, appears as a superior candidate at least for applications requiring stop-band capabilities, in that it features low-frequency band gaps of considerable extent. A comparison of the chiral and triangular lattices (the latter obtained by letting $L/R \rightarrow 1$) is provided by the parametric studies presented in the following sections.

Fig. 115.b shows the band diagram of a lattice characterized by a ratio $L/R = 0.60$. The changes in modal structure, modal density and band-gap location are very evident, demonstrating how a single configurational parameter strongly affects the dispersion characteristics of the lattice. The $L/R = 0.60$ lattice, in particular, is

characterized by a low-frequency band gap, which separates the first two branches from the third. In addition, the slope of the first two branches and the corresponding wave velocities are significantly lower than for the $L/R = 0.90$ lattice.

An attempt to explain the occurrence of band gaps between different sets of dispersion branches as the geometry of the lattice varies can be undertaken through the analysis of the associated wave modes shown in fig. 116. Fig. 116.a. displays the modes corresponding to the first five dispersion branches of the $L/R = 0.90$ lattice, calculated at the vertices O, A, and B of the irreducible Brillouin zone. The first and second mode at O correspond to a rigid-body mode, while the modes associated with locations A and B show how propagation for these polarizations occurs mostly through bending of the ligaments. The third mode is characterized by rotation of the circular node, while the fifth mode is the first for which relevant deformations of the circle can be observed. In particular, the mode at A corresponds to the lower bound of the second band gap which suggests how its occurrence may be related to relevant deformations of the circles within the unit cell. The fourth mode is not presented due to its lack of distinctive features and for the sake of brevity. Wave modes associated with $L/R = 0.60$ and depicted in fig. 116.b. seem to confirm the notion that the generation of the lowest band gap is mostly associated with significant internal deformations of the circles. Such deformations are evident for the second mode at A, which corresponds to the lower limit of the first band gap of the $L/R = 0.60$ lattice. This behavior also suggests that the circles may behave as internal inclusions in the lattice and that their stiffness and mass may be properly selected to achieve desired band-gap characteristics.

Band-gap occurrence estimated via unit cell analysis is verified by computing the harmonic response of lattices of finite extent for frequencies of excitation varying within the range considered in the band diagrams of fig. 115. The lattices comprise 13×17 chiral unit cells, and they are considered as simply supported along their edges.

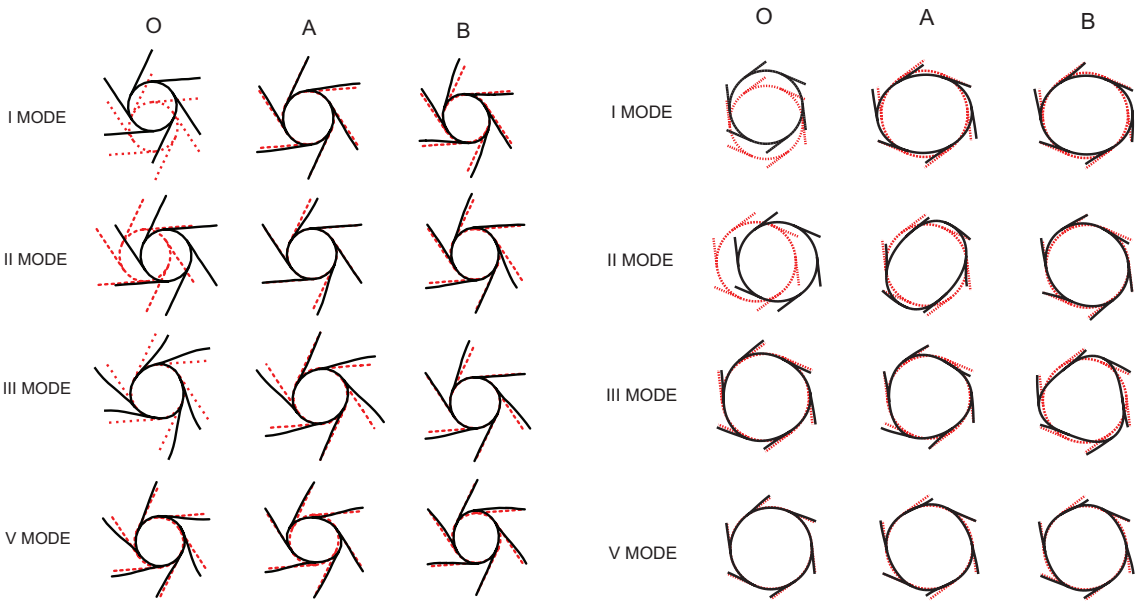

(a) $L/R = 0.90$ (b) $L/R = 0.60$

Figure 116: First, second, third and fifth wave modes at vertices O, A, and B of the *irreducible Brillouin zone*

A harmonic load is applied at the center of the lattice according to the configuration shown in fig. 117. The same discretization and finite-element formulation used for the unit cell analysis are employed for the generation of the discretized model of the finite lattice. The resulting finite-element model predicts the lattice displacements at nodal locations, whose root mean square sum is computed to estimate the response characteristics of lattices of finite extent at various frequencies. The results for the two lattices ($L/R = 0.90$ and $L/R = 0.60$) clearly show the presence of band gaps, at the frequencies predicted by the unit cell analysis and demonstrate the corresponding strong filtering effects on the response of the finite lattice (fig. 118).

7.3.3 Influence of unit cell geometry on band gaps.

The results presented in the previous section suggest the need for an investigation of the influence of unit cell geometry on width and location of possible band gaps. Specifically, attention is devoted to the effects of node wall thickness t_c and of the

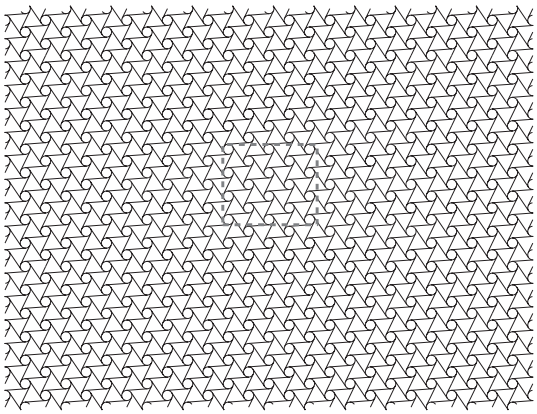

(a)

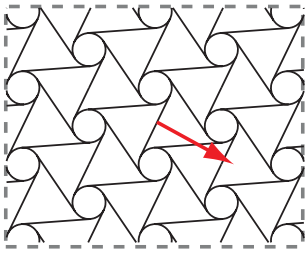

(b)

Figure 117: Configuration of finite lattice for evaluation of harmonic response and detail of loading configuration

topology parameter L/R. Both parameters affect the relative density of the lattice, defined as follows:

$$\frac{\rho*}{\rho} = \frac{2\sqrt{3}}{3}\frac{(2\pi r t_c + 3Lt_b)}{R^2}. \tag{131}$$

The relation between stiffness and mass of the circles and of the ligaments strongly affects the location and extent of band gaps. An obvious way to specify stiffness and mass of the circles is to change their wall thickness t_c, while reducing the L/R ratio corresponding to an increase in the radius r, and in turn to a reduction in the bending stiffness. figs. 119 and 120 show how the relative density is affected by t_c and L/R, where the subscript $'o'$ is used to denote the dimensions of the lattice listed in Table 10 used as a reference in the parametric studies to follow.

The extent and location of band gaps, as related to circle wall thickness, is evaluated for two lattices defined by $L/R = 0.60$ and $L/R = 0.90$. The results in fig. 121,

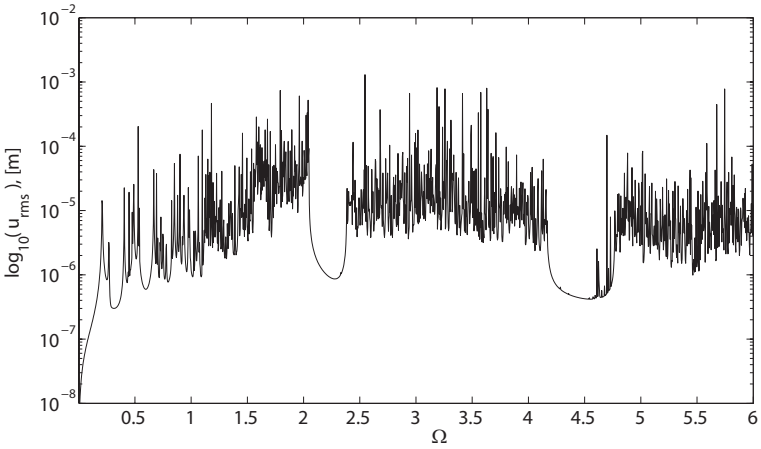

(a) $L/R = 0.90$

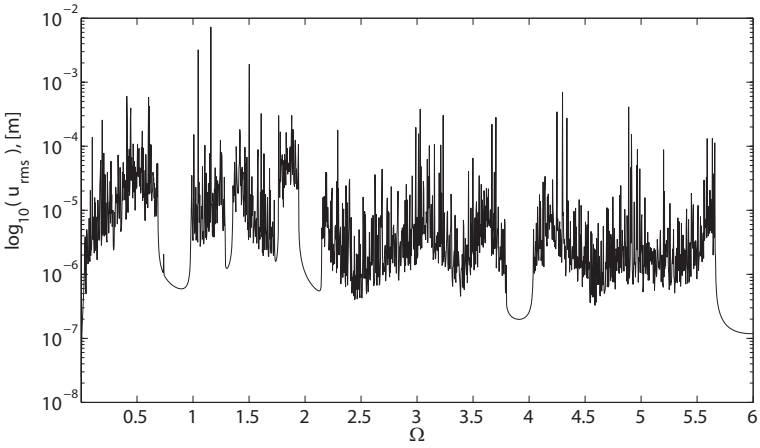

(b) $L/R = 0.60$

Figure 118: Root mean square response of finite lattices subjected to harmonic loads

where band gaps are represented as dark regions, show large sensitivity of the elastodynamic behavior of chiral lattices with respect to the circles' wall thickness t_c. This indicates t_c is a crucial design parameter which can be properly selected to obtain band gaps at desired frequencies. It is interesting to observe how large band gaps at higher frequencies appear as having a center frequency which increases with t_c. This suggests that the resulting added stiffness of the nodes causes their bending deformation to occur at higher frequencies, and confirms how this is a leading mechanism for band gap occurrence (see fig. 116). Finally, the first gap for $L/R = 0.90$ lattice

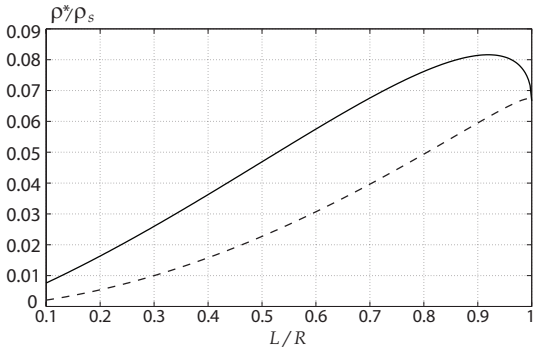

Figure 119: Relative-density dependence upon L/R, - - - $t_c/t_{c_0} = 0.2$, — $t_c/t_{c_0} = 1$

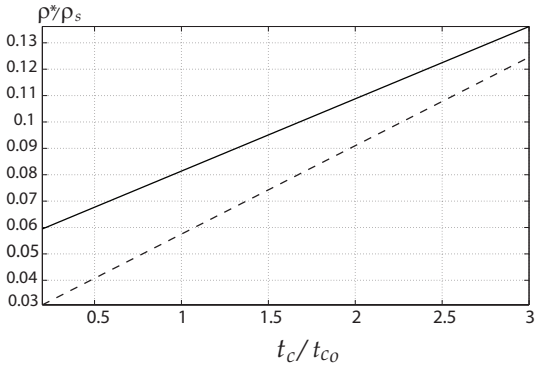

Figure 120: Relative-density dependence upon t_c/t_{c_0}, - - - $L/R = 0.90$, — $L/R = 0.60$

appears to become independent upon t_c for $t_c/t_{c_0} > 1$, which may indicate that the increase in stiffness is counterbalanced by the corresponding increase in mass.

A second study considers the dependence of band gaps upon topology parameter L/R. Results for two values of wall thickness are presented in fig. 122. Specifically, results in fig. 122.a are obtained for the minimum value of the previously considered t_c range, i.e. $t_c/t_{c_0} = 0.2$, which corresponds to extremely thin circles, while the results in fig. 122.b are associated with the reference wall-thickness value $t_c/t_{c_0} = 1$. Fig. 122 elucidates how the topology parameter L/R can be used as a tuning parameter for band gaps. The range of variation of L/R explores all the possible topologies which vary from a packed assembly of circles (see fig. 18) obtained for $L/R \to 0$, to the triangular lattice corresponding to $L/R \to 1$. It is interesting to note that for the

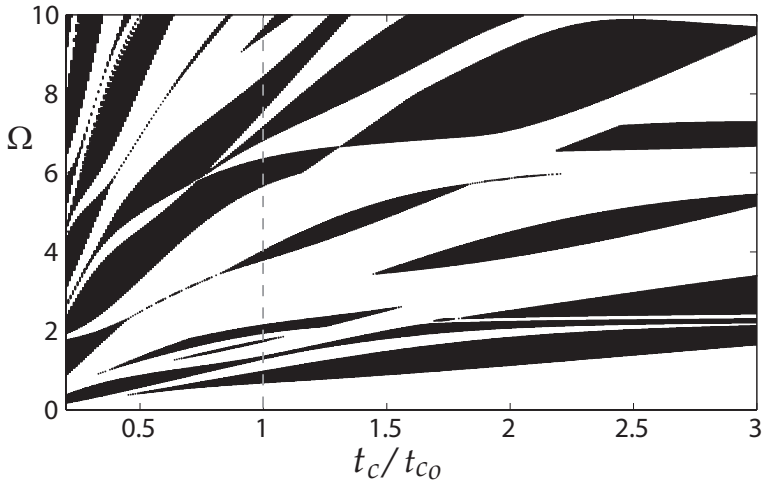

(a) $L/R = 0.60$

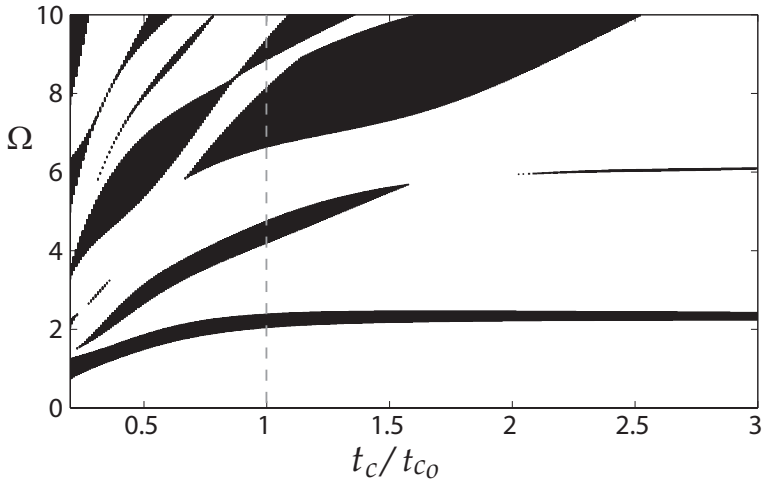

(b) $L/R = 0.90$

Figure 121: Band gap dependence upon t_c/t_{c_0}

latter (i.e. $L/R \to 1$), the obtained band gaps match exactly those predicted for a triangular lattice as reported in [75].

The results presented in figs. 121 and 122 demonstrate the design flexibility of the considered periodic lattice configuration. Of the two considered parameters, the wall thickness t_c appears as the most interesting one, as it allows tuning of the band gap distribution to be performed without the need for changes in the overall topology of the assembly. From this perspective, one may envision a manufacturing procedure

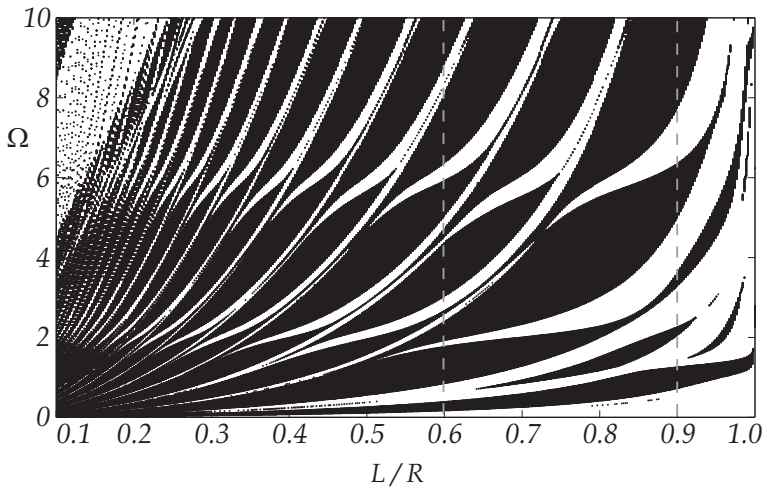

(a) $t_c/t_{c_0} = 0.2$

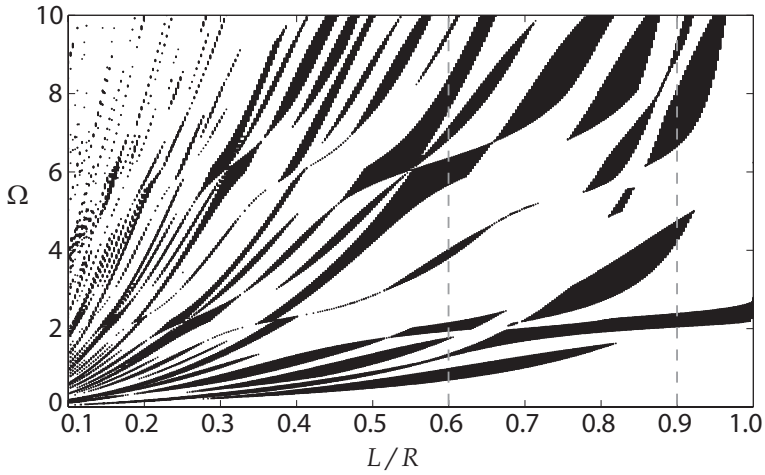

(b) $t_c/t_{c_0} = 1.0$

Figure 122: Band gap dependence upon L/R

which is able to generate the chiral lattice, and allows the flexibility to modify the wall thickness of the circles either locally, to introduce a discontinuity in periodicity, or over a number of consecutive cells defining a path along which acoustic waves need to be guided.

7.3.4 Phase Speeds and Group Velocities

A final analysis considers the dependence of phase speeds and group velocities upon frequency, direction, and lattice topology. The evaluation of wave speeds provides

important indications on the anisotropic nature of the lattice within a specified frequency range, it shows the existence of preferential directions of propagation and energy flow, and defines the dispersive nature of the medium. Dispersion, directionality and anisotropy all lead to wave-interference phenomena, which can be also exploited for effective focusing of the acoustic energy associated with propagating waves [83, 101]. Attention is devoted to the wave velocities of the first three modes, which could be directly associated with the wave modes of an equivalent isotropic medium, with the purpose of estimating the equivalent mechanical properties of the lattice along the lines of [75, 41].

In all results, velocities are normalized with respect to the phase velocity of the first mode estimated for $k \rightarrow 0, \omega \rightarrow 0$, which corresponds to the long wavelength, low frequency range where group and phase speeds are expected to be approximately equal.

Results for phase speeds corresponding to the first three modes for lattices defined by topology parameters $L/R = 0.60$ and $L/R = 0.90$ are shown respectively in fig. 123 and 124. These results are obtained for lattices with all other dimensions fixed to the values listed in Table 10. Fig. 123 presents polar plots of the phase speed for various values of normalized frequency. Curves for phase speeds corresponding to first and second modes are approximately circular at low frequencies, while they highlight the lattice anisotropy as frequency increases. Specifically, the polar curves clearly show the six-fold symmetry of the lattice, which is represented by lobes which become more and more relevant as frequency increases. A general trend for the first and second mode shows a decreasing phase speed as frequency increases. This behavior is in agreement with the fact that the corresponding dispersion branches in fig. 115.b are characterized by a decreasing slope as the wave vector approaches the edges of the first Brillouin zone. It is also interesting to note that the third mode shows a cut-off frequency at $\Omega \approx 1$, and a very limited variation over the first

Brillouin zone. The presence of a cut-off frequency and an almost flat dispersion branch correspond to a phase speed which approximately varies hyperbolically with respect to the wavenumber. This is confirmed by the strong variation in phase speed which is observed over the considered frequency range for the third mode. Similar considerations can be set forth from the analysis of the results for $L/R = 0.90$ shown in fig. 124, indicative of a behavior which is non-dispersive and isotropic over a much larger range of normalized frequencies and wavenumbers if compared to the $L/R = 0.60$ lattice for which strong directionality can be already observed at $\Omega \approx 0.3$.

Group velocity dependence upon frequency and direction for the considered configurations are presented in figs. 125 and 126. As expected, the group speeds for the first two modes in the low frequency limit are nearly identical to the corresponding phase speeds, confirming the non-dispersive behavior for long wavelengths. As frequency increases, however, group velocities show a very complex behavior which is characterized by caustics (cusps in group velocity distributions) of the kind observed in anisotropic media [101]. Such caustics are associated with strong energy focusing for propagating wave packets, resulting from interference between the various wave components propagating in the lattice plane. The third mode features very low group velocities in particular for $L/R = 0.90$, which is also a distinctive characteristic for this class of lattices.

The appearance of caustics in the group velocity diagrams of all considered wave modes and configurations is to be attributed to inflection points in the wave-front diagrams of fig. 114. To demonstrate the focusing of energy along preferential directions, the third wave mode corresponding to topology parameter $L/R = 0.90$ and normalized frequency $\Omega = 1.92$ is chosen as an example. The wave front associated with the aforementioned configuration is presented in fig. 127.a. An arbitrarily chosen set of wave vectors, numbered 1-9, corresponds to as many group velocities ($\bar{c_g}$) directions, also numbered 1-9. While the set of wave vectors approximately spans 90°, the

corresponding group velocity directions, which are normal to the corresponding wave front, appear to be mostly confined to two orientations as depicted in fig. 127.b. If a large set of wave vectors spanning 360° is considered (fig. 127.c), the corresponding group velocity vectors are mostly oriented in six directions as shown in fig. 127.d.

In certain instances however, it is possible to have the direction of group velocity coincide to that of wave vectors. This may occur only if the wave vector direction coincides with a symmetry axis of the frequency/wavenumber spectrum [101]. Collinearity of wave vectors and associated group velocity directions is confirmed in fig. 127.c, where the dashed arrow describes a group-velocity vector collinear to a given wave vector. The hexagonal symmetry of the chiral lattice, which also transpires in the frequency/wavenumber spectrum, then produces at least six such loci. Such occurrences nevertheless are not predominant for the chosen wave mode and frequency given the apparent elasto-dynamic anisotropy. If iso-frequency contours were to be perfectly circular, on the other hand, they would indicate that the direction of group velocity is always parallel to that of wave vectors, and moreover, that the frequency/wavenumber spectrum possesses infinite axes of symmetry. This may be the case for isotropic media, or in the case of low-frequency/wavelength regions corresponding to the first and second wave modes reported in fig. 124 and 126. To contrast isotropic wave propagation to the case presented above, the reader is referred to fig. 128, which corresponds to the first wave mode, topology parameter $L/R = 0.90$ and normalized frequency $\Omega = 0.30$. The same 9 wave vectors employed previously are superimposed onto the circular wave front currently considered. The corresponding group velocity vectors depicted in fig. 128.a and b are clearly aligned with their respective wave vectors. If a large set of wave vectors spanning 360° is considered, the corresponding group velocities evenly span the entire frequency/wavenumber spectrum as presented in fig. 128.c and d, indicating isotropic elasto-dynamic behavior.

In conclusion, the energy focusing suggested by caustics present in all considered

wave modes notably features a complex dependency upon frequency ω; the orientation and extent of cusps in group velocity diagrams, in fact, change according to both wave modes and frequencies. Chiral lattices, hence, offer considerable authority for steering elastic waves along desired directions. This could be accomplished by simply changing the excitation frequency of a disturbance-producing source.

7.4 Summary

In-plane wave propagation in chiral lattices is investigated through the application of Bloch analysis. The considered lattice features in-plane hexagonal geometry as well as chirality, and it is characterized by a set of parameters which significantly affect its elasto-dynamic behavior. The occurrence of band gaps, anisotropic behavior, and the dispersive characteristics of the considered lattices are evaluated for various combinations of characteristic geometric parameters. Of particular relevance are unique features such as strongly anisotropic behavior at higher frequencies, the significant dependence of band gap widths and center frequency on a limited set of characteristic geometric parameters, and the occurrence of caustics. The presented results suggest the possibility of utilizing the considered class of lattices for the design of novel phononic meta-materials.

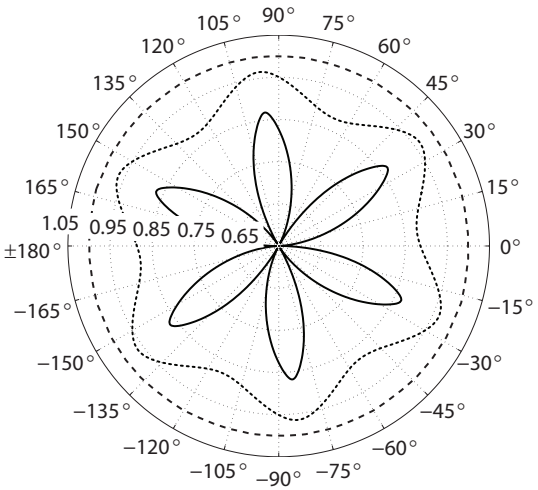

(a) Mode 1: - - - $\Omega = 0.05$, $\cdots$ $\Omega = 0.30$, — $\Omega = 0.45$

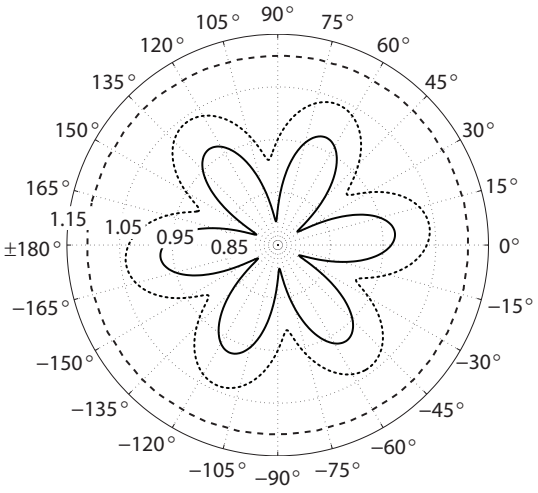

(b) Mode 2: - - - $\Omega = 0.05$, $\cdots$ $\Omega = 0.44$, — $\Omega = 0.57$

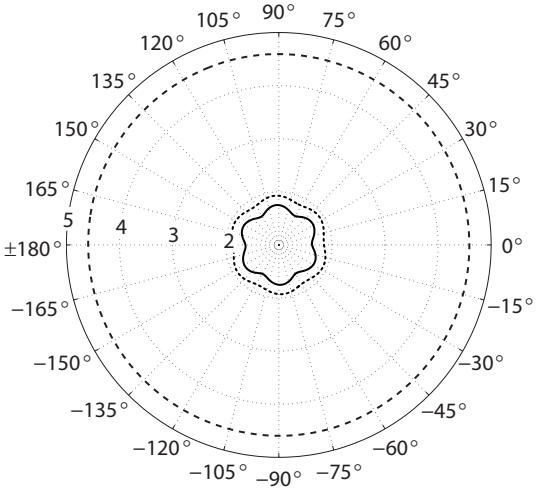

(c) Mode 3: - - - $\Omega = 1.00$, $\cdots$ $\Omega = 1.15$, — $\Omega = 1.20$

Figure 123: Phase velocity versus frequency for a lattice with $L/R = 0.60$

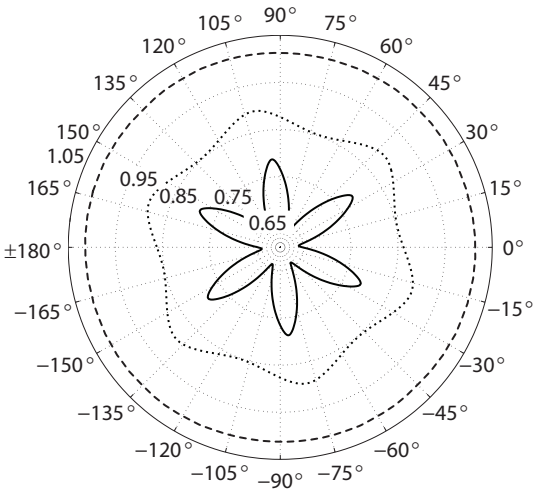

(a) Mode 1: - - - $\Omega = 0.30$, $\cdots$ $\Omega = 1.30$, — $\Omega = 1.55$

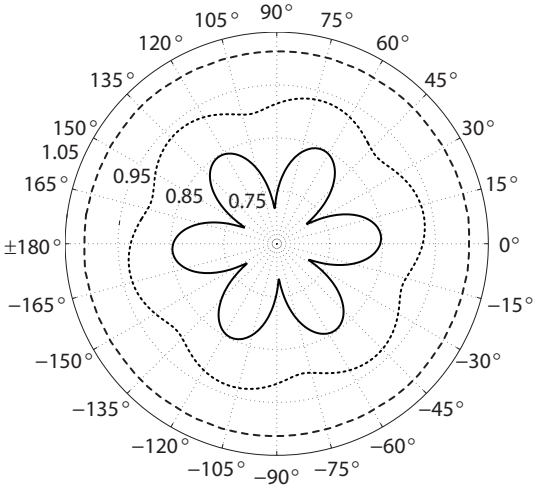

(b) Mode 2: - - - $\Omega = 0.30$, $\cdots$ $\Omega = 1.30$, — $\Omega = 1.62$

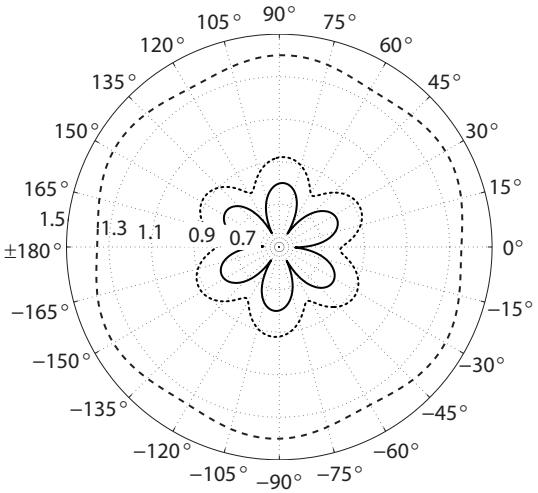

(c) Mode 3: - - - $\Omega = 1.84$, $\cdots$ $\Omega = 1.92$, — $\Omega = 1.97$

Figure 124: Phase velocity versus frequency for a lattice with $L/R = 0.90$

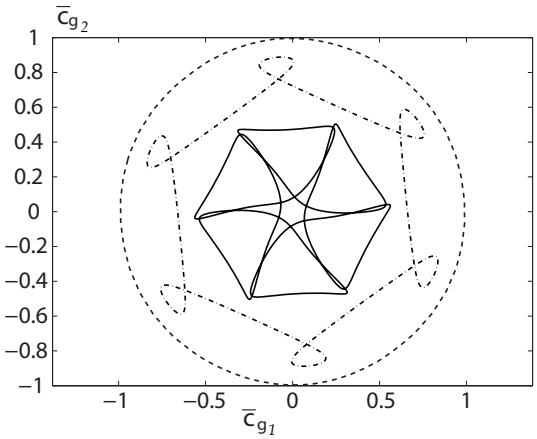

(a) Mode 1: - - - $\Omega = 0.05$, $\cdots$ $\Omega = 0.30$, — $\Omega = 0.45$

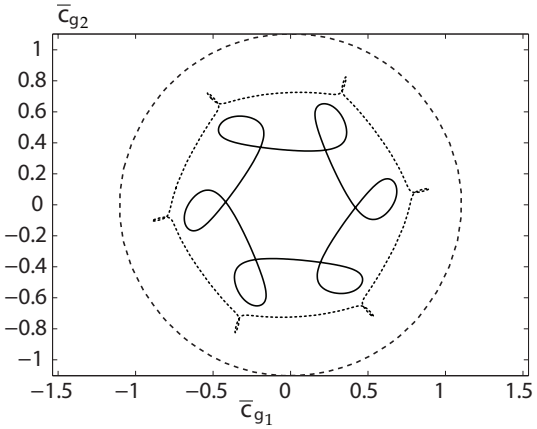

(b) Mode 2: - - - $\Omega = 0.05$, $\cdots$ $\Omega = 0.44$, — $\Omega = 0.57$

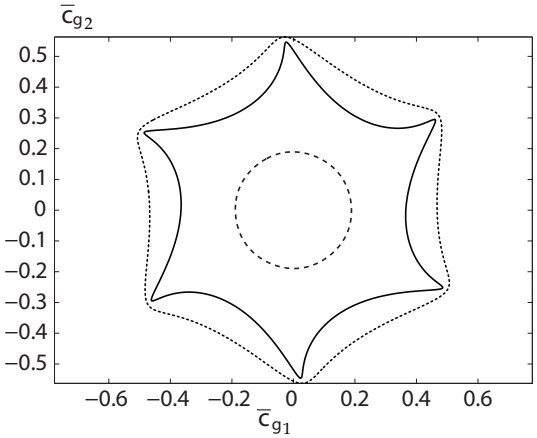

(c) Mode 3: - - - $\Omega = 1.00$, $\cdots$ $\Omega = 1.15$, — $\Omega = 1.20$

Figure 125: Group velocity components versus frequency for a lattice with $L/R = 0.60$

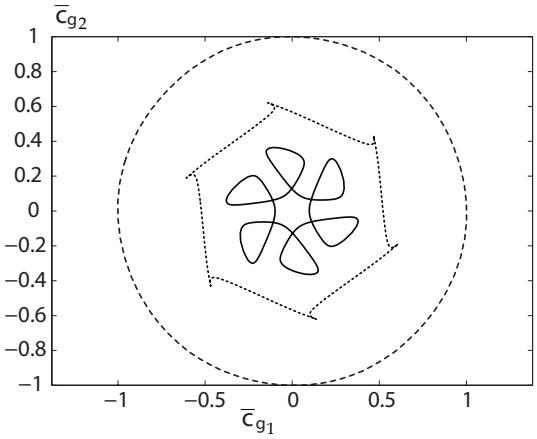

(a) Mode 1: - - - $\Omega = 0.30$, $\cdots$ $\Omega = 1.30$, — $\Omega = 1.55$

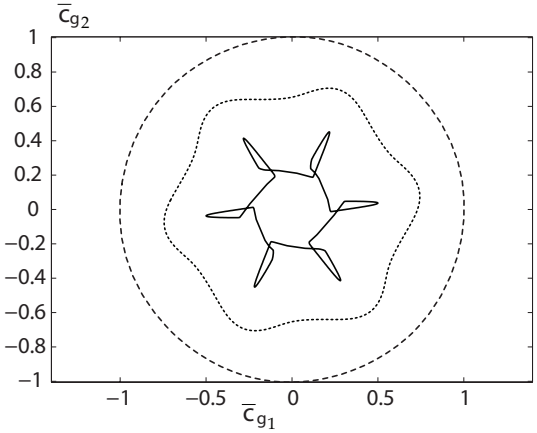

(b) Mode 2: - - - $\Omega = 0.30$, $\cdots$ $\Omega = 1.30$, — $\Omega = 1.62$

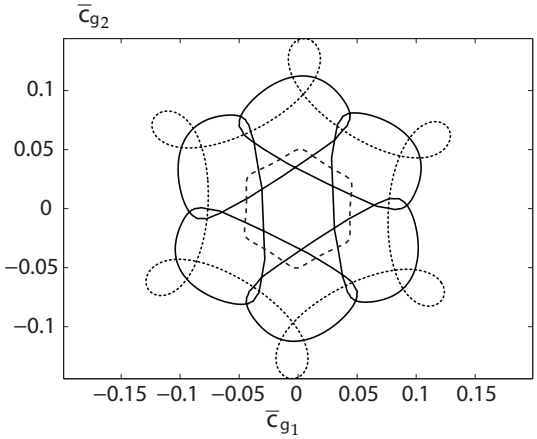

(c) Mode 3: - - - $\Omega = 1.84$, $\cdots$ $\Omega = 1.92$, — $\Omega = 1.97$

Figure 126: Group velocity components versus frequency for a lattice with $L/R = 0.90$

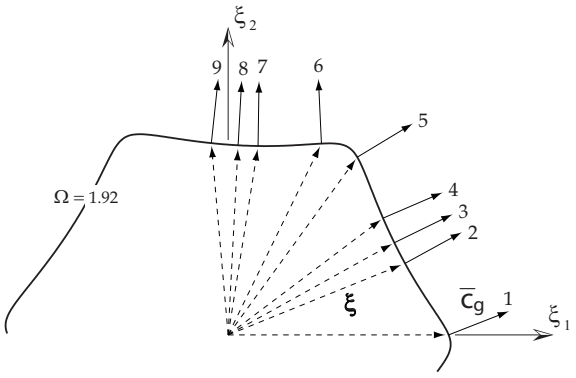

(a)

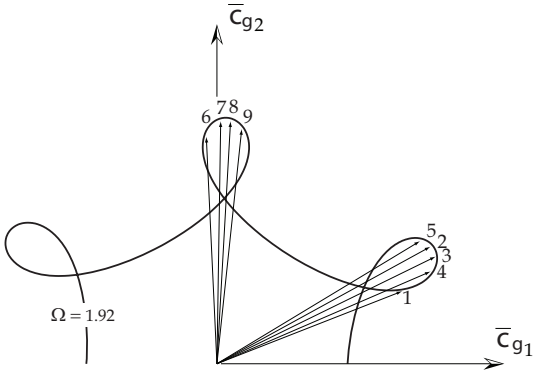

(b)

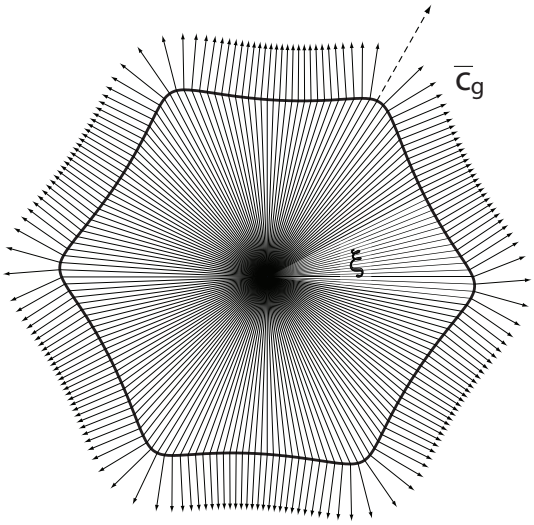

(c)

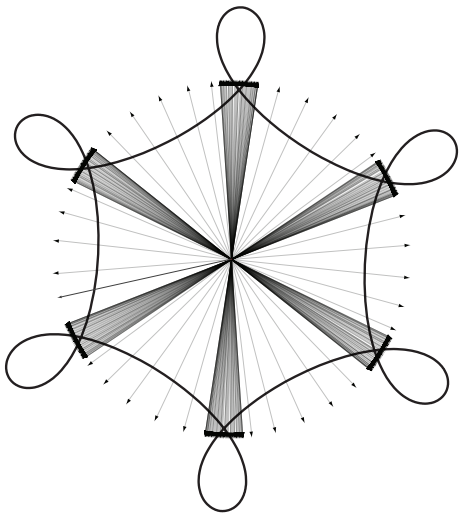

(d)

Figure 127: Caustics stemming from group velocity for $L/R = 0.90$, wave mode 3 and $\Omega = 1.92$

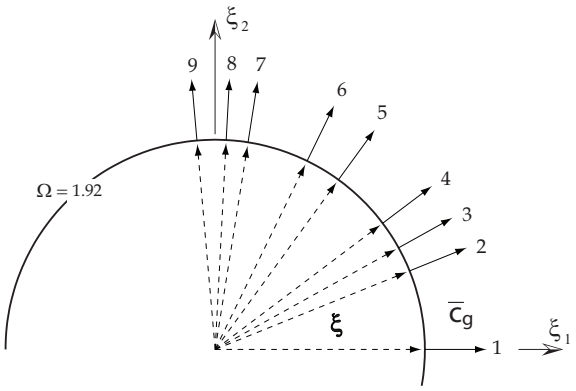

(a)

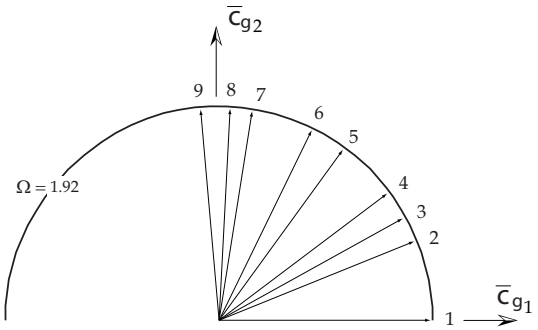

(b)

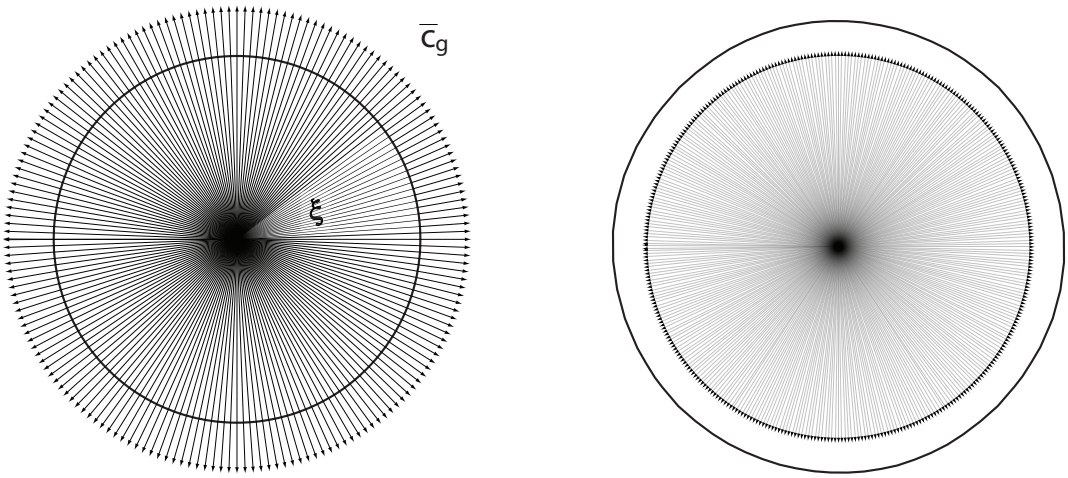

(c) (d)

Figure 128: Iso-frequency contours of dispersion relations and group velocity for $L/R = 0.90$, wave mode 1 and $\Omega = 0.30$

CHAPTER VIII

CONCLUDING REMARKS

8.1 summary

The research presented in this work investigates the elasto-static and elasto-dynamic response of hexagonal chiral lattices, which are composed of circular elements of acting as nodes connected by ribs or ligaments. Chirality denotes a geometry not invariant to reflections, or in other words, not symmetric to its mirror image. Hexagonal symmetry on the other hand is responsible for isotropic mechanical behavior. Previous findings documented in the literature reported that the chiral lattice is characterized by elastic properties strongly dependent upon a reduced set of geometric parameters, large-deformation capabilities, and a negative, in-plane Poisson's ratio equal to -1 characteristic of auxetic materials. These features instilled curiosity and motivated the research presented herein.

In-plane properties are determined with a refined analysis based on previous studies of the lattice's mechanical behavior documented in the literature. In-plane, equivalent elastic constants are determined through existing analytical methods and numerical models owing to the complexity of the structural topology. Specifically, Young's modulus and Poisson's ratio indicate that the chiral lattice features in-plane isotropic behavior, confirming previously documented analyses. In the literature on auxetic materials moreover, high shear stiffness resulting from the negative Poisson's ratio is often mentioned. The shear modulus for the chiral lattice, however, is found to be generally lower than that of the triangular lattice, but higher than that of square and hexagonal topologies. The estimated Young's modulus is the lowest of all considered periodic cellular solids. Poisson's ratio, shear modulus and Young's modulus

are proportional to the cube of the relative density. This is a characteristic of lattices whose mechanical behavior is dominated by bending deformations of slender, beam-like members. Out-of-plane elastic constants are determined with a 2-D representation of the unit cell. The shear modulus is the same in the x and y-directions but different than the in-plane value, suggesting transversally-isotropic mechanical behavior. Upper and lower-bound analytical estimates of the shear modulus are refined with finite-element models to include effects of out-of-plane thickness. The out-of-plane Young's modulus is also computed. Both shear and stiffness moduli are found to be proportional to the relative density.

Large deformation capabilities previously suggested in the literature are exploited to design a truss-core airfoil for both passive and active-morphing applications. The relative density and topology of the truss-core strongly affect the compliance of the proposed assemblies. Three aluminum truss-core-airfoil samples are manufactured and tested to confirm the compliance indicated by numerical models. An improved manufacturing technique, furthermore, has been employed to produce a chiral macro cell made of carbon-fiber material. The use of composite materials in particular allows embedding sensors within the truss-core members lending feasibility to the presented morphing concepts. Large-displacement capabilities are confirmed for both the aluminum truss-core-airfoil samples and the composite chiral macro cell. Numerical simulations of composite truss-core airfoils indicate that the achievable camber-wise deflections are twice as large than for the aluminum models. The unique dynamic response of chiral-core assemblies, furthermore, is exploited to design truss-core beams and airfoils with operational-deflection shapes denoted by localized deformations or kinks. In the case of truss-core airfoils in particular, the location of localized deflections can be controlled simply by selecting the appropriate excitation frequency. Importantly, operational deflection shapes are the result of excitation coinciding with

natural frequencies of the assembly, indicating high actuation authority. The aluminum airfoil samples were tested and corroborated the presence of kinks in good agreement with numerical models.

Finally, the elasto-dynamic response of the chiral lattice is investigated to assess the lattice's applicability as a phononic meta-material. Analyses of wave-propagation characteristics indicate a large number of stop bands of significant extent within the frequency range of the first ten wave modes resulting from the resonating of two topologically-distinct components: namely, nodes and ligaments. Dynamic deformations of the nodes are found to significantly affect elastic wave propagation, center frequency and stop-band magnitude. The presence of caustics in group-velocity diagrams indicates wave-focusing capabilities.

8.2 Research Contributions

The research presented in this thesis provides the following unique contributions:

- ◇ assessment of the in-plane and out-of-plane elastic properties of the chiral lattice;
- ◇ design of chiral truss-core airfoils for both passive and active-morphing applications;
- ◇ design of chiral truss-core assemblies with dynamic morphing capabilities via operational-deflection shapes featuring localized deformations;
- ◇ determination of the elasto-dynamic behavior of the chiral lattice with respect to phononic characteristics;

8.3 Limitations of the presented research

The complexity of the chiral topology hindered analytical determination of the in-plane mechanical properties for configurations with deformable circles, which are

instead based on corrected expressions obtained for simplified configurations. Existing techniques to determine equivalent elastic properties rely on the presence of a central joint, within the unit cell, at which internal components meet. Additional simplifications to derive elastic properties of cellular solids take advantage or reflection symmetry of the unit cell. The chiral lattice, however, features neither a central joint nor reflection symmetry. The resulting unit-cell analysis is hyperstatic. While various techniques that address redundant problems are available, they require the evaluation of potential energy, displacement-compatibility conditions and constitutive laws. Attempts to utilize these techniques lead to intractable analytical expressions resulting from the geometric complexity of the chiral lattice.

Expectations of in-plane, high shear stiffness of the chiral lattice associated with a negative Poisson's ratio, commonly mentioned in the literature, have been contradicted. The chiral lattice, in fact, is shown to be more compliant for shear-loading conditions than the triangular lattice.

The dependency of out-of-plane shear modulus on geometric parameters is equally complex. While upper and lower-bounds of the shear stiffness are expressed analytically, the influence of out-of-plane thickness requires the use of an interpolating polynomial.

8.4 Recommendations for Future work

8.4.1 Analytical methods for non-central cellular solids

While the shortcomings of the research presented in this thesis are certainly not welcome, they provide ample opportunities for future studies. In particular, existing analytical techniques to determine the elastic properties of cellular solids are most easily applicable to configurations denoted by reflection symmetry and the presence of a central joint. To this end, the formulation of novel analytical methods to handle non-central topologies would be of great scientific interest. The design of complex

deterministic cellular solids, for example, would be facilitated. Additional opportunities lay in the determination of micropolar constants, which may aid in clarifying the unusual internal stress distribution within the lattice when expanded or compressed.

8.4.2 Influence of manufacturing constraints on chiral lattices

The unique mechanical properties discussed in chapter 3 rely upon small lattice features such as circles, which do influence the global structural response even for vanishing radius. The limitations imposed by manufacturing constraints my hinder or at least alter the highly sensitive behavior to the topological characteristics of the lattice. Analytical models to assess to influence of deviations from the nominal lattice configuration, such as fillets where ligaments meet the circular components for example, may establish the sensitivity of mechanical behavior to manufacturing shortcomings.

8.4.3 Chiral honeycomb-core sandwich panels

Although it is found that the out-of-plane shear stiffness of chiral honeycombs is lower than that of current core geometries, such as the hexagonal honeycomb, additional considerations drive the design of sandwich panels. Core buckling for example is a very important characteristic. Preliminary studies of the bucking response of the chiral lattice based on linear analyses are documented in the literature. Complete investigations to determine the influence of imperfections however would provide a better assessment of chiral honeycombs as core components for sandwich panels.

8.4.4 Flow control via dynamic morphing

Dynamic operational-deflection shapes of truss core airfoils also provide unique opportunities for future research. The high actuation authority provided by the fact the localized deformations are associated with natural frequencies of the assembly indicates that truss-core airfoils may be employed for flow control. Previous studies on the dynamics of fluids in presence of oscillating walls, in fact, indicated a significant

drag reduction. Computational-fluid-dynamic simulations may then indicate if the kinks of truss-core airfoils can used to reduce drag or delay stall for example.

8.4.5 Phononic meta-materials

The most promising research possibilities stemming from the work presented in this thesis, however, is the design of phononic meta-materials with periodic cellular solids. In a 2-D framework the chiral lattice has already demonstrated very promising characteristics. Future work should hence be devoted to designing three-dimensional assemblies derived from the geometric arrangement of the chiral topology. An additional degree of freedom in the design of acoustic meta-materials may be provided by the inclusion of fluids in the periodic crystal. In particular, acoustic absorption provided by porous cell walls may affect band-gap extent and center frequency, and it may also provide additional impedance effects useful for steering elastic waves in desired directions.

REFERENCES

[1] Agarwal, B. D. and Broutman, L. J., *Analysis and Performance of Fiber Composites.* John Wiley, New York, 1980.

[2] ANSYS®, *Theory Reference.* ANSYS Academic Research, Release 11.0, 2007.

[3] Auld, B. A., *Acoustic Fields and Waves in Solids.* Malabar, FL: Krieger Publ. Co., 2^{nd} ed., 1990.

[4] Bae, J.-S., Seigler, T. M., Inman, D. J., and Lee, I., "Aerodynamic and aeroelastic considerations of a variable-span morphing wing," vol. 3, pp. 2378 – 2386, 2004.

[5] Bar-Cohen, Y., *Electroactive polymer (EAP) actuators as artificial muscles - reality, potential and challenges.* SPIE Press, 2001.

[6] Barlas, T. K. and Van Kuik, G., "Smart materials and structures," *Journal of Physics: Conference Series*, vol. 75, pp. 1–20, 2007.

[7] Bathe, K.-J., *Finite Element Procedures.* Upper Saddle River, NJ: Prentice Hall, 1^{st} ed., 1996.

[8] Bauchau, O., *AE 6106 Structural Analysis Lecture notes.* Georgia Institute of Technology, Fall 2004.

[9] Bettini, P., Airoldi, A., Di Landro, L., Sala, G., Spadoni, A., and Ruzzene, M., "Design and manufacturing of composite chiral structures with morphing capabilities," *Proceedings of the 26^{th} International Congress of the Aeronautical Sciences ICAS2008*, 2008.

[10] Bornengo, D., Scarpa, F., and Remillant, C., "Morphing airfoil concept with chiral core structure," *I MECH E Part G, Journal of Aerospace Engineering*, vol. G3, no. 8, pp. 185–192, 2005.

[11] Bowman, J., Sanders, B., and Weisshaar, T., "Identification of military morphing aircraft missions and morphing technology assessment," vol. 4698, pp. 121 – 132, 2002.

[12] Brillouin, L., *Wave Propagation in Periodic Structures.* New York, NY: Dover, 1953.

[13] Buter, A., Ehlert, U. C., Sachau, D., and Breitbach, E., "Adaptive rotor blade concepts, direct twist and camber variation," 2000.

[14] Caddock, B. D., Evans, K. E., and Masters, I. G., "Honeycomb cores with negative Poisson ratio for use in composite sandwich panels," *Proceeding of the ICCM/VIII*, vol. 3-E, 1991.

[15] Cadogan, D., Scarborough, S., Gleeson, D., Dixit, A., Jacob, J., and Simpson, A., "Recent development and test of inflatable wings," *Collection of Technical Papers - AIAA/ASME/ASCE/AHS/ASC Structures, Structural Dynamics and Materials Conference*, vol. 9, pp. 6428 – 6442, 2006.

[16] Cadogan, D., Smith, T., Uhelsky, F., and MacKusick, M., "Morphing inflatable wing development for compact package unmanned aerial vehicles," vol. 4, pp. 3205 – 3217, 2004.

[17] Campanile, L. and Sachau, D., "Belt-rib concept: a structronic approach to variable camber," *Journal of Intelligent Material Systems and Structures*, vol. 11, no. 3, pp. 215 – 224, 2000.

[18] Chang, C. C. and Ebcioglu, I. K., "Effect of cell geometry on the shear modulus and on density of sandwich panel cores," *Journal of Basic Engineering*, vol. 83, no. 4, pp. 513–518, 1961.

[19] Cook, R. D., Malkus, D. S., Plesha, M. E., and Witt, R. J., *Concepts and Applications of Finite Element Analysis*. Wiley, fourth ed., 2001.

[20] Dano, M. L. and Hyer, M. W., "Sma-induced snap-through of unsymmetric fiber-reinforced composite plates," *International Journal of Solids and Structures*, vol. 40, pp. 5949–5972, 2003.

[21] Dempsey, B. M., Eisele, S., and McDowell, D. L., "Heat sink applications of extruded metal honeycombs," *International journal of heat and mass transfer*, vol. 48, pp. 527 – 535, 2005.

[22] Deshpande, V. S., Ashby, M. F., and Fleck, N. A., "Foam topology bending versus stretching dominated architectures," *Acta Materialia*, vol. 49, pp. 1035–1040, 2001.

[23] Diaz, A., Haddow, A., and Ma, L., "Design of band-gap grid structures," *Structural Multidisciplinary Optimization*, vol. 29, no. 6, pp. 418–431, 2005.

[24] Diebels, S. and Steeb, H., "Stress and couple stress in foams," *Computational Materials Science*, vol. 28, no. 3-4, pp. 714–722, 2003.

[25] Dos Santos e Lucato, S. and Evans, A., "The load capacity of a kagome based high authority shape morphing structure," *Journal of Applied Mechanics, Transactions ASME*, vol. 73, no. 1, pp. 128 – 133, 2006.

[26] Dos Santos E Lucato, S., McMeeking, R., and Evans, A., "Actuator placement optimization in a kagome based high authority shape morphing structure," *Smart Materials and Structures*, vol. 14, no. 4, pp. 869 – 875, 2005.

[27] Doyle, J., *Wave Propagation in Structures*. Springer Verlag, second ed., 1997.

[28] Doyle, J., "A spectrally-formulated finite element for longitudinal wave propagation," *Int. Journal of Analytical and Experimental Modal Analysis*, vol. 3, pp. 1–5, 1998.

[29] Ebcioglu, I., Baltes, J., and Chang, C., "Effect of cell geometry on proportional limit shear stress of metallic foil sandwich panel core," pp. 5 –, 1961.

[30] Ebinger, T., Steeb, H., and Diebels, S., "Modeling macroscopic extended continua with the aid of numerical homogenization schemes," *Computational Materials Science*, vol. 32, no. 3-4, pp. 337–347, 2005.

[31] El-Raheb, M. and Wagner, P., "Transmission of sound across a trusslike periodic panel; 2-d analysis," *Journal of the Acoustical Society of America*, vol. 102, no. 4, pp. 2176 – 2183, 1997.

[32] Eringen, A. C., "Linear theory of micropolar elasticity," *Journal of Mathematics and Mechanics*, vol. 15, no. 6, pp. 909–923, 1966.

[33] Evans, A. G., Hutchinson, J. W., and Ashby, M. F., "Cellular metals," *Current Opinion in solid state & material science*, vol. 3, pp. 288 – 303, 1998.

[34] Evans, A. G., Hutchinson, J. W., and Ashby, M. F., "Multifunctionality of cellular metal systems," *Progress in Material Science*, vol. 43, pp. 171 – 221, 1999.

[35] Evans, A. G., Hutchinson, J. W., Fleck, N. A., Ashby, M. F., and Wadley, H. N., "The topological design of multifunctional cellular materials," *Progress in Material Science*, vol. 46, pp. 309 – 327, 2001.

[36] Evans, K. E., "Design of doubly curved sandwich panels with honeycomb cores," *Computers and Structures*, vol. 17(2), no. 2, pp. 95–111, 1991.

[37] Evans, K., Nkansah, M., Hutchinson, I., and Rogers, S., "Molecular network design," *Nature*, vol. 353, no. 6340, pp. 124 –, 1991.

[38] Fung, Y., *Foundations of solid mechanics*. Prentice Hall, 1968.

[39] Ghandi, M. V. and Thompson, B. S., *Smart Materials and Structures*. Chapman and Hall, 1992.

[40] Gibson, L. J. and Ashby, M. F., *Cellular solids: structure and properties*. Cambridge University Press, second ed., 1997.

[41] Gonella, S. and Ruzzene, M., "Homogenization and equivalent in-plane properties of two-dimensional periodic lattices," *International Journal of Solids and Structures*, 2008.

[42] Grediac, M., "Finite element study of the transverse shear in honeycomb cores," *International Journal of Solids and Structures*, vol. 30, no. 13, pp. 1777 – 1788, 1993.

[43] Grediac, M. and Vautrin, A., "Applying finite element computations for the determination of transverse shear moduli of honeycomb cores," *Metal Matrix Composites*, vol. 4, pp. 360 –, 1993.

[44] Grima, J. N., Gatt, R., and Farrugia, P.-S., "On the properties of auxetic meta-tetrachiral structures," *Physica Status Solidi B*, vol. 245, pp. 511–520, 2008.

[45] Herbert, E. G., Oliver, W. C., and Pharr, G. M., "On the measurement of yield strength by indentation," *Philosophical Magazine*, vol. 86, no. 33, pp. 5521–5539, 2006.

[46] Hodges, D. H. and Pierce, A. G., *Introduction to Structural Dynamics and Aeroelasticity*. Cambridge University Press, 2002.

[47] Hoff, N., "Bending and buckling of rectangular sandwich plates," Tech. Rep. TN 2225, NACA, 1950.

[48] Hoff, N., "Structural problems of future aircraft," *Engineering*, vol. 172, no. 4475, pp. 573 – 575, 1951.

[49] Hoff, N., "Thermal barrier – structures," *American Society of Mechanical Engineers – Papers*, pp. 6 –, 1954.

[50] Hussein, M. I., Hamza, K., Hulbert, G., and Saitou, K., "Optimal synthesis of 2d phononic crystals for broadband frequency isolation," *Waves in Random and Complex Media*, vol. 17, no. 4, pp. 491–510, 2007.

[51] Hussein, M. I., Hulbert, G., and Scott, R., "Tailoring of wave propagation characteristics in periodic structures with multilayer unit cells," in *Proceedings of 17th American Society of Composites Technical Conference*, 2002.

[52] Jones, R. M., *Mechanics of composite materials*. Taylor & Francis, second ed., 1999.

[53] Kelsey, S., Gellatly, R., and Clark, B., "Shear modulus of foil honeycomb cores," *Aircraft Engineering*, vol. 30, no. 356, pp. 294 – 302, 1958.

[54] Kelvin, L., *Baltimore Lectures on Molecular Dynamics and the Wave Theory of Light*. C. J. Clay and Sons, London, U.K., 1904.

[55] Kock, W. E., "Metallic delay lenses," *Bell System Technical Journal*, vol. 27, pp. 58 – 82, 1948.

[56] Kudva, J. N., "Overview of the darpa smart wing project," *Journal of Intelligent Materials Systems and Structures*, vol. 15, no. 4, pp. 261 – 267, 2004.

[57] Kumar, R. and McDowell, D., "Generalized continuum modeling of 2-D periodic cellular solids," *International Journal of Solids and Structures*, vol. 41, no. 26, pp. 7399–7422, 2004.

[58] Lakes, R. S., "Foam structures with a negative poisson's ratio," *Science*, vol. 235, pp. 1038–1040, 1987.

[59] Lakes, R. S., "Deformation mechanisms in negative poisson's ratio materials: structural aspects," *Journal of Materials Science*, vol. 26, pp. 2287–2292, 1991.

[60] Lakes, R. S., "Elastic and viscoelastic behavior of chiral materials," *Int. J. of Mechanical Sciences*, vol. 43, no. 7, pp. 1579 – 1589, 2001.

[61] Lakes, R. S. and Benedict, R., "Noncentrosymmetry in micropolar elasticity," *Internal Journal of Engineering Science*, vol. 20, no. 10, pp. 1161 – 1167, 1982.

[62] Leelavanichkul, S. and Cherkaev, A., "Why the grain in tree trunks spirals: A mechanical perspective," *Structural and Multidisciplinary Optimization*, vol. 28, no. 2-3, pp. 127 – 135, 2004.

[63] Li, J. and Chan, C. T., "Double-negative acoustic metamaterial," *Physical Review Letters E*, vol. 70, no. 5, p. 055602, 2004.

[64] Love, A. E. H., *A Treatise on the Mathematical Theory of Elasticity*. Dover Publications, 4^{th} ed., 1927.

[65] March, J., *Advanced Organic Chemistry: Reactions, Mechanisms, Structure*. John Wiley and Sons, New York, NY, fourth ed., 1992.

[66] Masters, I. G. and Evans, K. E., "Models for the elastic deformation of honeycombs," *Composite Structures*, vol. 35, no. 4, pp. 403–422, 1996.

[67] McGowan, A. M. R., Cox, D. E., Lazos, B. S., Waszak, M. R., Raney, D. L., Siochi, E. J., and Paul Pao, S., "Biologically-inspired technologies in NASA's morphing project," *Proceedings of SPIE - The International Society for Optical Engineering*, vol. 5051, pp. 1 – 13, 2003.

[68] Mohammadi, B., "Fluid dynamics computation with NSC2KE," Tech. Rep. 0164, INRIA, 1994.

[69] Monner, H. P., Sachau, D., and Breitbach, E., "Design aspects of the elastic trailing edge for an adaptive wing," October 1999.

[70] Moored, K. W. and Bart-Smith, H., "The analysis of tensegrity structures for the design of a morphing wing," *Journal of Applied Mechanics, Transactions ASME*, vol. 74, no. 4, pp. 668 – 676, 2007.

[71] Nowak, A. M., *Chiral nuclear dynamics*. Singapore, River Edge, NJ, 1996.

[72] Pabst, W., "Micropolar materials," *Journal of Ceramics-Silikáty*, vol. 49, no. 3, pp. 170–180, 2005.

[73] Page, J., Sukhovich, A., Yang, S., Cowan, M., Van Der Biest, F., Tourin, A., Fink, M., Liu, Z., Chan, C., and Sheng, P., "Phononic crystals," *Physica Status Solidi C: Conferences*, vol. 1, no. 11, pp. 3454 – 3462, 2004.

[74] Penzien, J. and Didriksson, T., "Effective shear modulus of honeycomb cellular structure," *AIAA Journal*, vol. 2, no. 3, pp. 531 – 535, 1964.

[75] Phani, A. S., Woodhouse, J., and Fleck, N. A., "Wave propagation in two-dimensional periodic lattices," *Journal of the Acoustical Society of America*, vol. 119, no. 4, pp. 1995 – 2005, 2006.

[76] Prall, D. and Lakes, R. S., "Properties of a chiral honeycomb with a poisson's ratio -1," *International Journal of Mechanical Sciences*, vol. 39, pp. 305–314, 1996.

[77] Psarobas, I. E., "Phononic crystals, sonic band-gap materials," *Special Issue of the Journal of Structural, Physical, and Chemical Aspects of Crystalline Materials*, vol. 220, no. 9-10, 2005.

[78] Richardson, L. F., "The deferred approach to the limit," *Philosophical Transactions of the Royal Society of London, Series A*, vol. 226, p. 299349, 1927.

[79] Roache, P. J., *Verification and Validation in Computational Science and Engineering*. Hermosa Publishers, Albuquerque, New Mexico, 1998.

[80] Ruzzene, M., "Vibration and sound radiation of sandwich beams with honeycombs," *Journal of Sound and Vibration*, vol. 277, pp. 741–763, 2004.

[81] Ruzzene, M. and Scarpa, F., "Control of wave propagation in sandwich beams with auxetic core," *Journal of Intelligent Material Systems and Structures*, vol. 14, no. 7, pp. 443 – 454, 2003.

[82] Ruzzene, M., Scarpa, F., and Soranna, F., "Wave beaming effects in two-dimensional cellular structures," *Smart Materials and Structures*, vol. 12, no. 3, pp. 363 – 372, 2003.

[83] Ruzzene, M., Scarpa, F., and Soranna, F., "Wave beaming effects in two-dimensional cellular structures," *Smart Materials and Structures*, vol. 12, no. 3, pp. 363 – 372, 2003.

[84] Schultz, M. R. and Hyer, M. W., "Snap-through of unsymmetric cross-ply laminates using piezoceramic actuators," *Journal of Intelligent Material Systems and Structures*, vol. 14, pp. 795–814, 2003.

[85] Sigmund, O. and Jensen, J., "Systematic design of phononic band-gap materials and structures by topology optimization," *Phylosophical Transactions of the Royal Society London, Series A (Mathematical, Physical and Engineering Sciences*, vol. 361, no. 1806, pp. 1001–1019, 2003.

[86] Sigmund, O., Torquato, S., and Aksay, I., "On the design of 1-3 piezocomposites using topology optimization," *Journal of Materials Research*, vol. 13, no. 4, pp. 1038 – 1048, 1998.

[87] Smith, S. W., Jacob, J. D., Jones, R. J., Scarborough, S. E., and Cadogan, D. P., "A high-altitude test of inflatable wings for low-density flight applications," *Collection of Technical Papers - AIAA/ASME/ASCE/AHS/ASC Structures, Structural Dynamics and Materials Conference*, vol. 2, pp. 1264 – 1276, 2006.

[88] Spadoni, A. and Ruzzene, M., "Structural and acoustic behavior of chiral trusscore beams," *Procedings of the ASME IMECE 2004 Noise Control and Acoustic Division, Anaheim, CA*, November 2004.

[89] Spadoni, A., Ruzzene, M., and Scarpa, F., "Dynamic response of chiral truss-core assemblies," *Journal of Intelligent Materials Systems and Structures*, vol. 17, no. 11, pp. 941–952, 2005.

[90] Spadoni, A. and Ruzzene, M., "Numerical and experimental analysis of the static compliance of chiral truss-core airfoils," *Journal of Mechanics of Materials and Structures*, vol. 2, no. 5, p. 965, 2007.

[91] Spadoni, A. and Ruzzene, M., "Static aeroelastic response of chiral-core airfoils," *Journal of Intelligent Materials Systems and Structures*, vol. 18, pp. 1067 – 1075, 2007.

[92] Tibert, A. and Pellegrino, S., "Review of form-finding methods for tensegrity structures," *International Journal of Space Structures*, vol. 18, no. 4, pp. 209 – 223, 2003.

[93] Trease, B. P. and Kota, S., "Synthesis of adaptive and controllable compliant systems with embedded actuators and sensors," *Proceedings of the ASME Design Engineering Technical Conference*, vol. 2006, pp. 13 –, 2006.

[94] Trease, B. p. and Kota, S., "Adaptive and controllable compliant systems with embedded actuators and sensors," *Proceedings of SPIE - The International Society for Optical Engineering*, vol. 6525, pp. 65251 –, 2007.

[95] Trenker, M., "Design concepts for adaptive airfoils with dynamic transonic flow control," *Journal of Aircraft*, vol. 40, no. 4, pp. 734 – 740, 2003.

[96] Wang, A. J., Kumar, R. S., and McDowell, D. L., "Mechanical behavior of extruded prismatic cellular metals," *Mechanics of advanced materials and structures*, vol. 12, pp. 185 – 200, 2005.

[97] Wang, A. J. and McDowell, D. L., "In-plane stiffness and yield strength of periodic metal honeycombs," *Journal of engineering materials and technologies*, vol. 126, pp. 137 – 156, 2004.

[98] Weiglhofer, W. S. and Lakhtakia, A., eds., *Introduction to Complex Mediums for Optics and Electromagnetics*, vol. PM123. SPIE Press, 2003.

[99] Wlezien, R., Horner, G., McGowan, A., Padula, S., Scott, M., Silcox, R., and Simpson, J., "The aircraft morphing program," *Proceedings of SPIE - The International Society for Optical Engineering*, vol. 3326, pp. 176 – 187, 1998.

[100] Wojciechowski, K., "Two-dimensional isotropic system with a negative poisson ratio," *Physics Letters A*, vol. 137, pp. 60–64, 1989.

[101] Wolfe, J. P., *Imaging Phonons: Acoustic Wave Propagation in Solids*. Cambridge University Press, 1998.

[102] Zenkert, D., ed., *The handbook of sandwich construction*. EMAS Publishing, 1997.